DOCTOR OF PHILOSOPHY

Development of MRI-compatible Transducer Array for Focused Ultrasound Surgery: The Use of Relaxor-based Piezocrystals

Qiu, Zhen

Award date:
2014

DOCTOR OF PHILOSOPHY

Development of MRI-compatible Transducer Array for Focused Ultrasound Surgery:

The Use of Relaxor-based Piezocrystals

Zhen Qiu

2014

University of Dundee

Development of MRI-compatible Transducer Arrays for Focused Ultrasound Surgery: The Use of Relaxor-based Piezocrystals

By

Zhen Qiu

UNIVERSITY OF DUNDEE

Doctoral thesis submitted in fulfilment of the requirements for the degree of doctor of Philosophy (PhD) to the school of Engineering, Physics and Mathematics, University of Dundee, Scotland, UK

February 2014

DECLARATION

I, Zhen Qiu, hereby declare that this thesis entitled, "**Development of MRI-compatible Transducer Array for Focused Ultrasound Surgery: The Use of Relaxor-based Piezocrystals**", submitted to University of Dundee for the degree of Doctor of Philosophy represents my own work. All references cited have been consulted by me; no part of the work referred to in this thesis has been supported in application of another degree or qualification of this university or any other university or institute of learning.

Signature: **Date:**

CERTIFICATE

This is to certify that Miss Zhen Qiu has done this research under my supervision and complied with all the requirements for the submission of this Doctor of Philosophy thesis to the University of Dundee.

Signature: **Date:**

ACKNOWLEDGEMENTS

I would like to express my deepest appreciation to all those who provided me the possibility to complete this dissertation. A special gratitude I give to my main supervisor Professor Sandy Cochran, who has guided, advised and helped me to go through the whole PhD study in many ways. I'd like to offer my great thanks to all the supports provided by Dr. Zhihong Huang, my second supervisor. I would like to thank Dr. Christine Démodé as well for her advices and encouragements through my studies, especially the suggestions in simulating.

I would like to express my great appreciation to my colleges, Mr. Roderick Habeshaw and Mr. Rui Cao, for their contributions in transducer array functional testing experiments. I am particularly grateful to Dr. Muhammad Sadiq for his help and cooperation for the material characterization work; and to Mr Graham Ceasey, for his great effort and contributions in fabricating and manufacturing the array transducers. My special thanks are extended to Diagnostic Sonar Ltd. (DSL) for lending the driving instruments used in this work, and to Dr Jack Ng at Heriot-Watt University for preparing the flexible printed circuits.

I would also like to thank my colleges and friends in the group for their companies. I appreciate all the knowledge we exchanged and all the laughs we shared together.

My deepest thanks I give to my parents and my fiancé, your love, support and tolerance have always been my source of courage and momentum to keep going.

Zhen Qiu

The research presented in this thesis was funded by Scottish Universities Physics Alliance (SUPA) Prize Studentship.

TABLE OF CONTENTS

LIST OF FIGURES

LIST OF TABLES

GLOSSARY OF TERMS

ABBREVIATION

AP	Anterior – posterior direction
AR	Aspect ratio
BCT	Breast conserving treatment
DOF	Depth of the focal zone
FUS	Focused ultrasound surgery
FEA	Finite element modelling
FWHM	Full width at half maximum
FOH	fiber optic probes
HIFU	High intensive focused ultrasound
HF	Head – foot direction
LE	Length extensional
LTE	Length-thickness Extensional
MRI	Magnetic resonance imaging
MRgFUS	MRI guided Focused Ultrasound Surgery
Mn: PIN-PMN-PT	Manganese Doped Lean Indium Niobate – Lead Magnesium Niobate – Lead Titanate piezocrystal material
PRAP	Piezoelectric resonance analysis program
PMN-PT	Lead Magnesium Niobate – Lead Titanate piezocrystal material
PIN-PMN-PT	Lean Indium Niobate – Lead Magnesium Niobate – Lead Titanate piezocrystal material
PCB	Printed ciucuit board
PZT	Lead zirconate titanate piezoelectric ceramics material
RE	Radial extensional
RL	Right – left direction
RFB	Radiation force balance
SD	Standard diviation
TE	Thickness extensional
TS	Thickness shear
US	Ultrasound
USgFUS	Ultrasound guided focused ultraound surgery

SYMBOLS

A_s	Source area
A_f	Cross-sectional area of the focus
c	the speed of sound
c^E_{ij}	Elastic stiffness constants measured with constant electric field
c^D_{ij}	Elastic stiffness constants measured with constant displacement field
D	Diameter of the disc plate or device
d_{ij}	piezoelectric strain constant

e_{ij}	piezoelectric stress constant
E_B	External electrical bias field
f	Frequency
$f\#$	f-number
f_e	electrical resonance frequency
f_m	mechanical resonance frequency
h	the height of the triangle element from the base
h_{ij}	piezoelectric stiffness constant
G	Focal gain
g_{ij}	piezoelectric voltage constant
k_{ij}	coupling coefficient
k	the width of the dicing kerf
k_{eff}	Effective coupling coefficients
p	Dicing pitch
P	Pressure
Q_M	Mechanical factor
s	Sensitivity of hydrophone
$s^E{}_{ij}$	Elastic stiffness constants measured with constant electric field
$s^D{}_{ij}$	Elastic stiffness constants measured with constant displacement field
T	Temperature
$T_{R\text{-}T}$	Rhombohedral to Tetragonal Phase Transition Temperature
T_C	Curie temperature
t	The thickness of the piezoelectric material
$\Delta\tau$	Propagating time delay of any element compared to centre element of the array transducer
VF	Volume fraction of composite
w	the pillar width within composite
$Y(f)$	Admittance spectrum
Z	Impedance
Z_{ac}	Acoustic impedance
$Z(f)$	Impedance spectrum
ε^S	permittivity under constant strain
ε^T	permittivity under constant stress
$\varepsilon_r{}^S$	Relative permittivity under constant strain
$\varepsilon_r{}^T$	Relative permittivity under constant stress

ABSTRACT

Focused ultrasound surgery (FUS) is considered as a promising approach for treating cancer and other conditions and is gaining increasing interest. However, the limited availability of experimental ultrasound array sources and multichannel electronics able to drive them hinder the research into FUS system configurations for patient conditions such as breast cancer.

The work in this dissertation explored the development of ultrasound arrays for MRI guided FUS, from the point of view of the potential piezoelectric material of choice. Two materials are of particular interests in this work: Binary $(x)Pb(Mg_{1/3}Nb_{2/3})\ O_3 - (1-x)PbTiO_3$ (PMN-PT) piezocrystal, and newly specialized FUS material, PZ54 ceramic. A characterization methodology was developed to fully characterize the materials of choice, under ambient and extreme conditions relevant to FUS applications. Practicalities of adopting these materials into FUS were studied by using the characterized materials in designing and fabricating FUS arrays. A spherical, faceted array geometry inspired by the geodesic dome structure was proposed and implemented for the first time. Four bespoke devices, each with 96 individual elements, were implemented using PZ26 ceramic, PZ26 composite, PZ54 composite and PMN-PT composite materials, respectively for comparison. The arrays were connected to commercial electronics afterwards, to explore a prototyping route for connecting FUS devices and modular driving systems.

It is concluded that PMN-PT piezocrystal and PZ54 ceramic material can offer excellent performance over conventional piezoelectric ceramics, although PMN-PT piezocrystal is sensitive to extreme conditions. The usable range of PMN-PT is suggested to be limited to 60°C in temperature and 10 MPa in pressure. However, PMN-PT piezocrystal could still be a potential alternative to conventional ceramics in FUS application if assisted with sufficient cooling circulation and bias field. The geodesic array geometry is also concluded to be able to achieve good focusing of ultrasound beam. With optimized phase control through multi-channel electronics, the focusing was improved with focusing gain up to about 30; the steering range of focus was explored within a volume of 5 x 5 x 10 mm^3 beyond the array's geometric focus, side lobes were limited to below the level of -9 dB in acoustic intensity. Larger numbers of individual controllable elements and alternative array designs will be explored in future to investigate application such as breast cancer treatment and potential pre-clinical trials.

CHAPTER 1 INTRODUCTION

Focused ultrasound surgery (FUS), a completely non-invasive therapeutic approach, is of increasing interest in the surgeon's armamentarium to treat cancer and other conditions. Breast cancer can be taken as an example. It is the most common cancer diagnosed and the leading cause of death from cancer in women worldwide. The majority of early-stage patients will undertake breast-conserving treatment (BCT) because of the equivalence of its results to total mastectomy, and its superior cosmetic outcome. FUS has been introduced as one of the developing measures in the process of BCT, and both experimental work and pre-clinical trials are showing promising results, guided either by ultrasound imaging (Wu et al. 2007) or magnetic resonance imaging (MRI) (Furusawa et al. 2006).

Attracting great attention in both laboratory and clinical research, FUS has been under development since the 1980s. However, there is still a paucity of experimental ultrasound array sources, hindering research into the development of FUS systems for better performance. As a core part of every FUS system, the development of FUS transducers can be investigated from the aspects of optimum array geometries, high performance piezoelectric materials, interconnection, and excitation methods and so on.

The principle of FUS is to transmit ultrasound energy into tissue, where the acoustic beam is focused and thermally ablates or mechanically damages tissue within its focal region with high intensity energy, thus high transmitting efficiency is critical for FUS transducers. Most commonly, this is achieved with a narrowband transducer, operating at a certain frequency. Therefore, the propagation dependence of ultrasound on tissue types and tumour locations requires specifically designed transducers to be manufactured for specific applications. As an example: the array transducer from ExAblate® for treating breast cancer and uterine fibroids has a frequency of 1 MHz, whilst a completely different transducer operates at 550 kHz is required for treating bone metastases.

Generally, one of the unsatisfactory aspects of many contemporary FUS systems is their limited frequency range, reducing their flexibility. To increase the resonance frequency range of transducers and still maintain good penetration of ultrasound, one option is the choice of piezoelectric material used in the transducer or array. Materials offering greater efficiency and bandwidth will directly improve the performance of the whole transducer and thus the system. Two materials are of particular interests in this thesis: PMN-PT piezocrystal and PZ54 ceramic material. PMN-PT is a relaxor-based ferroelectric single crystal, it has drawn attention because of its well-known reputation for broader bandwidth and large piezoelectric constants, such as coupling coefficient, $k_{33} \sim 0.9$ compared to 0.7 for PZT-4, and extraordinary $d_{33} \sim 2000$ pC/N, 6.5 times more than that of PZT-4 ceramic (Luo et al. 2008). The other material of interest, PZ54 ceramic (Ferroperm Piezoceramics A/S, Kvistgaard, Denmark), is a material newly designed specifically for FUS, with properties between 'hard' and 'soft' ceramics, with high permittivity while maintaining high mechanical factor Q_M.

1.1 Objectives

The target of the work described in this thesis is to explore the development of ultrasound devices compatible with MRI guided focused ultrasound surgery (MRgFUS), from the point of the view of piezoelectric materials of choice. As mentioned above, piezocrystal PMN-PT is of particular interest, along with the newly specialized FUS material, PZ54 ceramic, as a reference.

Prior to adopting the materials of choice into FUS, the performance of piezoelectric materials under extreme conditions relevant to FUS applications has been addressed. The practical issues of adoption of these materials were then studied through the design and implementation process of MRI-compatible FUS arrays using these materials. These two frameworks resulted in a list of tasks to be completed:

- **Basic material characterization**, to complete or extend references in the literature for these two relatively new piezoelectric materials.
- **Application-oriented characterization**, to investigate the behaviour of PZ54 ceramic and PMN-PT piezocrystal under practical temperature, pressure, and bias field conditions such that their feasibility in high power applications could be assessed.
- **Development of characterization system**, to provide temperature, pressure, and bias field conditions simultaneously for the investigation of application-oriented characterization to be carried out.
- **Development of MRI-compatible FUS array transducers**, to investigate the adoption of piezocrystal material into FUS application and associated practical issues.

- **Connection of experimental FUS devices to external drive electronics**, to allow multiple-channel phase control of the array and therefore performance characterization of the devices made in-house.

1.2 Contribution to Knowledge

The aim of utilizing new piezoelectric materials to fabricate ultrasound devices for FUS application makes this thesis useful for a wide range of audiences, including material scientists, transducer designers, and manufacturers. From the behaviour of the piezoelectric materials under practical conditions to the utilization of these materials in configurations to fabricate novel devices, this thesis covers a range of topics which may contribute in a worthwhile way to the future use of piezoelectric materials and ultrasound devices.

Full elasto-electric matrices with self-consistency for PZ54 ceramic and PMN-29%PT piezocrystal (Qiu et al. 2011a; Qiu et al. 2011b) were obtained from basic characterization work. The properties obtained will benefit both practical and theoretical research. The testing procedure for full matrix characterization was also established.

- A material characterization system was set up in the laboratory environment, allowing the effects on the materials of external temperature, pressure, and DC bias field conditions to be studied simultaneously (Qiu et al. 2011b).
- Application-oriented characterization using the system above was carried out with both PZ54 ceramic and PMN-PT piezocrystal material (Qiu et al. 2011b; Sadiq et al. 2011).
- A geodesic dome design was combined with a spherical, self-focused array geometry for FUS applications. The practicality of the concept has been proved by developing four 96-element array transducers using different materials of interest, including the newly developed piezocrystal material (Qiu et al. 2012).
- Arrays were successfully connected to external modular electronics. This offers a valuable prototyping route for FUS devices and shows that good focusing ability can be achieved with the geodesic array design (Qiu et al. 2013).

1.3 Thesis Structure

The complete thesis consists of seven chapters in total, which can be grouped into the four conventional sections: Background and Literature Review, Chapter 2 and Chapter 3; Materials and Methods, Chapter 4; Results and Discussion, Chapter 5 and Chapter 6; and Conclusions and Future Work, Chapter 7.

Chapters 2 and 3 review the literature background and development for two constituents of the research, respectively. Chapter 2 presents a detailed background of FUS, especially for MRI-guided FUS (MRgFUS) for treatment of breast cancer. The state of the art in FUS, MRgFUS, and MRgFUS with breast cancer are discussed, and an overview is provided of requirements for future development.

Chapter 3 addresses to the sources of the ultrasound energy. Starting with the basic components within an ultrasound transducer, the technical background of ultrasound transducers for FUS and their development are reviewed. Piezoelectric materials, as the core component, are reviewed thereafter. An overview of the historical development of piezoelectric materials is given first; the development and potential benefits of the new generation piezocrystals are emphasized afterwards with comparison to the performance of conventional piezoceramics. Last but not the least, the background on piezoelectricity and ferroelectricity are introduced, followed by their related parameters and the characterization methods, as well.

Chapter 4 presents the materials and methods used in order to implement this project. Following the actual workflow, the characterizations of the newly developed materials are introduced first, with the detailed experimental arrangements and procedures of both full matrix characterization and the application-oriented characterization. Using the material been characterized, the methods of fabricating the ultrasound transducers were followed. The general design and fabrication methods are illustrated by the implementation of a single element self-focusing bowl transducer. The novel methods to implement the geodesic faceted arrays are introduced in the following section. Finally, the methods used for characterizing the transducer arrays are presented.

Utilizing the same arrangement as for material and methods, the section on results has also been split into two chapters. Chapter 5 presents both results for full matrix characterization under ambient condition and the application-oriented characterization under elevated temperature, pressure and bias field; FEA model of a unit-cell, representing the 1-3 piezo-polymer composite, is performed with different imported material properties to further evaluate the benefit of pizeocrystals.

Chapter 6 presents the fabrication process for the geodesic faceted array transducers and their test results. The implementations of the active composite elements, the electrical connection and array assembling process are detailed and evaluated. Complex electrical impedances of the individual elements of the four arrays are tested for basic characterization; the connection of the array elements to the external driving electronics are realized in following section, which allows the arrays' focusing and steering capability to be tested as part of the functional testing, along with their frequency responses, linearities and their MRI compatibilities.

Chapter 7 gives a summary of the work, combining the conclusions and future work together.

1.4 Publications from this Work

Peer-reviewed:

Z Qiu; M Sadiq; C Demore; M Wallace; P Marin; K Mayne; S Cochran. Characterization of piezocrystals for practical configurations with temperature- and pressure-dependent electrical impedance spectroscopy. *2011 IEEE Transactions on Ultrasonics, Ferroelectrics, and Frequency Control*. vol.58, no.9, pp.1793-1803, Sep. 2011.

Proceedings:

Z Qiu, R Habeshaw, J Fortinec, Z Huang, D Christine and S Cochran. New Piezocrystal Material in the Development of a 96-element Array Transducer for MR-guided Focused Ultrasound Surgery. Presented at 2012 *International Society for Therapeutic Ultrasound Symposium.* June 2012

M R Sadiq, **Z Qiu**, C Demore, Z.Huang and S.Cochran, Characterization of PMN-29%PT as a Function of Temperature and Pressure. *2011 IEEE International Ultrasonic (IUS) Symposium, Florida, USA*, 2011

Robert T. Ssekitoleko, Gerry Harvery. Christine E.M. Démoré, **Zhen Qiu**, Muhammad. R. Sadiq, Sandy Cochran. Virtual Prototyping for the Design of High Frequency Ultrasound Transducer Arrays. *UIA Glasgow,* May 2011.

Z.Qiu, M.R.Sadiq, C.Démoré, Z.Huang and S.Cochran, Material Characterization for Ultrasonic Applications under Temperature and Pressure Conditions. *Piezo 2011, Electroceramics for end-user VI, Sestriere, Italy*, Feb. 2011.

Posters and oral presentations:

'Preliminary exploration of MRI Compatible Therapeutic Ultrasound Transducers in 1.5T and 3T MRI'. MR Safety Update by Institute of Physics and Engineering in Medicine, Nov., 2013, Royal Society of Edinburgh, Edinburgh, UK.

'A Geodesic Array using Piezocrystal Composites For Focused Ultrasound Surgery Driven by Modular Multichannel Electronics'. 2nd Focused Ultrasound Therapy Symposium, October 2013, Rome.

'Development of High Performance Faceted Bowl Arrays for Focused Ultrasound Surgery'. 11th Annual Ultrasonic Transducer Engineering Conference, (UTEC), 2013, Los Angeles, California, USA.

'Use of Piezocrystal materials in Diverse Applications', Ferroelectrics UK, 17-18 January 2013, Sheffield, UK

'Temperature and Pressure-Dependent Characterization of Three Generations of Single Crystal Materials using Electrical Impedance Spectroscopy and Laser Vibrometry'. 2012 International Workshop on Acoustic Transduction Materials and Devices (ONR), Pennsylvania, USA.

'Characterization of Piezocrystals for Applications with Variations in Temperature and Pressure'. 2011 International Workshop on Acoustic Transduction Materials and Devices, (ONR), Pennsylvania, USA.

'Piezo-Material Characterisation for Focus Ultrasound Surgery with Temperature-Dependent Electrical Impedance Spectrum'. 40th Annual Symposium of the Ultrasonic Industry Association, (UIA), 2011. Glasgow, UK.

'The development of an MRI-Compatible Focused Ultrasound Device for the Treatment of Rectal Cancer'. 40th Annual Symposium of the Ultrasonic Industry Association, (UIA), 2011, Glasgow, UK.

CHAPTER 2 FOCUSED ULTRASOUND SURGERY

This chapter offers an introduction to FUS and reviews the relevant literature, with a particular emphasis on MRgFUS and its application to breast tumours. The contents of this chapter are divided into three main sections as below:

- Introduction to FUS
- MRgFUS for breast cancer
- Current considerations in MRgFUS

2.1 Introduction to Focused Ultrasound Surgery

2.1.1 Ultrasound in Medicine

Ultrasound is defined as a sound pressure wave with a frequency greater than 20 kHz. In the field of modern medicine, ultrasound is widely adopted for its diagnostic capabilities and therapeutic uses are established and growing. Ultrasonography is the most well-known application of ultrasound as a diagnostic imaging tool, whilst investigations also highlight the capabilities of ultrasound as a therapeutic modality. Examples of ultrasonic applications in medicine are listed in Table 2-1, sorted by operating frequency and power intensity levels. Unlike diagnostic imaging or monitoring, which use frequencies up to 20 MHz in clinical work and 50 MHz or even higher in research, therapeutic applications usually use the relatively low frequency range below 5 MHz. Another key difference is that therapeutic applications use ultrasound to bring biological effects in thermal and mechanical terms into the body. Therefore much higher energy and intensity of ultrasound are used for therapeutic ultrasound applications.

The applications of therapeutic ultrasound have been expanded and developed continuously to encompass many clinical areas, such as surgical instruments, chemotherapy, physiotherapy, drug delivery, and FUS. Among these, FUS, or high intensity focused ultrasound (HIFU), is a promising surgical modality for cancer treatment. Although still at an early stage, FUS has already been considered as a possible alternative to conventional open surgery. The details of FUS will be discussed in the following sections.

Table 2-1 Ultrasound Uses in Medicine

	Diagnosis/Monitoring	Therapy	
		Therapeutic treatments	Surgery
Power Intensity (W/cm^2)	0.01 - 0.1	0.1 - 3.5	800 - 1500
Frequency	2 MHz – 20 MHz	20 kHz - 5MHz	250 kHz - 3 MHz
Applications	• Imaging • Blood flow motion monitor • Elasticity change monitor	• Bone cutting • Opening blood brain barrier • Destruction or lithiasis and blood clots • Modulation of pain • Drug delivery and release • Hyperthermia Ablation	• Focused Ultrasound Surgery

2.1.2 What is Focused Ultrasound Surgery?

Open surgery is the most ancient and direct method in the fight against cancer operating by removing the affected organs completely or partly. With the development of modern medical technologies and improving understanding of cancer, new techniques of management have been developed, with minimally invasive or non-invasive features. The major goals of those techniques are to significantly reduce local, regional, and systemic side effects, and to provide additional therapeutic options in the cases where conventional surgery fails (Zhou 2011).

FUS is one of the new techniques and is regarded as the only truly non-invasive modality for cancer treatment. The idea of this extracorporeal therapy is to thermally ablate only a small amount of tissue within its focal area, while sparing the surrounding and overlying tissue. Just as a magnifying glass can be used to focus sunlight to a spot with the intention to set fire, the ultrasound beam is generated from ultrasonic sources and focused to a tiny area located inside the human body. In practice, only at the focused area is there high enough power intensity to cause significant biological effects to tissue either by absorption-induced heating or mechanical cavitation. In the case of thermal ablation as the primary mechanism for tumour cell destruction, the temperature within the focal area should increase rapidly (1 - 3 s) from normal body temperature to above 56 ℃, even up to 80 ℃ (ter Harr et al. 1991), leading to instantaneous and irreversible cell death.

The application of FUS is represented in Figure 2.1. Since the lesions caused by ultrasound are usually much smaller in size than the tumour, a pre-planned sequence of sonications is required to cover the whole tumour.

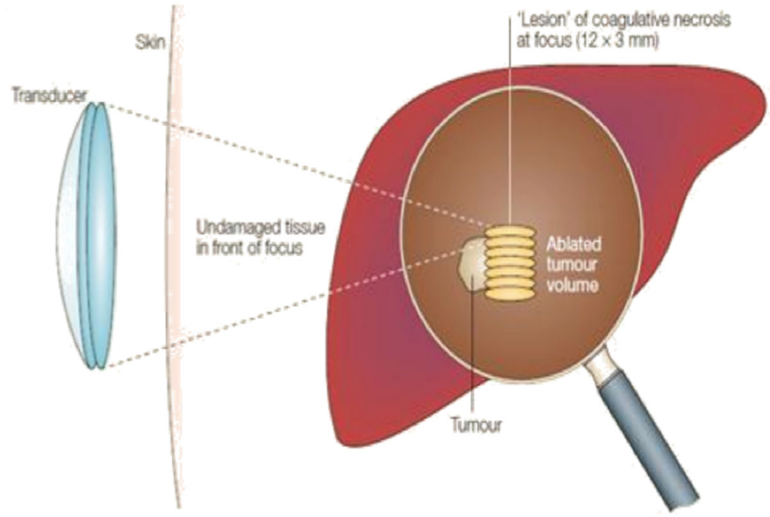

Figure 2.1 Schematic representation of FUS treatment. (Kennedy 2005)

Compared with traditional open surgery, FUS seems to provide promising survival rates in both the short and long terms. It also offers benefits to patients through reduced risk of infections and scar formation, less risk of side effects of anaesthesia, less pain, reduced in-hospital recovery time and thus reduced cost. Minimally invasive approaches like radio frequency ablation, percutaneous tumour excision, interstitial laser ablation and cryotherapy (Vlastos et al. 2007) are expected to have similar advantages. However, they still require at least percutaneous access to deep-seated tumours, which has increased risk of toxicity and bleeding compared with FUS ablation.

Although these minimally invasive modalities may require shorter treatment times, there is a limitation of lesion size up to a diameter of 3 - 4 cm; in contrast, FUS can treat larger volumes if it is used with proper treatment plans. In addition, FUS can be repeated, theoretically an infinite number of times, as there is no dose limit. Very helpfully in terms of long-term safety, it does not involve ionizing radiation either directly or from its imaging guidance methods (Zhou 2011).

2.1.3 The Biological Effects of Focused Ultrasound Surgery

The biophysical effects related to ultrasound propagation through tissue are traditionally divided into thermal and non-thermal effects. Thermal effects are caused by energy absorption, in turn causing tissue heating. Non-thermal effects have been separated into cavitation and other mechanical effects. Thermal ablation and acoustic cavitation are the two predominant mechanisms that lead to cell death in FUS. Although in the case of FUS or HIFU, biophysical effects refer principally to thermal ablation and coagulation, it is believed that both thermal and non-thermal effects are always combined *in vivo* in practice (Baker et al. 2001).

Thermal Effects

When propagating through tissue, ultrasound continuously loses acoustic energy due to absorption within the tissue. The acoustic energy is converted principally to heat, resulting in an increase in temperature. If the elevation of temperature reaches a certain threshold and the procedure lasts for a sufficient period, irreversible tissue damage can be caused.

The relationship of temperature and time for tissue thermal damage is characterized by the Sapareto-Dewey thermal dose equation, Equation 2.1. T_i is a series of temperature measurements; Δt is the time interval in minutes between measurements and R is a rate defined by $R = 0.5$ when $T > 43^{o}$C, and $R = 0.25$ when $T < 43^{o}$C.

$$t_{43} = \Delta t \sum_{i=1}^{N} R^{(43-Ti)} \qquad \text{Equation 2.1}$$

This equation demonstrates that tissue thermal damage is approximately linearly proportional to exposure duration and exponentially related to the temperature elevation. Although the threshold varies with tissue type, a reference thermal dose of 240 minutes at 43 ^{o}C (often quoted as t_{43}) is recognized to be sufficient to cause necrosis in all kinds of tissue (Sapareto et al. 1984). To achieve the equivalent biological effect, every temperature rise of 1^{o}C above 43^{o}C will reduce the exposure duration by half. Thus, based on the thermal dose t_{43}, a temperature of 56 ^{o}C held for 1.75 s will induce the reference level of tissue thermal damage (ter Haar 2001). Since the effects of thermal dose have been well established, thermal effects of therapeutic ultrasound can be predictable and controllable. Therefore thermal ablation has been considered as the primary mechanism currently used in FUS.

A typical lesion caused by FUS thermal ablation, seen in Figure 2.2 (a), is ellipsoidal in shape, with its long axis parallel to the ultrasound beam. The dimensions of the lesion are frequency dependent, but usually within a range of 1 - 2 cm along the beam axis and 1–3 mm in diameter at the full width half maximum dimensions. The thermal gradient between the focal region and surrounding tissue is visible in a sharp histological boundary formed between necrotic tissue – the lesion - and normal tissue (Chen et al. 1993), Figure 2.2 (b), which is no more than 50 µm (around 6 cells) in width (ter Haar et al. 1993).

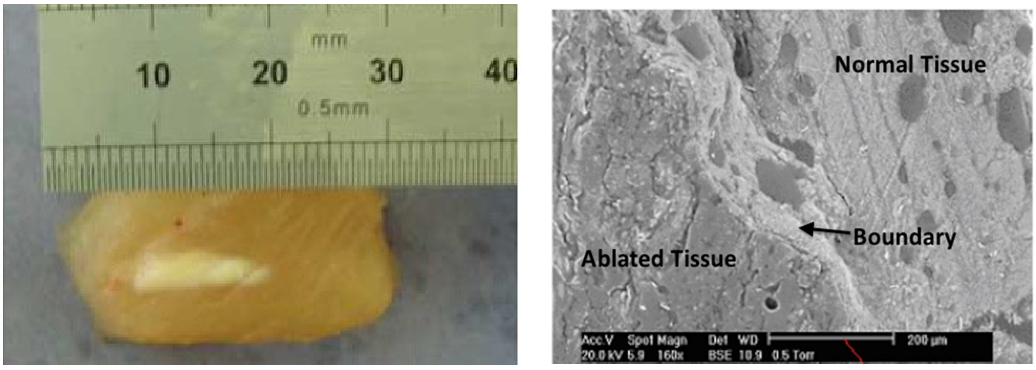

(a) (b)

Figure 2.2 (a) A cigar-shaped FUS lesion produced deep in poultry tissue.
(b) The boundary between normal tissue and ablated tissue shown in a x160 environmental Scanning Electron Microscopy image (Robertson 2007)

Non-Thermal Effects

Besides causing elevation of temperature in tissue, the realization of ultrasound as a mechanical wave also induces direct vibrational forces in tissue in its path. Ultrasound cavitation is a direct product of this mechanical vibration and one of the non-thermal effects of ultrasound. Dissolved gas is drawn out of solution by the changing acoustic pressure, and therefore microbubbles are generated. Thus cavitation can be defined specifically as "the formation of tiny gas bubbles in the tissues as the result of ultrasound vibration." (Low et al. 1994).

There are two types of cavitation: stable and inertial. When under an applied low-pressure acoustic field, the gas microbubbles oscillate in size with the changes of acoustic pressure. This type of oscillation is called stable cavitation. Stable cavitation will cause micro-streaming effects in the fluids around the bubble, which can induce bio-effects via the strong shear force. This localized shear force can cause transient damage to the membrane of the cell, which will benefit therapeutic ultrasound applications such as ultrasound enhanced drug or gene delivery (Mitragotri 2005). When exposed to a high-pressure acoustic field, the bubble oscillations become highly nonlinear. The rapid growth of the bubble will eventually lead to a violent collapse and destruction of the bubble. This is called inertial cavitation, Figure 2.3. Inertial cavitation generates shock waves with pressure as high as several hundreds MPa, and a high temperature as well, several thousand Kelvin, in the microenvironment (Mason 1998). Pressures and temperature at these levels will cause rapid, violent tissue destruction.

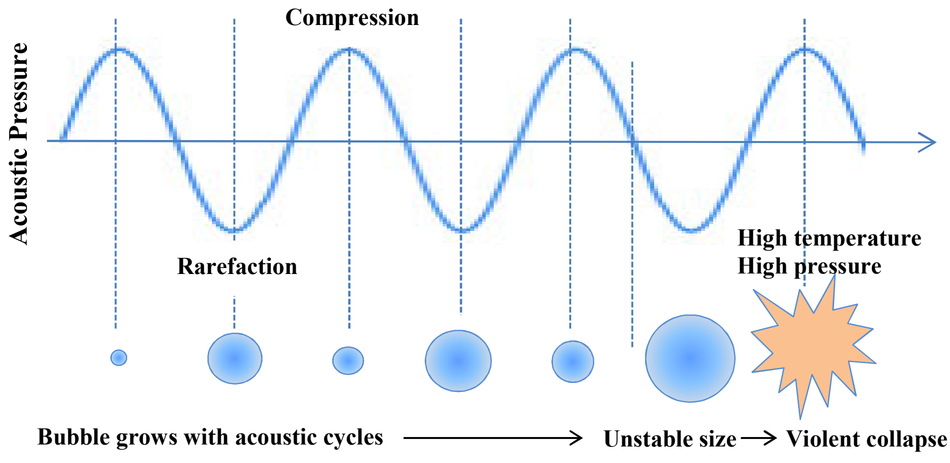

Figure 2.3 The formation of cavitation bubbles in an acoustic pressure field.

Although cavitation has been known for a long time as a mechanical biophysical effect of ultrasound, it is considered an inappropriate method for treating cancer due to its apparently random and uncontrollable properties. However, after many investigations carried out recently, cavitation has shown its capability to enhance or accelerate thermal tissue ablation. Both types of cavitation, inertial and stable, have been found to increase the absorption of ultrasound in tissue, which is potentially useful in reducing the energy transmission beyond the focus and shortening the treatment time (Sokka et al. 2003). Other researchers have also found that the temperature threshold of tissue damage can be reduced to half with the aid of ultrasound contrast agent (USCA). Thus the required time average power could be reduced by approximately 90% (McDannold et al. 2006).

Radiation force and acoustic torque are also induced by the mechanical vibration from ultrasound pressure waves. The radiation force in a standing wave can be used for cell manipulation; in a travelling wave, detectable tissue motion is induced and may lead to cell apoptosis as a specific bio-effect. Acoustic torque can cause a steady circular flow in the cellular environment, which may be responsible for increasing the permeability of cell walls and blood vessels (Hynynen 2008).

2.1.4 Image Guidance Technology for Focused Ultrasound Surgery

Unlike conventional open surgery in which surgeons can have direct visual access to the treatment procedure, FUS requires additional image guidance. Due to the non-invasive nature of FUS, the image guidance associated with it must be able to localize the targeted tumour accurately, identifying boundaries and structures surrounding the ultrasound beam path for treatment planning. The capability of temperature monitoring is also highly beneficial to ensure an therapeutically-effective thermal dose.

Magnetic resonance imaging (MRI) and ultrasound imaging itself are the two methods currently performed in conjunction with FUS (ter Haar 2007a). Ultrasound imaging provides excellent millimeter-range resolution deep in soft tissue, and has benefits such as relatively low cost, good portability and patient access. However the significant artefacts in ultrasound caused by bone have limited its application in certain organs, such as the brain with the skull surrounding it, and the liver and kidneys which are partly obscured by the ribs (Kennedy et al. 2003). Although most clinical experience of FUS treatment has used ultrasound imaging as guidance, more research and a larger number of studies are now focused on MRI guidance (Schmitz et al. 2008)

Magnetic Resonance Imaging Guidance

MRI is considered as the best candidate to guide focus ultrasound surgery and is the one utilized in the work described in this thesis.

MRI offers excellent 3D spatial resolution and high sensitivity in distinguishing between tumours and normal tissue, thereby ensuring accurate planning and targeting before treatment. The existence of MRI thermometry is another advantage, offering direct and accurate temperature measurement based on phase-shift images and thus allowing monitoring and control during treatment (Hokland et al. 2006).

In contrast to the excellent capability of real-time, intra-procedural tumour detection and temperature imaging, the high costs and relatively poor patient access should also be considered with MRgFUS systems. In order to work within the high magnetic field of the MRI system, the MRI compatibility of HIFU transducers and system design (Brosch et al. 2001; Wharton et al. 2007), patient selection and other factors must be taken into account (Melzer et al. 2012).

2.1.5 The Development of Focused Ultrasound Surgery

The biological effects of ultrasound on living microorganisms and animals were first observed by E. Newton Harvey in 1928; thereafter, ultrasound research has been extended to the biological field. The idea of using focused ultrasound with high intensity for thermal coagulation within tissue was first suggested by Lynn in 1942. Pioneering experiments followed in fresh liver tissue and animals to prove the feasibility of this non-invasive approach (Lynn et al. 1944).

In 1955, the Fry brothers carried out the first FUS human experiments in neurosurgery, to treat Parkinson's disease (Fry et al. 1955). Although lesions were generated successfully in the brain in this work, the development of the technique did not go any further in the next few decades; this can be attributed mainly to the necrosis which appeared on the adjacent scalp and skin lying in the path of ultrasound beam. The lack of targeting and monitoring techniques at that time also limited the progress of this research, and it was not until the 1990s that attention returned to FUS.

The development of modern imaging technology has significantly accelerated the adoption of FUS. Using ultrasound imaging for guidance, the first transrectal treatment for localized prostate cancer took place in Lyon, France, in 1993. Since then, FUS has been widely explored in many clinical and preclinical applications: brain, eye, prostate, breast, bone, uterine fibroids, liver, kidney, renal, and pancreatic tumours as outlined in Table 2.2 (Zhou 2011; Al-Bataineh et al. 2012).

The levels of clinical development and adoption of FUS vary around the world in terms of certifications and approvals. In Europe and the UK, the treatment of prostate cancer is the first FUS application approved by UK National Institute for Health and Clinical Excellence (NICE) (ter Haar 2007b). Other clinical applications are mostly limited to liver and kidney cancer trials (Illing. RO et al. 2005) and benign uterine fibroids. In the United States, the management of uterine fibroids with MRgFUS is the only application to receive approval so far from the Food and Drug Administration (FDA). China has the most clinical FUS experience of cancer management, including the treatment of breast cancer, primary and metastatic liver cancer, malignant and metastatic bone tumours, and other soft-tissue sarcomas (Wu et al. 2004). With the number of patients now exceeding 40,000, FUS has been proved a feasible modality for cancer treatment.

Table 2-2 The status of therapeutic FUS applications with different cancers

Cancer Applications	Clinical	Developmental	Experimental
Prostate cancer	✓		
Uterine fibroid cancer	✓		
Breast Cancer		✓	✓
Liver cancer		✓	✓
Kidney cancer		✓	✓
Pain relief of bone metastases			✓
Palliative ablation of pancreatic cancer			✓
Deep brain ablation for neuropathic pain			✓

Experimental: the applications are still in preclinical or clinical experimental stages
Developmental: those applications being translated into clinical practice
Table contents are adapted from review article (Melzer et al. 2012)

2.1.6 Currently-available MRgFUS Systems

A FUS system contains the following major components:

- The sonication unit with the transducer and associated electronics;
- The imaging unit, ultrasound or MRI scanner;
- The physical treatment table; and
- Advanced software for treatment planning, treatment control and data analysis.

Table 2-3 summarizes all the currently available systems in the commercial market, including the system name, manufacturer, focusing methods, imaging guidance methods and their clinical applications in practical treatments. Although most of the systems listed use ultrasound for image guidance, their clinical applications are very limited, either to certain types of cancer, like the Ablatherm^{TM} HIFU, and Sonablate-500 systems for prostate cancer; or to certain countries, China and South Korea, for example. FUS relies on imaging quality with good resolution and sensitivity for an accurate determination of tumour extent. For this reason, MRgFUS has quickly become more accepted and approved than ultrasound guided FUS (USgFUS).

The first clinical MRgFUS studies used single-element focused ultrasound systems integrated with the MRI scanner (Huber et al. 2001; Hynynen et al. 2001). The applications of these early clinical systems were limited by their small focal volumes and the lack of feasibility of moving the focus. The inability to use MRI thermometry at that time also limited the clinical practices of MRgFUS. In order to overcome the limitations of single transducer, fixed-focus ultrasound systems, MRI-compatible ultrasound phased array technology and quantitative MRI thermometry were studied and their feasibility has been proved. Together with the development of advanced software, these new technologies have been adopted into the new generation of clinical MRgFUS systems.

The first commercial MRgFUS system was produced by InSightec Ltd (Haifa, Israel) and named ExAblate® 2000. A spherically-curved, 208-element phased array is sealed in a degassed water-filled chamber that is mounted within the patient treatment table and integrated with a 1.5 T MRI scanner. A mechanical 2D positioning system driven by brass lead screws and piezoelectric motors is applied as well, to further enlarge the possible treatment region.

Table 2-3 Commercial FUS systems used in Clinical Treatments and their Applications

System	**Manufacture / Company**	**Focusing method**	**Imaging Guidance**	**Applications**
Ablatherm	EDAP-Technology, France	Single concave element	US	Transrectal; Prostate
Sonablate® 500	Focus Surgery Inc., Indiana, USA	Two concave elements mounted back to back	US	Transrectal; Prostate, Benign Prostatic Hyperplasia
TH-ONE	Theraclion, France	Single concave element	US	Extracorporeal; Hyperthyroid, Breast Fibroadenoma, Thyroid Nodules
Model-JC	Chongqing Haifu, China	Single flat element with concave acoustic lens	US	Extracorporeal; Uterine Fibroid, Breast, Liver, Bone, Prostate
FEP-BY02	Beijing Yuande Biomedical Eng. Inc., China	Phased Array	US	Extracorporeal; Uterine Fibroid, Breast, Liver, Bone, Pancreatic, Kidney
HIFUnit 9000	Shanghai A&S, China	Six self focus elements	US	Extracorporeal; Uterine Fibroid, Breast Cancer
HIFU-2001	Sumo Corporation Ltd. HK, China	Eight individual elements placed on concave surface	US	Extracorporeal; Uterine Fibroid, Primary Liver cancer, Bladder Cancer
ExAblate® 2000	InSightec Ltd, Israel	Phased Array	MRI	Extracorporeal; Uterine Fibroid, Breast, liver, bone metastases, prostate
Sonalleve	Philips, Netherland	Phased Array	MRI	Extracorporeal; Uterine Fibroids, bone metastases

The treatment of uterine fibroids using the ExAblate® 2000 received the European CE mark in 2002 and US FDA approval in 2004. Shortly afterwards, InSightec developed a new matrix phased array with approximately 1024 individual elements, Figure 2.4 (a). This is operated at a lower centre frequency, $f = 550$ kHz, for palliation of pain from bone metastases, called the Conformal Bone System, ExAblate 2100. This system received the CE Mark in June 2007 and US FDA approval in October 2012.

More recently, a clinical trial has been launched by InSightec using its ExAblate® Neuro system, called the ExAblate® 4000 head system. The key component of this system is a hemispherical phased array transducer with approximately 1000 elements, seen in Figure 2.4(b). The ExAblate® Neuro system gained its European CE Mark in December 2012 and various brain disorders have been addressed experimentally since then.

Philips (Philips Healthcare, den Hague, Netherlands) is developing its own commercial MRgFUS system as well: the Sonalleve MR-HIFU system. The system received the CE mark for treating uterine fibroids in 2009, and then for bone metastases in 2011. The treatments of prostate cancer and breast cancer with this system are presently undergoing development.

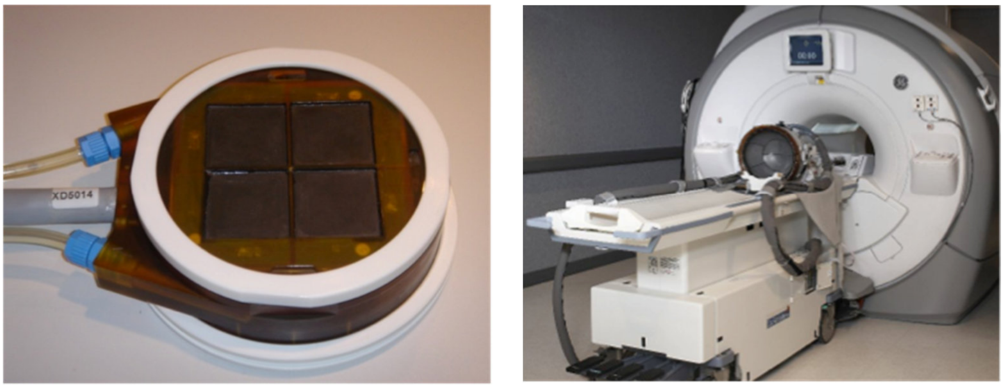

(a) (b)

Figure 2.4 (a) Approximately 1024 element matrix phased array integrated with ExAblate Bone system. (b) Hemispherical transducer of the ExAblate™ 4000 HIFU head system. InSightec Ltd, Haifa, Israel

2.2 MRgFUS for Breast Cancer

Breast cancer is a target in clinical MRgFUS studies and a potential application considered in more details here. Intensive research has shown the promising potential of MRgFUS for breast cancer treatment but there are still several challenges preventing it replacing open surgery completely or even taking its place as a routine technique.

To understand the current status of MRgFUS for breast cancer, the disease itself must be considered. This section thus starts with an introduction to breast cancer and then reviews and discusses the related issue of breast cancer treatment using MRgFUS.

2.2.1 Introduction to Breast cancer

Breast and Breast Cancer

The human breasts are located in the upper ventral region of the body, based on the chest wall. The female breast is an organ with the function of being a mammary gland. Glands and ducts are the core components of the breast; the former are grouped as lobes and lobules where milk is produced and the latter are the tiny tubes which carry the milk from the lobes to the nipples. Other contents of the breast are fatty tissue and fibrous supportive tissue. The anatomy of the breast is represented in Figure 2.5 (a).

The most common breast cancer, also known as breast carcinoma, forms in the lobules (lobular carcinoma) and ducts (ductal carcinoma) and sometimes the nipple (Paget's disease). Breast tissue is drained by lymphatic vessels that lead to axillary nodes and internal mammary nodes, shown in Figure 2.5 (b). When breast cancer spreads, it is frequently first to these nodes.

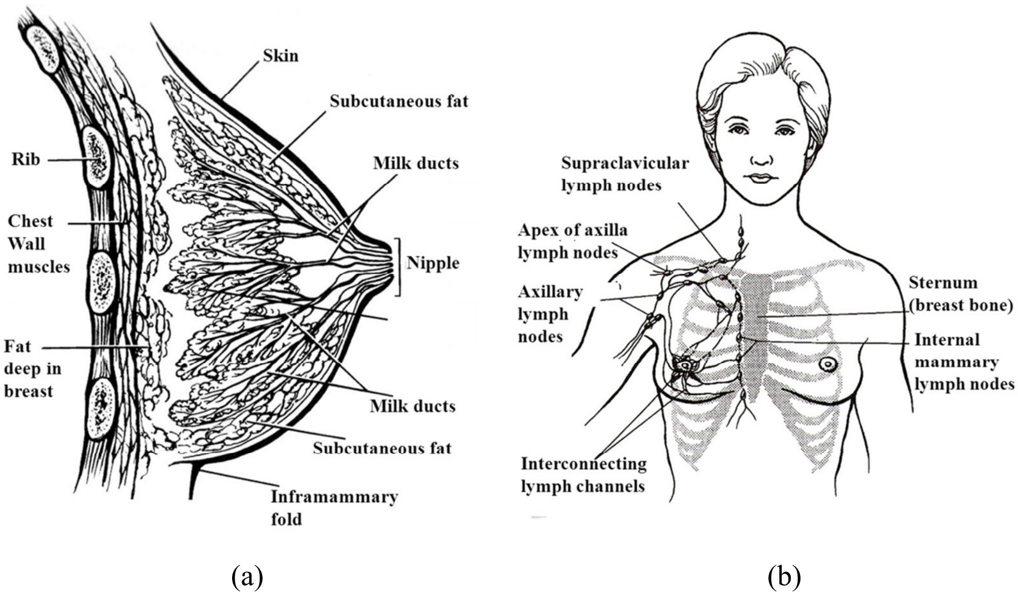

Figure 2.5 (a) Gross anatomy of the breast in female and its relationship in position with the chest wall and ribs. (b) The system of lymph nodes system around the breast, adopted from (Roses 1999)

Breast cancer is the most common cause of female death from cancer and has a significant frequency of incidence in both economically developed and developing countries. More than 1 million women are diagnosed with breast cancer worldwide each year, accounting for about 14% of total cancer deaths in 2008 (Jemal et al. 2011).

A breast tumour is a cohort of cells that lose control of their growth and are over reproduced. It can often grow very fast and spread into the surrounding areas, becoming malignant. In its early stages, cancer cells stay within the milk ducts and lobules, in which case the cancer is called *in-situ* breast cancer. In more advanced stages, when the malignant cells cross the wall of the duct or lobule to infiltrate adjacent tissue, it is called invasive cancer. It may spread to the lymph nodes and travel to other parts of the body via the blood vessels. Invasive ductal carcinoma (IDC) is the most common breast cancer with more than half of cases of this type (William L. Donegan et al. 2002)[P347-348].

Breast Cancer Staging

The stage of the cancer is the most important factor in deciding the best treatments for a patient. In clinical staging, the determination is based on the tumour size (T), whether lymph nodes are involved (N), whether the cancer is invasive or non-invasive, and whether spread or metastasis has happened (M). This is called, in short, the Tumour – Node - Metastasis (TNM) staging system.

Five stages have been distinguished in breast cancer (Roses 1999).

- Stage 0 is defined as non-invasive cancer;
- Stage 1 is invasive cancer, $T \leq 2$ cm, with no lymph node involvement;
- Stage 2 is invasive cancer, $2 < T < 5$ cm, or if the cancer has spread to the axillary lymph nodes;
- Stage 3 is similar to Stage 2, but with tumour size $T > 5$ cm, or spread to the lymph nodes near the breastbone, the skin, or the chest wall;
- Stage 4 indicates metastasis, when cancer cells have spread to other organs, usually the lungs, liver, bone, or brain.

Nowadays, most patients (75% to 80%) with breast cancer are treated at its early stages due to increased awareness and the development of early detection technology.

Treatment of Breast Cancer

Total mastectomy by surgically removing the whole breast was applied to all treated breast cancer cases till the 1980s. Nowadays, except for specific cases that are too serious, the majority of patients prefer breast-conserving treatment (BCT) for its superior cosmetic and thus psychological outcomes. This treatment aims to remove only the tumour with a safety margin of healthy tissue around it and spare the rest of breast. Post-operative radiation therapy is usually necessary to ensure the success of BCT. After a follow-up period of more than 20 years, it was reported that BCT offers results equivalent to total mastectomy for early stage breast cancer (Fisher et al. 2002; Veronesi et al. 2002).

In the process of BCT, noninvasive and minimally invasive treatments are desirable both to satisfy cosmetic demands and reduce patients' suffering. FUS, as a completely noninvasive technology, has great potential to be a reliable replacement for surgical removal, when the tumour is smaller than 2 cm in diameter. Breast cancer itself is a highly appropriate candidate for FUS as well. The shape of the breast offers an excellent soft-tissue window, as required by the FUS beam to reach the target region; furthermore, the breast can be immobilized easily, thus diminishing the effect of movement induced by patient's breathing.

In this context, many clinical trials and research programmes on breast cancer were carried out using FUS, guided by either ultrasound or MRI. Experience using USgFUS was reported mainly by Wu and his colleagues (Wu et al. 2003; Wu et al. 2005). In their clinical trials, USgFUS was combined with radiotherapy, chemotherapy, and tamoxifen. Pathology findings after the treatment revealed that complete necrosis was achieved in all patients (100%) with a safe margin of 1.5 to 2 mm. 55 month follow-up showed a 95% survival rate and 9% local recurrence rate.

Comparative studies have shown that MRI is the most sensitive and accurate imaging modality for diagnosing breast cancer. (Berg et al. 2004; Hata et al. 2004). It appears to be indispensable in estimating breast tumour extent, and in visualizing and delineating tumour margins. Therefore most researchers prefer using MRI as the image guidance for the treatment of breast cancer using FUS. The details of MRI guided breast FUS will be reviewed in the following sections.

2.2.2 Clinical Practice with MRgFUS Treatment of Breast Cancer

The first clinical application of FUS for benign breast cancer with MRI as guidance was reported in 2001, by Hynynen's research group. 11 fibroadenomas in nine patients were treated with a single element transducer embedded in a standard whole-body system (1.5T Signa, GE Medical Systems). Post-procedural T1-weighted images indicated that eight of 11 lesions (73%) were completely or partially treated. A set of long-term follow-up images of one fibroadenoma, Figure 2.6, showed no evidence of contrast material enhancement detected up to 3 years after the treatment (Hynynen et al. 2001).

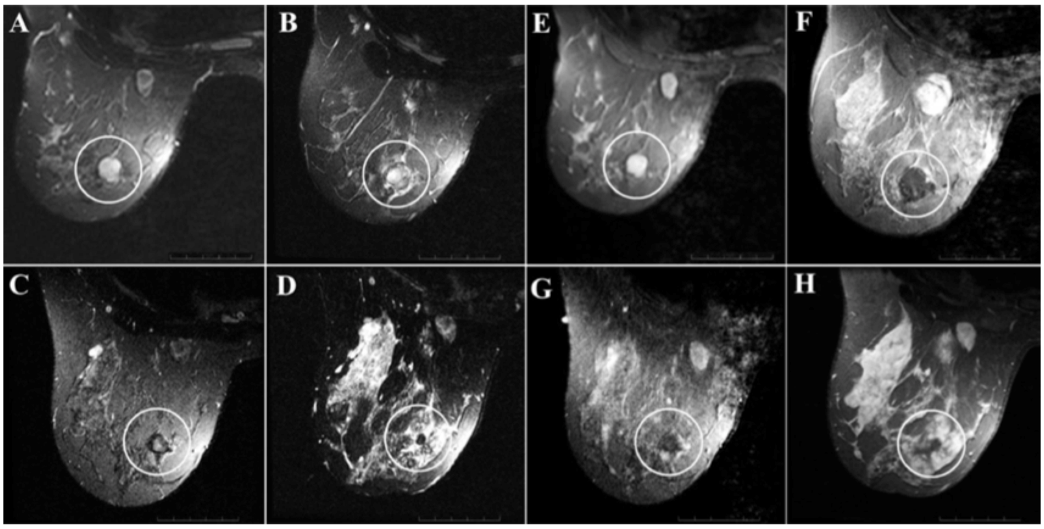

Figure 2.6 MRI shows complete response at long-term follow-up of a breast fibroadenoma (circled area) treated with MRI-guided FUS (Hynynen et al. 2001). These are fat-suppressed images A-D: T2 weighted; E–H, T1-weighted. A, E: 2 months before therapy; B, F: 7 days; C, G: 6 months; D, H: 3 years after therapy. Decreased contrast material uptake implied tissue devascularization and necrosis

Research on malignant breast cancer was carried out by Huber and colleagues (Huber et al. 2001). After a successful animal trial, a 56-year-old patient with Stage 2 invasive ductal carcinoma was treated. Conventional breast conserving surgery was applied five days after the ultrasound exposure to check the treated specimen. Following this, Gianfelice started the first Phase I trial of MRgFUS for breast (Gianfelice et al. 2003). 12 patients with invasive breast carcinomas were involved and FUS ablation was well tolerated. Excepting skin burns that occurred in two cases, there were no complications. The observations in this work also indicated the need to increase the total treatment area at the periphery of the tumour. A more recent Phase II trial was carried out with 30 patients by Furusawa et al. (Furusawa et al. 2006), using the ExAblate® 2000 system. Necrosis of the tumour volume was 96.9% $\pm$ 4%, as shown in pathology examination. Only minimal adverse effects were noted, especially when treatments were performed under local anesthesia. In ten years, a growing number of clinical trials have been carried out. The details of more clinical trials of breast cancer using MRgFUS have been reviewed and revealed the feasibility of MRgFUS for breast cancer treatment (Schmitz et al. 2008; Merckel et al. 2013).

2.2.3 Configuration of MRgFUS for Breast Tumours

The systems used for MRgFUS treatment of breast cancer are presently kept under continuous review, in both clinical work and research. For breast tumour treatment, MRgFUS systems typically employ a geometry in which the patient lies prone on the treatment table. A specially designed treatment application unit is required with a container or indentation to accommodate the breast, and a surrounding MRI breast coil for better image quality. The breast container is filled with warm degassed water or ultrasound gel for good acoustic coupling, and it should have a sufficient acoustic window for the ultrasound beam to penetrate. Based on the position where the ultrasound transducer is placed and its own structure, three different configurations have been developed so far, with related treatment application units.

The ExAblate® 2000 system from InSightec is used in most clinical applications. As noted previously in Section 2.1.6, this system has a bowl-shaped phased array with 208 elements mounted in a plastic container, filled with degassed, distilled water. The container is integrated within the patient table and covered with an acoustically transparent membrane as its acoustic window. In breast cancer treatment, the patient lies prone on the table and the breast is placed in the cavity of a breast pillow. The breast is pressed on the membrane not only to ensure a smooth skin interface within the cross-sectional area of the ultrasound path but also to prevent unnecessary movement. Figure 2.7 is a diagram of ExAblate system for breast tumour application. In this case the ultrasound wave propagates into the breast tissue from underneath. Due to the perpendicular relationship between the ultrasound beam and the chest wall, it is very hard to keep the nipple and ribs out of the beam path.

Compared with the ExAblate 2000 system, the configuration used in early MRgFUS systems was to place the transducer at the side of the breast (Huber et al. 2001). This arrangement orients the ultrasound beam approximately parallel to the ribs, thus minimizing the acoustic power deposition in the ribs and nipple. However, even using a phased array to steer the focus to some extent, the treatment has to be assisted by a complicated mechanical motion system to ensure the whole breast is within its treatable area.

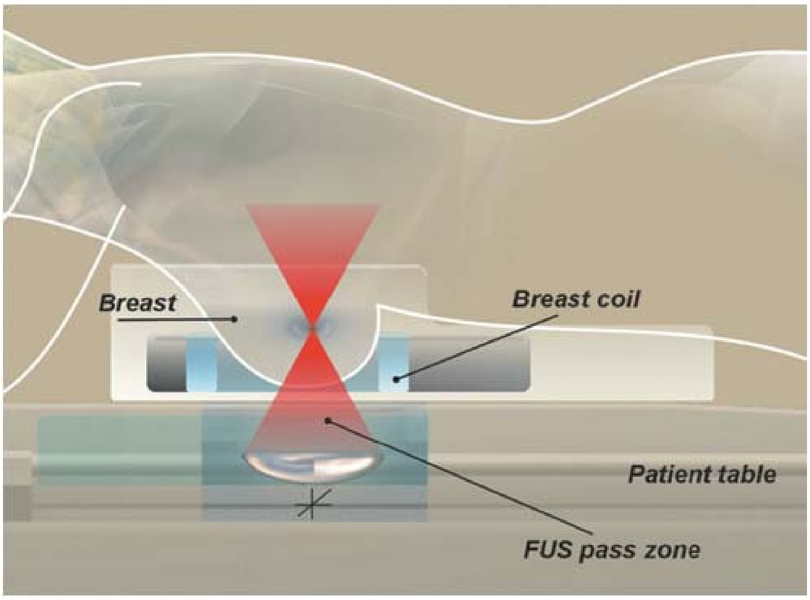

Figure 2.7 Schematic diagram of patient undergoing FUS treatment using the ExAblate system. The FUS beam is delivered to the breast tumour from underneath. (InSightec Ltd, Haifa, Israel).

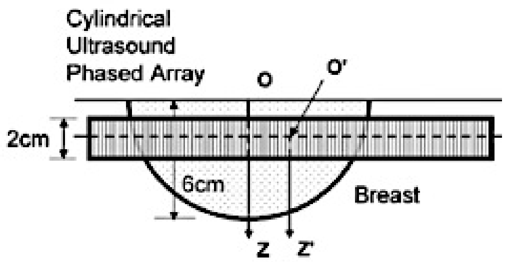

(a)

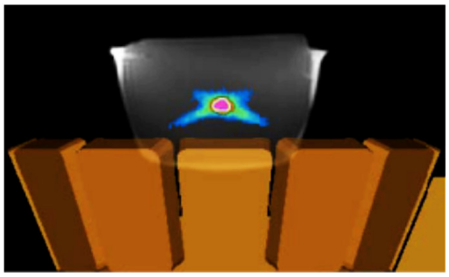

(b)

Figure 2.8 (a) Diagram of a cylindrical ring array surrounding a breast model. (Cheng Shiao et al. 2007) (b) The cylindrical phased array produced by Philips Healthcare (Mougenot et al. 2011).

To solve the above problems, which are also found in conventional hyperthermia therapy, two groups started numerical studies with two similar cylindrical ring arrays (Cheng Shiao et al. 2007; Bakker et al. 2009) to surround the whole breast, Figure 2.8(a). In the same way as placing a spatially localised transducer at the side of the breast, the acoustic beam in this configuration is oriented parallel to the ribs, therefore keeping them and the nipple out of the ultrasound path. Furthermore, the acoustic window is enlarged to the whole circumferential breast surface, thus reducing the power intensity at the skin compared with a single ultrasound beam from one direction.

Although their studies addressed hyperthermia applications rather than FUS, the feasibility of using a cylindrical phased array with a multi-focal pattern for breast tumour thermal therapy was demonstrated.

Similar configuration was adopted by Philips (Philips Healthcare, Vantaa, Finland). Figure 2.8 (b) shows the system diagram of Philips's new transducer for breast cancer MRgFUS. The transducer consists of 12 separate modules to form a circle around the breast. Each module is slightly angled to allow the focal point to be located above the transducer and has 32 individual elements. This therapy unit is designed to integrate with the Philips Sonalleve MR-HIFU system. Initial pre-clinical evaluation of breast tumour ablation using this system had started in 2011. However, no treatments have been performed or reported with a dedicated system specifically developed for breast cancer ablation.

2.3 Current Considerations relating to MRgFUS

2.3.1 General Challenges of FUS

FUS has been considered as one of the most feasible and effective alternatives to open surgery for cancer treatment. However, a number of significant challenges still limit its clinical applications. Ultrasound cannot propagate through air so organs like the lung and, to some extent, the bowel are left out as targets for FUS. Another problem is that bones absorb and reflect ultrasound strongly. This leads to overheating of bone or tissue overlaid during the treatment if the target tumour, such as liver or kidney, is located under bones like the ribcage. Optimization of the acoustic field is required (Gélat et al. 2012) to transmit sufficient energy through the ribcage whilst minimizing the energy deposited on the surface of the ribs. Using ultrasound to treat brain disease has always been considered difficult due to the unavoidable presence of the skull between the ultrasound source and the target. The problems are the high attenuation and heterogeneity of the skull which cause acoustic energy loss proximal to the target and overheating at the skull. In addition, the complex geometry of the skull significantly distorts ultrasound propagation, which causes defocusing of the beam.

The long treatment time associated with small individual lesions is one of the challenges that need to be overcome. As a single lesion is usually much smaller in size than the tumour, hundreds of sonications may be required to treat the whole tumour, so the treatment duration can be several hours, including cooling time after each sonication. Currently a 2 – 3 cm tumour will need approximately a 2-hour treatment time, which is still acceptable. However for patients with larger tumours, more than 4 - 5 cm in diameter, the long treatment time will be an obvious drawback of FUS.

Another limitation is respiratory-induced organ motion. The amplitude of the periodic motion of the liver can reach up to 25 - 50 mm during inhalation (Clifford et al. 2002), and still up to 10 mm even in immobile patients (M von Siebenthal et al. 2007). To minimize the influence of respiratory-induced organ motion, clinical practice with such organs has been performed in patients under general anesthesia or during breath-hold intervals. Efficient motion tracking techniques and the capability of fast, dynamic repositioning of the focal point are required to solve this problem.

Thermal dose is another issue being considered. Although the Sapareto-Dewey thermal dose equation defines the dose for ultrasound thermal ablation in soft tissue, densities and tissue properties can vary significantly between different types of tumour. The required energy level to achieve satisfactory ablation results for different types of tumour thus needs to be studied and determined.

2.3.2 Consideration of MRgFUS for Breast Cancer

Although significant numbers of clinical trials have been carried out or are underway, MRgFUS has not yet gained the approval specified for application to breast cancer. Several important issues are under consideration in clinical implementation of breast FUS ablation: patient selection; the size of ablated margins; and the methods for margin assessment and residual tumour detection after FUS treatment (Schmitz et al. 2008).

Patients are currently under very careful selection for FUS treatment. The main variables that can affect results are the size, type, and the position of the tumour. At this stage, FUS is limited to patients with early stage breast cancer only, tumour size ≤ 2 cm. Larger tumour size will significantly increase the treatment time and decrease the probability of completion of ablation.

The position of the tumour in the breast is another well-known limitation, based on clinical experience using the ExAblate® system: the tumour must lie at least 1 cm away from the skin surface and nipple to prevent skin burns, and at least 1 cm away from the chest wall to reduce rib pain. This selection barrier may be lowered by the use of cylindrical phased array ring transducers; however, although Phillips has built a transducer based on such a concept for their breast cancer system, no clinical trials have been reported yet.

Safety margin is one of the most critical factors affecting the outcome of MRgFUS treatment. To treat the tumour completely, without any microscopic residue left, a clear margin of at least 10 mm around it is recommended to be included in the ablation area (Singletary 2002). Therefore the imaging technique must accurately delineate all parts of the tumour, even for those branching components in the mammary ducts, for example, ductal carcinoma *in situ* (DCIS).

2.3.3 Future Directions of MRgFUS

The present generation of MRgFUS systems with integrated phased arrays has shown advantages in clinical practice. Early research demonstrated that a multi-element transducer significantly increases the potential ablation volume and focusing flexibility (Hynynen et al. 1996; Fjield et al. 1997). It can be expected that future phased array systems will have larger numbers of elements to apply more flexible sonication patterns and to further reduce the need for mechanical motion. Corresponding developments in MRI compatible array manufacture and driving hardware will be required as well.

The MRI scanner needed for MRgFUS is expensive to operate and maintain, and therefore long treatment time tying up the MRI scanner is an obvious drawback economically. To overcome this disadvantage, accelerating the treatment becomes essential for MRgFUS specifically. Experimental devices have been under investigation with closed-loop feedback that integrates rapid real-time MRI thermometry and ultrasound sonication together (Mougenot et al. 2004). Large treatment volumes can be achieved by moving the focal point along a certain path, such as a multispiral trajectory. At the same time, online MRI thermometry determines the completeness of treatment so that sonication is controlled to ensure the complete coagulation over target volume whilst minimizing exposure to the surrounding tissues. Thus the overall treatment time will be reduced.

The future developments in MRgFUS will move towards improving the feasibility of treatments of certain organs, such as brain with presence of the skull where magnetic resonance acoustic radiation force imaging (MR-ARFI) can be used to correct the aberration of the ultrasound beam caused by skull (Marsac et al. 2012); and the moving organs like liver and kidneys where dynamic MR imaging can be used to enable the motion detection (Ellis et al. 2013).

CHAPTER 3 ULTRASOUND SOURCES FOR FOCUSED ULTRASOUND SURGERY

This chapter places emphasis on the technical background and reviews the literature on ultrasound sources for FUS, including the source device itself, the piezoelectric element inside it, and characterization of this element. Starting with ultrasound transducers for FUS, the basic configuration and properties of transducers are introduced. Then referring to the core components in a transducer, developments in piezoelectric material are reviewed, especially new generations of piezocrystal. Piezoelectricity and the constitutive relations of piezoelectric materials are described in the last section of the chapter, as these are the foundations for measurement of piezoelectric properties. The outline of this chapter is thus as listed:

- Ultrasound transducers for FUS
- Piezoelectric materials for FUS
- Characterization of piezoelectricity

3.1 Ultrasound Transducers for FUS

This section will introduce the basic configurations of ultrasound transducers used in FUS. As focusing is the main characteristic of a FUS transducer, focusing techniques for both single element transducers and multi-element phased arrays are emphasized. Besides the focusing capability, other key properties which can be used for characterizing a FUS transducer are classified in this section. Last but not least, the development status of FUS transducers is reviewed, including the further directions required by FUS practice.

3.1.1 Basic Configuration of Ultrasound Transducer

An ultrasound transducer is the functional device that converting energy from mechanical to electrical and vice versa, in the other words, to receives and / or transmits acoustic energy. The basic components incorporated in a transducer are: the active piezoelectric element, matching layer, backing layer, associated drive electronics and a properly sealed casing for protection, safety and handling. Figure 3.1 represents the configuration of a typical single-element transducer with a flat element.

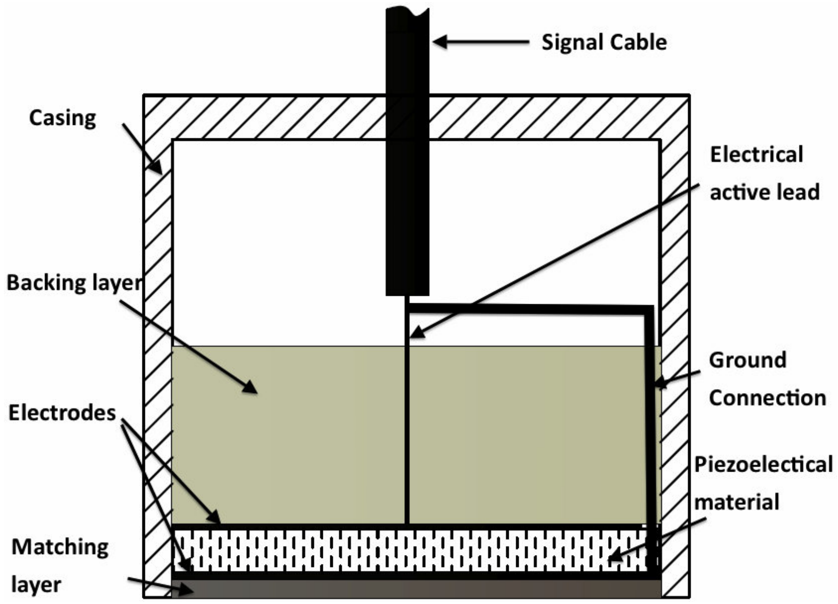

Figure 3.1 Typical components of a single-element ultrasound transducer

Active Piezoelectric Material

The active piezoelectric element is the core component of an ultrasound transducer, where the mechanical and electrical energy conversion happens. Piezoelectricity is the effect on which this energy conversion is based, as will be described in Section 3.2.1. Two electrodes are usually applied to the top and bottom surfaces of the piezoelectric material. When it is subject to acoustic pressure from the medium, an electrical field is generated between the two electrodes. This field can be measured and analyzed subsequently for ultrasound imaging. On the other hand, when a pulsed electric field is applied between the two electrodes through external means, mechanical resonance will be generated mainly in the direction perpendicular to the electrodes. This creates acoustic waves that will travel into a medium such as tissue in contact with the transducer through a couplant layer.

As the heart of an ultrasound transducer, the piezoelectric element largely determines the transducer's properties. The piezoelectric material, for example, resonates when its thickness is half - or multiples of half – the wavelength in the material. In other words, the resonant frequency of a given material depends on its thickness, which can be expressed as Equation 3.1, where *f* is the mechanical resonance frequency, *c* is the speed of sound within the piezoelectric material and *t* is the thickness of the material.

$$f = {}^{c}/_{2t} \qquad \text{Equation 3.1}$$

The behaviour of the piezoelectric material also directly relates to the performance of the transducer under different operating conditions. Therefore, a better understanding of piezoelectric material behaviour is necessary for transducer designers and, to a lesser extent, for FUS system operators.

Matching Layer

The matching layer is applied to the front face of the piezoelectric active element as shown in Figure 3.1. It is usually designed to have an intermediate acoustic impedance to reduce acoustic impedance mismatch between the piezoelectric element and the propagation medium. The acoustic impedance, Z_{ac}, of piezoelectric materials such as ceramics is around 20 - 30 MRayl, while that of human tissue is much lower, usually in the range 1.4 - 1.7 MRayl. In order to minimize the energy loss at the acoustic interface of two different media, multiple matching layers can be applied to bring the high acoustic impedance of the piezoelectric material close to that of the acoustic medium stepwise.

Although with obvious benefits, matching layers have not been applied widely with high power transducers, including transducers used for FUS. One key reason is the reduced heat dissipation they cause. Delamination is also experienced when working with matching layers at high transducer front-face intensities. Thus the transducers fabricated in this work do not have matching layers. In addition, in the case of a self-focused piezoceramic bowl transducer, the curvature of the bowl surface makes it difficult to cast a matching layer precisely with controlled thickness without subsequent machining. Since the equipment for such machining was not available during this work, matching layers for the spherical bowl shaped transducers were neglected. For the later, faceted phased-array transducers, piezocrystal – polymer composites were used as the active elements instead of monolithic piezoelectric materials. Due to the smaller mismatch in acoustic impedance between water and piezocrystal -polymer composites, a matching layer is not necessary. Furthermore, since the purpose of fabricating those transducers in this work was to compare the behaviour of different materials, allowing for the acoustic impedances of the materials themselves without optimization was an important consideration.

Backing Layer

The backing material in an ultrasonic transducer is applied behind the active element and usually comprises an epoxy loaded with powder. By choosing different powders, the density and acoustic impedance of a backing layer are adjustable. When driving the transducer with an electrical pulse, a light backing, having its acoustic impedance much less than that of the transducer, will reflect the energy back into the active layer to resonate, leading to a long pulse transmitted with low bandwidth and more energy output. On the contrary, a heavier backing, loaded with tungsten or alumina for example, to be well matched to the piezoelectric material means the backing will absorb energy effectively, leading to a short transmitting pulse and wider bandwidth. This is the usual choice in ultrasound imaging transducers (Grewe et al. 1990).

FUS transducers are categorized as high power devices that require maximum energy output. Light backing is usually chosen so that as much as possible of the acoustic energy is radiated through the front face of the transducer. Air is a perfect light backing (Ferenc A. Jolesz et al. 2007) [p7]; however its weak ability to dissipate heat can lead to the formation of hot spots on the surface of the piezoelectric material, which will cause serious damage. It also provides no physical support. The backing layer used in the present work was a mixture of epoxy and microballoons. Microballoons are hollow glass microspheres with diameters ranging from a few to hundreds of micrometers. Microballoon-filled epoxy is very lightweight with low density, forming an acoustically light backing, and it also provides additional mechanical support for the active elements in this work.

3.1.2 Focusing Technologies for FUS Transducers

Just as the name suggests, FUS requires a focused ultrasound beam in order to achieve high power concentrations in specific volumes of interest. For this purpose, focusing technologies are applied to FUS transducers either mechanically or electrically. This section will describe the current focusing technologies based on the number of active elements in ultrasound transducers.

Single-element Transducers

The single-element focused transducer has been used since the earliest research into FUS and it still plays an important role at the time of writing. It provides accurate focusing and is considered the simplest and cheapest FUS transducer. Single-element transducers are usually geometrically curved or coupled with an acoustic lens to focus the ultrasound beam along its propagation axis, as presented in Figure 3.2. When the focus needs to be moved, e.g. to sonicate a different volume within a tumour, then the single element transducer itself needs to be repositioned mechanically.

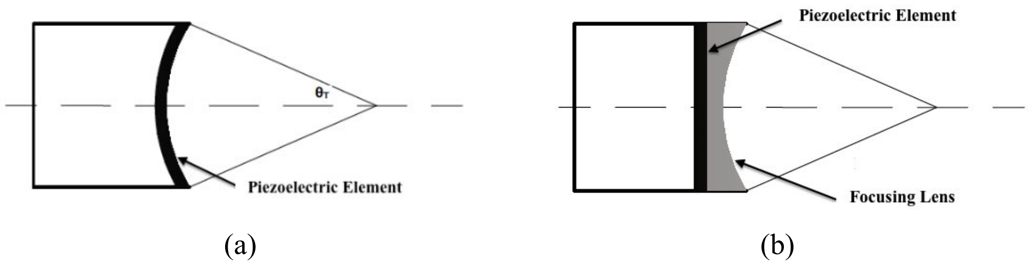

Figure 3.2 Focusing methods for single element transducers: (a) geometrically curved transducer; (b) shaped lens coupled transducer

The active element in the geometrically curved transducer in Figure 3.2 (a) is a spherically self-focusing bowl, referring to the section that remains when a sphere is transected by a plane. The focal point of the transducer occurs at the centre of the spherical bowl, at a distance equal to the radius of the sphere from the centre of transducer. The dimensions of the focal zone are dependent on the transducer diameter, *D*, the radius of curvature, *R*, and the driving frequency, *f*.

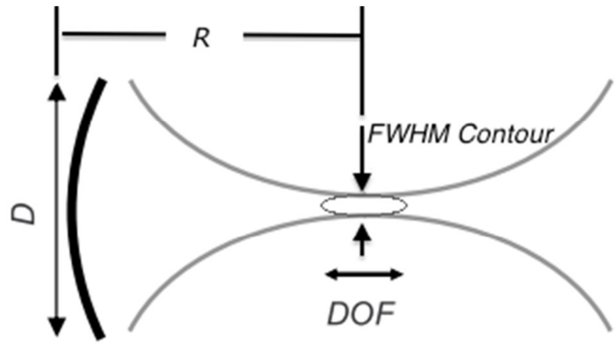

Figure 3.3 Focused beam profile generated with a spherically-curved transducer

As indicated in Figure 3.3, the diameter and length of the focal zone on the cross-sectional focal plane and along the axial plane, respectively, are determined by the full width at half maximum (FWHM), −6 dB pressure or -3 dB intensity contours. The depth of focal zone (DOF), d_{FZ}, is defined by (Lu et al. 1994)

$$d_{FZ} = 8\ \frac{\lambda}{f}\left(\frac{R}{D}\right)^2\ \sqrt{1+8\left(\frac{2\lambda R}{\pi D^2}\right)^2} \qquad \text{Equation 3.2}$$

The beam width is dependent on the wavelength λ and diameter of the transducer, which can be calculated as follows (Kino 1987) p.189:

$$BD_{(-6dB)} = \ ^{1.02R\ \lambda}\!/_{D} \qquad \text{Equation 3.3}$$

The focal volume of a geometrically curved transducer can then be predicted using Equations 3.2 and 3.3.

If a lens is used, the focus will not occur simply at the radius of curvature of the acoustic lens. Figure 3.2(b) shows an ideal lens with a planoconcave shape for FUS. The actual location of the focal point is affected by the difference in sound speed between the lens material and the propagation medium. The radially varying thickness of the lens will cause an alteration of the focal distance as well. These effects are not discussed further since acoustic lenses are not used in this work.

Phased array transducer

A phased array transducer is an assembly of multiple single-element transducers in which each element is driven by an individual RF signal with a specified phase. By calculating the set of phase (i.e. time) delays for a certain focal point, the ultrasound waves emitted by all of the elements can be made to overlap at the desired point with phase coherence and intensity maximisation. A phased array transducer has much greater flexibility than a single-element transducer: the ultrasound beam transducer is steered electronically via computer programming instead of mechanical steering, thus reducing not only the reliance on a mechanical positioning system, but also the time required to move the focus.

Transducer arrays can be arranged in different element patterns and configurations, such as a line (1D linear array), a two-dimensional grid (2D matrix phased array), concentric rings (1D or 2D annuli) or a radial circular design (1D circular ring). Figure 3.4 presents the typical array designs: A 1D linear array, the most commonly used array in ultrasound imaging, as distinct from FUS, has relatively easy manufacturing and packaging; however, its steering ability is limited to one direction only; 2D matrix array has the most flexibility to steer a focused beam throughout a 3D volume; As an intermediate design, a 1.5D matrix array can steer the focus along one axis at different depths and angles while reducing the unwanted beam artefacts in the other direction. However, both matrix arrays will have to balance the need of large number of elements and the challenges of electronics and driving system; the 1D annular array has symmetrically focused beams can be steered along the array symmetrical axis, but cannot be off the axis; while the 2D segmented annular array is a combination of linear and annular arrays, which will have some steering capability at different focal distances and angles.

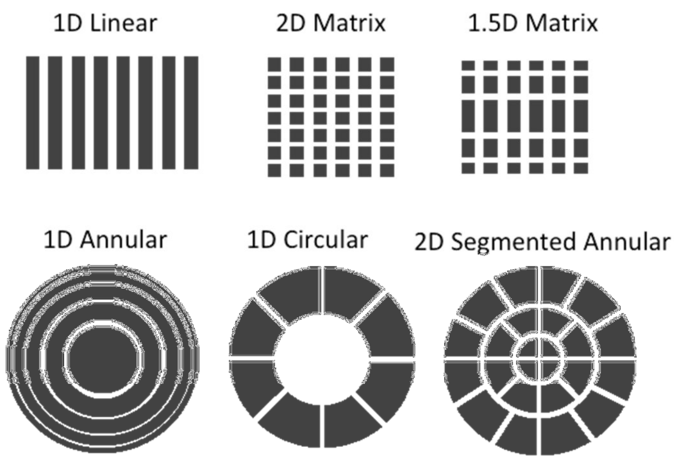

Figure 3.4 Typical design patterns for phased array transducers

The Phased Delay Law

In FUS treatments, capabilities and feasibility are enhanced if the focus can be placed along and across the array axis. Optimization of phase delays can generate multi-focal beam patterns as well, to increase the volume of the thermally ablated region and thus reduce the overall treatment time. As mentioned earlier, focusing and steering can be achieved by introducing the time delays indicated by Figure 3.5. The differential delays compensate for the transmitting time delay related to the positions of the elements and the focal point.

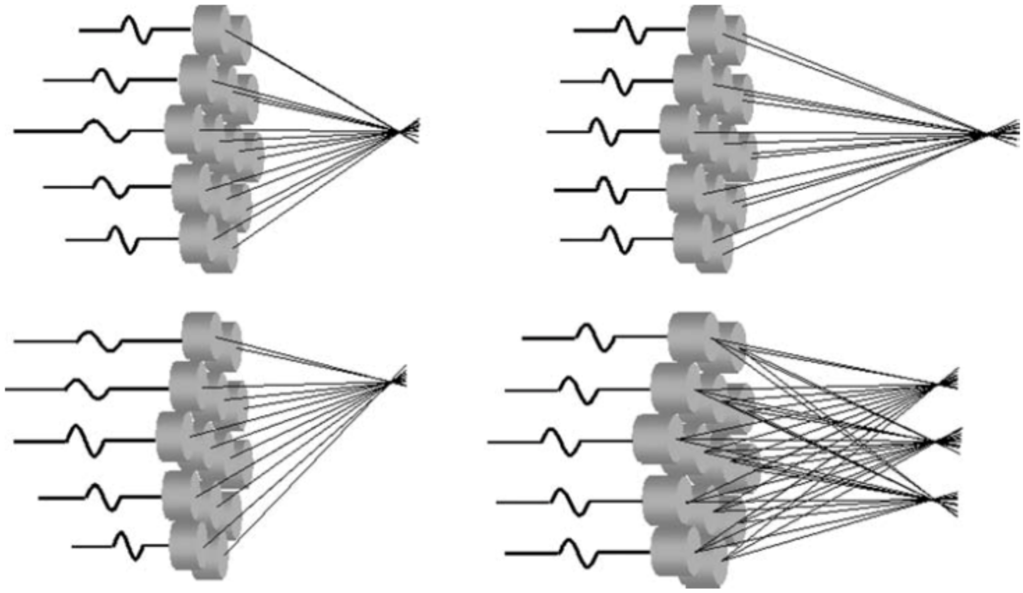

Figure 3.5 A diagram showing phased array focusing with the ability to control the position of the focus or foci by phase delay laws. (Ferenc A. Jolesz et al. 2007)

Assuming the array elements are point sources, each source is positioned at x (x_n, y_m), and the beam is angled and focused at focal point F. The phase delay law can be expressed by the differences of the propagation time (Nakahata et al. 2012):

$$\Delta\tau(x;F) = (|F - x_0| - |F - x|)/c \qquad \text{Equation 3.4}$$

where c is the speed of sound in the propagation medium, and x_0 is the centre element of the array transducer, which is usually set to the origin, and $\Delta\tau$ is the time differences of the sound propagation between any element within the array transducer and the centre element. The focal point F can be indicated by the incident angle θ and rotational angle φ according to the coordinate system defined in Figure 3.6: $F = (R \sin\theta \cos\varphi, R \sin\theta \sin\varphi, R \cos\theta)$. Therefore the delay law imposed on the array elements can be expressed as:

$$\Delta\tau_{nm}(x;F) = \frac{R}{c}\left[1 - \sqrt{(\sin\theta \cos\varphi - \frac{x_n}{R})^2 + (\sin\theta \sin\varphi - y_m/R)^2 + \cos^2\theta}\right]$$

Equation 3.5

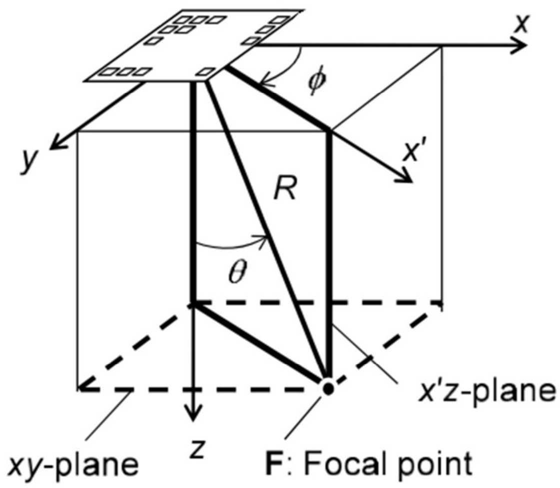

Figure 3.6 Definition of the coordinate system and focal point of a 2D matrix phased array transducer, diagram adopted from (Nakahata et al. 2012)

3.1.3 Key Properties of FUS Transducer

Similarly to other types of ultrasonic transducers, some general characteristics must be considered for FUS, such as the electrical impedance of the active element, resonance frequency, acoustic power output and power transmitting efficiency. Besides, as FUS requires delivery of a focused ultrasound beam to a target volume, the focusing quality and focusing performance over the region of interest, also called the steering ability, are considered as specific properties for FUS transducers, especially for phased arrays.

Complex Electrical Impedance and Resonance Frequency

The complex electrical impedance and resonance frequency can be obtained from measurements of a transducer's impedance spectrum with an impedance analyser, which provides the impedance magnitude and phase spectra over a range of frequency, as in the example in Figure 3.7. The local minimum and maximum in the impedance magnitude spectrum indicate the resonances of a piezoelectric element: electrical resonance with minimum impedance magnitude, and mechanical resonance with maximum impedance magnitude. Their corresponding frequencies are called the electrical and mechanical resonance frequencies, f_e and f_m, respectively.

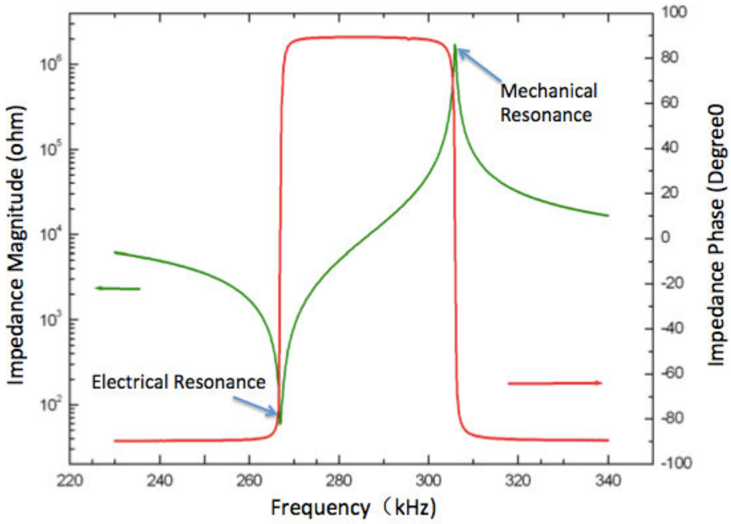

Figure 3.7 Example of electrical impedance and phase spectra with frequency

Because of electrical impedance matching, a receiving transducer usually works most efficiently at f_m, and a transmitting transducer at f_e. Therefore the driving frequency of a FUS transducer should be f_e. However, the driving frequency is usually determined in practice by choosing the frequency near resonance at which the value of the complex impedance is as close as possible to 50 Ω, or most easily electrically matched to 50 Ω, the electrical output impedances of most drive amplifiers. Unmatched electrical impedance to the drive system not only increases the energy loss, therefore decreasing the efficiency of the system, but also risks damaging both the transducer itself and the drive electronics.

Acoustic Power Output and Efficiency

A FUS transducer is required to deliver sufficient power for thermal ablation in tissue. For safe and effective treatment in the clinic, it is essential to know and thus to measure the acoustic power output. Many techniques have been developed to measure the acoustic output of FUS transducers, such as through thermo-acoustic sensors (Fay et al. 1994), fiber optic probes (FOH), piezoelectric hydrophones (Zhou et al. 2006), laser interferometry (Wang, Y. et al. 2007) and radiation force measurement (Hill 1970). Among these methods, measurement using a radiation force balance is convenient and has better accuracy than other methods (Madelin et al. 2005; Junho et al. 2009) in obtaining the total acoustic power output of a FUS transducer.

Transmitting efficiency, K_{eff}, describes how much energy is transferred overall from electrical to acoustical. It can be described as the ratio between acoustic output power and electrical input power, where, in Equation 3.6, W_{AC} is acoustic power and W_E is electrical power.

$$K_{eff} = \frac{W_{AC}}{W_E} \qquad \text{Equation 3.6}$$

The electrical power can be determined either from the power meter measurement or by Equation 3.7:

$$W_E = V_{rms}^2 \cos\theta \,/|Z| \qquad \text{Equation 3.7}$$

where V_{rms} is the root mean square (rms) voltage applied to the FUS transducer, |Z| is the impedance magnitude and θ is the impedance phase.

The efficiency of a transducer in a system is directly affected by the electromechanical coupling coefficient of the piezoelectric material, but also by many other aspects, such as the application of matching layer and backing, and electrical matching for electrical impedance.

Focusing Quality

The focusing quality of a FUS transducer can be represented as focusing gain, *G*, which is defined as the ratio of the focal and source pressure amplitudes obtained in the acoustic medium. Considering a self-focusing single-element transducer as an example, the focal gain can be expressed approximately by Equation 3.8 (Cobbold 2007):.

$$G = 2\pi h/\lambda \qquad \text{Equation 3.8}$$

where h is the height of the spherical bowl arch and λ is the wavelength in the propagation medium, such as tissue.

G can also be visualized by mapping the beam profile of the transducer, most commonly by scanning the acoustic field of the transducer with a hydrophone in a tank of degassed water. As an example, Figure 3.8 presents the beam profile of a spherically curved single element transducer, fabricated in this project with piezoceramic PZ54, plotted in terms of acoustic pressure.

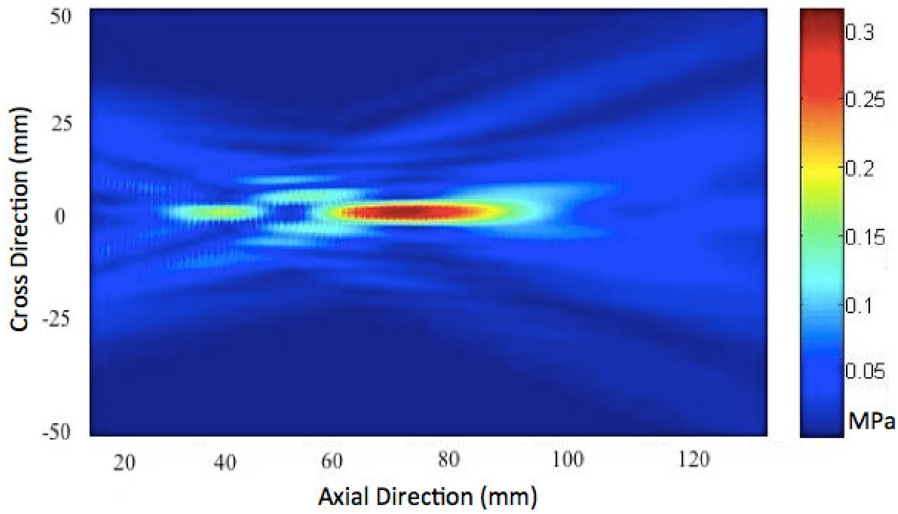

Figure 3.8 Mapped acoustic pressure field of the geometrically curved single element transducer made of PZ54 ceramic.

With the information on focal volume revealed from the acoustic beam profile, *G* can then be examined approximately through experiments. In this approach, *G* is defined by the square root of the ratio of the source area A_s to the focal area A_f, expressed in Equation 3.9 (Bacon 1984):

$$G = \sqrt{A_s/A_f} \qquad \text{Equation 3.9}$$

where $A_s = \pi\,(D / 2)^2$, and A_f is the cross-sectional area of the focus, which is defined as that the pressure amplitude is greater than exp(-1) times the value at the focus. If the mapped FWHM -6dB area is used, it should be multiplied by 10 / 3·ln (10):

$$A_f = \pi \cdot \left(\frac{FWHM\ beamwidth}{2}\right)^2 \cdot \left(\frac{10}{3 \cdot \ln 10}\right) \qquad \text{Equation 3.10}$$

Generally, *G* is directly related to the geometry of the transducer, the shape of the focus, and frequency. For geometrically focused transducers, transducer geometry can be expressed as f-number, *f#*, which is the ratio of the radius of curvature, *R*, to the transducer's aperture, *D*. A small *f#* will result in a tight focus with higher intensity. Researchers have shown that *f#* should be around one for FUS applications to obtain a trade-off between peak intensity and focal distance; this also reduces near field heating generated by the transducer to avoid unwanted skin burns during sonication (Damianou et al. 1993).

Higher frequency has the effect of narrowing the acoustic beam. Although it will cause a decrease in penetration depth, it results in a tighter focus with smaller cross-sectional diameter at the focal plane and smaller *DOF* as well.

To summarize, a bigger aperture, *D*, shorter focal depth, *R*, and higher driven frequency bring in a tight focus, therefore leading to a higher focusing gain, *G*.

Steering range

The steering range is a particular property of the phased array which expresses the focusing performance of array transducer over the region of interest. Typically, the available steering range of a geometrically-focused FUS array to place its focal point is of the order of 1 cm along and off the axis of symmetry (Gavrilov et al. 2000; Hand, J. W. et al. 2009). Focusing far from the natural focus reduces the energy intensity at the focus and increases the secondary lobes.

The steering range can be investigated by connecting the array transducer to multichannel electronics, and applying sets of delays and excitation amplitudes relating to the targeted focal position. The acoustic field of the transducer can then be mapped. It is typically acceptable if the intensity peak in secondary lobes is more than 10 dB lower than that at the focus, guided by accepted levels for safe treatment (Ebbini et al. 1991).

The steering range is determined primarily by the element configuration, the centre-to-centre element spacing, and individual element dimensions. Large numbers of individual elements will increase the steering range but there is an obvious trade-off between the number of elements and the complexity of phased array and electronics design.

Frequency Response

The frequency response of a transducer has a peak frequency and covers a more or less broad range of frequencies. A FUS transducer usually has a narrow bandwidth, aiming to transmit as much power as possible, and a certain frequency for a specific application. Therefore the FUS treatments for different tissue types and locations of solid tumours will tie up different expensive FUS devices. Generally, one of the unsatisfactory aspects of many contemporary FUS systems is their limited frequency range, reducing their flexibility. Recent research has shown interest in broader bandwidth while still keeping good ultrasound penetration by the means of using piezo-composite as active element (Hand, J W et al. 2009). The adoption of new piezocrystal materials started in this thesis could be a solution as well.

3.1.4 FUS Transducer Development: the State of the Art

With its key role in the FUS system, the transducer is the component in which ultrasound is generated and focused into a desired volume. A single element transducer, as noted previously, generates a single lesion at a certain fixed distance during each sonication, leading to FUS treatments that must rely on mechanical motion of the transducer and long treatment times. To increase flexibility and reduce mechanical complexity, in a similar way to the development of ultrasound imaging arrays, the development of therapeutic transducers is presently shifting from single element transducers to multi-element transducers, in other words, phased arrays with electronic beam steering capability.

The development of FUS arrays is focused on the requirements of clinical practices. As mentioned, one of the challenges for FUS treatment is the long treatment time; research therefore has been carried out on accelerating and enlarging lesion formation. With phased arrays, multiple foci can be generated simultaneously during a single sonication, also called the split-focusing technique (Daum et al. 1999; Patel et al. 2008). The coagulation volumes can be enlarged up to 5 cm^3 in a single ultrasound exposure, in 20s sonication time. Similarly, a toric FUS transducer was designed and fabricated for large volume thermal ablation (Melodelima et al. 2007), as shown in Figure 3.9. The transducer is composed of eight curved elements, each with its focal area spatially located next to the focus of adjacent elements. During operation, each element is active alternately and consecutively resulting in a coagulated volume on average 9.1 ± 4.6 cm^3 obtained in 40 seconds.

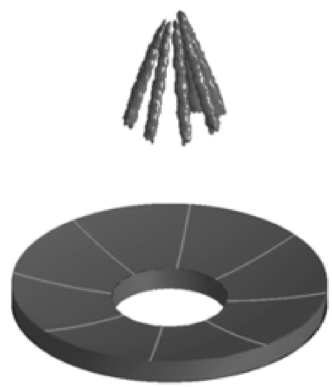

Figure 3.9 Diagram of the toric transducer, with eight elements distributed according to the toric geometry (Melodelima et al. 2007)

Based on a similar principle, dual frequency and dual focus transducers were investigated as well (He et al. 2005; Jeong et al. 2010). With Figure 3.10 (a) as an example, the transducer consists of two elements, with different radii of curvature and responses at different frequencies. The two foci generated by the two elements overlapped, therefore resulting in an enhanced focal area. A recently reported spherically-focused phased array, in Figure 3.10 (b), is divided into two mechanically interleaved sub-arrays (Auboiroux et al. 2011). By modifying the orientation of each individual emitter, each sub-array has its own focus, shifted from the natural focus. The resulting compound steering range is the union of two adjacent steering areas, which leads to a larger steering range than would be achieved using a classic spherically-focused array with the same number of elements.

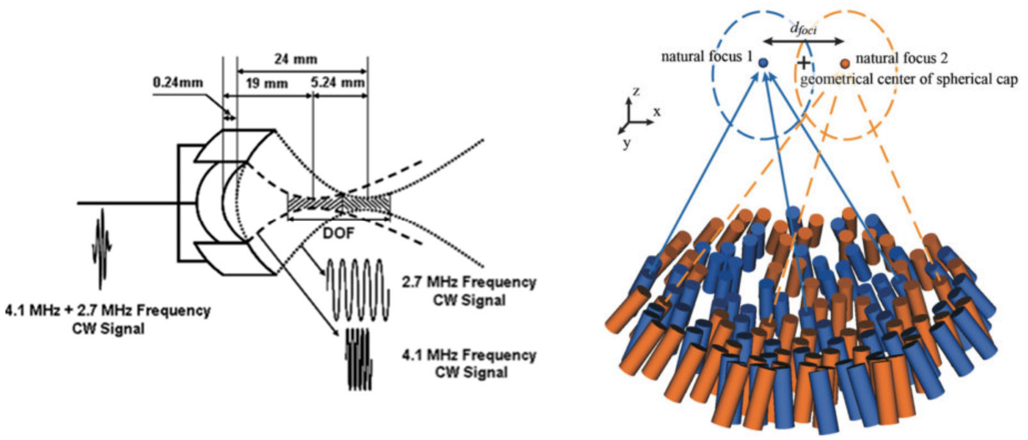

(a) (b)

Figure 3.10 (a) The dual frequency, dual-focus therapeutic transducer(Jeong et al. 2010); (b) Spherically focused array with two mechanically interleaved sub-arrays (Auboiroux et al. 2011).

During clinical practices, mechanical movement of ultrasound devices is sometimes unavoidable, even with phased arrays. The development of FUS arrays is therefore directed at increasing steering ability and minimizing side lobe effects at the same time. As mentioned in previous section, the steering range of an array is strongly dependent on its element configuration, to which research has been addressed as well. The first phased array transducer constructed for FUS was an annular array in the early 1980s (Do-Huu et al. 1981). Since then, various array configurations have been investigated such as: concentric ring with added sectors (Fjield et al. 1997); 1.5D array, also called a cylindrical array (Seip et al. 2005; Gin-Shin et al. 2008); and, most often, 2D arrays, with either a periodic pattern e.g (Daum et al. 1999) or a random pattern e.g (Hand, J W et al. 2009).

Recent research from Philips (Raju et al. 2011) proposed array element-patterning designs that are both non-periodic and space-filling for FUS. Figure 3.11 shows their implemented piezoceramic bowl with single-rectangular shaped elements arranged aperiodically, defined via electrode patterning on piezoceramic's convex side. Their simulation works show that space-filling and aperiodic array designs offer higher power for the same total transducer surface area compared with random arrays, while maintaining acceptable grating lobe levels and reduced element numbers.

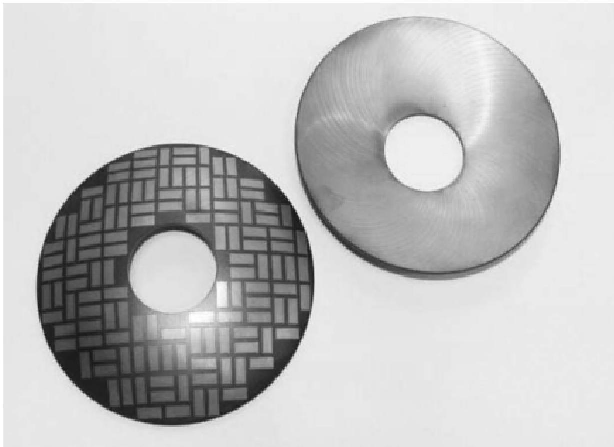

Figure 3.11 Diagram of the toric transducer, with eight elements distributed according to the toric geometry (Raju et al. 2011)

The development of transducers is also application-related. Clinical trials using FUS to treat neural diseases have begun again quite recently, after a long hiatus. To address the challenges of overheating at the skull and the significantly distorted ultrasound propagation through skull, a large-scale phased array with sufficiently large number of elements is needed for brain treatment. InSightec Ltd has developed a 1,000 element hemispheric array for their ExAblate Neuro system (InSightec Ltd, Haifa, Israel), in Figure 3.12. The large surface of this array maximizes the delivery of energy into the focal target but generates only low power density in the near field to prevent overheating of the skull. The large number of elements allows precisely controllable beam steering and focusing by phase and amplitude corrections. Junho Song and Hynynen also developed a similar hemispherical phased array with 1372 elements (Junho et al. 2010). This array uses individual piezoelectric cylinders operated in the lateral mode as a way to reduce the electrical impedance of the transducer element to minimize the effort and cost of electrical matching circuit design.

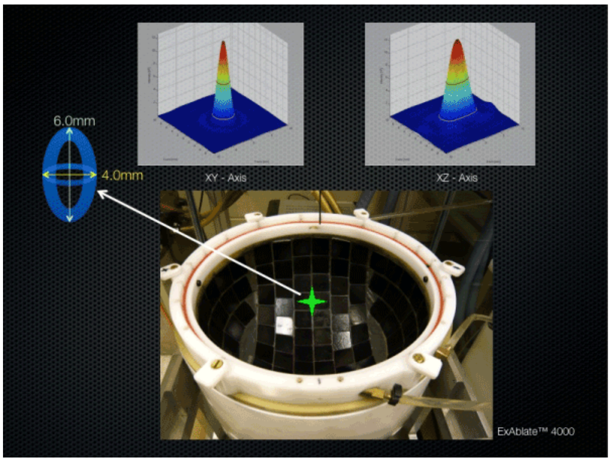

Figure 3.12 The hemispheric transducer of the ExAblate™ 4000 HIFU headsystem. (T Hölscher et al. 2011)

There is no best design in the development of a FUS array. In general, phased arrays for FUS require large apertures for adequate focal spatial localization, and large effective surface coverage to provide sufficient power. It is also necessary, on the one hand, to have enough individual driven channels for improved steering ability without the presence of secondary grating lobes while, on the other hand, minimising the total number of channels to simplify manufacturing and electrical matching construction. Generally speaking, there is a trade-off in phased array transducer design and fabrication between the transducer's structure, its performance, and the difficulty in fabrication.

3.2 Piezoelectric Materials for FUS.

3.2.1 Piezoelectric Material Development

Typical piezoelectric materials can be divided into two main groups, one termed crystals, like quartz (SiO_2), and the other termed piezoceramic, like barium titanate (BaTiO3) and lead zirconate titanate (PZT). The polymer polyvinylidene fluoride (PVDF) shows relatively strong piezoelectricity as well, related to its conformation of molecular bonds rather than the crystal structure. There are still other natural materials that exhibit piezoelectric properties as well, like silk, dry bones and DNA, but the effect is relatively weak. Focusing on the materials used in this work, this section will briefly introduce piezoceramics, piezocrystals and piezocomposites.

Piezoelectric Ceramics

Piezoelectric ceramics ("piezoceramics") are the most commonly and widely used piezoelectric materials in ultrasound devices. The first ceramic was developed as a new type of polycrystalline ferroelectric material made with $BaTiO_3$ in the 1940s. Conventionally, piezoceramics are created from a mixture of a ceramic powder and an appropriate binder or binders. The mixture is then pressed and sintered at high temperature. A poling process is required as the orientation of domains inside the ceramic grains are random initially. By applying a high DC field at a temperature close to the ceramic's Curie point, T_c, the domains are aligned with the field direction. This anisotropic state remains after poling, causing a large enhancement in piezoelectric properties. A major advantage of piezoceramics is that they can be fabricated into various shapes and the direction of polarization can be controlled.

With subsequent developments, Jaffe at al. discovered the strong piezoelectric effects in lead zirconate and lead titanate solid solutions (Jaffe et al. 1954), leading to the development of PZT piezoceramics. To date, the different types of PZT are the most widely used and readily commercially available piezoelectric materials, though the presence of lead has led to legal threats to their use. They are now available with a wide range of piezoelectric, dielectric, and elastic properties. They can be simply classified as piezoelectrically soft and hard ceramics (Jaffe et al. 1965). PZT-4, also known as PZ26 (Meggit Ferroperm, Kvistgaard, Denmark) and PZT-5H (PZ29) ceramics are typical hard and soft ceramics, respectively. The piezoelectric coefficients, such as k_t and d_{33}, and permittivity for PZT-4 are lower than for PZT-5H. However, PZT-4 has less energy loss in both mechanical and electrical terms. Its higher T_c also makes it particularly appropriate for ultrasound applications requiring high power output, while PZT-5H is more suitable for use as source and receiver at the same time.

Over the past six decades, efforts have continued to improve the properties of PZT ceramics for particular applications. PZ54 ceramic (Meggit Ferroperm, Kvistgaard, Denmark) is such a specifically designed material, for FUS. It is harder than PZT-5H but softer than PZT-4; thus it has the advantages of PZT-4 in terms of reduced mechanical and electrical losses, but also very high permittivity, to deliver high power with small volumes of material.

Piezocrystal

Before piezoelectric ceramics were developed, the most common piezoelectric materials were single crystals such as quartz and Rochelle salt. However, their use in transducers was rapidly superseded by the ceramics after World War II, as ceramics can have much larger piezoelectric responses. For four decades, there was no major change then, in 1990, Shrout et al. reported the dielectric behaviour of a new family of single-crystal piezoelectric materials ("piezocrystals") based on lead magnesium niobate doped with lead titanate, $(x)Pb(Mg_{1/3}Nb_{2/3})\,O_3 - (1-x)PbTiO_3$ (PMN-PT) (Shrout et al. 1990). Four years later, PMN-PT piezocrystal material was used in an ultrasonic probe for the first time at Toshiba. Its outstanding properties were widely recognized in subsequent research, publicized as a revolution for ultrasound transducers (Oakley et al. 2000).

Unlike PZT ceramics, piezocrystal is usually grown from seed crystals over a period of days or weeks. Current growth technology has successfully achieved maximum 4" diameter boules (Chen et al. 2005), potentially increasing to 5" diameter (Luo et al. 2010). In terms of piezoelectric behaviour, although somewhat similar to PZT in many characteristics, the particularly attractive properties of single crystal are very high coupling coefficient, $k_{33} \approx 0.9$, and piezoelectric strain coefficient, $d_{33} \approx 1400$ pmV^{-1}. A separate section 3.2.3 will review and discuss the advantages of the new piezocrystal family, thus no more details are mentioned here.

Piezocomposites with enhanced performance

Since the 1970s, composites of piezoelectric and non-piezoelectric material ("piezocomposites") have become widely used as the basis for ultrasound transducers, rather than monolithic piezoceramic plates, with significantly improvements in performance. Piezocomposites usually consist of a matrix of piezoelectric pillars embedded in a suitable polymer. Figure 3.13 is an example of piezocomposite with 1-3 connectivity, meaning that the piezoelectric is connected in one dimension – i.e. through the thickness - and the polymer is connected in all three dimensions. There are ten possible connectivities classifying the structural arrangements in composites (Newnham et al. 1978), but 1-3 connectivity has emerged as most common in practices.

For a 1-3 composite, fabrication can be achieved by the dice-and-fill technique, where kerfs are cut in two perpendicular directions in a bulk ceramic with a diamond or resin blade. The bulk ceramic wafer is usually thicker than the required thickness, so that the ceramic pillars are still attached to the uncut stock. The grooves are then backfilled with the polymer and the excess ceramic stock and polymer can be lapped off the bottom and top surfaces.

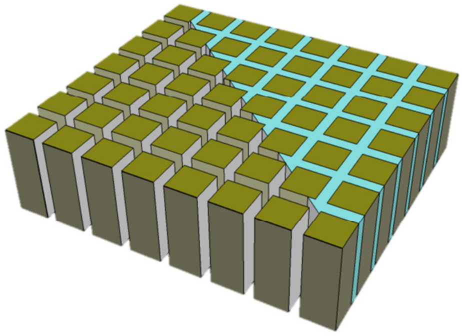

Figure 3.13 1-3 piezoelectric composite with half section of pillars of a piezoelectric material embedded in a polymer matrix

Due to the tall thin pillars, the composite exploits the efficient length-extensional mode with higher electromechanical coupling coefficient, $k_{33} > k_t$, while still operating in an overall plate thickness, k_t, mode. This is one of the main benefits of composites. Another advantage of interest is the reduced acoustic impedance. The inclusion of polymer reduces the average material density and the corresponding acoustic impedance, thus providing a better acoustic matching to biological tissue than a solid piezoelectric material. However, the permittivity is also reduced.

The effective properties of a composite can be expressed as a function of the ceramic volume fraction (VF), with 0% corresponding to pure polymer and 100% corresponding to bulk piezoelectric material (Smith et al. 1991). Volume fractions of 40% - 70% define the range of interest for particular applications. 60% volume fraction is chosen in this work for adequate power generation, whilst giving a good compromise between the acoustic impedance and the dielectric constant. The design of composite is a trade-off between the volume fraction, the element-to-element pitch, and the pillar aspect ratio (AR), i.e. the ratio of height to width of the pillars, usually recommended to be close to 3:1 to avoid extraneous intrapillar acoustic modes.

3.2.2 FUS Requirements for Piezo Material of Choice

FUS requires devices capable of radiating high acoustic power into tissue, therefore a piezoelectrically hard material, with high mechanical quality factor Q_M, to handle the high signal level is best. Large electromechanical coupling coefficient k_{ij} and high dielectric permittivity ε are also desired to meet the demands of high power applications. In practice, these material properties are related to the transducer performance: a 'hard' material means low dielectric and mechanical losses can be maintained during medical treatment; larger coupling coefficient k_{ij} represents the broader bandwidth and higher sensitivity of medical transducers; and higher dielectric constant ε means lower electrical impedance of the material itself and therefore becomes useful in matching electrical impedance. In addition, a high Curie temperature, T_C, or transition temperature is desired to have wider temperature usage range and improved temperature stability and independence (Zhang et al. 2013).

Research has shown that Q_M, k_{ij} and ε can only be enhanced at the expense of each other (Zhang et al. 2005). Similarly, higher T_C can be maintained only by sacrificing the dielectric and piezoelectric performance of the material. Therefore, traditional piezoelectric materials have been modified to meet the requirements of new medical applications, such as FUS. In addition, as new therapeutic devices follow the general trend towards miniaturisation, their structure has to be fine grained (Wolny 2005). Table 3-1 compares the newly developed material, PZ54, specifically for FUS, with the most common hard ceramic material, PZT4 (PZ26).

Table 3-1 Comparison of new FUS material (PZ54) with standard PZT4 material

	ρ (kg/m^3)	$\varepsilon_r^s{}_{33}$	T_C (°C)	k_t	d_{33} (10^{-12}C/N)	Q_M
PZT4	7700	1300	330	0.47	290	>1000
PZ54 (HIFU)	7800	2800	225	0.48	500	1500

* *Material properties obtained from manufacturer's online database (Meggit Ferroperm, Kvistgaard, Denmark)*

As presented, ε and k_{ij} of PZ54 ceramic are improved compared to that of PZT4 ceramic, especially ε, whilst the Q_M is maintained at the high level, meaning the mechanical loss of PZ54 is low as it relates to $1/Q_M$. At the same time, the operating temperature has not been significantly reduced which still sufficiently covers the temperature operation envelope of FUS.

3.2.3 New Generations of Single Crystal Materials (PMN-PT)

The modification and optimization of piezocrystal materials are also being explored. Here, the relaxor- $PbTiO_3$ crystals are reviewed specifically.

Relaxor-based single crystal piezoelectric materials ("piezocrystals"), such as $Pb(Mg_{1/3}Nb_{2/3})\ O_3$ - $PbTiO_3$ (PMN-PT) and $Pb(Zn_{1/3}Nb_{2/3})\ O_3$ - $PbTiO_3$ (PZN-PT) have been well recognized for their outstanding piezoelectric performances compared conventional ceramics. In particular, the attractive properties of piezocrystal are its very high longitudinal coupling coefficient, $k_{33} \approx 0.9$, and piezoelectric strain coefficient,

$d_{33} > 1400$ pmV^{-1}. In this project, PMN-PT piezocrystal is the material of choice for both characterization work, Chapter 5, and array implementation, Chapter 6, therefore it is the family of piezocrystals considered in this section.

Over the last 15 years, piezocrystal materials have found applications in a wide range of actuators, sensors and medical transducers, for ultrasound imaging particularly. The main benefits of using piezocrystal over polycrystalline ceramics are the improved sensitivity and bandwidth when the material is operated in the pillar mode, in the form of piezocomposite material. Another advantage is that piezocrystal will not be affected by microstructure issues such as grain size and porosity; for the applications of miniaturization and high frequencies, they still exhibit excellent properties (Park et al. 1997). With micromachining techniques such as fine mechanical dicing or combining photolithography and dry etching techniques (Changgeng et al. 2013), high frequency imaging transducer devices have been investigated, and the center frequency can go up to 80 MHz, with axial resolution as high as 35 µm (Jiang et al. 2008; Li et al. 2011).

Currently, PMN-PT piezocrystal is commercially available. However, the cost is much higher than ceramics, which remains consistently around \$0.01/mm^3. In contrast, the price of PMN-PT material was as high as \$15/mm^3 at the beginning, due to the difficulties in growing useable amounts of crystal from a single boule (Wallace 2007). With improving growth techniques and higher volume manufacturing, the cost of PMN-PT has dropped in recent years to \$0.5 - 1/mm^3, varing between different manufacturers.

Besides the high cost, the main drawbacks of PMN-PT piezocrystal material are its low coercive field, $Ec \sim 2$ - 3 kV/cm, and low mechanical quality factor Q_M. The material also suffers from temperature limitations: T_C is around 130 °C and the rhombohedral to tetragonal phase transition temperature, $T_{R\text{-}T}$, can be as low as 60 °C. This has restricted the material's acceptance in many applications, particularly for use at high power levels. Thus, extensive research has been carried out to develop new piezocrystals with expanded temperature and electric field usage ranges.

Generations of Piezocrystal

Based on the above mentioned relaxor-based crystal systems, investigations were carried out in order to find the next generation of piezocrystals with higher T_C and $T_{R\text{-}T}$. It was found that $Pb(In_{1/2}\ Nb_{1/2})O_3\text{-}PbTiO_3$, for example, possess relative high T_C near its respective morphotropic phase boundary (MPB), and therefore higher coercive field of $E_C \approx 5.5$ kV/cm for PIN-PMN-PT piezocrystal , at least more than twice that of PMN-PT crystals. The phase transition temperature is on the order of 125°C, resulting in a much broader usable temperature range, and more stable dielectric and piezoelectric properties (Zhang et al. 2008b).

To distinguish the different relaxor-based crystals, the binary crystal system, PMN-PT piezocrystal, was categorized as Generation I, while the piezocrystals having higher T_C, T_{R-T} and E_C, such as PIN-PMN-PT piezocrystal in the ternary system were categorized as Generation II. Furthermore, in order to meet the requirements of high power applications, Generation III relaxor-based crystals have been explored to have low dielectric loss and mechanical loss for reduced the heat generation (Zhang et al. 2011). By adding small amounts of acceptor dopants, such as manganese (Mn), Q_M of Mn-doped PIN-PMN-PT increases 4 - 5 times to 700 – 1000, keeping the equally high electromechanical coupling coefficient in the meantime (Luo et al. 2010). Generation III doped ternary piezocrystal is the best potential candidate for FUS transducer applications.

Selected piezoelectric properties of three generations of piezocrystals compared to common hard and soft ceramics are listed in Table 3-2.

Table 3-2 Selected piezoelectric properties of three generations of piezocrystals compared to hard (PZT-4) and soft (PZT-5H) ceramics

Symbol	**PZT-4**	**PZT-5H**	**PMN-PT**	**PIN-PMN-PT**	**Mn:PIN-PMN-PT**
$\varepsilon_r{}^T{}_{33}$	1320	2800	5400	4200	3811
$\varepsilon_r{}^s{}_{33}$	700	1220	910	729	553
k_t	0.47	0.52	0.6	0.57	0.58
k_{33}	0.68	0.75	0.91	0.91	0.92
d_{33} (10^{-12}C/N)	328	574	1540	1320	1340
g_{33} (V m/N)	0.028	0.023	0.032	0.036	0.040
Q_m	2714	76	60-100	175-250	700-1000
ρ (kg/m^3)	7700	7460	8100	8100	8100
T_C (ºC)	330	235	65-95	100-140	110-140

* *Ceramic properties obtained from manufacturer's online database (Meggit Ferroperm, Kvistgaard, Denmark); PMN-PT (Zhang et al. 2008a); PIN-PMN-PT and Mn: PIN-PMN-PT (Luo et al. 2010). All piezocrystal materials are <001>poled.*

Besides the developments of the three generations of piezocrystal mentioned above, piezocrystal wafers can be oriented along certain crystallographic directions to optimise their piezoelectric properties. This is because the relaxor-based crystals exhibit anisotropic performance, and their piezoelectric properties are dependent on the crystal cut direction and the direction of the poling field relative to the crystal axis. For example, the surface shear mode (the d_{36} mode) was investigated recently by developing an ultrasound sensor with <011> cut and poled rhombohedral PIN-PMN-PT piezocrystal. By comparing with other sensors made with standard thickness mode and shear mode resonators, the sensitivity of the modified crystal was observed to be 10 times higher (Kim et al. 2012).

During the work for this thesis, only Generation I binary PMN-PT piezocrystal was commercially available. There are now six main commercial suppliers: TRS Technologies, Inc. (State College, PA, USA), Sinoceramics, Inc. (USA: State College, PA, USA; China: Shanghai, P.R. China), H.C. Materials Corporation (Bolingbrook, Illinois, USA), IBULE Photonics (Incheon, Sourth Korea), Morgan Technical Ceramics (Berkshire, UK) and APC International, Ltd. (Mackeyville, PA, USA). For Generation II ternary PIN-PMN-PT piezocrystal, TRS Technologies and H.C. Materials Corporation are the only commercial suppliers, whilst Generation III doped ternary piezocrystal is still unavailable in the market, with only limited samples available for academic research. That is the main reason for the fact that, although the doped ternary piezocrystal may be best for FUS and other high power applications, the work reported here was focused on Generation I binary material.

3.3 Characterization of Piezoelectricity

3.3.1 Piezoelectricity

Piezoelectricity is a linear effect of certain solid materials. It refers to conversion from mechanical to electrical energy and vice versa. In the equilibrium state, charge distribution is symmetric in solids and there are no electric dipole moments. However, when external stress is applied, the charges in solids are displaced and an electrical potential difference is generated. This effect was found by the Curie brothers in 1880, and is referred to as the direct piezoelectric effect. A year later, the converse piezoelectric effect was deduced by Lippmann from thermodynamic principles and proved immediately by the Curies.

When piezoelectric material is placed in an electrical field, mechanical strain is generated internally. If an AC electric field is applied, mechanical vibration will be generated at the AC frequency. The direct piezoelectric effect is used in ultrasound transducers to translate acoustic waves into electrical signals, while the converse piezoelectric effect transmits acoustic waves by converting electrical energy to mechanical. If the dipole moment can be reversed by the application of a large electric field, the material is said to be ferroelectric; this covers all piezoceramics and piezocrystals used in this work.

3.3.2 Crystal Structure

Piezoelectricity is strongly connected with crystal symmetry (Auld 1981). Only non-central symmetric materials will have piezoelectricity. 21 of 32 crystallographic classes do not have central symmetry, of which only 20 classes have piezoelectric effects. All piezoceramics and piezocrystals in this work have a perovskite unit cell structure. Figure 3.14 shows the perovskite structure of lead titanate ($PbTiO_3$) in the cubic and tetragonal crystalline forms. An electric dipole moment occurs when the positive charge centre is offset from the centre of negative charge, Figure 3.14(b). Any deformation of the crystal structure can affect the strength of the dipole moment in a piezoelectric material.

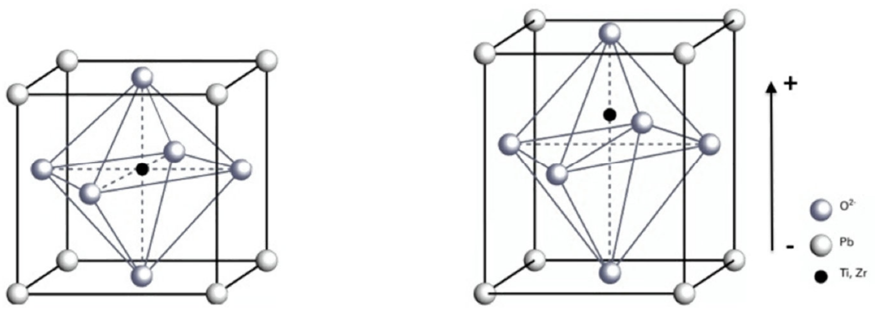

(a) (b)

Figure 3.14 The crystal structure of lead titanate, $PbTiO_3$ (PT) with (a) cubic structure above T_C; and (b) tetragonal structure below T_C, with an electric dipole moment present

Figure 3.15 is the composition - temperature phase diagram of PZT ceramic. For piezoceramic with a composition near its morphotropic phase boundary (MPB), the structure of the unit cell presents as a cube when the environmental temperature is above T_C; when the temperature is below T_C, the structure transfers into a tetragonal state; and if the temperature is cooled below a phase transition temperature $T_{R\text{-}T}$, the unit cell structure will transfer from tetragonal to rhombohedral (Jaffe et al. 1971).

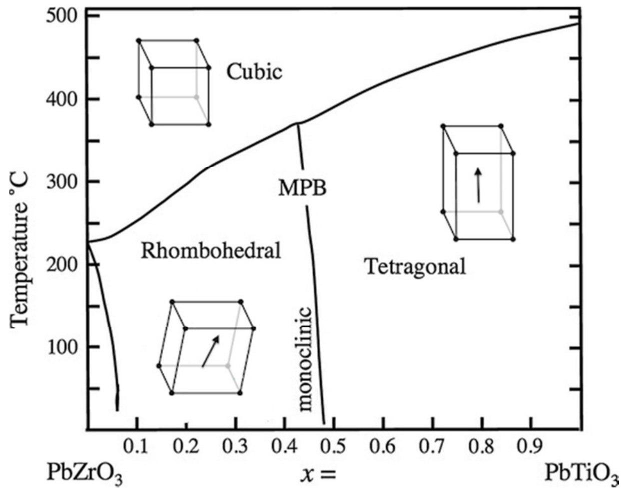

Figure 3.15 Composition- temperature phase diagram of PZT ceramics ((Welberry et al. 2010), adapted)

Since crystal structure transitions affect piezoelectric performance, it is important that the material is used in a stable state with the best possible piezoelectric properties. Hence $T_{R\text{-}T}$ and T_C are crucial parameters of a piezoelectric material of choice. The piezoceramic materials, PZ26 and PZ54 (Meggit Ferroperm, Kvistgaard, Denmark) used in this work did not experience the phase transition issue. On contrary, PMN-PT piezocrystals suffer from limitations caused by low $T_{R\text{-}T}$ within a common operating temperature range, as can be seen from the phase diagram of Figure 3.16. Solid circles and the related phase boundaries are adapted from (Shrout et al. 1990). *C*, *R* and *T* refer to cubic, rhombohedral and tetragonal regions. The diagonally shaded area represents the monoclinic, *M*, phase region (Ye et al. 2001). Results in Chapter 5 will present more details of the phase transition effects on piezocrystals.

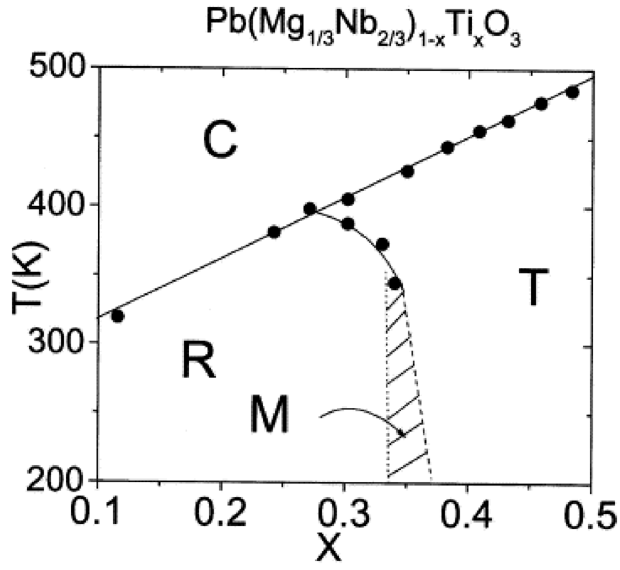

Figure 3.16 Composition- temperature phase diagram of piezocrystal $Pb(Mg_{1/3}Nb_{2/3})1\text{-}xPb(Ti_xO_3)$ (From (Shrout et al. 1990; Ye et al. 2001), adapted).

3.3.3 Piezoelectric Constitutive Relations

Mathematically, piezoelectricity can be described as the relationship between the stress, *T*, strain, *S*, electric field, *E*, and electric displacement, *D*, in the material. Piezoelectric materials are anisotropic and thus the electrical and mechanical constants and piezoelectric properties are also anisotropic. To take the orientation into account, tensor notation is adopted. The symmetric stress tensor, **T**, and strain tensor, **S**, can be reduced for compactness from a 3 x 3 matrix to a six-element column vector. The reference axes are shown in Figure 3.17. The coordinates are denoted by subscripts 1, 2, and 3, corresponding to the Cartesian directions *X*, *Y*, and *Z*; shear about these axes is represented by the subscripts 4, 5, and 6, respectively. The positive direction of polarization is usually chosen to be along the 3-axis.

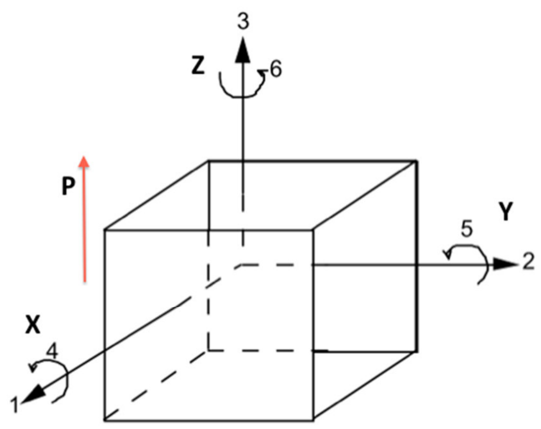

Figure 3.17 Reference axes for piezoelectric behaviour.

Assuming that no elastic deformation occurs inside the piezoelectric material, there will be a linear relation between the components of *T*, *S*, *E* and *D*. Four equivalent sets of the piezoelectric constitutive relations can then be expressed, defined in the IEEE Standard on Piezoelectricity (IEEE Standards ANSI/IEEE 176-1987), Equation 3.11 and 3.12 list two sets of four of constitutive relations as examples:

$$T_I = c_{IJ}^E S_J + e_{iI} E_j$$

$$D_i = e_{iJ} S_J + \varepsilon_{ij}^S E_j \qquad \text{Equation 3.11}$$

and

$$S = s_{IJ}^E T_J + d_{jI} E_j$$

$$D_i = d_{iJ} T_J + \varepsilon_{ij}^T E_j \qquad \text{Equation 3.12}$$

where the *I* and *J* subscripts index from 1 to 6, indicating the reduced notation for the elastic fields, elastic constants and one subscript of the piezoelectric constants. Subscripts *i* and *j* index through 1 (*X* axis), 2 (*Y* axis), and 3 (*Z* axis), for the dielectric constant and the other subscript of the piezoelectric constants. c_{IJ}^E - coefficients are the elastic stiffness constants measured with constant electric field E_j; s_{IJ}^E - coefficients are the elastic compliance constants at constant electric field E_j; d_{iJ} is the piezoelectric charge constant; e_{iJ} is the piezoelectric stress constant, and ε_{ij} is permittivity. The superscript (^{S}) means the material is under constant strain, i.e. the clamped condition, and (^{T}) indicates the situation under constant stress, the free, unclamped condition.

In the equations, the dimensions of the d and e matrices are 3 × 6, those for ε^T and ε^S are 3 × 3, and those for c and s are 6 × 6. Thus Equation 3.13, for example, can be written in matrix form, as follows:

$$\begin{bmatrix} S_1 \\ S_2 \\ S_3 \\ S_4 \\ S_5 \\ S_6 \\ \hline D_1 \\ D_2 \\ D_3 \end{bmatrix} = \left[\begin{array}{cccccc|ccc} s_{11} & s_{12} & s_{13} & s_{14} & s_{15} & s_{16} & d_{11} & d_{21} & d_{31} \\ s_{12} & s_{22} & s_{23} & s_{24} & s_{25} & s_{26} & d_{12} & d_{22} & d_{32} \\ s_{13} & s_{23} & s_{33} & s_{34} & s_{35} & s_{36} & d_{13} & d_{23} & d_{33} \\ s_{14} & s_{24} & s_{34} & s_{44} & s_{45} & s_{46} & d_{14} & d_{24} & d_{34} \\ s_{15} & s_{25} & s_{35} & s_{45} & s_{55} & s_{56} & d_{15} & d_{25} & d_{35} \\ s_{16} & s_{26} & s_{36} & s_{46} & s_{56} & s_{66} & d_{16} & d_{26} & d_{36} \\ \hline d_{11} & d_{12} & d_{13} & d_{14} & d_{15} & d_{16} & \varepsilon^T_{11} & \varepsilon^T_{12} & \varepsilon^T_{13} \\ d_{21} & d_{22} & d_{23} & d_{24} & d_{25} & d_{26} & \varepsilon^T_{12} & \varepsilon^T_{22} & \varepsilon^T_{23} \\ d_{31} & d_{32} & d_{33} & d_{34} & d_{35} & d_{36} & \varepsilon^T_{13} & \varepsilon^T_{23} & \varepsilon^T_{33} \end{array}\right] \begin{bmatrix} T_1 \\ T_2 \\ T_3 \\ T_4 \\ T_5 \\ T_6 \\ \hline E_1 \\ E_2 \\ E_3 \end{bmatrix} .$$

Equation 3.13

3.3.4 Piezomaterial Matrix

Constitutive Relations for Matrix

Either Equation 3.11 or 3.12 is sufficient to define the material properties of a piezoelectric material fully. From one set, using the relations between coefficients listed in Equation 3.14, a different set can be obtained by using straightforward matrix algebra operations.

$$[s^D] = [c^D]^{-1}, [s^E] = [c^E]^{-1}, [\varepsilon^T] = [\beta^T]^{-1}, [\varepsilon^S] = [\beta^S]^{-1}; \quad \text{(a)}$$

$$[d] = [\varepsilon^T][g] = [e][s^E], [e] = [c^E][d] = [h][\varepsilon^S]; \quad \text{(b)}$$

$$[g] = [s^D][h] = [d][\beta^T], [h] = [\beta^S][e] = [g][c^D]; \quad \text{(c)}$$

$$[s^E] - [s^D] = [g]^t[d] = [d]^t[g] ,$$

$$[c^D] - [c^E] = [h]^t[e] = [e]^t[h]; \quad \text{(d)}$$

$$[\varepsilon^T] - [\varepsilon^S] = [d]^t[e] = [e]^t[d],$$

$$[\beta^S] - [\beta^T] = [h]^t[g] = [g]^t[h]; \quad \text{(e)}$$

… … Equation 3.14

Table 3-3 lists the piezoelectric coefficients present in the constitutive relations and elasto-electric matrix. For the materials used in ultrasound transducers, the d- and g-

coefficients are of practical significance. In Equation 3.12, if there is no stress component, d_{33} will be the only non-zero value in the Equation, which can then be expressed as Equation 3.14:

$$d_{33} = S_3/E_3 \quad \text{Equation 3.15}$$

Thus d_{33} describes the deformation for a given applied electric field, which corresponds to the converse piezoelectric effect. The g-coefficient expresses the change in electric field with a given stress, which is equivalent to pressure if the transducer is used as a detector. In this case it determines the transducer output voltage sensitivity. For a FUS transducer aiming to transmit energy, the d-coefficient is of particular importance.

Table 3-3 Piezoelectric Coefficients in Constitutive Relations. (From (Cobbold 2007), adapted)

Coefficients	Name	SI Units
c^D, c^E	Elastic stiffness	Newton/metre^2
s^D, s^E	Elastic compliance	1/(Newton/metre^2)
d	Piezoelectric charge constant	Coulomb/Newton = 1/(Volt/metre)
e	Piezoelectric stress constant	Coulomb/ metre^2
g	Piezoelectric voltage constant	(Volt×metre)/ Newton
h	Piezoelectric stiffness constant	Volt/metre = Newton/Coulomb
ε^T, ε^S	Permittivity	Farad/metre

Reduced Elasto-electric Matrices

As previously noted, the poling process for piezoelectric materials creates an axis of symmetry along with a poling direction (3 – axis) within the material, which leads to a huge simplification in the elasto-electric matrix. The electrical and mechanical properties of piezoelectric material then appear to share or have related values in any direction normal to the axis. Furthermore, many of the coefficients in the matrix are zero due to symmetry. Therefore the maximum number of independent coefficients is very much reduced.

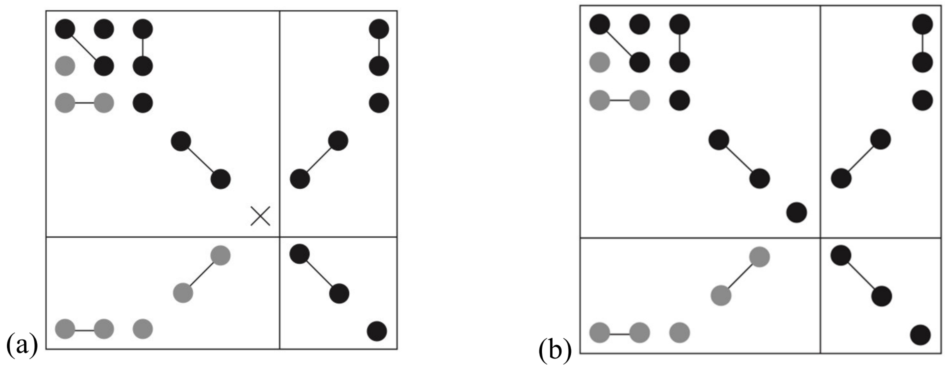

Figure 3.18 Coefficients in elasto-electric matrices for (a) PZT ceramics – crystal class *6mm*; and (b) piezocrystal PMN-PT – crystal class *4mm*. (Linked dots: Numerical equality; Grey dots: Defined by symmetry of dark dots; Cross: Indicates 2 x (s_{11} - s_{12}) or (c_{11}-c_{12}) / 2)

Figure 3.18 illustrates elasto-electric matrices for PZT ceramic and PMN-PT piezocrystal. PZT is a perovskite with hexagonal symmetry, defined as class *6mm*, with the number of distinct coefficients reduced from 81 to only 10, Figure 3.18 (a). The elastic constant matrix [*c*] or [*s*] has 6 × 6 coefficients and can be reduced to five distinct values. Similarly, the numbers of piezoelectric constants ([*d*], [*g*], [*e*], [*h*]) are reduced from 18 to 3 and permittivity has only two distinct values. For materials of class 6mm, the elastic constant S_{66} is not an independent one, which can be obtained from equation below:

$$s^E_{66} = 2 \text{ x } (s^E_{11} - s^E_{12}) \qquad \text{Equation 3.16}$$

PMN-PT piezocryssstal is classified as tetragonal symmetry, class *4mm*, with 11 independent elasto-electric coefficients. Its crystal symmetry introduces one more elastic coefficient *c* ($_{66}$) than *6mm* symmetry, Figure 3.18 (b). The IEEE standard (IEEE Standards ANSI/IEEE 176-1987) quoted previously is correct only for *6mm* symmetry. For *4mm* material, a different set of the constitutive relations is defined with a slightly modification based on IEEE standard (Xuecang et al. 1998). The elastic coefficient *s* ($_{66}$) for a *4mm* material can be obtained from Equation 3.17:

$$s^E_{66} = 4s^E_{45:z11} - 2 \text{ x } (s^E_{11} + s^E_{12}) \qquad \text{Equation 3.17}$$

where $s^E_{45:z11}$ and s^E_{11} are the elastic compliance coefficients extracted from rotated and normal length-thickness extensional (LTE) resonance modes, respectively. s^E_{12} is calculated from measurement of the breathing resonance mode:

$$N_S^2 = \frac{1}{4\rho(s^E_{11}+s^E_{12})}\left[1+\left(1-\frac{8}{\pi^2}\right)\left(\frac{s^E_{12}}{s^E_{11}+s^E_{12}}\right)\right] \qquad \text{Equation 3.18}$$

where ρ is the material density and N_s is the complex series frequency constant which is a function of the longest lateral dimension of the sample w_1 and the series resonant frequency f_s:

$$N_s \quad = w_1 \times f_s \qquad \text{Equation 3.19}$$

3.3.5 Resonance Method for Material Characterization

As discussed previously, piezoelectric materials have certain characteristic frequencies at which they resonate with greater amplitude than at other frequencies. The measurement of characteristic frequencies allows evaluation of the piezoelectric and elastic properties of piezoelectric material, which are strongly coupled to particular resonant modes.

To measure the resonances of a sample, an AC signal with its frequency swept is applied to the material in a specific shape, and with specific aspect ratio and polarization orientation. The current amplitude and its phase are recorded. Dividing the drive voltage by the current will then determine the complex impedance over the swept range of frequencies (Sherrit et al. 2007). The characteristic frequencies can be recorded from the frequency spectrum. A typical resonance plot of impedance versus frequency for a piezoelectric plate near one of its fundamental resonances is shown in Figure 3.7. Based on the resonance frequencies, all the fundamental piezoelectric constants can be calculated except for dielectric constant, according to the constitutive relations presented in Section 3.3.3.

The IEEE standard on Piezoelectricity (IEEE Standards ANSI/IEEE 176-1987) described the resonance methods for measurement of ceramic samples with *6mm* symmetry. Five basic resonant geometries are identified with poling directions and recommended aspect ratios to ensure the target resonant behaviour is the main motion in the specified direction, and well separated from any others in frequency. The identified geometries are presented in Table 3-4: radial extensional (RE), thickness extensional (TE), length extensional (LE), length-thickness extensional (LTE) and thickness shear (TS). The black arrows indicate the poling directions and the grey shaded areas illustrate the electrodes. However, as quoted in previous section, *4mm* piezocrystal requires a slightly different set of sample geometries. More practical details about the samples used for characterizing both types of material are provided in Chapter 4.

Table 3-4 Common resonance geometries for characterizing piezoelectric materials

Resonant Mode	Aspect Ratio	Sample
Radial Extensional (RE) Mode	$20t < D$	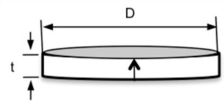
Thickness Extensional (TE) Mode	$10t < l$, $10t < w$	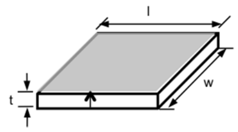
Length Extensional (LE) Mode	$5w < t$, $5l < t$	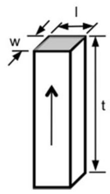
Length-Thickness Extensional (LTE) Mode	$10t < l$, $3t < w$	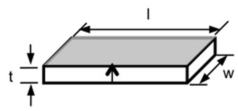
Thickness Shear (TS) Mode	$10t < l$, $10t < w$	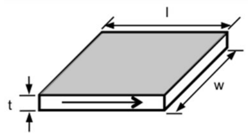

D is the diameter for disc plate, *t*, *l* and *w* are thickness, length and width respectively.

Consider the case of a TE plate with a thickness t, the electrodes on the major surfaces of area, A, and the poling direction perpendicular to the electrodes. The linear thickness mode equation can be defined as:

$$Z = \frac{t}{i\omega A\varepsilon_{33}^{S}}\left[1 - \frac{k_t^2 \tan\left(\frac{\omega}{4f_p}\right)}{\frac{\omega}{4f_p}}\right] \qquad \text{Equation 3.20}$$

According to the IEEE Standard, $\omega = 2\pi f$ is the angular frequency, and f_p and f_s are the parallel and series resonance frequencies at which the real part of the impedance spectrum $Z(f)$ and admittance spectrum $Y(f)$ are maximum, respectively. The coupling coefficient k_t can be calculated using:

$$k_t^2 = \frac{\pi f_s}{2f_p}\tan\left(\frac{\pi}{2}\cdot\frac{f_p - f_s}{f_p}\right) \qquad \text{Equation 3.21}$$

The elastic stiffness constant $c^D{}_{33}$ is defined as follows, where ρ is the density of the material under test:

$$c_{33}^{D} = 4\rho t^2 f_p^{\ 2}$$ Equation 3.22

Equation 3.20 can then be represented as:

$$Z = \frac{t}{i\omega A\varepsilon_{33}^{S}}\left[1 - \frac{k_t^2 \tan\left(\pi f t\sqrt{\rho/c_{33}^{D}}\right)}{\pi f t\sqrt{\rho/c_{33}^{D}}}\right]$$ Equation 3.23

To avoid confusion, it should be noted that the IEEE standard considers the material to be loss-less or low loss, such as PZT ceramic, and the approximation is made that $f_n = f_p$, and $f_m = f_s$, where f_n indicates the frequency at which the impedance magnitude has a maximum, while f_m is the frequency at which the impedance magnitude has a minimum. In the work presented in later chapters of this thesis, f_m (minimum impedance) is represented as electrical resonance frequency f_e, and f_n (minimum impedance) is represented as f_m in which m stands for mechanical resonance.

The PRAP Method

To account for losses in the material, a range of methods has been developed. In the characterization work presented here, the piezoelectric resonance analysis program (PRAP, TASI Technical Software, Ontario, Canada) method was applied. All the constants excluding geometry and density are treated as complex, using their imaginary parts to determine the loss components. In this section, the complex properties are represented with superscript *.

The PRAP method is a combination of the methods of Smits (Smits 1976) and Sherrit et al. (Sherrit et al. 1992). Following the methods of Sherrit et al., f_p and f_s are the frequencies corresponding to the maxima in the real part of $\omega \times Z(f)$ and $Y(f) / \omega$ in this program, instead of $Z(f)$ and $Y(f)$ used in IEEE Standard. The complex parallel and series resonance frequencies, f_p^* and f_s^*, respectively, can be calculated from the observed f_p and f_s. Using TE resonance as an example, by replacing f_p with f_p^* in Equation 3.23, an initial value of $c^{D}_{33}{}^*$ can be calculated.

The Smits' method is a powerful fitting technique in that it will fit three points of the data from the experimental impedance spectra exactly in the convergence limit. With an initial estimated $c^{D}_{33}{}^*$ value, plus two observed impedance values at any two frequencies near resonance, $k_t{}^*$ and permittivity $\varepsilon^{S}_{33}{}^*$ can be calculated from Equation 3.23. By substituting into Equation 3.23 these calculated values of $k_t{}^*$ and $\varepsilon^{S}_{33}{}^*$, and one observed impedance value at a third point of choice on the $Z(f)$ spectrum, an improved $c^{D}_{33}{}^*$ can be obtained. This process is repeated until the difference in the values of $c^{D}_{33}{}^{*}$ obtained from current and previous steps is minimised.

The PRAP method improves on Smits' method by introducing a more accurate $c^{D}_{33}{}^{*}$ obtained from Sherrit's methods. The impedance value at f_p is used as one of the three data points for the calculation. Two other impedance values $Z(f_1)$ and $Z(f_2)$ are required near the resonance, following the rule $f_1 < f_p < f_2$. Similar to the Smit's methods, using the $c^{D}_{33}{}^{*}$ obtained from Sherrit's methods together with $Z(f_1)$ and $Z(f_2)$, $k_t{}^{*}$ and $\varepsilon^{S}_{33}{}^{*}$ can be calculated from Equation 3.23; using $Z(f_p)$ and $k_t{}^{*}$ and $\varepsilon^{S}_{33}{}^{*}$ obtained from the previous step, a new $c^{D}_{33}{}^{*}$ is calculated. The process is then repeated until the values of $c^{D}_{33}{}^{*}$, $k_t{}^{*}$ and $\varepsilon^{S}_{33}{}^{*}$ converge.

The PRAP method fits the experimental impedance spectra and evaluates the material constants around a limited region covering the resonance, and the values are only valid within this region. The calculated parameters from PRAP are less dependent on the choice of two frequency points, f_1 and f_2, when compared to the Smit's method, although it still could have an uncertainty of 10% or more (Kin Wing et al. 1997) if the two frequencies are too close or too far from f_p.

CHAPTER 4 MATERIALS AND METHODS

Having reviewed ultrasound sources for FUS in chapter three generally, this chapter describes the material and methods used for work reported in this thesis. The material characterization for both basic and application-oriented work are detailed in Section 4.1, generally following the order of material samples used, characterization system setup and experimental procedure applied. Sections 4.2 and 4.3 address the development of the FUS transducers implemented in this work, with Section 4.2 presenting the general design and manufacturing methods illustrated by the implementation of a single element self-focusing bowl transducer, and Section 4.3 focusing on the novel methods to implement the geodesic faceted arrays. The array characterization methods are presented in Section 4.4. This chapter not only demonstrates common material and methods used in the work, but also forms part of the outcomes of this project, especially Section 4.2.

The outline of this chapter is thus listed as below:

- Piezomaterial characterization methods
- Transducer design and fabrication: single element transducer and geodesic array
- Transducer characterization

4.1 Piezomaterial Characterization Methods

Piezomaterial characterization is necessary at every stage in the development of an ultrasound transducer, in order to understand the different aspects of effects on the transducer's performance. This section outlines the methods and procedure developed in the present project to characterize piezomaterial, based on the use of an impedance analyser to determine the impedance characteristics of materials, and then the use of commercial software to analyse the material coefficients. Full elasto-electric matrices of both *6mm* piezoceramic and *4mm* piezocrystal were obtained with the basic characterization methods and procedure detailed in Section 4.1.1; specialised experimental arrangements for material characterisation included testing at elevated temperature and pressure are outlined as well, in Section 4.1.2.

4.1.1 Basic Characterization of Piezoelectric Materials

It is very useful for both theoretical studies and device designs to obtain complete sets of elastic, piezoelectric and dielectric constants of the piezoelectric material. The resonance method described in the IEEE standard is used in this work. Multiple samples of PZ54 ceramic and PMN-29%PT were characterized under ambient temperature and pressure conditions and PIN-PMN-PT piezocrystal were also characterized for comparison. The results obtained using the materials and methods described here are presented in Chapter 5, including full elasto-electric matrixes for all three materials along with data on the consistency and uniformity of piezoelectric materials across multiple samples.

Material Samples for Full Matrix Characterization

As introduced in Chapter 3, the resonance characterization method requires multiple samples with various geometries to avoid interference between modes. The different crystal structures of piezoceramic, PZ54, and piezocrystal, PMN-PT and PIN-PMN-PT, lead to slightly different requirements of the sample sets to obtain the respective piezoelectric matrices.

PZ54 Ceramic Sample

PZ54 ceramic material, in the *6mm* crystal class, requires five different resonance modes for full matrix characterization according to IEEE standard, as indicated in Table 3 - 4. However, due to the limitation in availability, only four sample geometries, listed in Table 4-1, were used in this work to extract five resonance modes. The relevant samples were provided by Ferroperm Piezoceramics A/S (Kvistgaard, Denmark). The disc samples, (a), resonate in the RE mode at low frequency, around 150 kHz with diameter 16 mm, and the TE mode at higher frequency, around 2.24 MHz with thickness 1 mm. Therefore both RE and TE resonances can be analysed with a single disc sample by defining appropriate frequency ranges. The other three resonance modes can be extracted from bar sample (b) LE (d_{33}) and plate samples (c) LTE (d_{31}) and sample (d) TS (d_{15}), respectively.

Besides the five basic resonance modes, an additional mode, Length Shear (LS), from a long-thin bar can be analysed as well, with its poling direction parallel to the electrode surfaces. However, measurement of the LS bar is not included in the final calculations here, because of the difficulty of finding the correct LS resonant response in the impedance spectrum. Since the LS mode is not a requirement for full matrix characterization and the properties extracted from the LS mode can be covered by the

TS mode, the exclusion of the LS bar does not affect the completion of the full elasto-electric matrix.

Five PZ54 specimens were available for each of the LE, LTE and TS modes and three discs for the TE/RE mode. The original dimensions of the d_{33} bars and d_{31} plates provided by the manufacturer were quite large. Although having better aspect ratios in terms of separating resonant modes from any others, the resonance frequencies of the samples were relatively low. In order to carry out measurements on these samples, the 4295A impedance analyser (Agilent Technologies, CA, USA) used in this work was calibrated in the low frequency range below 100 kHz, despite this being below the recommended range.

With all the measurements taken with the original samples, two each of the d_{33} bars and d_{31} plates were lapped and/or diced into smaller dimensions, specified as modified samples in Table 4-1. The modifications increased the resonance frequencies, such as f_e, from around 85 kHz to 158 kHz for the LE mode, and from 76 kHz to 156 kHz for the LTE mode, now locating these frequencies within the recommended usable range of the impedance analyser. With no obvious differences observed between measurements of the original and modified samples, this indicates that the calibration below 100 kHz was effective. Therefore the results from both samples were used for later statistical analysis and full matrix calculation.

Table 4-1 PZ54 piezoceramic samples

Specimen Geometry	Vibration Mode	Specimen Specification	Plate Geometry (l x w x t mm^3)	No. of Samples
(a) 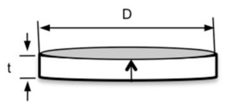	Thickness / Radial Extensional Mode	k_t disc	$D = 16, t = 1$	3
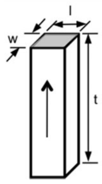 (b)	Length Extensional Mode	d_{33} bar	19 x 19 x 2	5
		Modified d_{33} bar	10 x 10 x 2	2
(c) 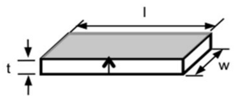	Length-Thickness Extensional Mode	d_{31} plate	20 x 6 x 2	5
		Modified d_{31} plate	10 x 3 x 1	2
(d) 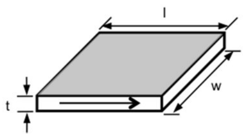	Thickness Shear Mode	d_{15} plate	19 x 19 x 1	5

<u>Piezocrystal samples</u>

Two piezocrystal materials were tested in this work under the scope of basic characterization, Generation I binary crystal (PMN-29%PT) and Generation II ternary crystal (PIN-PMN-PT, exact composition unavailable). The samples were specified to allow full matrix characterization according to the IEEE standard, but with changes appropriate to the *4mm* symmetry of the piezocrystal rather than the *6mm* symmetry of piezoceramic. Besides TE, LE, LTE and TS resonance modes, the reduced *4mm* symmetry of piezocrystal requires an additional resonance mode to obtain the full elasto-electric matrix characterization: the rotated (45°) LTE mode. The aspect-ratio rule still applies to the rotated LTE sample ($d_{31}^{45:Z}$ plate) as well, but the cut of the plate is rotated 45° about the <001> axis, shown as sample (d) in Table 4-2. Similarly to PZ54 k_t discs, the k_t plates of PMN-PT crystal were utilized to obtain both the TE mode in the high frequency range and the LTE mode in the low frequency range, the so called breathing mode for piezocrystals.

The complete set of Generation I PMN-29%PT samples for full matrix characterization were commercially supplied by Sinoceramic Inc (Shanghai, China), listed as Samples (a – e) in Table 4-2. The d_{33} bar sample, (b), drew particular concern in this work since it did not provide LE mode results to match published data. Therefore larger bars, sample (f), named McLaughlin bars (McLaughlin et al. 2005) were tested for parameters related to the LE mode. Despite their thickness-to-width ratio of only 3, rather than the value of 5 specified as standard, these bars exhibited good unimodal electrical impedance characteristics at the bar mode resonance and they were thus used to obtain the parameters reported later.

For Generation II ternary PIN-PMN-PT piezocrystal, the samples required were similar to those presented in Table 4-2 for PMN-PT crystal material. However, unlike the PMN-PT for which a full IEEE sample set was available from the manufacturer, only seven k_t plates (10 x 10 x 1 mm^3), five d_{33} bars (2 x 2 x 9.5 mm^3), and five d_{15} plates (10 x 10 x 1 mm^3) were obtained from TRS Technologies (State College, PA, USA). The missing geometries are the LTE d_{31} plate, and the rotated LTE $d_{31}^{45:Z}$ plate. To complete the sample set, two out of the seven k_t plates were diced into two d_{31} plates and two $d_{31}^{45:Z}$ plates, respectively, with dimensions 10 x 3 x 1 mm^3.

In addition to the samples already noted, several more PMN-29%PT k_t plates were available from different suppliers, allowing the consistency and uniformity of the material to be checked across not only samples but also suppliers. Along with the six k_t plates obtained from Sinoceramic. Inc, another five were purchased from MTC ElectroCeramics (Morgan Technical Ceramics, Southampton, UK) with the same dimensions of 10 x 10 x 1 mm^3. Three more k_t plates were provided by TRS Technologies (State College, PA, USA), and ten plates (10 x10 x 0.5 mm^3) from APC International, Ltd (Mackeyville, USA). This gave 24 plates in total; the measurements are presented in Chapter 5.

Table 4-2 PMN-29%PT piezocrystal sample

Specimen Geometry	Vibration Mode	Specimen Specification	Plate Geometry (l x w x t mm^3)	Cut[2]	No. of samples
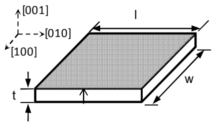 (a)	Thickness Extensional / Breathing Mode	k_t plate	10 x 10 x 1	(ZXt) 0°	6
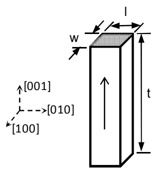 (b)	Length Extensional Mode	d_{33} bar	2 x 2 x 10	(ZXt) 0°	5
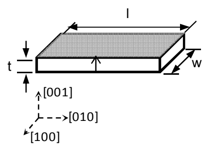 (c)	Length-Thickness Extensional Mode	d_{31} plate	10 x 3 x 1	(ZXt) 0°	5
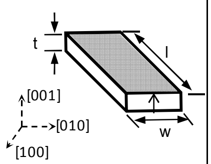 (d)	45°Rotated Thickness Extensional Mode	$d_{31}^{45:Z}$ plate	10 x 3 x 1	(ZXt) ±45°	5
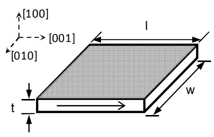 (e)	Thickness Shear Mode	d_{15} plate	10 x 10 x 1	(ZXt) 0°	5
(f) 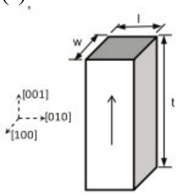	Length Extensional Mode	d_{33} bar	4 x 4 x 12	(ZXt) 0°	3

[1]All samples are poled along [001] direction

[2]Cut notation as defined is ANSI/IEEE Std 176–1987, p. 26

Experimental Arrangement

Basic piezoelectric material characterization under ambient conditions is very widely practiced. Figure 4.1 presents the experimental arrangement used in this work. All the samples noted in the previous section were mounted in a specially constructed fixture directly attached to a 4395A Network / Spectrum / Impedance Analyser (Agilent Technologies, CA, USA). In this fixture, the sample is placed on a gold-plated lower surface and contact is made to the upper surface with a spring-loaded, gold-plated Coda-Pin connection (Coda Systems Ltd., Essex, UK). Electrical impedance spectra of all the specimens were recorded by the impedance analyser, operating in its impedance analysis mode for this project, and at the lower end of its recommended 100 kHz – 5 MHz frequency range. Full calibration of the analyzer and fixture compensation were applied prior to the measurements reported here. A maximum of 801 data points were taken over the selected frequency range, this being the limit of the 4395A.

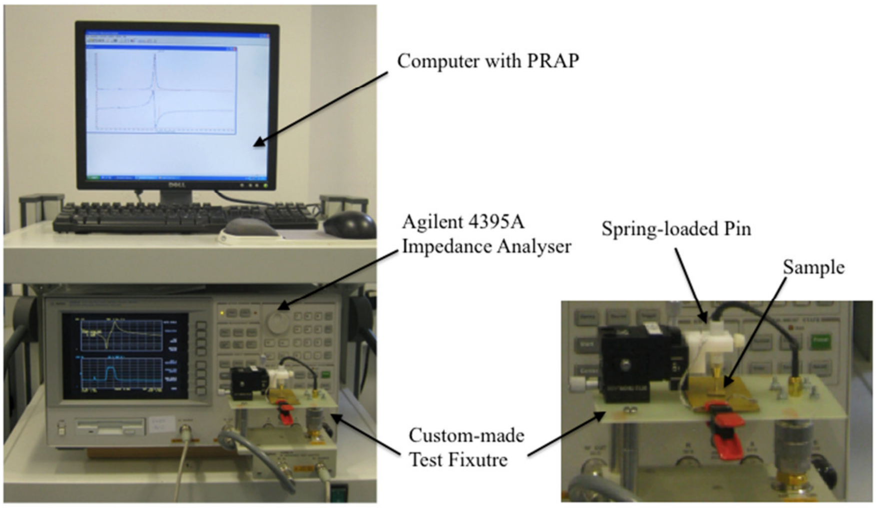

Figure 4.1 Experimental arrangement for basic material characterization

Software and Analysis Procedure

The Piezoelectric Resonance Analysis Program (PRAP, TASI Technical Software Inc., Kingstong, Canada) is a Microsoft Windows-based program which can be used to determine the full piezoelectric matrix of a material by cross-referencing several impedance spectra data. These spectra can be acquired directly from the impedance analyser into PRAP, where the following resonance analyses are carried out.

PRAP allows the determination of complex elastic, piezoelectric, and dielectric properties of piezoelectric materials. There are currently two symmetry modules available in PRAP: SYM6MM module for analysing piezoceramics with *6mm* crystal symmetry, and SYM4MM module for piezocrystals with *4mm* crystal symmetry. Prior to analysing a resonance spectrum, the correct symmetry for the material is selected, along with the correct resonance mode, and the order of the resonance peak in the spectrum.

PRAP can be used in two analysis modes. The first involves minimal automation, with PRAP parametrically fitting the appropriate resonance for the sample, such as in Figure 4.2, identified manually by the user. The parameters are complex, incorporating loss. In a more highly automated mode, PRAP can aid the user in identifying the appropriate resonance. Both of these analysis modes generate parameters for only a single mode. In this work, piezocrystals were found to be highly susceptible to unwanted modes, leading to the need for care during the basic curve-fitting process. Therefore the minimally automated mode was universally adopted, which has the advantage of permitting the analysis of apparently noisy or badly coupled resonance spectra.

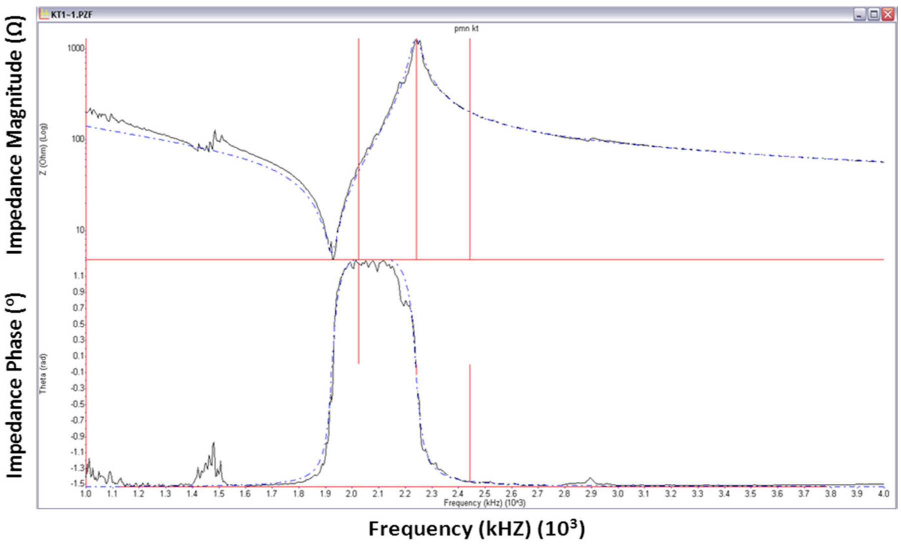

Figure 4.2 Screenshot of fitted impedance spectrum in PRAP for a 10 x 10 x 1 mm PMN-PT k_t plate

As noted previously, multiple specimens of the same sample geometries were available, and repeated measurements on individual samples were carried out. This allowed reporting of the average of the material properties with the standard deviations. By combining a set of analyzed resonance spectra in a PRAP compound file, the statistical distribution of material properties can be studied. The average is defined as:

$$\overline{x} = \frac{1}{N}\sum_{i=1}^{N} x_i \qquad \text{Equation 4.1}$$

where N is the number of available measurements for each property. The standard deviation of each property is determined from:

$$\sigma = \frac{1}{N}\sqrt{\sum_{i=1}^{N}(x_i - \overline{x})^2} \qquad \text{Equation 4.2}$$

This generates an unambiguous set of parameters but not a complete elasto-electric matrix. These average parameters were then transferred into a bespoke spreadsheet to obtain the missing matrix elements. The standard deviations define the stepping limits for adjusting the value of certain key parameters during the procedure of constructing a self-consistent matrix, detailed in the next section.

Reduced Matrix Construction

As noted above, the collection of impedance spectra of a set of IEEE sample geometries is used to generate a set of parameters in this work but not a complete elasto-electric matix. To translate the parameters into a complete matrix, additional calculations are required to determine the properties that cannot be measured directly. A spreadsheet was created for those calculations, with the derivations transferred from constitutive relations between piezoelectric properties. For *6mm* ceramic, as an example, the measurements of RE, TE, LE and TS resonance modes provide nine out of the 10 independent constants of the [s^E, d, ε^T] matrix, with the elastic constant $s^E{}_{13}$ missing. This constant can be calculated using an equation derived from Equation 3.14 (a):

$$s_{13}^{E} = \frac{\left(1 - c_{33}^{E} s_{33}^{E}\right)}{\left(2 \times c_{13}^{E}\right)} \qquad \text{Equation 4.3}$$

In the above equation, $c^E{}_{13}$ cannot be provided by direct measurement either but from calculation, using Equation 4.4 (Sherrit et al. 2007):

$$c_{13}^{E} = \frac{(e_{33} - d_{33} c_{33}^{E})}{2 d_{31}} \qquad \text{Equation 4.4}$$

Once the representation of matrix, [s^E, d, ε^T] is completed, it can be transformed into other representations of matrix based on the constitutive relations indicated in Equations 3.14. It might be noticed that the transformation using the calculated value of $s^E{}_{13}$ may not show good agreement with the properties measured for the various resonance modes, such as $c^D{}_{33}$ in the [c^D, h, ε^S] matrix. Therefore the parameters related to $s^E{}_{13}$ need repeated checks and adjustments until the value of $c^D{}_{33}$ in the transformed matrix agrees with the value determined from the TE mode. To this end, properties measured mainly from LE and LTE modes, such as d_{33} and d_{31} used in Equation 4.4, can be adjusted within their range of standard deviation. Full sets of derivation of equations for calculating the material properties can be found in Appendix A.

Matrix Construction

To summarize, the transformation from direct measurements of material properties from multiple samples into a complete, self-consistent matrix requires an iterative procedure in which comparison and adjustment are involved. The construction of the full elasto-electric matrices in this work can be simplified and summarized in the following steps:

- Multiple samples of multiple geometries were prepared and tested following the IEEE standard on piezoelectricity. PRAP software was used for data analysis to obtain the complex elastic, piezoelectric, and dielectric properties of the samples. Visual confirmation of analysis was provided by the fitted spectra.
- Averages of directly measured properties were used as primary input for calculations to complete the property matrix, which was carried out in a bespoke spreadsheet.
- Once the preliminary matrix was obtained, the comparison between the calculated values and the measured values and published data in the literature led to the adjustment of corresponding properties, by stepping the average value of certain parameters up and down within their standard deviations. This procedure was repeated until the discrepancies of all dependent properties were minimized.
- After a full set of constants had been determined, the electromechanical coupling coefficients, *k*, were calculated using the piezoelectric constants d_{ij} or e_{ij} and the dielectric permittivity ε_{ij}. Although coupling coefficients can be obtained directly from measurement, the calculated values were used in the final matrix. The main consideration here is to ensure the self-consistency of the matrix.
- The relations presented in Equation 3.14 can be used to further check the consistency of the obtained matrix.
- The physical validity of the matrix can be evaluated via some fundamental principles as follows:
    1. The electromechanical coupling coefficients k_{ij} should be always less than one. If any *k* for any vibration mode is larger than one, then the related constants must be reviewed.
    2. The signs of some piezoelectric constants can be determined in advance. For both *4mm* and *6mm* symmetries, it is accepted that $d_{31} < 0$. Since all the constants should have the same signs, e_{31}, g_{31} and h_{31} should therefore all be negative as well (Bogdanov 2000).

3. As the strain energy of the stable crystal material must be positive, some other conditions should also be satisfied: $c^E_{44} > 0$; $c^E_{66} > 0$; $c^E_{11} > |c^E_{12}|$; along with $(c^E_{11} + c^E_{12}) \times c^E_{33} > 2(c^E_{13})^2$ (NYE 1985) [pp138-142].
4. The volume compressibility must be positive (Jiang et al. 2003); this can be expressed as the sum of the nine coefficients in the compliance matrix: $s_{11} + s_{22} + s_{33} + 2(s_{12} + s_{23} + s_{31})$ (NYE 1985)[pp145-146]. For *4mm* and *6mm* symmetries, the principle can be applied as $2s^E_{11} + 2s^E_{12} + 4s^E_{13} + s^E_{33} > 0$, for example.
5. Some elastic compliance constants must be negative as well, such as s^E_{12} and s^E_{13} for *4mm* symmetry (Jiang et al. 2003).

4.1.2 Application-Oriented Characterization under Varying Environmental Conditions

Self-heating is a critical issue for many ultrasound transducers, especially for those driven at high power. The temperature rise induced within the piezoelectric materials will affect its performance. Pressure also has a significant effect on piezoelectric materials, which makes it a key consideration for applications such as medical ultrasonic cutting and drilling and in other areas such as underwater sonar. For FUS transducers, the effect of rising temperature during operation is the primary concern. The pressure effect may not be critical for FUS but the acoustic pressure near the transducer surface can be up to 7 MPa during sonication at clinical power intensities, based on previous research within group (J. Gao, private communication) (Gao 2011), Therefore both the temperature and pressure effects were investigated in this work.

Based on the methods described in the previous section for basic characterization, the materials were explored under simultaneously elevated temperature and pressure. By recording the impedance spectra over ranges of temperature and pressure, the variations of piezoelectric properties can then be extracted over those ranges. The effect of DC bias field on piezocrystal was also investigated as Generation I piezocrystal, PMN-PT, is often operated with an applied bias field.

Material Samples

PZ54 ceramic and PMN-PT piezocrystal were tested in this work. The samples used for application-oriented characterization are from the same sets as those for basic characterization. Although full geometries, except LE bars, can be investigated through the characterization setup detailed in the next section, only the results from TE samples are presented. This geometry is sufficient for 1D modelling and illustrates the complex behaviour of the piezoelectric material. It also allows for trends in behaviour to be observed.

For the work here, one PZ54 disc sample out of three discs was picked, with diameter Φ = 16 mm and thickness 1 mm, shown in Figure 4.3 (a). Additional arrangements were necessary for PMN-PT samples. Due to the requirement from an associated project to use the piezocrystal in an underwater sonar system, the maximum pressure target for PMN-PT was set to be P_{max} = 20 MPa to simulate the pressure at 2000 m water depth. Since the laboratory equipment could apply a uniaxial load with maximum amplitude F_{max} = 1000 N, the supplied sample area 10 x 10 mm^2 needed to be reduced to reach P_{max}. For TE mode samples with a width to thickness ratio requirement of 10, the original sample was thinned from 1 mm thick to 0.5 mm with a precision lapping/polishing machine (PM5, Logitech Ltd, Glasgow, UK) and then cut into four quarters with surface area of 5 x 5 mm^2, Figure 4.3 (b), using a precision dicing saw (MicroAce 66, Loadpoint Ltd., Wiltshire, UK). The missing electrode from the thinning process was reapplied with conductive silver paint (Agar Scientific Ltd, Essex, UK). Although re-poling was possible for this project, it was not used since previous experience suggested the properties of PMN-PT may change after repoling (Wallace et al. 2007) and the aim was to make measurements on the material as supplied.

(a) 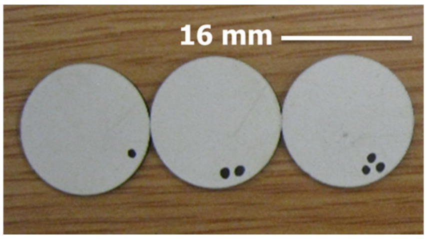

(b) 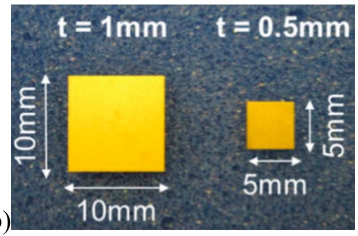

Figure 4.3 Material samples used for application – oriented characterization (a) PZ54 TE disc (b) PMN-PT original TE plate and modified plate after thinning and dicing.

Experimental Arrangement

The set up for testing under conditions of elevated temperature and/or pressure is shown in Figure 4.4. The sample was installed in the oven of an Instron material testing system (MTS) (SID 5564J3038, Instron Ltd., High Wycombe, UK) which can produce temperatures from ambient up to 250°C. The oven provides access for the loading bars to apply uniaxial pressure through its base and top. Tufnol applicator bars (Tufnol Composites Ltd., Birmingham, UK) were constructed, ending in a coaxial stainless steel anvil arrangement to maintain alignment, Figures 4.4(c) and 4.5(a). If required, the DC bias voltage was applied with a high-voltage power supply (PS/EH01P100L, Glassman

High Voltage Inc., NJ) decoupled from the impedance analyzer with a 0.1 μF capacitor rated to 3 kV in series with the sample.

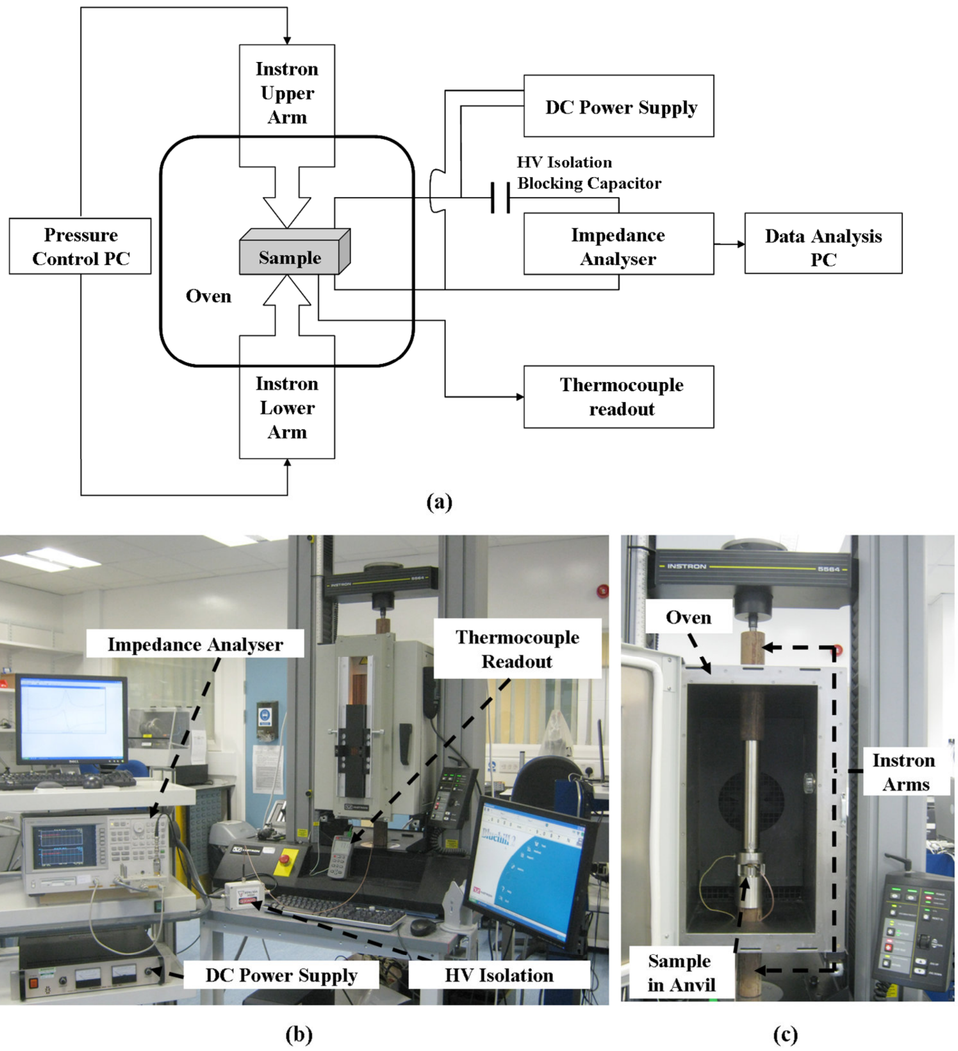

Figure 4.4 Experimental setup for application-oriented characterization with variation in temperarture, pressure and bias field, (a) block diagram (b) general view of physical setup and (c) detail of arrangements for applicator bars.

The electrical contacts with the sample were provided by a fixture made from glass-fiber reinforced polymer (GFRP) printed circuit board (PCB). The GFRP PCB has low acoustic impedance and is extremely lossy, therefore effectively isolating the sample acoustically from the steel anvil. Sample spacers were made for each sample, as illustrated in Figure 4.5(b) with the geometries matching the tested samples. These spacers help not only to maintain the position of the sample but also to prevent short circuit connections between the top and bottom electrodes.

(a)  (b) 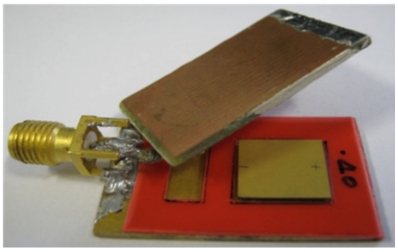

Figure 4.5 Close-up view of (a) anvil with sample holder fitted in (b) sample holder with PMN-PT sample and its matching sample spacer

In operation, the Instron MTS controlled and monitored the load applied to the sample. The temperature was controlled by the Instron oven but monitored by a thermocouple positioned adjacent to the sample. The impedance analyzer was connected to the sample with RG316 heat-resistant coaxial cable (MRG316.0125, Belden Inc.). All cables were kept as short as possible to minimize the possible capacitance brought into the measurements.

Experimental Conditions

PZ54 ceramic material was tested over the temperature range 0 - 120°C, and uniaxial compressive pressure in the range 0 - 5 MPa, with 1 MPa / step, which covers the operating envelope found in FUS applications. For PMN-29%PT piezocrystal, due to the significant variations in properties with temperature, the maximum temperature applied was up to 130ºC, beyond T_c. Pressure was applied up to 20 MPa, in steps of 2 MPa, since medical ultrasonic cutting and underwater sonar are additional interesting applications for piezocrystals. External electrical bias field (0 - 2 kV/cm) was applied to PMN-29%PT, because of its low coercive field. The test conditions are summarized in Table 4-3.

Table 4-3 Experimental conditions for application-oriented characterization

Material	T (°C)	P (MPa)	E_B (kV/cm)
PZ54 disc	0 - 120	0 – 5	N/A
PMN-29%PT plate	0 - 130	0 – 20	0 - 2

The Instron oven used here does not have a cooling function and can thus provide only heating, not cooling below room temperature. To apply the low temperature condition 0

– 20ºC, the applicator bars and the steel anvil were placed in a laboratory -80ºC freezer for at least two hours prior to the experiment. The chilled applicator bar and anvil were then attached to the system quickly, and the experiments started when the temperature reached 0ºC.

Experimental Procedure

As explained previously, temperature and pressure conditions were applied to the PZ54 disc simultaneously, while for the PMN-PT piezocrystal plate, the temperature, pressure and DC bias field were combined together as relevant factors. To carry out the experiments, the procedure is presented in Figure 4.6. At each temperature step, the required pressure cycles were completed; for PMN-PT samples, the electric field cycles were completed for each pressure cycle as well. With both pressure and electric field cycles finished, the oven was set to raise its temperature to the next step, after which the pressure and electric field cycles were repeated.

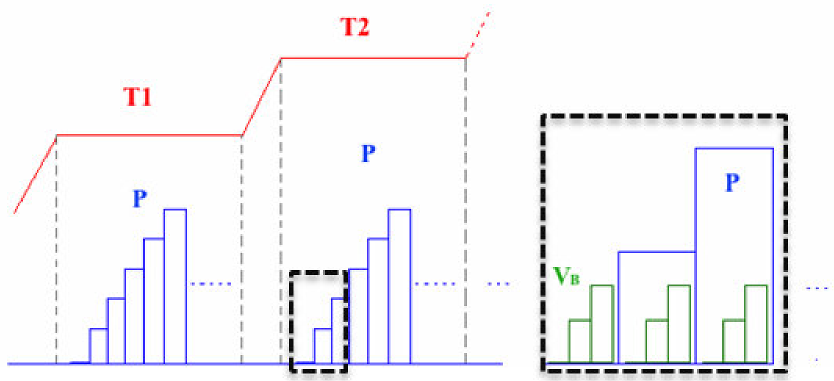

Figure 4.6 Systemic diagram of experimental procedure

Impedance spectra were recorded with PRAP after each step in T, P and E_B. With the testing of PMN-PT sample as an example, 30 spectra were acquired for step in T. After all the spectra been acquired, the post-analysis of individual spectra were carried out in PRAP, with the results presented in Chapter 5.

4.2 Transducer Design and Fabrication

This section describes the materials and methods used for FUS transducers fabricated in this work. Two types of transducer were built: the first prototypes were simple transducers with geometrically curved single elements of PZ54 ceramic; the other type are phased array transducers with 96 elements, arranged to have a natural focus chosen to be similar to that of the single element transducer. Although the phased array configuration was designed to introduce piezocrystals into the FUS application, various materials were used to build devices to prove feasibility and for performance comparison.

4.2.1 General Development Process

The development of an ultrasound transducer always starts with the determination of the specifications, usually based on the target application. The design procedure which follows includes the overall configuration, the material of choice, and sometimes simulation and modelling to predict and improve the performance. Fabrication is the realization of transducer, and the process has to be carefully determined to provide ease of use and high efficiency. Each component should be considered in the realization process: the piezoelectric material preparation, interconnection, application of backing and matching layers, the assembly and packaging. The order of process flow varies from case to case, but is broadly as shown in Figure 4.7, which presents the process used to fabricate the transducers in the present work. The final step is to test and evaluate the completed transducer against the application specification.

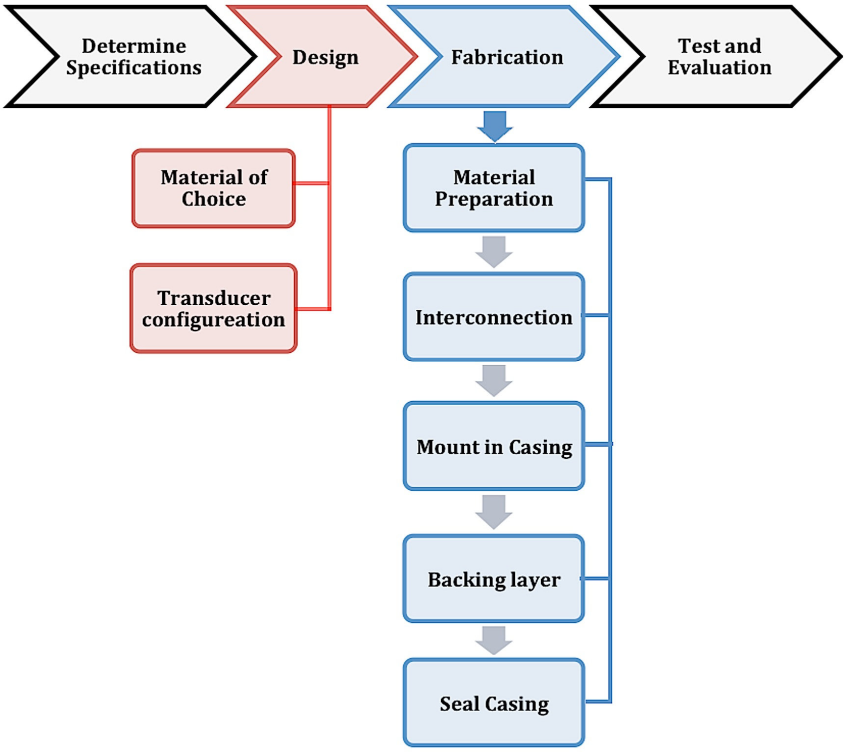

Figure 4.7 General flowchart of transducer fabrication process

Based on the general fabrication process, the fabrication methods of the single element transducer of PZ54 ceramic is introduced in Section 4.2.2, as an example, and the implementations of the 96-element phased array transducers are presented in Section 4.3. Common materials and methods used for both single element transducer and multi-element arrays, conductive epoxy and backing material for instance, are detailed in Section 4.2.2, so the later section can focus mainly on the novel design and fabrication process of the faceted phased arrays.

4.2.2 Single Element Transducer Fabrication

Material of Choice

A single-element, self-focusing bowl transducer was fabricated in this work as the first FUS transducer prototype, Figure 4.8. The piezoelectric element used is geometrically curved with a spherical bowl shape, aperture 60 mm and radius of curvature 75 mm. The material was PZ54 (Ferroperm, Kvistgaard, Denmark) with a thickness of 2 mm and a resonance frequency f_e = 1MHz. These numbers were defined by the manufacturer; however, they also become the references in this work for designing the 96-element faceted bowl transducers, because of the requirement for comparison between a perfect bowl-shaped transducer and a faceted bowl transducer.

The casing of the transducer comprises a machined cylindrical tube, a ring spacer and a rear cover for sealing. All the components were designed and machined to fit each other and the piezoelectric element. The inner side of the ring spacer was glued to the piezoelectric element using fast cure epoxy, while the outer side was attached to the cylindrical housing. PVC was chosen for these components due to the ease of machining and its compatibility with MRI scanning.

The magnetic permeability of the electrical connection is the main concern when it comes to the MRI compatibility of the transducer, as piezoceramic and piezocrystal are non-magnetic, as is the PVC casing. The selection of cable was carried out carefully with RG58 C/U coaxial cable with 50 Ω impedance (RS, 521-7900) chosen for the main connection as it has both inner conductor and braided outer shield made of tinned copper.

Transducer fabrication process

For the single element transducer, the purchased ceramic bowl avoided preparation of the material itself. Thus the main concern was how to connect the cable to the front face of the element from the back. Initially, conductive paint was considered to take the front electrode to the back of the element, by painting the side edge and connecting the front side to a separated area on the back. This would allow easy connection on the back of the element for both active and ground signals. However, the sharp edges of the PZ54 along the path of the paint were considered to be sites of possible failure under the applied high current for FUS and a more direct means using wire connection was finally chosen.

Two small holes, diameter 1.5 mm, were drilled by precision powder blasting at the Microsystems Engineering Centre (MiSEC), Heriot-Watt University, and the front side connection was made with wires penetrating through these holes. To prevent possible short circuit connection between the two faces, the electrode on the back was scratched manually to create two small triangle-shape areas separated with the remaining back surface electrode, Figure 4.8(c). For safety, the front face of element was chosen as the electrical ground, with the high voltage drive signal sealed inside the package. Coaxial cable was used with its inner conductor for signal connection and braided shield for ground. Two cables were connected to the element due to the large size of the transducer and to minimize the risks of connection failure.

The electrical connection between the cable and element were made with conductive silver epoxy (G3349, Agar Scientific, UK). Both inner conductor and braided shielding of the cable were placed and fixed in position with tape on two faces respectively before applying the epoxy, Figure 4.8(b, c). The curing time and overall conductivity depend primarily on temperature, with the relations are listed in Table 4.4. Although curing at under 100°C for 10 minutes is recommended by the manufacturer in order to achieve the maximum conductivity and adhesion, the transducer was placed in oven at 70°C for 20 min to avoid melting the plastic casing.

Table 4-4 Conductive epoxy curing temperature and corresponding time required

Temperature (^{o}C)	Time (mins)
79-121	5-10 mins
>24	Few hours
<24	Not recommended

The backing material was a mixture of micro glass balloon (S38, 3M, Minnesota, USA) and epoxy (Epofix, Struers A/S, Denmark). The Epofix epoxy consists of a part A resin and part B hardener, with a mixing ratio of 25:3 by weight. The micro glass balloon was added to the epoxy mixture until the weight ratio reached 1:1. The micro balloon loaded mixture at this stage had a dry and slightly powdery texture, Figure 4.8(d), and the mixing had to be done by hand with a kneading technique. The reason for adding so many micro-balloons is to minimize the density and thus the acoustic impedance, ensuring maximum power is reflected back into the active element.

The back surface of the piezoelectric ceramic was degreased using isopropanol before the backing mixture was compressed in the casing. The micro-balloon loaded epoxy was applied layer by layer and pressed firmly to prevent air spaces forming. Longer coaxial cable was connected after applying the backing layer; the connected joints were covered by silicon for electrical insolation, Figure 4.8(e). Finally, the transducer was sealed watertight, Figure 4.8(f).

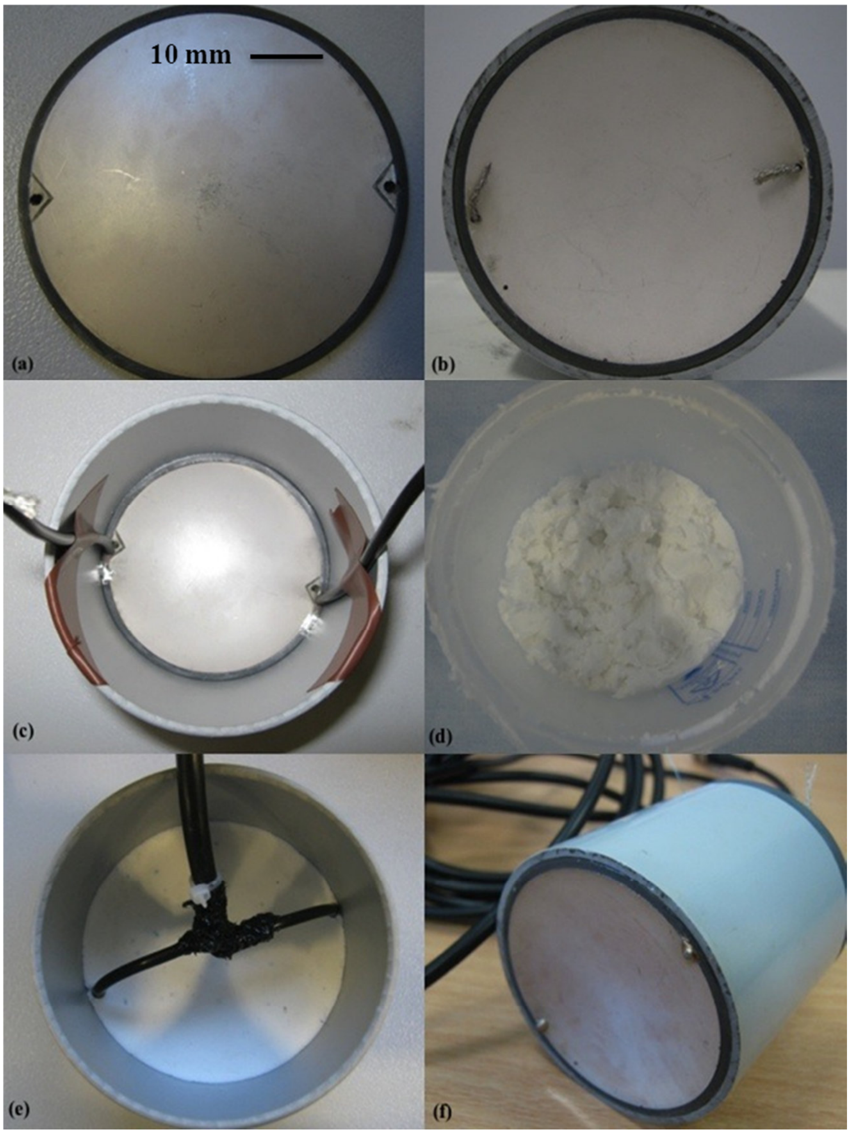

Figure 4.8 Fabrication process of single element transducer

The electrical impedance of this transducer was matched to 50 Ω at f_m. The consideration of choosing f_m as driven frequency rather than f_e is that the impedance at f_m is closer to 50 Ω than that at f_e, resulting in less efforts in impedance matching. Another consideration is the extra electrical effects to the transducer's electrical resonance caused by long cable connection. To test the transducer behaviour in the MRI scanner, the minimum length of cable is 5 m to deliver the power from operator room to scanning room. Although the cable used is coaxial, the 5-meter length still affect the transducer's behaviour, with f_e reduced significantly whilst f_m was not affected. The matching circuit was built with a transformer and capacitors; considering the strong magnetic field in the scanner, the circuit was placed at the other end of long cable, instead of being close to the transducer itself.

4.3 Faceted Array transducer Design and Fabrication

As discussed in Section 3.2.3, piezocrystals have shown advantages in improving the performance of medical transducers, especially those used for ultrasound imaging. FUS has not been considered commonly as an application of piezocrystals yet. However the large electromechanical coupling coefficients and other high piezoelectric coefficients of these materials are promising and attractive as a route to further development of transducer devices. Four prototype faceted bowl transducers were fabricated in this project, aiming to explore the practical issues associated with adoption of piezocrystals for MRgFUS.

A concave geometry is the most typical type to concentrate an ultrasound beam in a localized focal zone (Ebbini et al. 1991). This geometry provides higher focal intensity gain with a natural focus compared with a planar array with similar dimensions. It also requires fewer elements and smaller time delays to move the focus over a range of interests, the secondary lobe level is also lower during focus shifting. Therefore, a spherical-sectioned, concave geometry was chosen for the FUS phased array transducer in this work. However, the fabrication of curved sections using piezocrystal is not possible because of the natural material orientation within the crystal. Thermoforming concave composite is also questionable because of the temperature limitations of the piezoelectric crystal. Instead, a faceted spherical structure was devised, inspired by the geodesic design in architecture, with 24 triangular flat plates, with four slightly different shapes, positioned geometrically in place.

The focusing capability of faceted bowl shape transducers is of concern; this was evaluated using the spherical self-focusing bowl transducer as a reference. To this end, the general specifications of the faceted bowl transducers were fixed and chosen to be as close as possible to those of the single element, spherical self-focusing bowl transducer, in Section 4.2.2. The initial driving frequency of the array was set to be 1 MHz; the F-number was set to be $f\# = 1.25$, the array aperture was set at 60 mm; and the focal distance at 75 mm.

In this section, the geometrical construction of the faceted transducers is introduced first, followed by the fabrication process for both general transducer manufacturing and material preparation. As the transducer was designed to be driven as a 96-element phased array, the multi-element interconnection method applied is described finally.

4.3.1 Geodesic Dome Structure

The geodesic dome was invented by R. Buckminster Fuller in 1954. It is a faceted spherical structure composed of small triangles that are approximately equal, with the vertices of the triangles all lying on the surface of a sphere. Although the planes of the triangles are inside the sphere physically, the geodesic dome still closely approximates a sphere. There are many constructions of geodesic dome; here, a section from a 6V icosahedron dome structure was chosen to build the transducer, illustrated in Figure 4.9(a) where the chosen section is highlighted. The name 6V refers to the number of subdivisional points applied to the icosahedron in order to bring it close to sphere. The larger the number of subdivisions, the closer the structure can be brought to a perfect sphere. The 6V structure has a nearly hexagonal shape from the top view and ensures that the general specifications of this design, aperture and focal distance, listed in Table 4-5, will be approximately the same as those of the single element curved transducer.

Table 4-5 General design specifications of faceted array transducer and corresponding parameters of single element curved bowl transducer

Specifications	**Faceted Array**	**Curved bowl**
Frequency	1 MHz	1.1 MHz
Elements	96	1
Aperture	62 mm	60 mm
Focal Distance	74.5 mm	75 mm*
F-number	1.2	1.25
Surface Area	$2.52 \cdot E^3$ mm^2	$2.95 \cdot E^3$ mm^2

* The actual focal distance of the single element curved bowl transducer was measured later to be 72 mm.

24 triangular flat plates are required to form the structure, with four slightly different shapes and five side lengths denoted as D, F, G, H, and I. Triangles are named after their three sides taken in a clockwise direction: DFG/DGF, HGG, and HII. HGG and HII are isosceles triangles while DFG and DGF are scalene triangles. The calculated lengths of the sides and their corresponding angles are listed in Table 4.6 and the geometrical configurations of the 24 pieces are illustrated in Figure 4.9(b). The number of pieces required for DFG, DGF, HGG, and HII triangles are 6 for each type.

(a)

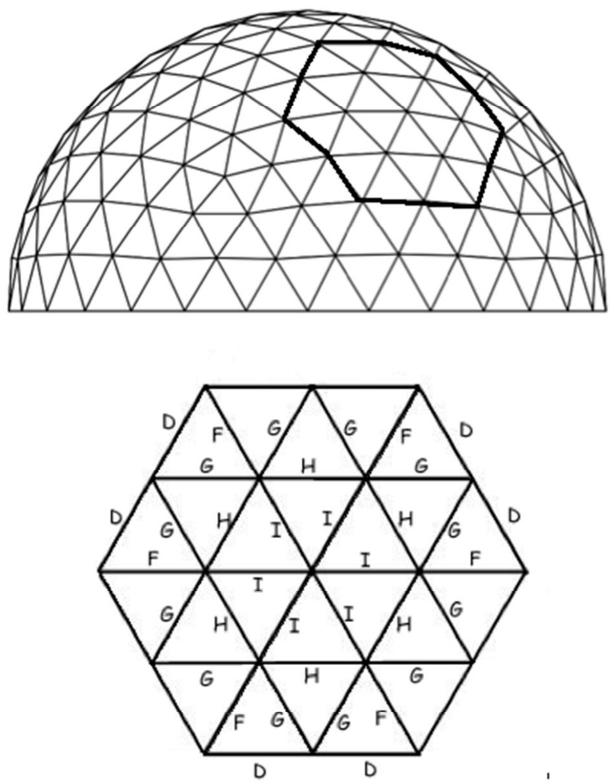

(b)

Figure 4.9 (a) 6V icosahedron dome structure with highlighted section used for faceted transducers; (b) Configuration of 24 triangle plates with four different shapes

Table 4-6 Calculated lengths of sides and their corresponding angles

Triangles	L_1 (mm)	L_2 (mm)	L_3 (mm)	α_1	α_2	α_3
DFG	15.21	14.85	15.44	60.25	61.80	57.95
HGG	16.15	15.44	15.44	63.06	58.47	58.47
HII	16.15	16.24	16.24	59.64	60.18	60.18

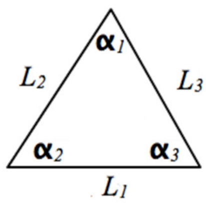

$L_{i\ (i\ =\ 1,2,3)}$ are the side lengths of triangles where i refer to the 1st, 2nd, and 3rd letters respectively of the triangles' names.

To further increase the steering ability of the faceted phased array, more individual elements are required based on the same geometrical structure. For that reason, each triangular plate was sub-divided into four smaller triangular elements by dicing the plate half way through its overall thickness. The number of individual elements thus increased to 96 without increasing the fabrication difficulty of placing elements geometrically in place. Figure 4.10 is a diagram of the 96-element phased array, with Figure 4.10(b) showing the backside of the transducer with 96 sub-divisions, and Figure 4.10(c) showing the front, with 24 geometrical triangular pieces. For these 96 elements, each element was driven by an individual active signal connected to the back, while a common ground was shared at the front for the sake of simplifying the fabrication process.

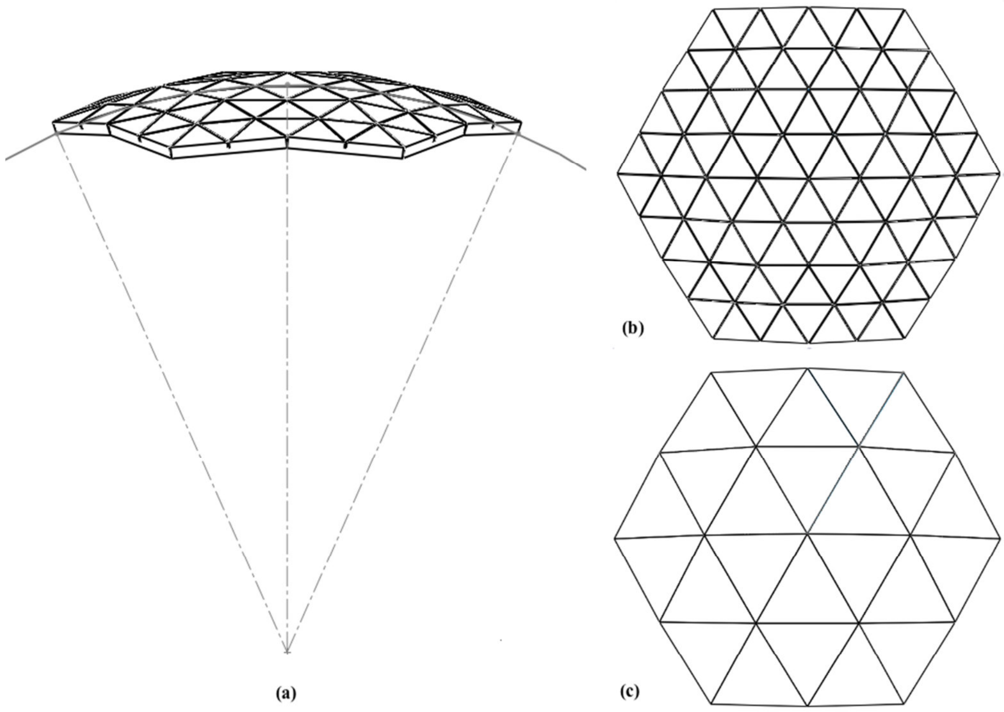

Figure 4.10 Diagram of faceted 96-element phased array (a) overview, (b) back and (c) front of the transducer elements

4.3.2 Implementation of Faceted Array Transducer

This section describes the techniques and methods used in this work to implement the faceted array transducer. Figure 4.11 is a representation of the array transducer built in the Solidworks 3D CAD design program (DS SolidWorks Corporation, Waltham, USA). In order to realize this model, a sequence of tasks is required that includes:

- **The implementation of the active elements** involving the work of fabricating the piezo-polymer composites from bulk piezoelectric materials, and dicing composites plates into triangular shaped elements.
- **The implementation of electrical connection** refers to the realization of both interconnection and external connection. Specific interconnection components and external connectors were built in house.
- **The assembling of the array transducer** starts with the determination of the assembly process flow. Fabrication-related accessories or components, and materials of choice are critical concerns as well.
- **The driving configuration of the array transducer** refers to connecting the array to external multi-channel driving electronics. To achieve this goal, the connecting allocation of element-to-channel has to be studied.

This section of the thesis is divided into several sub-sections for individual procedures mentioned above: composite dicing, lapping, and element dicing; interconnection and external connection; the assembly procedure; and the drive configurations.

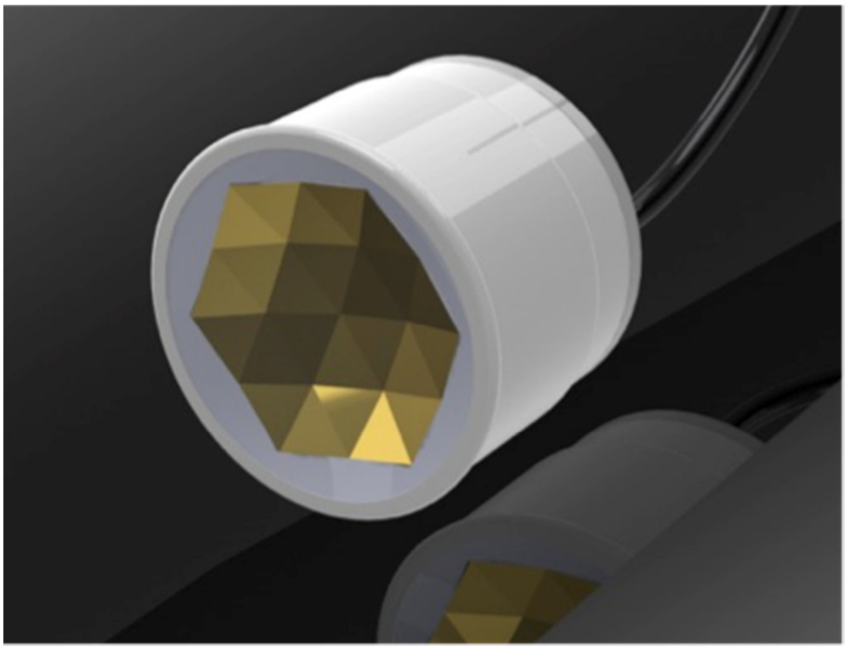

Figure 4.11 Computer-aided design representation of faceted spherical sectioned array transducer.

Composite Preparation

As discussed earlier, piezoelectric material-polymer composite is an appropriate form of material to work with piezocrystals, to allow full exploitation of the advantages related to the high coupling coefficient, $k_{33} > 0.9$. Therefore, the active piezoelectric elements used here were all composite plates with 1-3 connectivity. The composites were fabricated using the dice-and-fill technique (Savakus et al. 1981) with precision dicing, filling with passive material, and removing extra material with a lapping machine as the main processes. Electrode application is also involved as the final step of composite preparation.

In this work, the composites were fabricated following the processes, represented in Appendix B-1. The bulk piezoelectric sample was precision diced in two perpendicular directions to form pillars, and the blade cut slightly deeper than the final desired thickness. A certain thickness of un-cut piezoelectric material was retained as a substrate, Step (a). On completion of the dicing procedure, the sample was released from the dicing saw chuck and placed into a PTFE mould with UV tape as the base. Epofix epoxy (Struers A/S, Denmark), the polymer of choice, was then filled into the grooves to embed the sample completely, Step (b).

Degassing was applied carefully to minimise the existence of any gas bubbles within the composite. The epoxy prior to filling was first placed in a desiccator attached to a vacuum pump. A low-pressure vacuum was created, forcing air bubbles within the mixture to rise to the surface and collapse when air was blown back in. The epoxy was then slowly added from one corner of the block with a pipette to fill the dicing grooves, and the filled block was placed back into the vacuum chamber to further remove any remaining gas bubbles. A method of repeating low-high pressure cycles several times with 1-2 minutes for each cycle ensures the bubbles between pillars will be forced to rise towards the surface. The sample was then cured at room temperature for a period of 8 hours.

After the epoxy was fully cured, the sample was released from the mould for lapping process. The sample was bonded to a chuck and mounted in a lapping machine jig to remove the extra substrate material and epoxy on each side until a desired thickness was reached, Step (c). The desired thicknesses of three materials was predicted by computing method (Smith et al. 1991), in MATLAB program (The Mathworks, UK), presented in Appendix C-1.

Dicing and lapping are two crucial procedures in terms of making piezoelectric-polymer composite, and are addressed in detail later.

15 composite samples were required to form a single faceted bowl transducer. The original square composites were then glued into groups using fast curing epoxy and then diced into triangle elements, Step (d-e), according to the dimensions listed in Table 4-6.

Composite Dicing

A MicroAce 66 Dicing saw (Loadpoint Ltd., Wiltshire, UK) was used in this work to dice bulk piezomaterial samples into matrices of pillars. The device is a semi-automatic cutting and scribing machine with a high power air bearing spindle. Two-point vision alignment is available in a video scope system, and the system resolution is 0.1 mm along the dicing direction, 100 nm in the dicing pitch direction and 100 nm in depth. The material sample is fixed onto a tape-ring holder with tape mounting and the work piece is then secured on a porous chuck by means of an internal vacuum. During the dicing process, chilled water is applied to the fitted bladed as coolant and to remove any particles or residue from the cutting process. The machine is controlled by a Windows-based operating system allowing the dicing programme to be saved. The design parameters for dicing a composite are outlined in Figure 4.12.

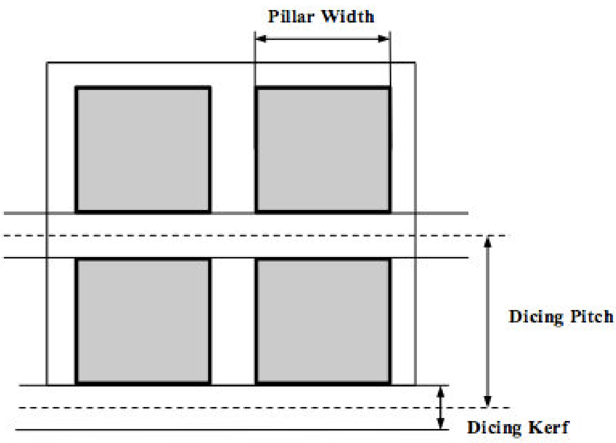

Figure 4.12 Dicing parameters for preparing a 1-3 composite.

The dicing saw is programmed to cut the sample periodically with a specified distance known as the dicing pitch, which is a summation of the pillar width (w) and the dicing kerf (k). The VF can be determined from Equation 4.5:

$$VF = {w^2}/{(w+k)^2} \times 100\% \qquad \text{Equation 4.5}$$

The dicing kerf strongly relates to the thickness of the blade but is commonly wider, with an additional 10 ~ 15 % of actual blade thickness, which is quite dependent upon the type of material being cut, the blade characteristics, mounting method and the cutting parameters. For a desired volume fraction, the final pillar width will be calculated after the kerf has been obtained from pre-dicing trials. Equation 4.5 can be transformed for determining the pillar width Equation 4.6, and dicing pitch, Equation 4.7:

$$w = {k\sqrt{VF}}\Big/{(1-\sqrt{VF})} \qquad \text{Equation 4.6}$$

$$p = w + k \qquad \text{Equation 4.7}$$

The key parameters for dicing process include the spindle speed, feed rate, coolant rate, and cut depth. The determination and optimization of cutting parameters is a process of experience-based adjustment and a balance between quantity and quality of cutting. The detailed parameters for cutting ceramics and single crystal materials used in this work are presented in Chapter 6. In general, soft but brittle materials, such as piezocrystal, will need a lower spindle speed and lower feed rate for clean, chip free cuts. The blade diamond size should be smaller and concentration level should also be lower to minimize chipping and damage to the material. To further prevent fragile pillars from being damaged, the relatively large dicing depth, up to 1.85 mm, required in this work was achieved with a specified number of pecks. Experience from dicing trials showed the cut depth per peck should be limited to 0.5 mm maximum to ensure good dicing quality. The cooling water was set to a low flow rate of around 0.6 l/min in total including both blade coolant and blade wash to prevent the diced pillars been flashed away.

Composite Lapping

The lapping procedure was completed with a PM5 lapping and polishing machine (Logitech Ltd, Glasgow, United Kingdom), to remove the stock and excess epoxy. This device can slowly grind the surfaces of a sample to a desired thickness or alternatively polish the sample surface. The PM5 has automatic plate flatness control which continually monitors and corrects for any deviations of the plate shape and flatness.

For lapping, the sample was bonded onto a pre-flattened glass substrate with wax (Logitech Ltd, Glasgow, United Kingdom). The minimum temperature required for the wax to melt was 60^{o}C, whilst 80^{o}C is recommended by the manufacturer for easiest application. Due to piezocrystal's well-known sensitivity to temperature, 60^{o}C was determined to be the temperature limit during the fabrication processes in this work. The glass substrate was first heated up to 80°C using a hotplate and the wax was smeared on the surface at this temperature. The temperature was then cooled down to 60°C and the piezocrystal sample was placed onto the wax. The sample and the substrate were then moved to a mounting jig preheated to 60°C where pressure was applied to the top of the sample for even bonding. The whole set up was then left to cool down to room temperature. The reason for preheating the mounting jig is to prevent a rapid solidification of wax as the jig's steel substrate would accelerate the cooling of the glass substrate.

The sample and glass substrate were then mounted on the lapping jig with a vacuum. 9 µm and 20 µm calcined Al_2O_3 powder suspensions were used as the abrasives to meet different surface finishing requirements. A steel lapping plate with radial grooves was used for all the lapping work in this thesis.

Both sides of the composite plates must be lapped so that the pillars can appear on both the top and bottom surfaces. After lapping is done on one side, the sample is detached from the glass substrate by heating up the wax, and then re-bonded on the substrate again with the other side facing up. This process might have to be repeated several times according to different fabrication cases. Thus the more removable thickness remaining at the beginning the better thickness control can be achieved.

<u>Element Dicing</u>

As planned, 15 square composite plates were fabricated from each of the three piezoelectric materials. Based on the pre-designed dimensions of the triangular elements in table 4-6, four diced, lapped composites plates out of 15, each with a surface area of 15 x 15 mm^2, were glued together in line to be cut into six HII triangular plates, whose dimension perpendicular to the side H is 14.09 mm. The remaining 11 plates with surface area 14 x 14 mm^2 were glued into two groups, one for cutting out 12 DFG/DGF triangular plates with dimension 13.09 mm perpendicular to side D; and the other for six HGG plates with dimension 13.16 mm perpendicular to side H.

The square plates were glued together using fast curing epoxy (Araldite® Rapid). Plates were fixed in line on the tape first. A ruler was used to ensure the plates were all placed in line. The tape was then flexed to enlarge the gap between composite plates into which the epoxy could be filled. After the epoxy had filled the gaps between the composite, the tape was flattened onto the table. Excess epoxy squeezed out of the gap or on the composite surface was removed carefully under a microscope, using acetone solution with cotton swabs as applicator. The gaps filled with epoxy were then examined under a microscope and any unfilled gaps or holes were refilled with more epoxy, to prevent possible electrical shorting after applying electrodes.

Electrode application

Since the electrodes supplied on the material are lapped off during fabrication, the final step in preparing the composite plates is to reapply the electrodes to the two faces of the samples. The active side of each sample, which was to be diced later into four sub-elements, was painted with silver ink electrode (118-09A/B, Creative Materials Incroporated, USA) mixed from two parts with a ratio of 100 to 1.5 by weight. This ink has excellent adhesion and is very resistant to scratching. Although it takes up to 16 hours to cure at a temperature of 60^{o}C, it successfully withstood being peeled off by either the saw blade or the mounting tape. For the other side of the composite plates, Electrodag 1415M conductive silver paint (AGAR Scientific Ltd, Stansted, United Kingdom) was applied to achieve a smoother finish. The thin consistency of conductive silver paint allowed easy application compared to silver ink or silver paste but also maintained good electrical conductivity and cured rapidly at room temperature.

Interconnection Methods

The 3D structure of the faceted bowl design is the main challenge in establishing interconnections between array elements and the electrical driving system. The application of the backing layer is another consideration, as the microballoon - epoxy mixture is not only used as a backing but also as a mechanical support for all the piezoelectric components. Therefore, direct contact between the piezoelectric plates and the backing layer has to be maintained while establishing electrical connection to each element. As the transducer is designed for FUS applications involving continuous high power drive signals, direct connection using coaxial cables is preferred.

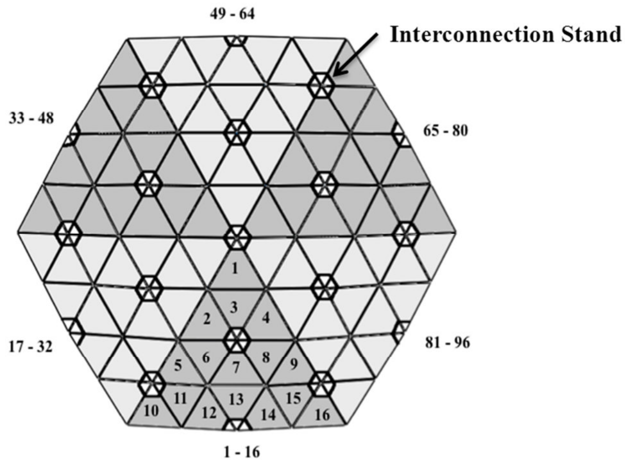

Figure 4.13 Sectional arrangement for 96 interconnections.

For interconnection, the bowl was divided into six sections with 16 elements in each section. The elements were numbered section by section in a clockwise direction, from 1 to 96. In each section, the numbers of the elements were allocated in order from the centre to outside, and left to right as illustrated in Figure 4.13. The colour of the coaxial cable for each section was chosen to be uniform within a section but different from other sections in order to distinguish between sections.

Given the thermal sensitivity of piezocrystal material, soldering was not considered as an option to establish electrical connections between the cables and the array elements. Conductive silver epoxy (G3349, Agar Scientific, UK) was therefore used. Since this requires time in an oven for complete curing, the cable has to be secured in place during that process. To that end, an interconnection stand was required, marked in Figure 4.13 as well, not only to hold the cable in place while curing the silver epoxy but also to accelerate the process by allowing connections for several cables to be established at the same time.

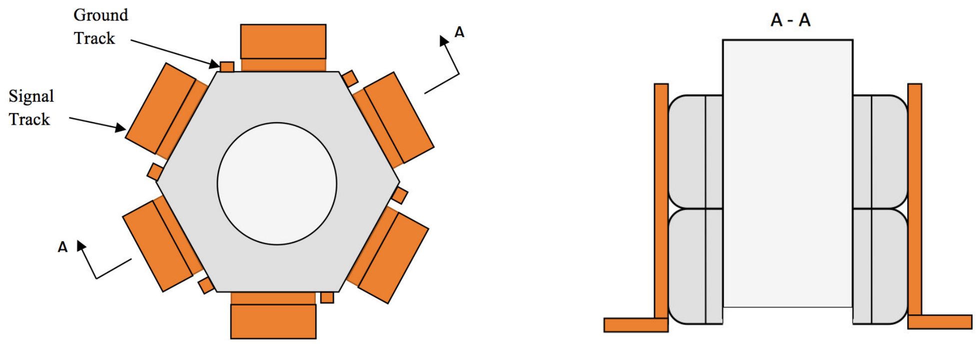

(a) (b)

Figure 4.14 Schematic diagram of custom-made interconnector for faceted bowl transducer (a) top view (b) side view

As shown in Figure 4.14, the interconnecting stand for each set of connections was a hexahedron, built using two plastic nuts stacked together with a section of slot head screw (291-341, RS Components, Northants, UK). The hexahedron shape of the stand allows a perfect separation for six connections in space to minimize the cross talk between elements. The ground and active connection routes are interleaved to further minimize crosstalk. A small chamber was left at the bottom of the screw for the epoxy used to hold the stand in place. A total of 19 stands was required for each array, with 13 stands having 6 cables connected and the remaining six having 3 cables.

The material for the nuts was chosen as nylon for its MRI compatibility, with an M2.5 thread size for a suitable overall dimension. With the final choice of nut (528-132, RS Components, Northants, UK), the stand has a width of 4.9 mm, and height of 3.6 mm, which balances easy handling with minimizing the space occupied on the back of the array.

To complement the stands, a small piece of flexible PCB with copper traces was attached around each stand, with one end for connecting with coaxial cable via soldering, and the other end for connecting the array elements using conductive epoxy. The pattern was drawn in CAD software (DraftSight, Dassault Systemes), and printed on flexible PCB sheet, with 50 μm thick polyimide sheet and 18 μm thick copper. The pattern, as presented in Figure 4.15, contains active signal traces and interleaved ground traces.

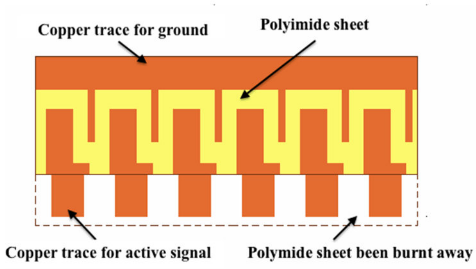

(a)

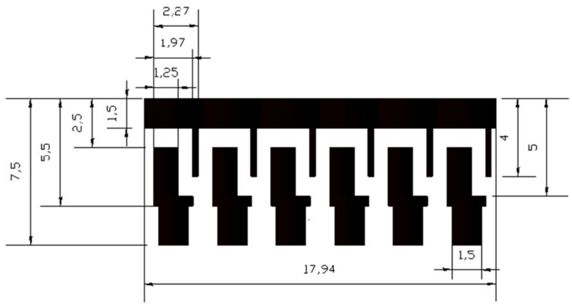

(b)

Figure 4.15 (a) Schematic drawing (b) dimensioned sketch (in millimetre) of flexible printed circuit design for interconnection

The PCBs were printed at Microsystems Engineering Centre (MiSEC), Heriot-Watt University (Edinburgh, United Kingdom). After the design was transferred to the flexible PCB sheet, part of the polyimide material, marked in Figure 4.15(a), was removed by laser direct writing (Zing 24 Laser System, Epilog Laser, US) to separate the legs and allow them to fan out 360° around the stand. The other ends extended to AWG36, MRI-compatible micro-coaxial cables.

External connection

With 96 individual cables emerging from the array transducer, it is necessary to have a secure connecting link between the cables and external electronics. The solution here was to connect the cable ends to PCB with a PCB connector as the output end. Figure 4.16 shows the board design. The pattern has 17 main traces, among which are 16 traces for connecting the 16 elements within one section of the array and one trace at the side for a ground connection. Similar to the design of the flexible circuit for the interconnects, the ground extends between those main traces to provide track to track shielding.

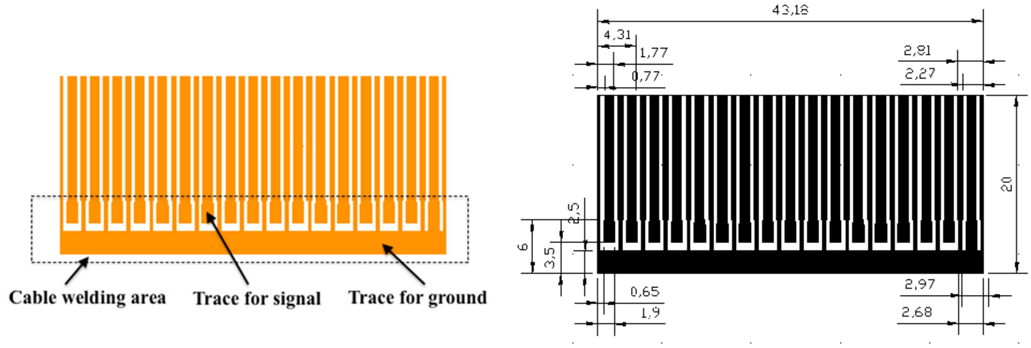

(a) (b)

Figure 4.16 (a) schematic drawing (b) dimensioned sketch (in millimetre) of the board design for external connection

The artwork was printed on both sides of a double-sided PCB, so one PCB will connect the elements within two adjacent array sections and therefore three boards are necessary for all 96 elements. Double row PCB connectors with 34 pins (1-215307-7, TE Connectivity, PA, USA) were soldered to the other end of the main traces. The width of traces and spaces were determined with consideration of both the dimensions of the PCB connector, with 2.54 mm pitch, and the trace requirements for power levels. The PCBs are printed in-house, the fabrication processes can be found in Appendix D.

The Assembly Procedure for Faceted Array

After active elements and interconnecting stands being prepared, the assembling procedure of the faceted array can be started, however, there are challenges needs to be considered prior to the process.

One key challenge during assembly is to place the 24 triangular plates in their positions to form the correct geodesic dome structure. To this end, a spherically curved fabrication mould was designed in SolidWorks, with faceted surfaces to indicate the pre-designed position for each plate. The mould was printed in ABS with rapid prototyping. The 24 triangular plates can then be placed on the mould and attached together later using fast-curing epoxy.

Securing the triangular element plates in positions before applying permanently adhesive was another challenge because of the 3D structure. A layer of temporary adhesive was needed between the surface of the fabrication mould and the plates. Several requirements were considered to choose the adhesive material:

- It should be temporary and removable to allow release of the whole assembly from the mould;
- It should have a low viscosity to minimise the thickness of the temporary bonding layer.
- It should be easy to remove and clean without leaving residue on elements. If solvent is necessary to remove the adhesive it should not cause deterioration of the electrodes.

Combining all these considerations, honey was chosen over other common adhesives, such as silicon grease. The adhesion of honey is sufficient to hold the plates on the mould but is low enough to ensure the mould can be released easily. The viscosity of honey means it can be brushed into a thin enough layer without adding significantly to the dimensions of the mould, and has less possibility to be squeezed into the spaces between elements. Honey can also be removed easily and surfaces can be cleaned with warm water.

Two additional spacers were prepared prior to assembly, one as a transducer spacer and the other as a mould spacer. The spacers were ring-shaped discs with their inner boundaries matched with the outer boundaries of the fabrication mould. Both spacers were built by 3D rapid prototyping. The mould spacer was placed first around the fabrication mould, with the transducer spacer on top, ensuring both upper and lower surfaces of the transducer spacer were located at the same level as the outer edges of the plates.

The active elements were glued together after all the plates were placed in positions and then glued to the transducer spacer, which was glued to the transducer casing later. In this way, extra mechanical support was provided to the element assembly. The transducer spacer also had a small hole in the ring through which cable was passed for grounding.

The process steps to assemble the transducers are illustrated in Figure 4.17. Corresponding to the procedure flowchart, the whole realization process is listed below:

(a) Place the spherically curved faceted fabrication mould with the mould spacer around it on UV tape, which is secured to a larger glass plate. The position of the transducer spacer should be fixed on the mould spacer with tape, to prevent possible movement during fabrication.

(b) Warm up liquid honey in hot water bath to further thin it, then brush on the top surface of the fabrication mould, to cover one of six triangular sections.

(c) Place triangular piezoelectric plates on the honey-painted section of the fabrication mould, plate by plate. The arrangement follows the configuration shown in Figure 4.9(b). The bottom faces of the elements are placed tightly against each other while the upper faces will have small gaps between elements, as shown in Figure 4.17(c). With one section covered by composite plates, process (b) and (c) are repeated until all the triangular plates are placed in position.

(d) Fast curing epoxy (Araldite® Rapid) is filled into gaps between the piezoelectric plates to secure their positions permanently. The spherical section assembly of piezoelectric plates is then glued to the transducer spacer.

(e) Fill the bottom chambers of the interconnection stands with fast curing epoxy (Araldite® Instant), which sets in 90 seconds, and position the stands on the back of the element assembly. The copper legs of the stands are then connected directly to the back electrodes of the elements using conductive silver epoxy (G3349, Agar Scientific, UK). The assembly is then left in a pre-heated oven at 60^{o}C for 30 min, to cure the silver epoxy.

(f) Glue the assembly into the casing, a section of plastic pipe, and apply the backing layer using micro-balloon filled epoxy (K1 glass bubble, 3M, USA; Epofix, Struers, UK). The ground wire has to be placed in position through the hole left in the transducer spacer before the backing layer is applied.

(g) Release the assembly from the fabrication mould. Close the casing with a rear cover and seal the transducer watertight.

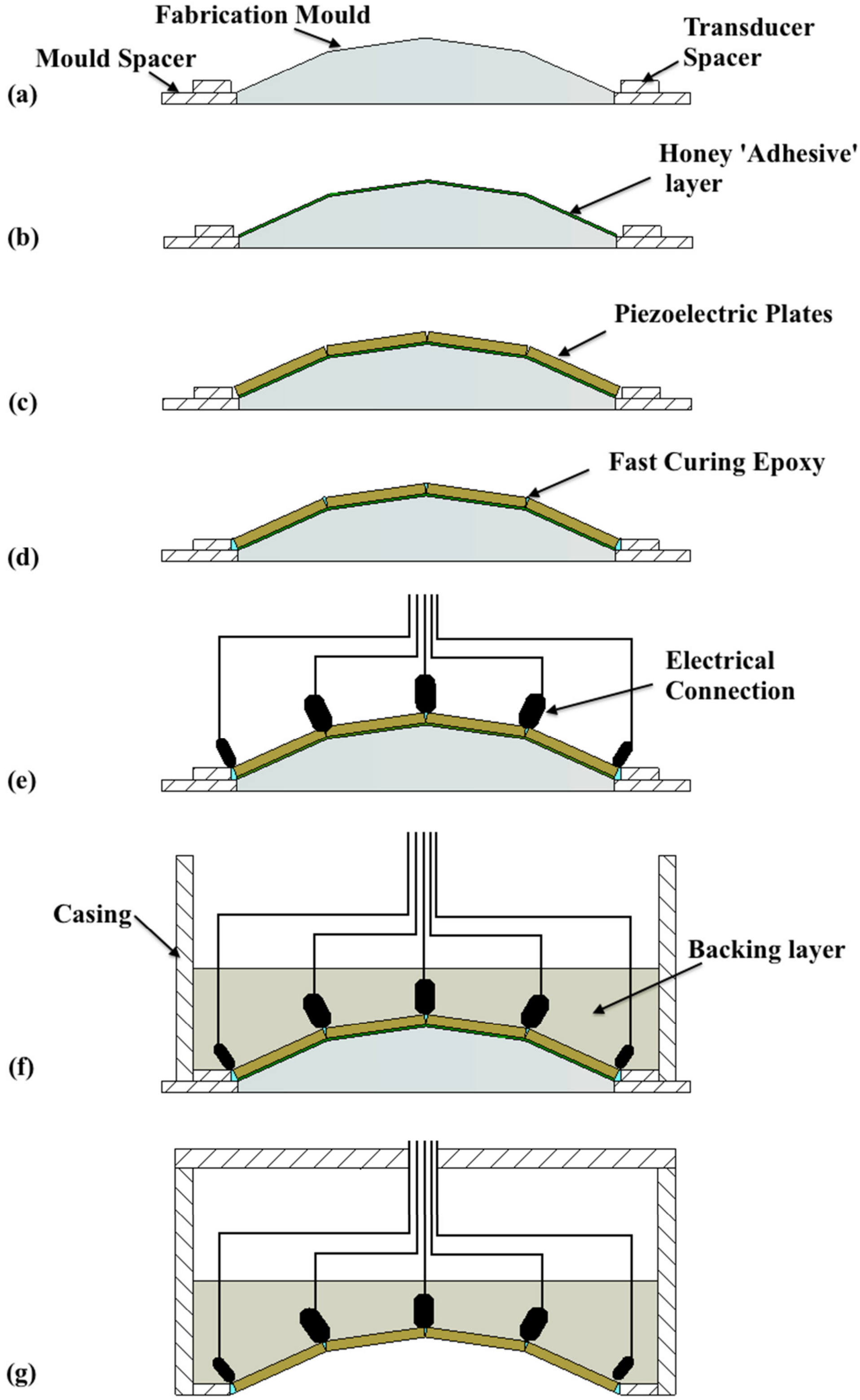

Figure 4.17 Fabrication process chart of Faceted Bowl Phased Array

Array Driving Configuration

Although it is feasible to drive all 96 elements of the array transducers independently, a driving electronics system with 96 individual channels was not available for this project. As alternatives, two driving configurations were applied to the arrays for different experiments.

Single channel arrangement

Under this arrangement, the array elements were excited with a single signal. A connection adaptor was built with PCB pin connectors and wires soldered to a small piece of strip board: 96 elements were connected in parallel and driven by the same signal at the same time. f_m was used as the excitation frequency in this case as the impedance of the whole array was much closer to 50 Ω, around 30 - 40 Ω, than it would have been if driven at f_e.

This arrangement was used to test the natural focusing ability of the faceted structure. Natural focused fields of the arrays were mapped in water with no delays applied to each element.

Multi-channel arrangement

To either electrically shift the focus or improve the focusing gain of a phased array, it is necessary to have multiple channels of driving signal with various phase delays. In the work reported here, a 32-channel ultrasound transmit system (DSL32T, Diagnostic Sonar Ltd, Livingston, UK) was available for a limited period. This system, shown in Figure 4.18, is based on a 32-channel transmitting card produced by Diagnostic Sonar, interfacing with a PXI-mounted FlexRIO 5754 FPGA card (National Instruments, Newbury, UK), controlled with LabVIEW from a host computer. The system generates pulse-width modulated square waves to deliver an approximate sine wave signal to each channel. The phase is controlled and adjusted in 11.25^{o} increments for each channel, over the range of $0^{o} \leq \theta < 360^{o}$.

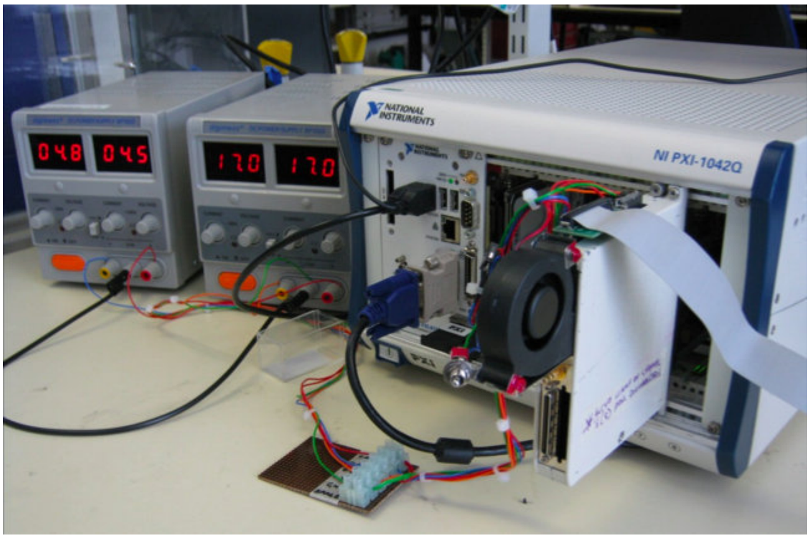

Figure 4.18 DSL32T system with two DC power supplies, one for providing input signal for the system, another for powering the fan.

In order to connect the array transducer to the DSL32T system, the 96 elements had to be grouped into 32 channels. Although there are many possibilities in terms of the grouping, one pattern was chosen and applied at this stage of the work. As shown in Figure 4.19, sets of three adjacent elements of the array were grouped together as one channel, resulting in 32 larger elements. The 2D segmented annular pattern, representing a combination of annular and circular arrays, was intended to allow the focus to be steered along the array's central axis, and off the axis slightly. Each group was given a channel number from one to 32, arranged as shown in Figure 4.19.

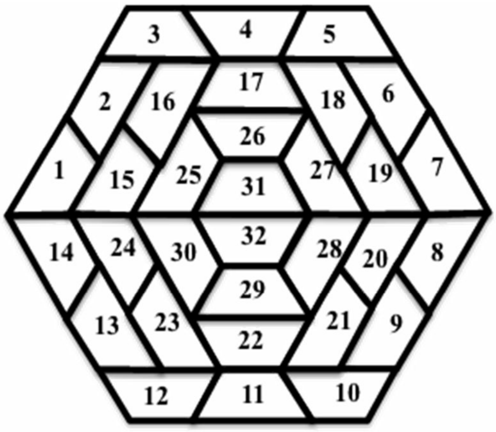

Figure 4.19 Grouped pattern of the array transducer for connecting to DSL32T driving system

The physical grouping of the elements was achieved by joining the relevant tracks on a PCB, with 96 connections to the array elements as input and 32 grouped channels as outputs. The board was designed with DesignSpark PCB (RS Components, Northants, UK), and then made in house. The 32 channels were assigned to two output ports with 34 connections each. Port 1 consists of channels 1 - 16, with the remaining connections as ground; similarly, Port 2 contains channels 17 - 32 plus ground connections. Two 34-core ribbon cables (Spectra-strip, 132-2801-034, Amphenol, Kent, UK) with lengths of 1.5 m connected the board outputs to the DSL32T system.

The board output configuration ensures that the ribbon cable has active signals interleaved with grounds, to avoid possible interference between channels over the given length. However, this configuration does not match the input port on DSL32T system. Therefore an additional PCB was necessary to translate the signal configuration at the ends of the ribbon cables into the matching configuration to DSL32T system. Figure 4.20 shows the approach applied in this work to connect the custom-made array transducers to the commercial driving system.

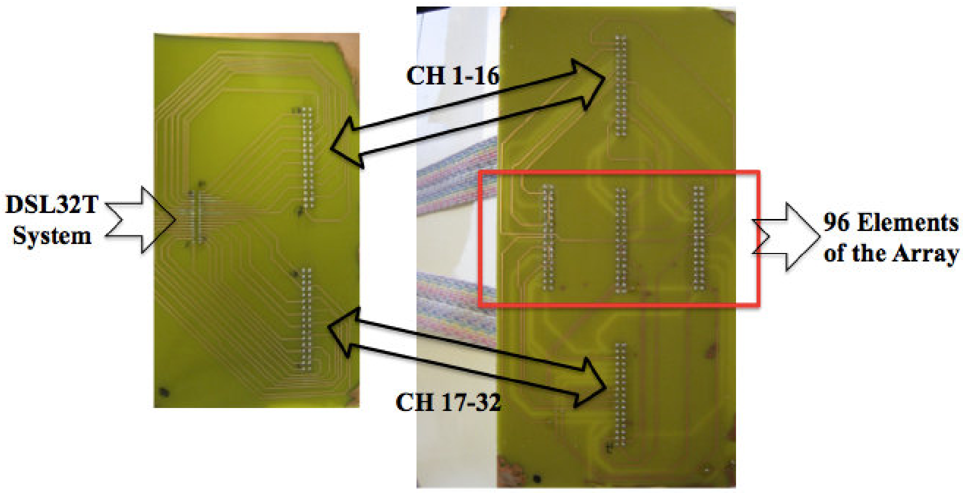

Figure 4.20 The final board and cable layout to connect the 96-element arrays to the DSL32T system

As mentioned, the drive frequencies for the composite arrays were determined according to the driving arrangements and the corresponding electrical impedances of the elements. f_e was used when the arrays were driven as 32 individual channels as impedances of groups of three elements are a few hundred ohms at f_e compared with a few kilohms at f_m.

4.4 Transducer Characterization

The transducers implemented in this work were all characterized for their electrical impedances, operating frequency, ultrasound beam profile, focusing quality and steering range, acoustic power output, and their MRI compatibility.

For each characteristic, the electrical impedances and frequencies were obtained as the basic characterization of transducers through impedance analyser measurements; the beam profile, focusing and steering quality of the four faceted arrays were investigated by mapping their acoustic fields in a water tank; the acoustic power output was measured using a radiation force balance; and finally, MRI images were recorded with transducers in an MRI scanner to test whether they are compatible with the MRI environment.

This section is therefore divided into four sub sections, with Section 4.4.1 for the methods for basic characterization; Section 4.4.2 for acoustic field characterization; Section 4.4.3 for acoustic power output characterization; and then Section 4.4.4 for MRI compatibility characterization.

4.4.1 Basic Characterization Methods

As indicated previously, basic characterization of the transducers was carried out with an impedance analyser (4395A, Agilent Technologies, CA, USA). The magnitude and phase of the electrical impedances were recorded for each element of the faceted arrays. The measurements were made under laboratory conditions, with water or air loading in front of the arrays. BNC cable with two free ends connected the array elements to the impedance analyser. The cable length was minimized; in addition, fixture compensation was carried out to further remove any possible effects of the cable.

Impedance measurement is the quickest, most convenient way to check whether a transducer is functional. The optimum driving frequency can be determined by choosing an appropriate value of complex impedance near resonance. Effective coupling coefficient, k_{eff}, can usually follow from measurement of resonance frequencies. It partly indicates the difference between the electrical and mechanical resonance frequencies, and can be calculated using Equation 4.8:

$$k_{eff} = \sqrt{\left({f_m}^2 - {f_e}^2\right)/{f_m}^2} \qquad \text{Equation 4.8}$$

k_{eff} also gives some indication of a transducer's bandwidth.

4.4.2 Acoustic Field Characterization

The ultrasound fields generated by transducers fabricated in this project were characterized using a hydrophone moved in the field in 3D, in order to map the acoustic pressure. The system setup can be found in Figure 4.21.

The scanning system allows motion along its three axes x, y and z, with a resolution of 3.8 µm. A PC with a preloaded LabVIEW program (National Instruments, Berks, UK) provides the overall control and data acquisition. The device under test was immersed facing downwards in a $440 \times 500 \times 300\ \text{mm}^3$ ($l \times w \times h$) water tank filled with degassed water. A 0.5 mm diameter needle hydrophone (Precision Acoustics Ltd., Dorchester, UK) was placed underneath the array vertically, and the motion increment was set to be 0.5 mm, 1/3 of wavelength. The sensitivity of the hydrophone is $s = 408.5$ mV / MPa at 1 MHz. The peak-to-peak output voltage $Vp\text{-}p$ of the hydrophone was recorded and analysed offline for pressure conversion in a MATLAB program (The Mathworks, Cambs, UK). Acoustic intensity, I, was calculated with Equation 4.9:

$$I = {P_{rms}}^2 \Big/ Z_{ac} = \left(V_{p-p}/2\sqrt{2} \cdot s\right)^2 \Big/ (\rho \cdot c) \qquad \text{Equation 4.9}$$

where Z_{ac} is the acoustic impedance of water, P_{rms} is the root mean square acoustic pressure, ρ is density of water, and c is the sound speed in water.

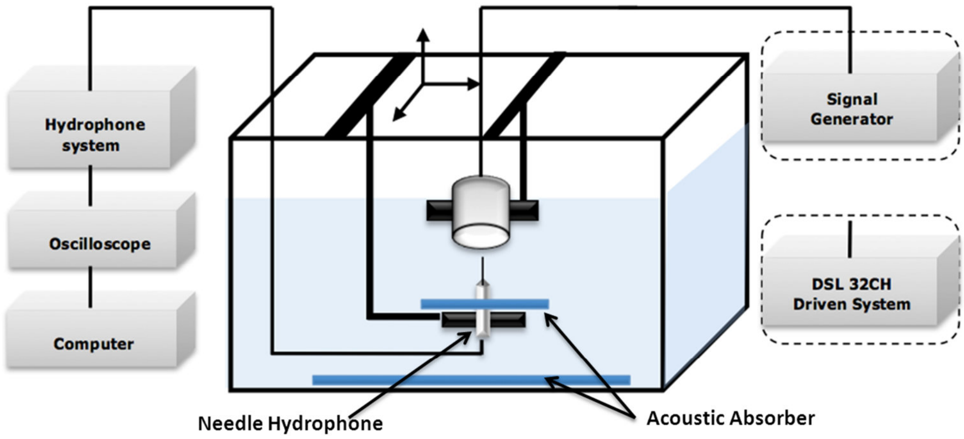

Figure 4.21 System setup for acoustic field mapping

Because of the vertical arrangement of the ultrasound transducer and hydrophone, two pieces of acoustic absorber were used, with a large piece covering the bottom of the water tank, and a small piece around the hydrophone, as marked in Figure 4.21, to avoid possible distortion of the acoustic field caused by reflection and standing waves.

During the mapping experiments, the array transducers were either driven by a functional generator with all the elements joined together as one channel, or by the DSL32T system with 32 grouped channels. The signals applied to the array transducers were kept low, as the needle hydrophone used was not designed for high power and high intensity measurements.

So far there are no direct methods that allow the acoustic field of a FUS transducer to be characterized at clinical power levels, at which the acoustic intensity can reach several thousands of W/cm^2. Specific hydrophones have been designed for FUS transducers, like a reflective needle hydrophone (Wang, Yuebing et al. 2007) and the recently developed fibro-optic probe hydrophone (FOPH) (Zhou et al. 2006). Another promising method based on acoustic holography (Sapozhnikov et al. 2003) combines the indirect measurement of high intensity fields with computer programing to reproduce the transducer's surface pressure distribution, by back-propagation, and then the emitted acoustic field, by the Rayleigh integral method.

4.4.3 Acoustic Power Output Characterization

In order to measure the acoustic power output of array transducers, a radiation force balance (RFB) (Precision Acoustics Ltd., Dorchester, UK) was set up with a conical target. The frequency range of this system is 1 - 10 MHz and the power range is 10 mW to 100+ W. However, limited by the rated power tolerance of the absorbing target, the maximum acoustic power that can be measured using this setup is less than 20 W.

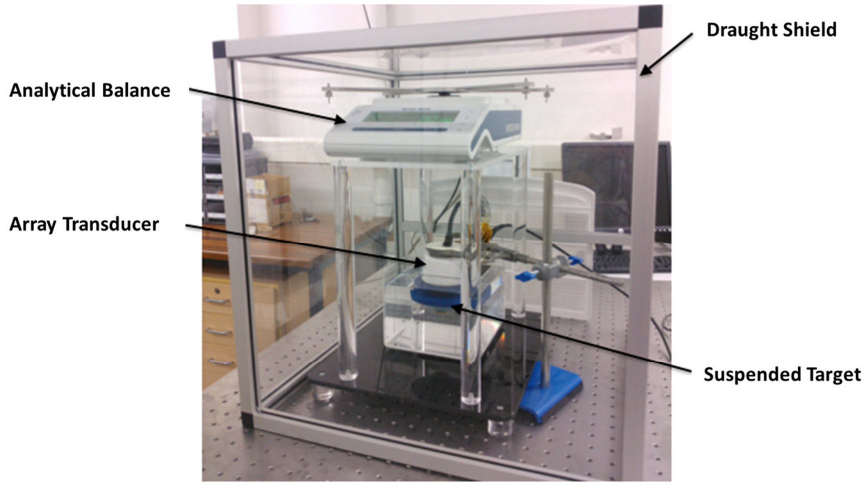

Figure 4.22 Experimental setup for acoustic power measurement using radiation force balance

As shown in Figure 4.22, the absorbing target was suspended in a small water tank filled with degassed water, and the transducer was mounted on a retort stand to radiate downward onto the target. The distance between the transducer and the absorber was controlled to be around 10 mm, as advised by the manufacturer, aiming to minimize the absorption in water along the wave path. One element of the array was activated during the experiments by a function generator (Model 33250a, Agilent Technologies, CA, USA) and an RF power amplifier (1020L, Electronics & Innovation, New York, US), with power gain 53 dB and a power meter integrated to monitor the forward and reverse electrical power to the transducer. Due to its extremely high sensitivity, the RFB system was covered by a glass draught shield during the operation, in order to avoid the disturbance of airflow.

The RFB system was connected to a computer for data acquisition and analysis. The actual acoustic power can be obtained directly, with factors such as frequency, transducer geometry and water temperature, pre-defined in the program, and considered automatically when analyzing the results.

Based on the measurements of the acoustic power, two sets of experiments were carried out to compare the material performance through one element of the arrays:

- **Experiment One**: Sweep the driving frequency from the function generator while driving the element with a specified electrical forward power. The frequency ranges for all four arrays were fixed from 500 kHz to 1.8 MHz; with 25 kHz step size near resonance and 100 kHz step away from resonance. The output amplitude of the signal generator was adjusted to ensure the same 5 W forward electrical power delivered to the array.

- **Experiment Two**: Drive the element at the centre frequency obtained from the first experiment at a series of different input power levels. The input voltage to the power amplifier was varied from 0.5 V_{p-p} to 2 V_{p-p}, with a step of 0.1 V_{p-p}. The experiments were carried out three times for each array to obtain averaged results.

From these two experiments, information about the frequency response, linearity, and acoustic power output can be compared between the different piezoelectric materials used in this project.

4.4.4 MRI Compatibility Characterization

With MRI as guidance, MRgFUS requires the ultrasound transducers to be positioned within the MRI system making the compatibility and safety of the ultrasound sources within the MRI environment of particular interest.

There are three categories to define MRI safety (ASTM standards):

> *MR safe*: *an item that poses no known hazards in all MR environments.*
>
> *MR Conditional*: *an item that has been demonstrated to pose no known hazards in a specified MR environment with specified conditions of use. Field conditions that define the specified MR environment include field strength, spatial gradient, dB/dt (time rate of change of the magnetic field), radio frequency (RF) fields, and specific absorption rate (SAR). Additional conditions, including specific configurations of the item, may be required.*
>
> *MR Unsafe: an item that is known to pose hazards in all MR environments.*

For medical devices, MRI tests are required to investigate any interference caused by the MRI environment in the external devices; any interference caused by the external devices to the MR system; and any interference caused between different external devices. In terms of common investigations, electromagnetically induced forces and torques, RF field induced interference on imaging quality, voltages caused by RF and switched gradient magnetic fields, and MRI artefacts and quality reduction are of particular interests.

The current standard test methods for measurements, recommended by the FDA, are ASTM F2052 for magnetically induced displacement force on medical devices in the MRI-environment; F2213 for magnetically induced torque on medical devices in MRI; F2182 for RF induced heating near passive implants during MRI; and F2119 for evaluation of MR image artefacts from passive implants. However, for FUS devices, there is no specific standard method available yet for a full safety test. As an extracorporeal device aiming for treatment, the testing of FUS devices in an MRI environment has mainly focused on treatment planning and temperature monitoring. In most cases, MRI image artefacts are not considered as a direct safety issue. However, it is critical to define the position and shape of the FUS transducer, which will affect the determination of the treatment plan.

The single element self-focused bowl transducer fabricated as a reference device in this work had been tested previously in an MRI environment. However, the investigation of the faceted arrays remained in its early stages. In this section, the passive compatibilities of the four arrays tested within a 3T Siemens MRI system, Figure 4.23(a), are reported. The distortion and artefacts produced by the arrays in MRI images were studied. Characterization was generally guided by ASTM F2119, although it is issued for passive implants. Prior to investigation of potential image artifacts produced with the four arrays, the magnetically induced displacement and torque produced by the static magnetic field were briefly tested. No obvious displacements and torque were noticed from these measurements, consistent with the choice of non-magnetic and low-permeability materials for the arrays.

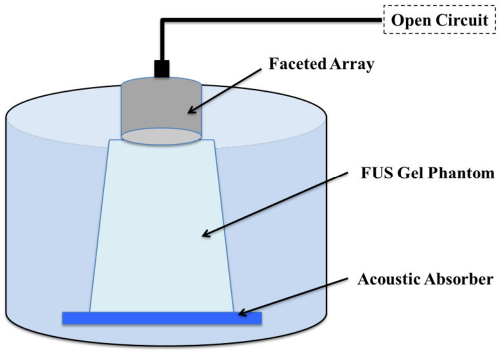

(a) (b)

Figure 4.23 (a) 3T MRI at Cancer Research Center, Dundee, UK (b) diagram of experimental setup for placing array inside the scanner

Figure 4.23 represents the experimental setup. The front face of the array under test was immersed in a cylindrical tank of degassed water, although the standard has emphasized that the device should be immersed into a solution, ideally of $CuSO_4$, 1 – 2 g/L. In fact, $CuSO_4$ solution was initially prepared for the tests. However, the solution discoloured the gel phantom used and brought the risk of its properties changing. Therefore, degassed water was used. This is actually more practical for FUS applications since the array is an extracorporeal device, and degassed water is the actual acoustic medium used during treatments.

The DQA Gel Phantom (ATS Laboratories Inc. USA) was placed directly beneath the transducer. The bottom of the tank was covered with ultrasound absorber (Precision Acoustics, Dorset, UK), and the clearance between the device and the each side of the tank was 35 mm, which was enough to achieve adequate field homogeneity. The same configuration of setup could be used for active MRI compatibility tests as well. For the passive MRI compatibility tests, the phantom and absorber sheet serve as the reference objects. The external connectors of the arrays were secured on the side of the water container, remaining open circuit. The cable was oriented to be perpendicular to magnetic field, in order to minimize distortion caused by the cabling.

Pairs of spin echo images were generated with the phantom only and with both phantom and array in the field of view. The phantom was scanned first, as a reference. Each array was then fixed on the top of the phantom to repeat the scanning sequences. Artifacts can be assessed by the differences between reference and array images.

The MR imaging test environment is given in Table 4-7. The images were scanned in three planes, sagittal, coronal and transversal. The plane definitions can be found in Appendix J-1. For images containing both the phantom and array, for each orientation, two sets of images were required, using both readout and phase-encoded directions.

Table 4-7 3T MR imaging parameters for testing passive artefacts of faceted array transducers

Bandwidth (kHz)	FOV	Slice Thickness (mm)	Matrix Size	Pulse sequence	TR/TE (ms)
123	180	5	192x192	Spin Echo	500/20

4.5 Chapter Conclusion

This chapter presented the materials and methods used in this work. The first half was focused on material characterisation work, and the second half on transducer implementation, which includes the array design, fabrication and application arrangements. It should be noted that the methods presented in this chapter represent the original results generated from this work as well, for example the fabrication process of the array.

CHAPTER 5 PIEZOELECTRIC MATERIAL CHARACTERIZATION

This chapter presents the results from piezoelectric material characterization. The basic characterization processes, at ambient temperature and atmospheric pressure, were carried out first, aiming to obtain reliable properties of certain materials. The full elasto-electric matrices of PZ54 piezoceramic and PMN-29%PT piezocrystal are presented in Section 5.1.1, along with preliminary results from Generation II ternary PIN-PMN-PT piezocrystal. Non-uniformity of selected properties across several samples is reported in Section 5.1.2. Following basic characterization, the materials were tested at elevated temperature and pressure to investigate material behaviour under practical conditions. The results are presented in Section 5.2. The effect of DC bias field was considered additionally for PMN-PT single crystal due to its low coercive field. The last section of this chapter compares the performance of various ceramic and single crystal materials in FEA modelling. A single pillar of piezoelectric material embedded in polymer epoxy was simulated using the material properties measured in previous sections, to link the material characterization to the performance of materials in devices for FUS.

To summarize, the results presented in this chapter are listed as below:

- Basic characterization of piezoelectric material
- Application-oriented characterization of piezoelectric material
- The behaviour of a unit cell FEA model of 1-3 composite using the material properties that have been measured

5.1 Basic Characterization

The results of testing three materials, PZ54 ceramic, PMN-29%PT piezocrystal, and PIN-PMN-PT piezocrystal, at ambient temperature and atmospheric pressure are presented in this section. Two sets of results can be obtained from this basic characterization work. As the first set of results, full elasto-electric matrices were obtained and compared with available published matrices. The full matrices are technically necessary for FEA, though expert users may omit specific data from them if the relevant modes are not present in the transducer to be modeled. Material consistency and non-uniformity across multiple samples are also discussed, in the second set of results.

The material sample sets were defined according to IEEE standard geometries. PZ54 ceramic samples were provided by Meggitt- Ferroperm A/S (Kvistgaard, Denmark), and PMN-29%PT piezocrystal samples were purchased from Sinoceramic (Shanghai, China, and State College, PA, USA). Although the Generation II ternary PIN-PMN-PT piezocrystal was not used practically in this work because of its late availability, it was tested here as it provides future possibilities for FUS. Those samples were purchased from TRS Technologies (State College, PA, USA).

5.1.1 Full Elasto-Electric Matrix

As noted previously, repeated measurements on individual samples were carried out between multiple specimens of the same geometries, and the average of the material properties were used to obtain the missing matrix elements. The statistical distribution of material properties obtained from PRAP direct analyses can be found in Appendix E -1 for PZ54 piezoelectric ceramic, and Appendix E -2 for PMN-PT piezocrystal.

PZ54 Piezoelectric Ceramic

As a newly developed material specified for FUS applications, the full elasto-electric matrix for PZ54 ceramic material did not exist till the data presented here were measured. The manufacturer provided only a few key parameters, not even sufficient to meet FEA requirements. Table 5-1 shows the full matrix for PZ54 ceramic measured in this work and a comparison is made between the measurements and the reference values available in the data sheet from manufacturer.

Although the comparison is limited to only a few parameters, there is generally good agreement between measurements and referenced values. As far as the percentage differences are concerned, the results are quite strongly related to sample geometry. For parameters extracted from the TE plate, the differences are generally within 5%, within 4% for h_{33}, and <1% for the elastic stiffness constants c^{E}_{33} and c^{D}_{33} and coupling coefficient k_t. In contrast, the LE bar sample gave the biggest differences in related properties with s^{E}_{33} and d_{33} both showing differences of more than 25%.

To evaluate the accuracy of the matrix, the properties were imported into an FEA model to simulate impedance spectra of different geometries. Figure 5.1 shows the comparative results for the TE disc sample. The measured spectrum was from a single measurement of a single sample. Due to the sample's disc geometry, the TE resonance is coupled strongly with other resonances, such as the harmonic resonances of the radial mode. Despite this, good agreement of the overall TE resonance can be observed.

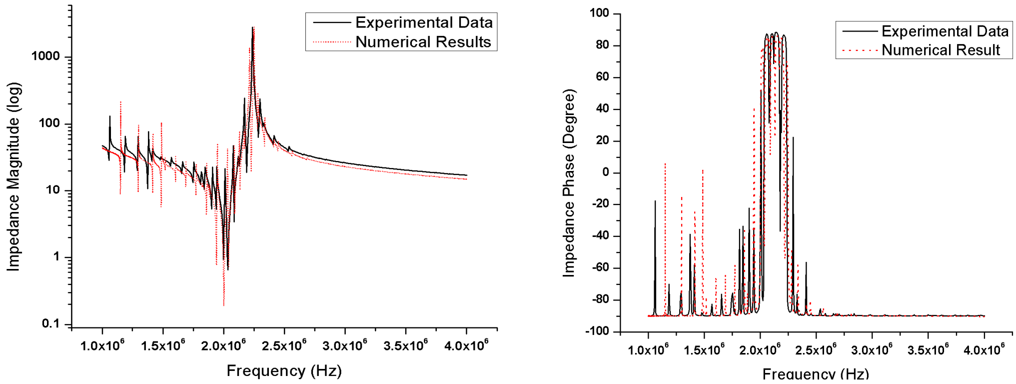

Figure 5.1 Comparison of electrical impedance (a) magnitude and (b) phase versus frequency for experimental measurement (solid black line) and numerical result (dotted red line) for a PZ54 disc sample resonating principally in the TE mode.

PMN-29%PT Single Crystal

There are relatively few statements in the literature of the full elasto-electric matrix for PMN-PT single crystal. The Materials Research Laboratory, Pennsylvania State University is the main contributor in both industrial and scientific research. The most frequently quoted matrices are one for PMN-33%PT single crystal (Zhang et al. 2001) and for PMN-29%PT (Zhang et al. 2008a; Zhang et al. 2008b), both poled in the <001> direction.

Table 5-2 presents the full elasto-electric matrix measured in the present work and published with peer review for PMN-29%PT piezocrystal. The data are generally in reasonably good agreement with the literature as most of the parameters are within 20% tolerance. However, the ratio between s^E_{11} and s^E_{33} was concerning during the measurement. In the literature, s^E_{33} usually exceeds s^E_{11} significantly (Zhang et al. 2002), but here the two values are nearly equal. The value of s^E_{11} presented here was measured from the d_{31} plate while s^E_{33} depends on measurements from the d_{33} bar, Table 4-2, sample (f). Although the thickness-to-width ratio is only three, rather than the value of 5 specified as standard, these bars exhibited higher s^E_{33} values than the standard bar, sample (b) in Table 4-2. The reason behind this has not been confirmed; it is suspected that this is a matter of poling as bars are the most demanding for poling.

Unlike the ∞mm or $6mm$ symmetry material, s^E_{66} cannot be measured directly but instead must be calculated from Equation 3.16, involving $s^E_{45:z11}$ and s^E_{11}, the elastic compliance coefficients extracted from rotated and normal LTE resonance modes, respectively, and s^{E}_{12} which is calculated from measurement of the breathing resonance mode, Equation 3.17.

Figure 5.2 shows the comparison between numerical results and experimental measurement again for PMN-PT single crystal, importing the measured matrix properties into the FEA model of the TE plate. The measured impedance spectrum was from a single measurement of a single sample. Excellent agreement of the TE resonance can be observed in the plot, but lateral modes are lacking in the simulation.

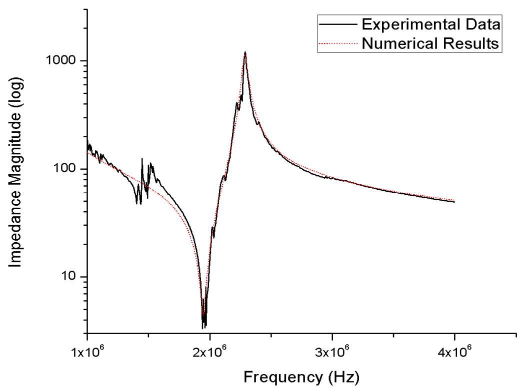

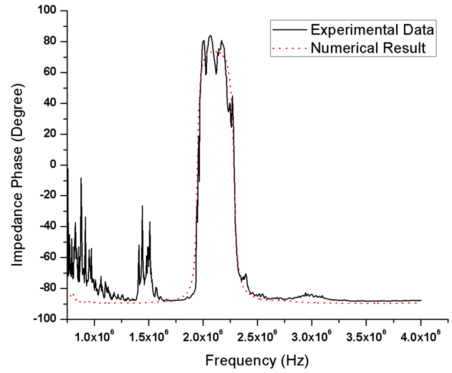

Figure 5.2 Comparison of electrical impedance (a) magnitude; (b) phase versus frequency for experimental measurement (solid black line) and numerical result (dotted red line) for a PMN-PT TE (k_t) plate,

PIN-PMN-PT Single Crystal

As noted earlier, a complete sample set was not available commercially for PIN-PMN-PT piezocrystal. Unlike the first two materials which had full IEEE samples sets purchased from manufacturers directly, the preparation of the PIN-PMN-PT sample set was completed in Dundee. With samples presenting TE, LE and TS modes purchased from TRS Technologies (State College, PA, USA), the LTE (d_{31}) plate, and the rotated LTE ($d_{31}^{45:Z}$) plate were diced out of two of the k_t plates.

The full elasto-electric matrixes of PIN-PMN-PT single crystal, both measured and published (Luo et al. 2008), are shown in Table 5-3. The matrixes agree with each other generally. However, there are significant differences between measurement and the published reference data in $s^{E}_{66,}$ and the related $s^{D}_{66,}$ $c^{E}_{66,}$ and c^{D}_{66}. The rotated LTE $d_{31}^{45:Z}$ plates are considered to be responsible for these differences, as the stiffness constant $s^{E}_{45:z11}$ used to calculate s^{E}_{66} in Equation 3.12 was directly measured from the rotated LTE mode. By reversing the calculation, the value of $s^{E}_{45:z11}$ based on the referenced values of s^E_{66}, s^E_{11} and s^E_{12} was expected to be approximately 50% more than the value from the present measurement. Two new plates were cut from another TE plate and measurements and analysis were repeated, but there was no significant difference. Although the reason for the discrepancy is unknown, one possibility is that the dicing process used to cut the samples caused damage.

For *4mm* crystals, there are some fundamental principles to determine and discard unreasonable data, as detailed in Chapter 4. One of these is that $c^E_{66} > 0$ (Jiang et al. 2003). As shown in Table 5-3, all of s^E_{66}, s^D_{66}, c^E_{66}, and c^D_{66} are negative, which should have led to their elimination; however, as the research here on PIN-PMN-PT crystal was still at the early stage, the matrix is presented as measured. Further improvements may be achieved if material preparation is reviewed. However, it is possible to conclude that the need for six separate samples for full material characterisation is overly onerous given other concerns about piezocrystal growth and supply under present conditions.

Table 5-1 Full Elasto-Electric Matrix of PZ54 Piezoelectric Ceramic

(a) Elastic compliance constants, S_{ij} (10^{-12} m^2/N), and elastic stiffness constants, C_{ij} (10^{10} N/m^2)

	s^E_{11}	s^E_{12}	s^E_{13}	s^E_{33}	s^E_{55}	s^E_{66}	s^D_{11}	s^D_{12}	s^D_{13}	s^D_{33}	s^D_{55}	s^D_{66}
Measured	13.7	-5.0	-5.6	13.8	35.1	37.3	12.5	-6.2	-3.6	9.1	25.6	37.3
Reference[1]	13.8	N/A	N/A	18.6	N/A	N/A	N/A	N/A	N/A	9.5	N/A	N/A
Difference[2]	-0.7%			-25.8%						-4.3%		
	c^E_{11}	c^E_{12}	c^E_{13}	c^E_{33}	c^E_{55}	c^E_{66}	c^D_{11}	c^D_{12}	c^D_{13}	c^D_{33}	c^D_{55}	c^D_{66}
Measured	12.1	6.7	5.8	11.9	2.9	2.7	14.1	8.7	5.9	15.6	3.9	2.7
Reference	14.6	N/A	N/A	11.9	N/A	N/A	N/A	N/A	N/A	15.6	N/A	N/A
Difference	-17.2%			0.3%						0.0%		

(b) Piezoelectric coefficients, d_{ij} (10^{-10} C/N), e_{ij} (C/m^2), g_{ij} (10^{-3} Vm/N), h_{ij} (10^8 V/m)

	d_{33}	d_{31}	d_{15}	g_{33}	g_{31}	g_{15}	e_{33}	e_{31}	e_{15}	h_{33}	h_{31}	h_{15}
Measured	3.44	-1.63	4.13	16.4	-7.8	23.2	22.2	-4.2	11.73	16.3	-3.2	9.1
Reference	4.8	-2.0	N/A	18.9	-7.9	26.8	21.6	-5.6	N/A	17.0	N/A	N/A
Difference	-28.2%	-18.9%		-13.3%	-1.7%	-13.4%	2.8%	-25.5%		-4.0%		

(c) Electromechanical coupling factor k_{ij} and relative dielectric permittivity ε_{ij}

		k_t	k_{33}	k_{31}	k_{15}			ε^T_{r33}	ε^T_{r11}	ε^S_{r33}	ε^S_{r11}	
Measured		0.49	0.57	0.30	0.53			5082	1355	926	1220	
Reference		0.485	0.700	0.340	N/A			2867	N/A	1441	N/A	
Difference		0.5%	-18%	-11%				-17%		7%		

[1] Matrix Data obtained as reference from Ferroperm Full Data Matrix [online].

[2] Difference between measurements and published reference: (Measured - Reference) / Reference x 100%

Table 5-2 Full Elasto-Electric Matrix of PMN-29%PT Single Crystal

(a) Elastic compliance constants, S_{ij} (10^{-12} m^2/N), and elastic stiffness constants, C_{ij} (10^{10} N/m^2)

	s^E_{11}	s^E_{12}	s^E_{13}	s^E_{33}	s^E_{55}	s^E_{66}	s^D_{11}	s^D_{12}	s^D_{13}	s^D_{33}	s^D_{55}	sD66
Measured	50.5	-20.2	-23.6	52.0	14.5	21.0	41.0	-29.7	-3.5	9.6	13.1	21.0
Reference[1]	52.1	-24.6	-26.4	59.9	16.0	28.3	41.8	-34.8	-3.9	10.3	14.0	28.3
Difference[2]	-3.1%	-17.9%	-10.5%	-13.2%	-9.4%	25.7%	-1.9%	-14.7%	-10.7%	-6.7%	-6.2%	25.7%
	c^E_{11}	c^E_{12}	c^E_{13}	c^E_{33}	c^E_{55}	c^E_{66}	c^D_{11}	c^D_{12}	c^D_{13}	c^D_{33}	c^D_{55}	cD66
Calculated	10.6	9.2	10.5	11.5	6.9	4.8	7.8	6.4	8.7	16.7	7.6	4.8
Reference	12.4	11.1	10.4	10.8	6.3	3.5	12.6	11.3	9.3	16.8	7.1	3.5
Difference	-14.7%	-17.5%	1.3%	6.5%	9.4%	36.0%	-38.1%	-43.5%	-6.6%	-0.6%	7.2%	36.0%

(b) Piezoelectric coefficients, d_{ij} (10^{-10} C/N), e_{ij} (C/m^2), g_{ij} (10^{-3} Vm/N), h_{ij} (10^8 V/m)

	d_{33}	d_{31}	d_{15}	g_{33}	g_{31}	g_{15}	e_{33}	e_{31}	e_{15}	h_{33}	h_{31}	h_{15}
Measured	13.8	-6.5	1.3	30.3	-14.4	10.8	21.2	-5.9	8.8	24.4	-7.1	8.2
Reference	15.4	-7.0	1.6	32.2	-14.6	11.9	22.3	-3.9	10.3	27.7	-4.8	8.7
Difference	-10.5%	-7.0%	-21.6%	-5.8%	-1.1%	-9.7%	-5.1%	50.3%	-14.5%	-11.9%	48.9%	-5.8%

(c) Electromechanical coupling factor k_{ij} and relative dielectric permittivity ε_{ij}

	k_t	k_{33}	k_{31}	k_{15}	ε^T_{r33}	ε^T_{r11}	ε^S_{r33}	ε^S_{r11}
Measured	0.57	0.89	0.43	0.31	5082	1355	926	1220
Reference	0.60	0.91	0.44	0.35	5400	1560	910	1340
Difference	-9.9%	-1.9%	-2.0%	-11.8%	-5.9%	-13.1%	1.8%	-9.0%

[1] Matrix Data obtained as reference from (Zhang et al. 2008b)

[2] Difference between measurements and published reference: (Measured - Reference) / Reference x 100%

Table 5-3 Full Elasto-Electric Matrix of PIN-PMN-PT Ternary Single Crystal

(a) Elastic compliance constants, S_{ij} (10^{-12} m^2/N), and elastic stiffness constants, C_{ij} (10^{10} N/m^2)

	s^E_{11}	s^E_{12}	s^E_{13}	s^E_{33}	s^E_{55}	s^E_{66}	s^D_{11}	s^D_{12}	s^D_{13}	s^D_{33}	s^D_{55}	s^D_{66}
Measured	44.6	-21.4	-21.8	45.6	15.3	-1.9	35.7	-30.3	-5.1	10.4	11.5	-1.9
Reference	49.0	-20.0	-26.5	57.3	15.2	39.4	38.2	-30.8	-4.0	10.3	14.3	39.4
Difference	-9%	7%	-18%	-20%	1%	-105%	-7%	-2%	28%	1%	-20%	-105%
	c^E_{11}	c^E_{12}	c^E_{13}	c^E_{33}	c^E_{55}	c^E_{66}	c^D_{11}	c^D_{12}	c^D_{13}	c^D_{33}	c^D_{55}	c^D_{66}
Measured	12.0	10.4	9.7	11.4	6.5	-51.3	16.4	14.9	6.5	16.1	7.1	-51.3
Reference	11.9	10.5	10.4	11.4	6.6	2.5	12.3	10.9	9.0	16.7	7.0	2.5
Difference	0%	-1%	-7%	0%	-1%	-2154%	33%	37%	-27%	-4%	1%	-2154%

(b) Piezoelectric coefficients, d_{ij} (10^{-10} C/N), e_{ij} (C/m^2), g_{ij} (10^{-3} Vm/N), h_{ij} (10^8 V/m)

	d_{33}	d_{31}	d_{15}	g_{33}	g_{31}	g_{15}	e_{33}	e_{31}	e_{15}	h_{33}	h_{31}	h_{15}
Measured	10.9	-5.5	1.0	18.1	-6.0	7.4	29.2	-14.7	10.9	25.8	-9.4	7.7
Reference	13.2	-6.3	1.1	18.6	-4.8	6.9	35.6	-17.0	8.8	28.9	-7.4	6.5
Difference	-17%	-14%	-3%	-2%	24%	-4%	-18%	-13%	24%	-11%	27%	18%

(c) Electromechanical coupling factor kij and relative dielectric permittivity εij

		k_t	k_{33}	k_{31}	k_{15}				ε^T_{r33}	ε^T_{r11}	ε^S_{r33}	ε^S_{r11}	
Measured		0.54	0.84	0.43	0.27				4201	1054	795	978	
Reference		0.57	0.91	0.47	0.25				4200	1335	729	1200	
Difference		-5%	-8%	-9%	7%				0%	-21%	9%	-18%	

[1] Matrix Data obtained as reference from(Luo et al. 2008)

[2] Difference between measurements and published reference: (Measured - Reference) / Reference x 100%

5.1.2 Uniformity of Piezoelectric Materials

As noted previously, a larger numbers of samples than the minimum required to obtain a full elasto-electric matrix was available in the work reported here. This allowed characterization to estimate the consistency and uniformity of piezoelectric materials across multiple samples. Sample-to-sample variation is unavoidable and will affect the accuracy of the matrix directly.

Not only were multiple sample geometries tested, but repeated measurements on individual samples were carried out to obtain the matrices presented in Section 5.1.1. Figure 5.3 presents the variation of material properties measured from four different resonance modes. Although five or more resonance modes were tested to get the full elasto-electric matrixes, only the four required in common for *6mm* ceramic and *4mm* piezocrystals are presented here, from the TE, LTE, TS and LTE modes. Four parameters were picked for each resonance mode, respectively, as representative of the coupling coefficient k_{ij}, dielectric permittivity ε_{ij}, piezoelectric coefficient e.g. e_{ij} and d_{ij}, and compliance, s_{ij}, or stiffness, c_{ij}, constant.

For certain parameters, the statistical analyses are based on all of the related resonance analyses in PRAP files, including those from measurements of multiple samples of the particular mode, and repeated measurements of individual samples. Mean, standard deviation, and maximum and minimum values are presented in the graphs, with the boxes used to indicate the standard deviations and the bars for sample maximum and minimum.

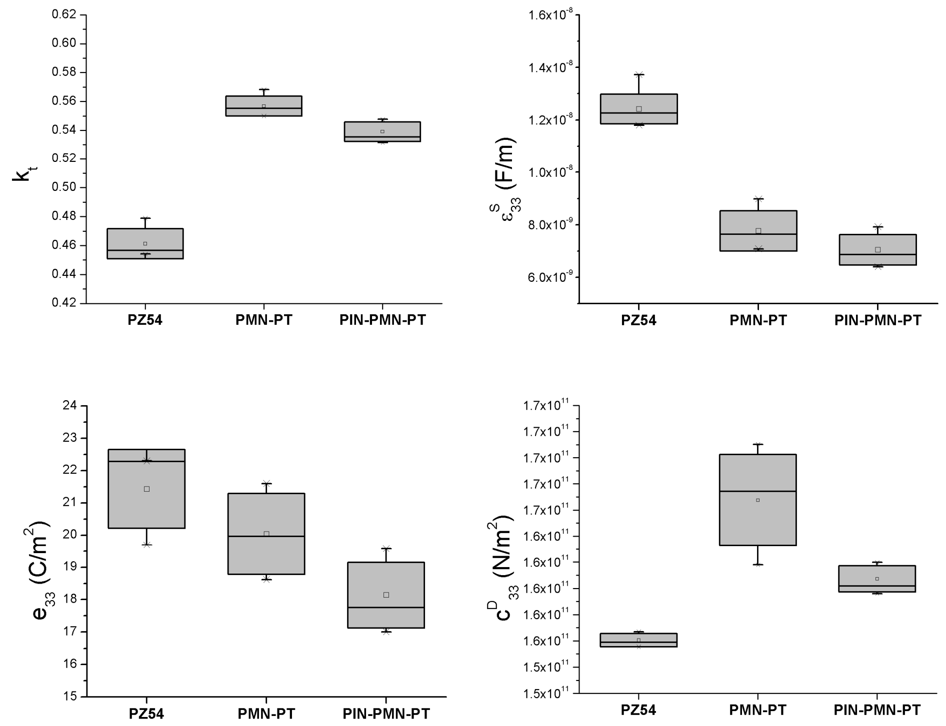

(a) TE mode measurement

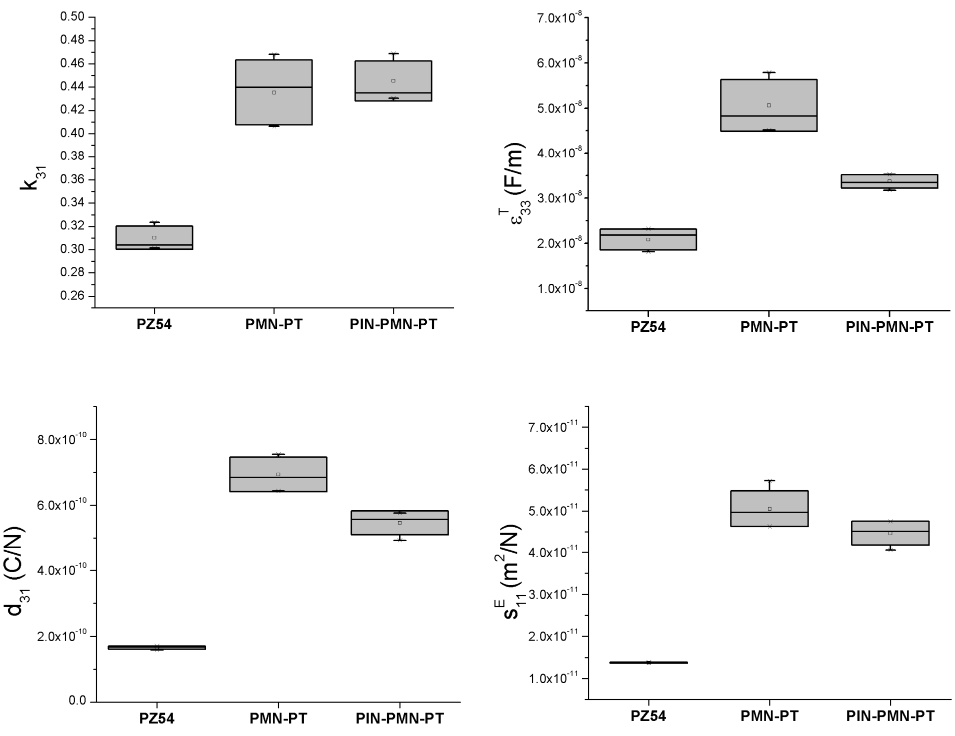

(b) LTE mode measurement

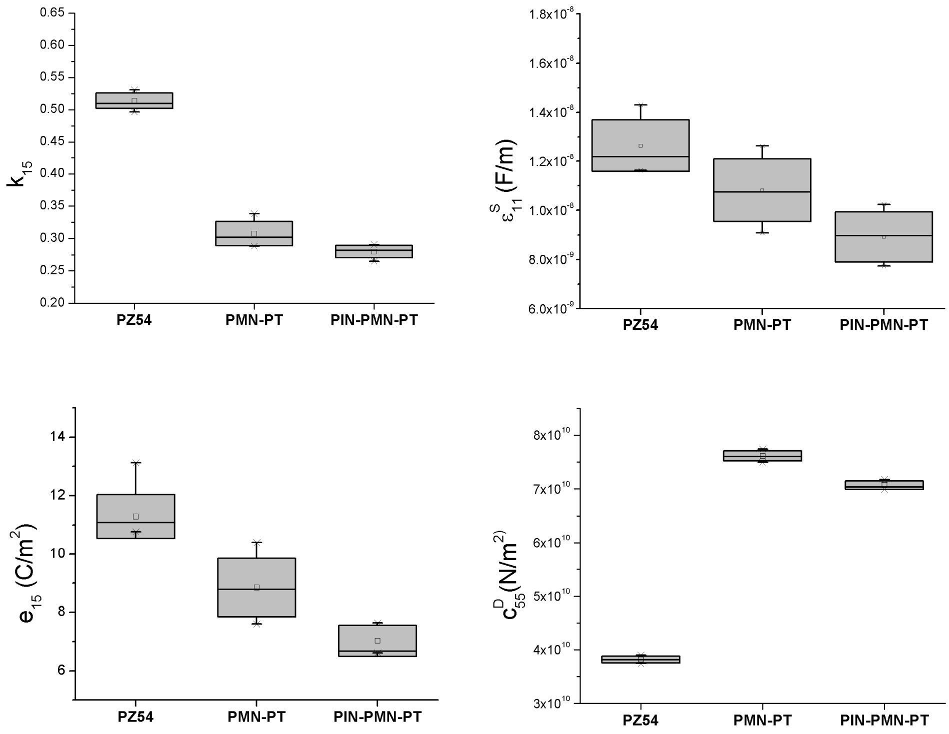

(c) TS mode measurement

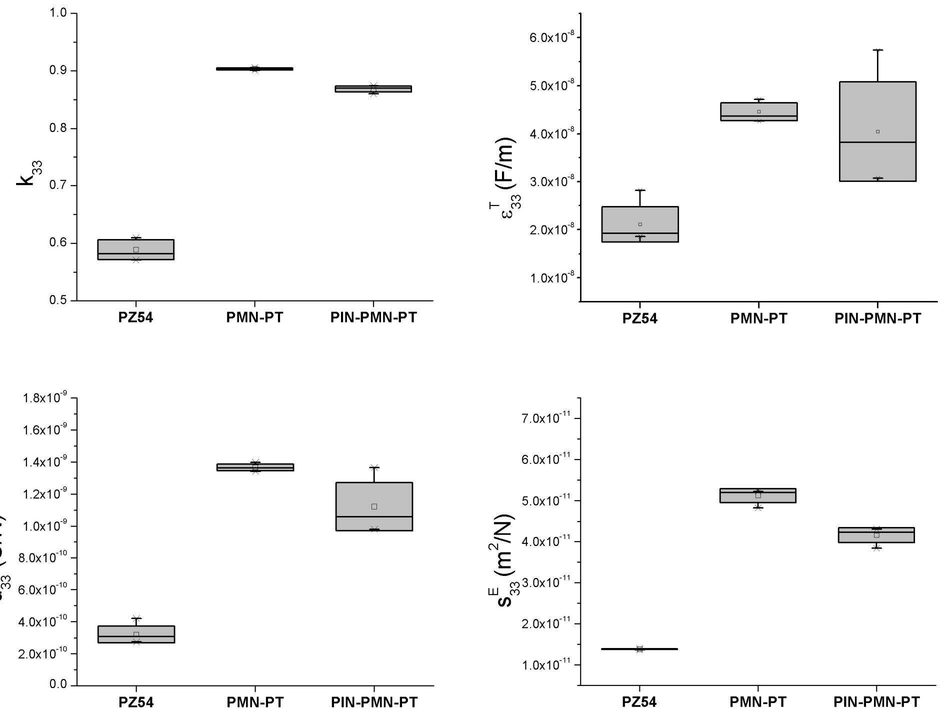

(d) LE mode measurement

Figure 5.3 Material uniformity of various sample geometries with different resonance modes (a) TE plates, (b) LTE plates, (c) TS plates and (d) LE bars.

In general, the PZ54 piezoceramic material shows better uniformity than piezocrystal material, as expected. As an exception, the measurements from the TE disc, Figure 5.3(a), have bigger variations between samples. This may be because the discs tested had a smaller radius to thickness aspect ratio than the geometry specified in the IEEE standard. This meant the thickness resonance was significantly coupled with other resonances, as is apparent in Figure 5.1. Between the two piezocrystals, the PIN-PMN-PT behaves slightly better in this work than PMN-PT in terms of uniformity. However this statement is not conclusive as the two materials were from two different suppliers.

5.1.3 Section Discussion and Conclusions

In this work, full elasto-electric matrixes have been obtained for PZ54 ceramic, PMN-29%PT and PIN-PMN-PT single crystal. The measured properties of PZ54 ceramic and PMN-PT had been imported into a simple FEA model, and the numerical results of the impedance spectrum of a LE plate have shown reasonably good agreement with the experimental measurements. Uniformity results of materials from sample to sample were presented as well.

As noted previously, the transformation from direct measurements of material properties into a complete, self-consistent matrix requires iteration in which comparison and adjustment are involved. In the present work, although the PRAP provide measurements as complex, the ideal linear behaviour of materials is quantified as the first step and the constitutive relations used for matrix are based on IEEE standard which considers the piezoelectric materials to be lossless, therefore only the real parts of the parameters was used. The averages of direct measured properties were imported into calculations to complete the property matrix. The availability of published matrixes allowed comparison with calculated values which led to adjustment of corresponding properties. This procedure was then repeated until the discrepancies of all dependent properties were minimized. With this approach, however, errors in some parameters leads directly to errors in others. For example, the larger the errors in d_{31} and d_{33}, the larger will be the relative errors of e_{31} and e_{33}. In PMN-PT, this can lead to unstability since both d_{31} and d_{33} are very large in these systems (Jiang, 2003).

Nevertheless, the results here have shown that reasonable full elasto-electric matrices can be obtained. The complete sets of material constants shown in Table 5 - 1 to 5 – 3 are self-consistent, despite difficult shear constants for PIN-PMN-PT. However, for the practical application of these materials, it is not guaranteed that the data sets are physically reliable due to the fluctuation of properties from sample to sample, especially for piezocrystals.

One of the main reasons cited in the literature for the property non-uniformity between samples in piezocrystal systems is the loss of Pb during crystal growth. When the chemical composition of Pb is near the morphotropic phase boundary, the material properties are extremely sensitive to composition fluctuation. It has been found that a 1% PT composition variation may cause up to 50% variation in some properties (Jiang et al. 2003). On this basis, the end-users of single crystal material must be concerned about property variations between samples not only from different manufacturers, but even in different production batches from the same manufacturer.

24 pieces of PMN-29%PT k_t plates were available for measurements during the present work, purchased from four suppliers: APC International, Ltd (Mackeyville, USA), Sinoceramic. Inc (Shanghai, China), MTC ElectroCeramics (Morgan Technical Ceramics, Southampton, UK) and TRS Technologies (State College, PA, USA). Measurements were carried out with all 24 samples to extract the properties which could be determined from the TE mode. Since the behavior of the TE plate was regarded to be the most stable and uniform due to its ease of poling and measurement, the standard deviations for key parameters were expected to be smallest compared with other resonance modes. Citing specific results, the standard deviation is 5% for c^D_{33}; 4% for k_t; 10% for e_{33} and 17% for permittivity ε^S_{33}. The values of k_t and ε^S_{33} are presented in Figure 5.4.

Dielectric permittivity is another property that significantly affects the final elasto-electric matrix. The permittivity can be determined directly from more than one resonance mode. Of particular interest, ε^T_{33} can be measured from both the LE and the LTE modes, while ε^S_{33} can be measured from the LTE and TE modes. The average values should be considered as the primary choice. However, taking that approach in the present work, the variations of permittivity were significant and unreasonable results were obtained. In the cases here, for both ceramic and piezocrystal, the permittivities measured from the LTE mode were eliminated as outliers, after careful consideration. The discrepancies may be due to frequency dispersion and experimental errors in the measurements, which can propagate significant errors for piezoelectric constants in the corresponding calculations.

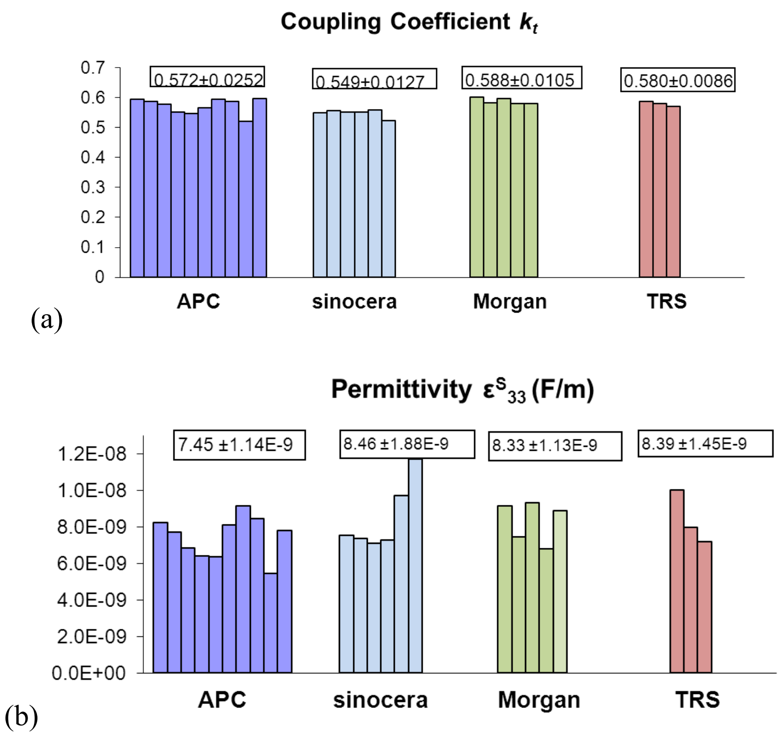

Figure 5.4 (a) Coupling coefficient, k_t, and (b) permittivity, $\varepsilon^S{}_{33}$, measured on TE (k_t) plates, using samples from four single crystal suppliers.

5.2 Application Oriented Characterization under Elevated Temperature, Pressure and Bias Field

When piezoelectric material is made into an ultrasonic device, there is a possibility that the material will be subject to significant temperature and pressure through its use. In many ultrasonic applications, including FUS, as well as underwater sonar and medical ultrasound cutting devices, temperature rises induced by self-heating during operation may affect the performance of the ultrasound transducers. In addition, the material may need to withstand high pressures or large stress variation. Any variation in piezoelectric material properties with temperature and pressure must be considered in the design of susceptible ultrasonic devices.

Piezoelectric material characterisation reported in this section was aimed towards applications, using the relatively easily accessible measurement system outlined in the previous chapter. PZ54 piezoceramic and PMN-29%PT piezocrystal were characterized over a typical operating temperature range simultaneously with applied uniaxial compressive stresses. Variation in key material parameters with temperature and pressure are presented. Due to the low coercive field of PMN-PT, a DC bias field was applied at the same time and its effects were studied as well. The range of temperature was 0 – 130^{o}C in this work, pressure 0 - 20 MPa, and DC bias field 0 - 2 kVcm^{-1}, all applicable simultaneously.

In the same way as for the basic characterization under ambient temperature and pressure, the electrical impedance spectra were recorded first and these were then used to extract corresponding properties. Examples of the spectra with frequency are plotted in Section 5.2.1 for PZ54 piezoceramic and PMN-PT piezocrystal. The temperature, pressure and bias field dependent properties were drawn from the spectra and are presented in Section 5.2.2.

5.2.1 Impedance Spectra with Elevated Temperature and Pressure

To illustrate the basis of the calculations of material properties with variation in temperature and pressure, Figure 5.5 shows electrical impedance magnitude and phase spectra of PZ54 ceramic for 0°C ≤ T ≤ 120°C, with and without compressive stress for a TE disc; Figure 5.6 shows a similar set of data for PMN-PT piezocrystal but with a slightly bigger temperature range, 0°C ≤ T ≤ 130°C. The PZ54 TE sample was a disc with diameter 16 mm, thickness 1 mm, whilst the PMN-PT piezocrystal was a 5 x 5 x 0.5 mm^3 square plate thinned and diced out of a standard 10 x 10 x 1 mm^3 TE plate. Although uniaxial compressive stresses were applied variously to the samples stepwise: 0 - 5 MPa with 1 MPa step for PZ54 ceramic, and 0 - 20 MPa with 2 MPa step for PMN-PT, only the spectra under no compressive stresses and 5 MPa are presented here as examples. The frequency range for these graphs was chosen to include the TE mode resonance.

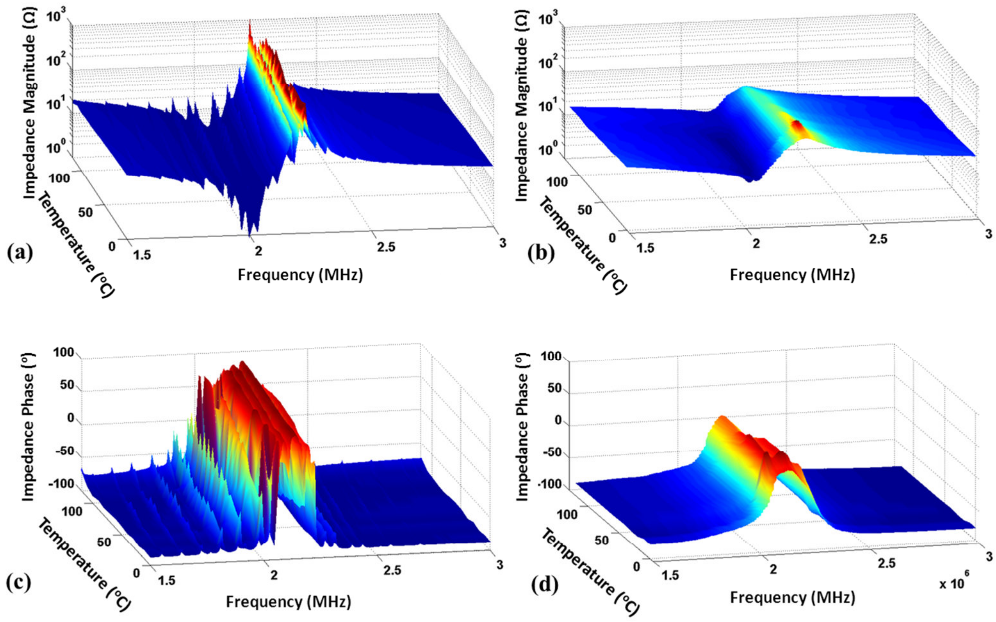

Figure 5.5 Electrical impedance spectra variation with temperature: PZ54 piezoelectric ceramic (a) impedance magnitude and (c) impedance phase spectrum without compressive pressure; (b) impedance magnitude and (d) impedance phase spectrum under 5 MPa pressure

It is apparent from Figures 5.5(a) and (c) that the thickness resonance mode of the PZ54 disc sample is strongly coupled with other resonance modes, presumed to be the radial resonance and its harmonics. Considering the main thickness resonance mode, PZ54 ceramic is relatively stable over temperature, as expected. Minor modes and their resonance frequencies below the main resonance increase with temperature; this is clearer to see in the phase spectra. Although these minor modes are not considered further here, it is evident that material behaviour changes with temperature.

In contrast, Figures 5.5 (b) and (d) present the impedance spectra of the same sample but under 5 MPa compressive stress. The applied pressure has obviously impeded the vibrations in both the thickness and planar directions, manifesting itself as decreases in the resonance magnitude, especially for the minor planar resonances which have, as a consequence, been removed from the spectra. The pressure has also increased the influence of temperature towards the piezoelectric behaviour, which decreases further with elevated temperature.

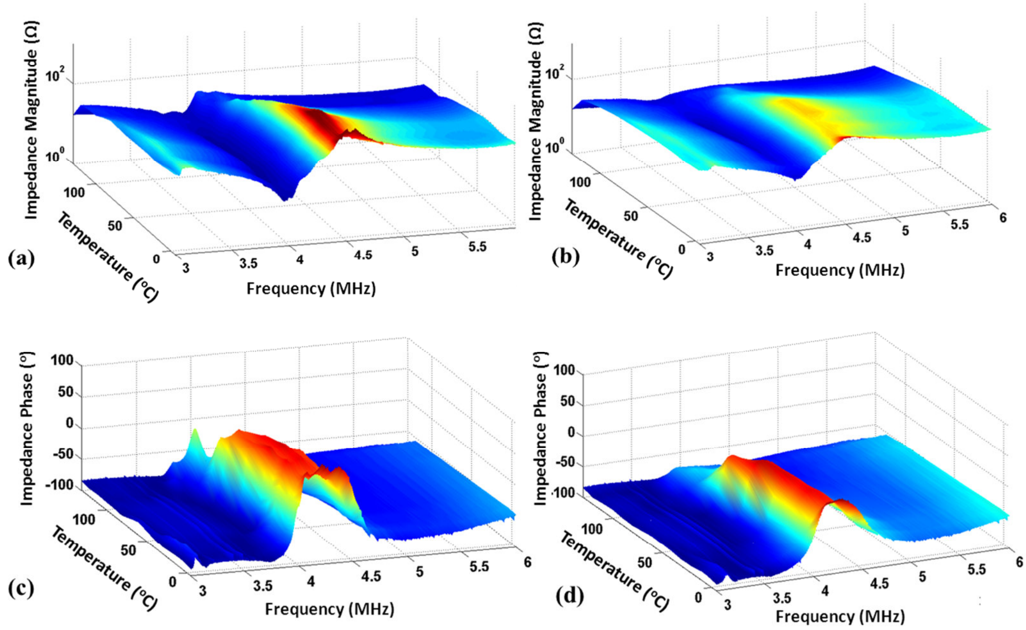

Figure 5.6 Electrical impedance spectra variation with temperature: PMN-PT piezocrystal (a) impedance magnitude and (c) impedance phase spectrum without compressive pressure; (b) impedance magnitude and (d) impedance phase spectrum under 5 MPa pressure

Figures 5.6 (a) and (c) are the impedance magnitude and phase spectra of PMN-29%PT with temperature, under ambient pressure. Consideration of the thickness mode resonance can be divided into four temperature ranges. In the range 0°C < T < 20°C, the thickness mode resonance is clearly visible, but with significant perturbations in both the magnitude and phase. In the range 20°C < T < 80°C, there is a very clear thickness mode resonance and the material is operating piezoelectrically as intended. The main phase transition zone around $T_{R\text{-}T}$ (Zhang et al. 2010) occurs in the range 80°C < T < 120°C. In this range, the piezoelectric activity drops very significantly, then recovers to some extent, with evidence of multimodal behaviour. Finally, for T > 120°C, the material is depoled and piezoelectric behaviour disappears. This behaviour is clearer in material parameters presented later.

Although not realized in the same way, the work of McLaughlin et al. (McLaughlin et al. 2005) also seeks to interpret complex measured data within the domain of the material phase diagram. As with McLaughlin's work, it is possible to reach the conclusion from Figure 5.6 that PMN-29%PT should be exploited only in circumstances where temperature is controlled and within the range 20°C < T < 80°C.

The compressive pressure affected PMN-29%PT in the same way as PZ54 ceramic. The resonances were attenuated under pressure in terms of magnitude especially.

Furthermore, the pressure had apparently prevented the recovery of the piezoelectric activity after the phase transition point, shown clearly in Figure 5.6 (c).

5.2.2 Variation in Piezoelectric Properties with Temperature, Pressure and Bias Field

With the use of the PRAP software, it is possible to derive specific material properties from the data shown in Figure 5.5 and Figure 5.6. Here the key parameters that are important for ultrasound transducer design, k_t, $\varepsilon^{S}{}_{r33}$, e_{33} and $c^{D}{}_{33}$ have been extracted for PZ54 and PMN-29%PT. Although permittivity at constant stress, $\varepsilon^{T}{}_{33}$, is more convenient to measure (IEEE Standards ANSI/IEEE 176-1987), and is favoured by material productions, permittivity at constant strain, $\varepsilon^{S}{}_{33}$, is more significant for ultrasounic applications and FEA. Relative permittivity is presented here.

The variations of these four parameters of PZ54 ceramic are presented with both temperature and pressure, in Figure 5.7; corresponding data for PMN-29%PT are presented as two terms due to the additional presence of bias field: Figure 5.8 shows the results with applied E_B and elevated temperature; and Figure 5.9 shows the variations with applied pressure and E_B, at ambient temperature (T ≈ 20°C). Three bias field levels were applied, E_B = 0, 1 and 2 kV/cm, in the direction of the poling field. The results are tabulated in Tables 5-4 to 5-5 as well.

Variation for PZ54 Ceramic with T and P

As illustrated in Figure 5.7, with linear relationships in general, reasonable variations are shown from temperature 0 to 120°C, and with pressure increases from 0 to 5MPa. Both k_t and e_{33} of PZ54 ceramic decrease with increasing pressure while k_t decreases and e_{33} increases with elevated temperature. $\varepsilon^{S}{}_{r33}$ exhibits the largest variation with temperature, up to 26.4% using T = 20°C (ambient temperature) and P = 0 MPa as a reference; in contrast, the effect of pressure on $\varepsilon^{S}{}_{r33}$ is relatively small, causing a decrease of around 11%. $c^{D}{}_{33}$ increases with temperature in general with variation around 4%. The pressure affected $c^{D}{}_{33}$ to a minimal extent, with no clear trend shown in the lower temperature range. The trend becomes clearer for $T \geq 90$°C, and generally $c^{D}{}_{33}$ decreases with pressure.

Table 5-4 lists the variation of properties of PZ54 ceramic with temperature, under ambient and 5 MPa compressive pressure. The variations were calculated using the values under ambient temperature (20°C) for each pressure condition. The applied pressure further decreased k_t and increased $\varepsilon^{S}{}_{r33}$ with temperature. The overall variations, except in k_t, for the differences between maximum and minimum changes, were reduced by the presence of pressure in general.

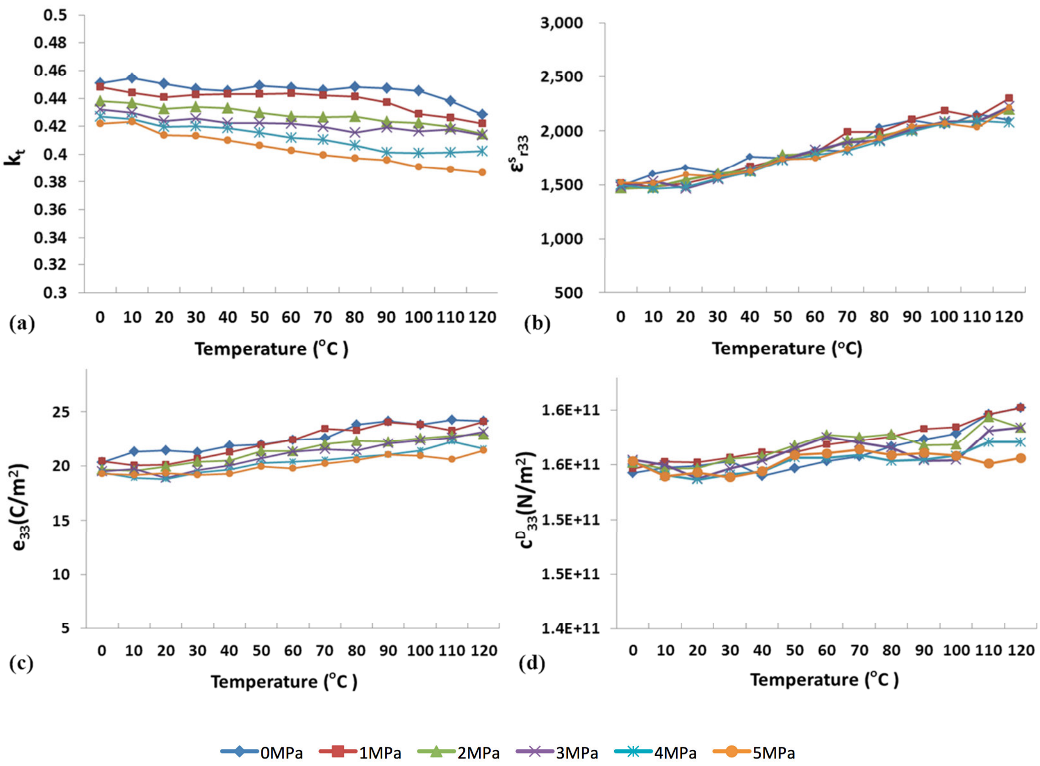

Figure 5.7 Variation with T and P in PZ54 parameters (Qiu et al. 2011b) ((a) thickness mode coupling coefficient (b) relative permittivity at constant strain; (c) piezoelectric stress constant; (d) stiffness at constant electric displacement

Table 5-4 Variation in PZ54 ceramic parameters with T and P for 0°C ≤ T ≤ 120°C (Reference T = 20°C)

Applied Pressure		0MPa	5MPa
k_t	+	0.0%	0.0%
	-	-5.2%	-6.5%
ε^S_{r33}	+	26.4%	38.8%
	-	-10.2%	-4.7%
e_{33}	+	12.9%	10.7%
	-	-5.1%	-0.2%
c^D_{33}	+	3.5%	0.9%
	-	-0.4%	0.2%

+: maximum variation above the reference. -: maximum variation below the reference.

Variation for PMN-PT Piezocrystal with T, P and E_B

Compared with PZ54 ceramic, the performance of PMN-29%PT piezocrystal is significantly more temperature-dependent. Further evidence of the complexity of the phase transitions in this material within the temperature range is shown in Figure 5.8. In Figure 5.8(a), k_t shows reasonable uniformity from ambient temperature up to around 60°C. Nevertheless, variation upward from the value at 20°C of about 20% is evident, occurring particularly in the temperature interval 60 - 80°C. The decreasing trend is broken when an expected peak occurs between 80^{o}C and 120^{o}C, in line with the phase transition temperature zone.

Above 120^{o}C, the material is depoled, and piezoelectric behaviour disappears completely. However, with the presence of the bias field, the material maintained its high performance till a higher temperature range, and even showed signs of repoling under a field, $E_B = 2$ kV/cm, at temperature $T > 120^o$C. This is in good agreement with literature about poling conditions for PMN-PT piezocrystal (Feng et al. 2006).

Variations in ε^S_{r33}, e_{33} and c^D_{33} in the temperature range 20 - 80^{o}C are also apparent from Figure 5.8(b-d) and Table 5-5, notably an increase in ε^S_{r33} of more than 50% when there is no bias field and an increase in e_{33} of more than 10% when a bias field is present. As noted in relation to Figure 5.6, some variation is also seen in all four properties at temperatures below ambient. Therefore, the ideal usable range for transducer made of PMN-29%PT is approximately 20°C < T < 60°C according to the results here.

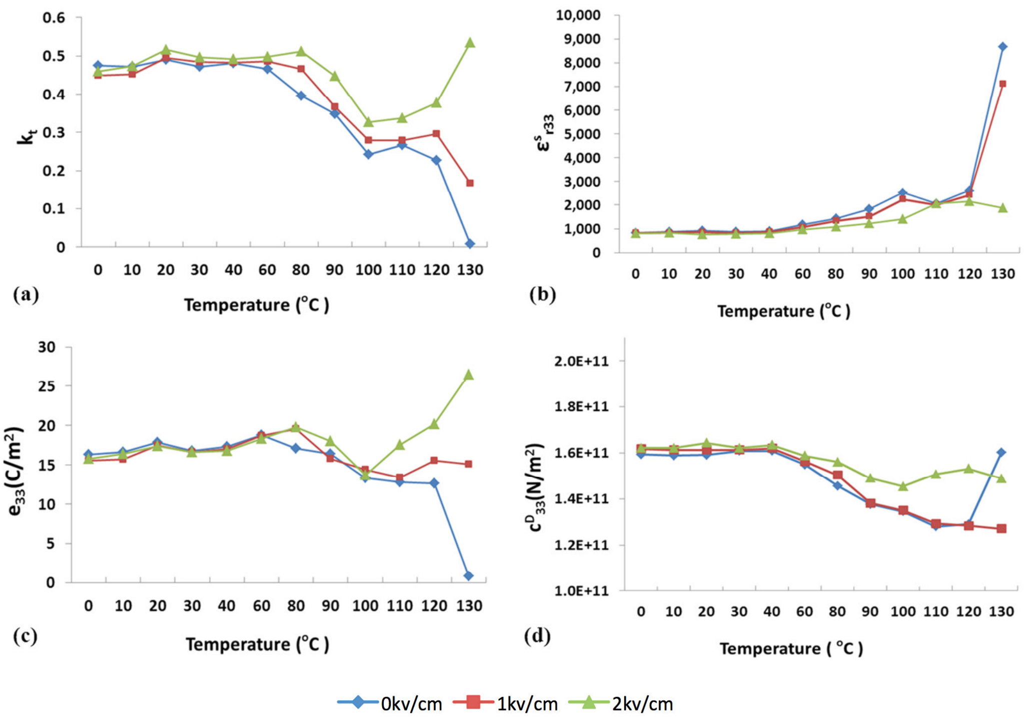

Figure 5.8 Variation with T and V_B in PMN-29%PT parameters (Qiu et al. 2011a) (a) thickness mode coupling coefficient (b) relative permittivity at constant strain; (c) piezoelectric stress constant; (d) stiffness at constant electric displacement

Table 5-5 Variation in PMN-29%PT parameters with T and E_B for 20°C ≤ T ≤ 80C (Reference T = 20°C; P = 0 MPa) (Qiu et al. 2011a)

Bias Field, E_B		**0 kVcm^{-1}**	**1 kVcm^{-1}**	**2 kVcm^{-1}**
ε^S_{r33}	+	53.70%	55.50%	40.10%
	-	-5.20%	-4.70%	0.00%
k_t	+	0.00%	0.00%	0.00%
	-	-19.20%	-6.10%	-4.70%
c_{33}^D	+	1.10%	0.40%	0.00%
	-	-8.50%	-6.90%	-5.00%
e_{33}	+	5.20%	12.10%	13.90%
	-	-5.90%	-4.80%	-4.10%

+: maximum variation above the reference. -: maximum variation below the reference.

Figure 5.9 presents the measurements at ambient temperature with applied E_B and pressure P. Compared with temperature, pressure affects material relatively little. Broadly, ε^S_{r33} increases with pressure but decreases with E_B, while the trends in k_t and c^D_{33} are the opposite of those for ε^S_{r33}, with a reduction as P increases and an increase with E_B. Finally, the piezoelectric stress constant, e_{33}, generally reduces with both increasing pressure and bias field.

As well as the general trends, other perturbations in the characteristics are evident. ε^{S}_{r33}, c^{D}_{33}, and e_{33} all show large variations relative to their trends for 0 MPa $\leq P \leq$ 10 ~ 12 MPa. Variations that appear more systematic are evident at higher pressures in all three of these properties. The behaviour of the coupling coefficient, k_t, is generally simpler. However, a perturbation is evident in the decreasing trend as pressure increases in what might be termed the transition zone for the other three properties, $P \approx$ 10 to 12 MPa. As shown in Table 5-6, ε^{S}_{r33} again exhibits the largest variation, increasing by more than 20% for $0 \leq P \leq 20$ MPa, regardless of E_B. Also notably, k_t falls by more than 10% for the same pressure range.

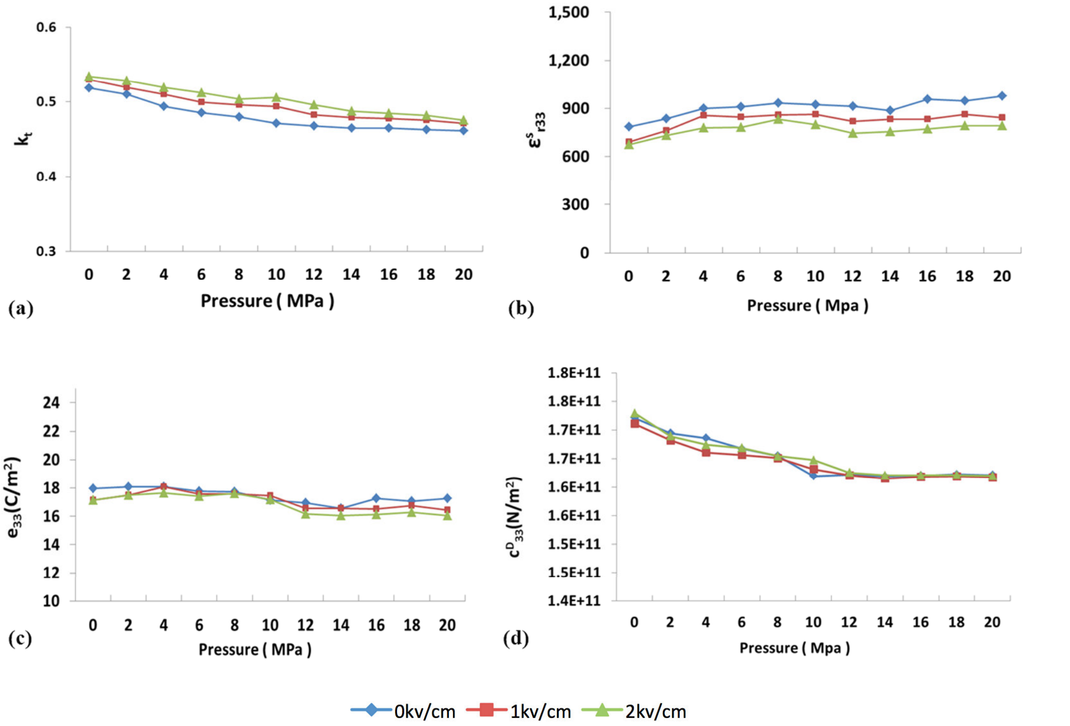

Figure 5.9 Variation with P and E_B in PMN-29%PT parameters. (Qiu et al. 2011b) (a) thickness mode coupling coefficient (b) relative permittivity at constant strain; (c) piezoelectric stress constant; (d) stiffness at constant electric displacement

Table 5-6 Variation in PMN-29%PT parameters with P and E_B (Reference P = 0 MPa; $T \approx 20°C$) (Qiu et al. 2011a)

Bias Field, E_B		**0 kVcm^{-1}**	**1 kVcm^{-1}**	**2 kVcm^{-1}**
ε^{S}_{r33}	+	24.20%	22.30%	23.80%
	-	0.00%	0.00%	0.00%
k_t	+	0.00%	0.00%	0.00%
	-	-11.10%	-10.90%	-11.00%
c_{33}^{D}	+	0.00%	0.00%	0.00%
	-	-5.90%	-5.30%	-6.30%
e_{33}	+	0.80%	4.60%	2.90%
	-	-7.80%	-4.80%	-6.40%

+: maximum variation above the reference. -: maximum variation below the reference.

5.2.3 Section Discussion and Conclusions

In this section two materials, PZ54 ceramic and PMN-29%PT piezocrystal, were explored under elevated temperature and pressure, using the experimental measurement system developed for this purpose. The temperature and pressure conditions were determined according to the possible applications for the materials. A temperature range $0 \leq T \leq 120^{o}C$ was applied to PZ54 ceramic and compressive pressure was added to the sample from 0 - 5 MPa. The determination of these ranges was based on preliminary experiments carried out in the ultrasound lab to simulate the operating environment of piezoelectric materials during FUS applications. The investigated temperature range for PMN-PT piezocrystal was extended to 130°C to explore its complex phase transitions and depoling effect. The pressure range of interest was also extended, up to 20 MPa, according to other applications for which PMN-PT piezocrystal might be suitable, such as underwater sonar where the pressure varies from atmospheric to approximately 20 MPa at 2000 m (Kinsler et al. 2000, [p438-439]), and ultrasonic medical cutting tools with sandwich configuration transducers where pre-stress of at least 20 MPa is desired to ensure effective acoustic coupling and efficiency.

Although rarely seen in the materials literature, both Figure 5.5 and 5.6 are of a type familiar to transducer engineers. In their domain, the behaviour it suggests would usually be interpreted in terms of transducer structure. The relative properties were analysed based on the electrical impedance spectroscopy under their possible operating conditions. As expected, the results show that the variations in key characteristics of PZ54 with pressure and temperature are relatively small for the whole testing envelope. In contrast, PMN-PT has the potential for much higher performance; however it is only suitable for use within a limited operating envelope, $20^{o}C \leq T \leq 80^{o}C$, in line with the conclusion of McLaughlin at al (McLaughlin et al. 2005). DC bias field is also necessary if the piezocrystal is used for FUS or any other high power application to help maintain its high performance over a large range of operating conditions. As an improved newer generation, PIN-PMN-PT ternary and doped ternary piezocrystals may be a better candidate for FUS; comparisons between PMN-PT and PIN-PMN-PT piezocrystals have been reported elsewhere (Sadiq et al. 2011).

As noted previously, 1–3 connectivity piezopolymer composite is the material of choice in this work to fabricate geodesic bowl transducers to demonstrate practical material performance for FUS. The behaviour of the composite material depends strongly on k_{33} and d_{33}, and therefore the bar-shape sample is the ideal object to test. However, because of the present limitation in bias field for thick samples, the complete characterization of the LE bar samples could not be carried out in the work presented here. Instead, the TE plate geometry was used, as the simplest option. From this, temperature- and pressure-dependent data were obtained for k_t, $\varepsilon^{S}{}_{r33}$, e_{33} and $c^{D}{}_{33}$. Although this set of properties is incomplete when compared with the demands of many widely-used modelling systems, it is sufficient for 1-D modelling, such as with the KLM equivalent circuit (Krimholtz et al. 1970).

The results presented in this section were obtained from one sample and one cycle of measurement for each material. Therefore the results are representative of only those specific samples. However, they still clearly illustrate the behaviour of the piezocrystal material, as well as allowing trends in this behaviour to be seen. For PMN-29%PT piezocrystal, there are differences between the values for parameters shown in Figure 5.7 and 5.8 at 20°C with no applied pressure or bias field and the value in Table 5.2. These differences are not unexpected because different specimens were used to accommodate the destructive nature of many of the tests, as well as the dicing and lapping processed required for sample preparation.

Although this experimental setup assembled in this work is viable in a laboratory environment, there are some possible improvements. First, the applied pressure is uniaxial rather than hydrostatic. Second, the setup does not allow for the kind of localized self-heating that may arise under high-drive conditions. However, it is still believed the results will provide valuable indications of temperature-related performance issues, particularly in circumstances in which even local high-drive conditions may generate uniform heating.

5.3 Unit Cell Simulation

As discussed earlier, the recommended form of material for piezocrystal materials is the composite with 1 - 3 connectivity, due to its high electromechanical coupling coefficient, k_{33}, in the efficient LE mode. It is because of this that the PMN-PT crystal plates used in this work were converted by the dice-and-fill process into piezopolymer composites, and the same process was applied to ceramic as well, both PZ26 as a standard reference material and PZ54, as a new ceramic specifically developed for FUS.

To further understand how piezocrystal would benefit the FUS application, a single pillar of piezoelectric material embedded in polymer epoxy was modeled in PZFlex (Weidlinger Associates, Los Altos, CA). This model is a unit cell of the 1 - 3 piezocomposite plate that can represent the performance of the complete composite structure. Used in this way, FEA predicts interpillar lateral coupling and modes within the composite microstructure but not the lateral mode effects of any particular overall plate geometry. The pressure outputs were recorded in water very near the front face of the unit cell. Electrical impedance magnitude and phase spectra were calculated as well. A total of five materials was investigated including PZ26 ceramic, PZ54 ceramic, and the three generations of piezocrystal outlined in Chapter 3.

5.3.1 The Unit Cell Model

Due to its periodic structure, it is easy to divide a 1 - 3 composite into unit cells, as illustrated in Figure 5.10(a). Furthermore, the square pillars are quarter-symmetric through a central vertical axis. Thus an FEA model of the composite can be simplified using a quarter section of a single unit cell, indicated in Figure 5.10(b).

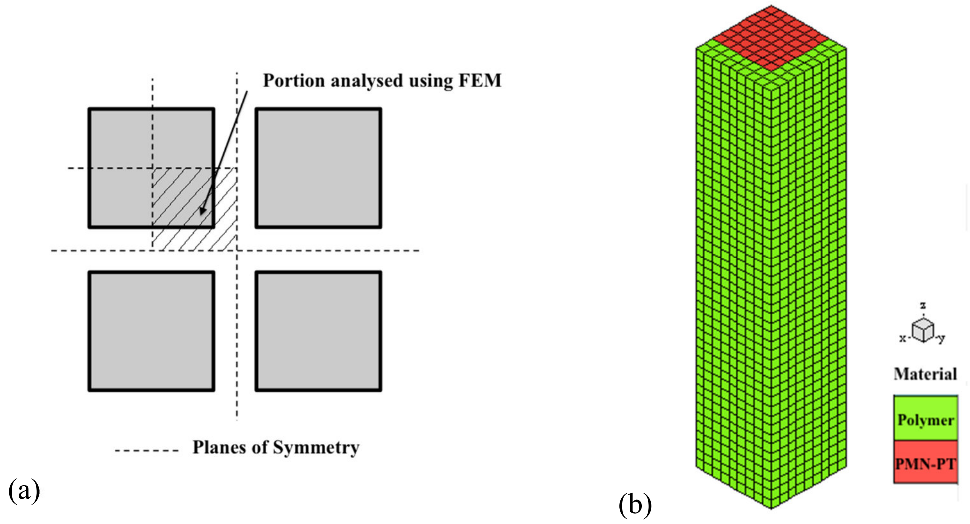

Figure 5.10 (a) The unit cell and the symmetry that exists in a square section composite. (b) The meshed unit cell model in FEA model.

To make the model as close as possible to reality, a short column of water was placed in front of (i.e. above) the unit cell, with an absorbing boundary on its top surface. The bottom surface of the unit cell was air-loaded, corresponding approximately to the microballoon-filled epoxy used here in experimental devices, so the boundary condition was set to be free. In addition, the other four sides were defined to be symmetrical boundaries for this quarter unit cell structure. The model is plotted in Figure 5.11, with the structure mirrored in both the x and y directions to complete the unit cell model.

The polymer of choice in this model is the hard-set epoxy (CY1301/HY1300, Robnor Resins, Wiltshire, UK). For piezoelectric materials, the material properties of five materials concerned in this work were imported into the model in turn. PZ54 ceramic, PMN-PT and PIN-PMN-PT crystals have been discussed previously, and their measured properties were used directly in the simulations. For the other two materials, PZ26 ceramic and Generation III Mn:PIN-PMN-PT piezocrystal, where measurement was not possible, material properties were obtained from the manufacturer's data sheet (Ferroperm Piezoceramics A/S, Kvistgaard, Denmark) and the literature (Luo et al. 2010), respectively. The full matrixes of these two materials can be found in Appendix F-1 and F-2.

Three sets of simulated results were recorded for comparison between the materials. Electrical impedance and phase spectra were the first two sets of data, providing information about resonance frequencies and electrical impedance at specific frequencies. Pressure output was recorded in water: all the pressure data were captured across one plane, drawn in Figure 5.11, which was two elements vertically away from the piezoelectric surface. The data were then averaged, to remove any effects caused by the ultrasonic beam pattern, and plotted in the frequency domain.

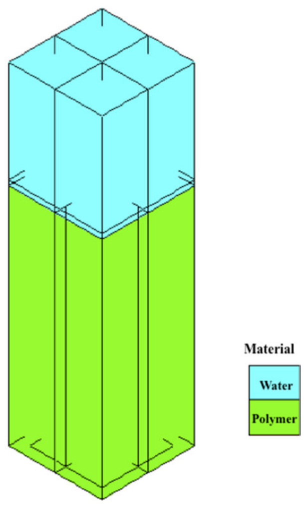

Figure 5.11 Simulated model of unit cell with water loaded.

To compare the material performance under the same conditions, the geometry of the model was modified for each material. The general rules were:

- The composite should have its electrical resonance at 1 MHz;
- The volume fraction should be 60%;
- The aspect ratio of pillar thickness to width should be around 3:1.

The geometries of similar models for the five materials are listed in Table 5-7.

Table 5-7 The Geometries of the composites based on unit-cell models for five materials

Unit (mm)	**PZ26**	**PZ54**	**PMN-29%PT**	**PIN-PMN-PT**	**Doped PIN-PMN-PT**
Thickness	1.45	1.723	1.055	1.085	1.05
Pillar width	0.464	0.551	0.338	0.347	0.338
Polymer width	0.135	0.160	0.098	0.101	0.098

After the geometry of the model was defined, the next step was to mesh the model. The size of the meshing is determined by the number of elements per wavelength, which was set to 60 for a 1 MHz drive signal, according to the PZ Flex user manual (Weidlinger Associates, CA, USA).

Prior to simulating the unit cell model with different materials, it is necessary to consider the issue of scaling factor between simulations. As the pressure outputs are presented after FFT analysis, functions with different time bases will show the same shape of graph but may have different linear scaling factors. One way to compare different outputs is therefore to ensure that the time step (Δt), total number of points (NT), and maximum time ($tMAX$) are identical for all simulations, where

$$tMAX = NT \times \Delta t. \qquad \text{Equation 5.1}$$

To remove the effect of scaling factors, the five models were run first to monitor the results and the required simulation time. Based on the minimum value of time step and the maximum runtime required to allow the electrical charge in the each model to ring down to zero, the optimal time step was set to be 2.5 ns (sampling frequency 400 MHz), and the runtime was determined to be 0.4 μs for all five simulations. The drive signal is a 1-cycle sinusoid with amplitude of 1 V.

5.3.2 Unit Cell Results

As stated earlier, electrical impedance magnitude, phase, and averaged pressure output in water versus frequency were recorded as results from the unit cell model and five sets of material properties were imported in turn to generate corresponding results.

Figures 5.12 - 5.16 are the results for PZ26, PZ54, (Gen. I) PMN-PT, (Gen. II) PIN-PMN-PT and (Gen. III) Mn:PIN-PMN-PT, respectively. For ease of comparison, all results are plotted with the same axis scales.

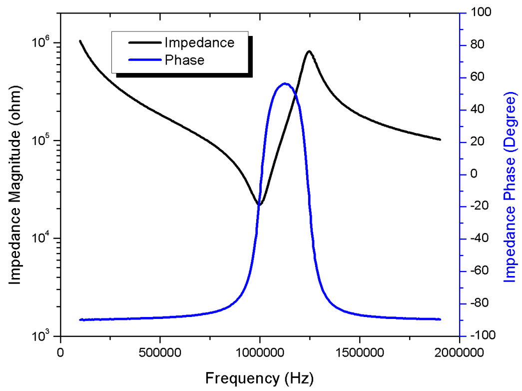

(a)

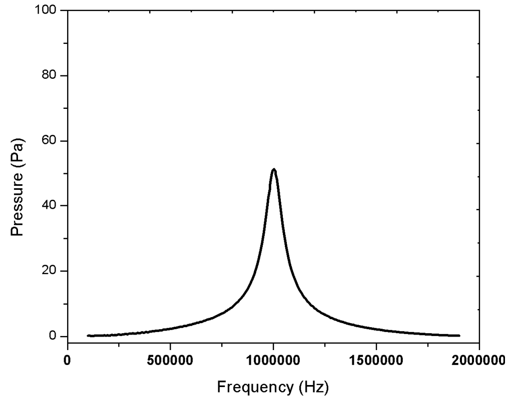

(b)

Figure 5.12 Simulated results of PZ26 unit cell model (a) electrical impedance magnitude and phase; (b) averaged pressure output

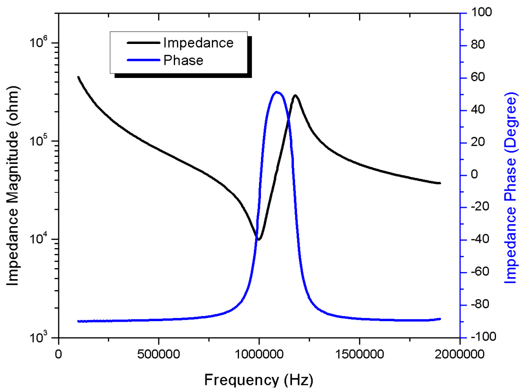

(a)

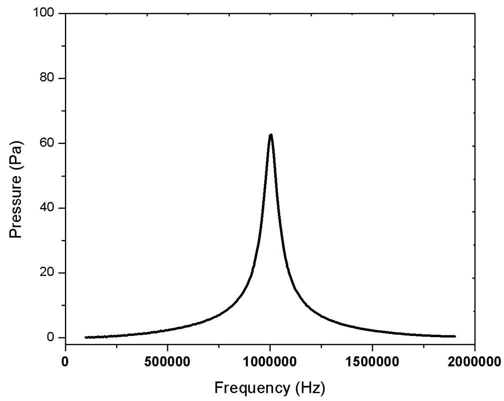

(b)

Figure 5.13 Simulated results of PZ54 unit cell model (a) electrical impedance magnitude and phase; (b) averaged pressure output

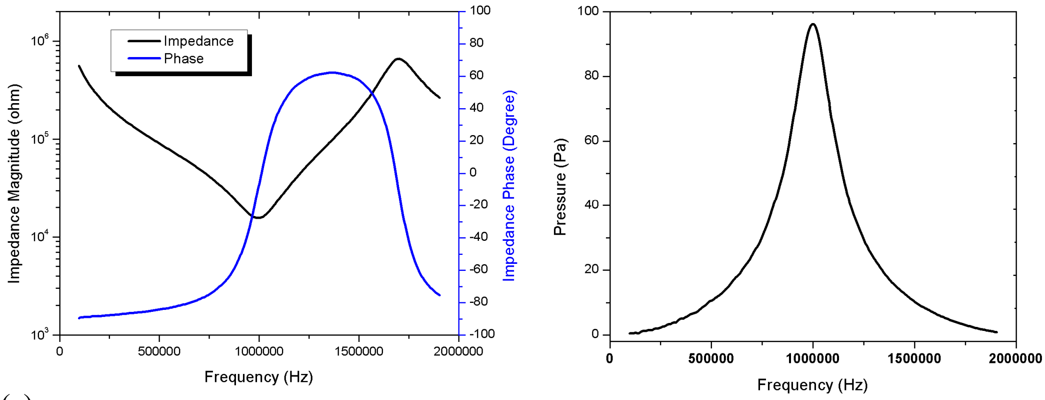

(a) (b)

Figure 5.14 Simulated results of PMN-PT unit cell model (a) electrical impedance magnitude and phase; (b) averaged pressure output

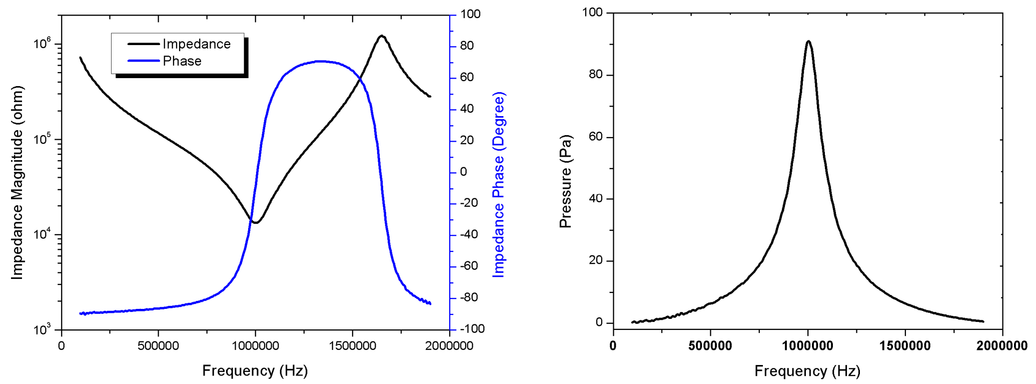

(a) (b)

Figure 5.15 Simulated results of PIN-PMN-PT unit cell model (a) electrical impedance magnitude and phase; (b) averaged pressure output

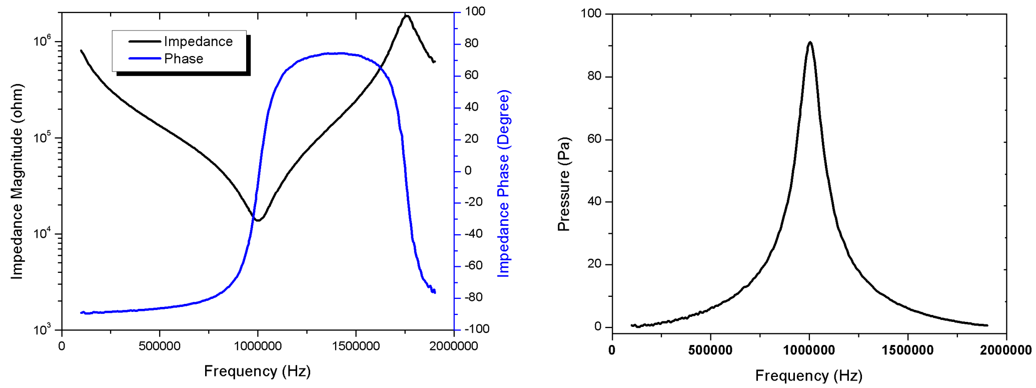

(a) (b)

Figure 5.16 Simulated results of Mn: PIN-PMN-PT unit cell model (a) electrical impedance magnitude and phase; (b) averaged pressure output

Table 5-8 Results from simulations of unit cell models

	PZ26	**PZ54**	**PMN-29%PT**	**PIN-PMN-PT**	**Doped PIN-PMN-PT**
Impedance @ *fe* (kΩ)	21.9	9.91	15.6	13.2	13.7
Effective Coupling Coefficient k_{eff}	0.59	0.53	0.81	0.80	0.82
Max Pressure Output (Pa)	51.3	62.8	96.3	91	91

Table 5-8 extracts relevant information from the simulation results in Figure 5.12 - 16 and Table 5-7, including the impedance magnitude at electrical resonance, effective coupling coefficient, and maximum pressure output averaged across the plane near the pillar surface.

Normalization was applied to the data presented in Table 5-8 with respect to PZ26 ceramic, and the results are plotted in Figure 5.17. In general the PZ54 and piezocrystals, as the potential materials of choice for FUS, significantly improve the performance of the piezocomposite. The three generations of single crystal behave similarly here in terms of impedance and pressure outputs. A thickness reduction of more than 25% is possible compared with PZ26 if the same resonance frequency is maintained. The electrical impedance magnitudes are up to 40% less at f_e, 1 MHz in this study, which may benefit electrical matching in practice in FUS arrays. The effective coupling factor and pressure output under same drive conditions both increased, by up to 38% and 88%, respectively. Although PZ54 shows a decrease in effective coupling factor by 10%, there is still a 20% increase in pressure output; the low electrical impedance is also consistent with its design as a material with a high permittivity compared with PZ26.

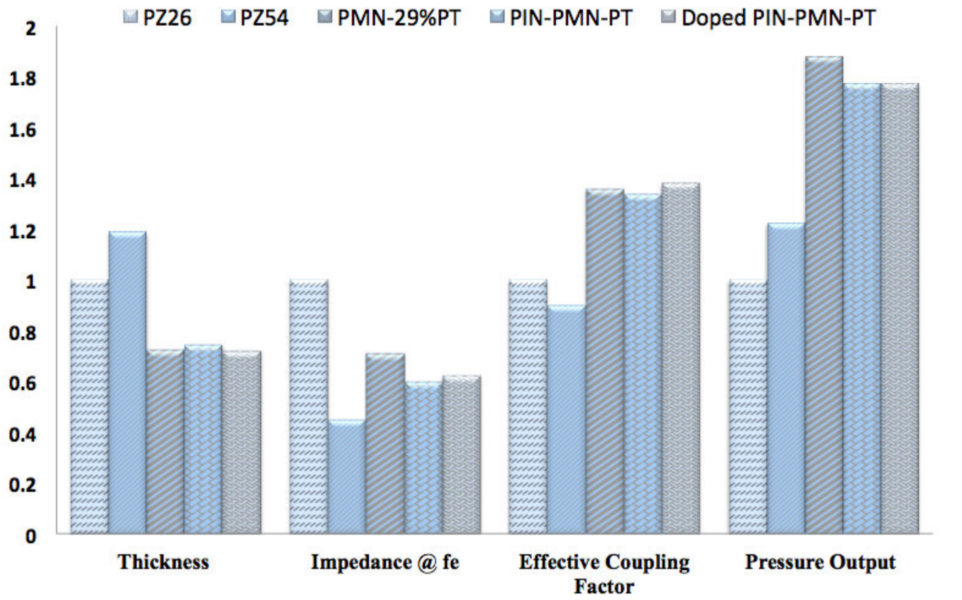

	PZ26	PZ54	PMN-29%PT	PIN-PMN-PT	Doped PIN-PMN-PT
Thickness	1	1.19	0.73	0.75	0.72
Impedance @ fe	1	0.45	0.71	0.60	0.63
Effective Coupling Factor	1	0.90	1.36	1.34	1.38
Pressure Output	1	1.22	1.88	1.77	1.77

Figure 5.17 Normalised results for five materials with respect to PZ26 ceramic

5.3.3 Section Discussion and Conclusions

An FEA model was built in PZFlex to simulate the behaviour of a quarter unit cell, representing a piezopolymer composite with 1–3 connectivity. Comparisons were made between five piezoelectric materials: PZ26 and PZ54 ceramics, and PMN-PT, PIN-PMN-PT and Mn: PIN-PMN-PT piezocrystals. The pressure output in water of the unit cell model, a key concern for FUS applications, was recorded, along with the magnitude and phase of electrical impedance as the primary results. The geometry of the unit cell, including the thickness and pillar and polymer widths, were also compared between the materials; these were adjusted to make sure the different materials resonated at the same frequency.

Overall, the comparison shows that piezocrystals should significantly benefit FUS by almost doubling the pressure output compared to piezoelectric ceramics for a given input signal. In other words, only half the electric power should be required to achieve the same degree of thermal ablation during FUS operation. Such an improvement in terms of efficiency would also result in lower requirements of electronic components under high power conditions. Among the three piezocrystals, PMN-PT binary crystal offers the highest pressure output. However, the later generations of piezocrystal: ternary and Mn-doped ternary crystals are likely to suit the FUS application better because of their improved stability over temperature, even though their pressure outputs are slightly less than that of PMN-PT binary crystal. The reduced electrical impedance magnitudes at resonance will reduce the level of electrical impedance mismatch to be overcome between transducer array elements and external electronic components. Furthermore, piezocrystals provide broader bandwidths, raising the possibility of increasing the operating frequency range of FUS transducers and allowing flexibility in FUS procedures.

Referring to the model itself, Lamb wave propagation causing inter-element / pillar coupling has not been a particular concern in this work, even though it would appear in any composite / array configuration. A major reason for this is that the composite plates which have been studied effectively have complete, uniform electrodes, and no evidence of inter-pillar activity has been found around the fundamental thickness mode resonance (Hayward et al. 2006). Losses and non-linear behaviour in piezoelectric materials under high power excitation has not been considered either. In the first place, the PZFlex package cannot represent piezoelectric nonlinearities caused by high input voltages. Therefore the input signal to the unit cell was simply set to an amplitude of 1 V. Although high power drive signals are usually applied in FUS, the small test signals here fit the purpose of material comparison. In addition, it is very likely that the polymer phase in composite material would overheat at drive levels lower than those at which nonlinearities appear in the piezoelectric phase.

5.4 Chapter Conclusions

In this chapter, basic piezoelectric material characterization and application-oriented characterization were carried out, with the two materials of interests of this project: PZ54 piezoceramic and PMN-29%PT piezocrystal. The basic characterization processes were developed in-house, at ambient temperature and atmospheric pressure, aiming to obtain reliable properties of certain materials. As results, full elasto-electric matrices of PZ54 piezoceramic and PMN-29%PT piezocrystal are obtained, along with preliminary results from Generation II ternary PIN-PMN-PT piezocrystal. Basic characterization revealed properties of PZ54 ceramic material and PMN-29%PT piezocrystal from commercial suppliers under ambient conditions to be generally in good agreement with the properties reported in the literature by commercial suppliers from their own material.

Variation in the properties of six nominally identical samples under ambient conditions was significant, for example in k_t and permittivity.

Following basic characterization, the TE sample of the two materials were tested at elevated temperature and pressure to investigate material behaviour under practical conditions. The effect of DC bias field was considered additionally for PMN-PT single crystal due to its low coercive field. To this end, an experimental measurement system was set up. This system has demonstrated the possibility of applying standard characterization techniques based on the fitting of sets of equations to resonance characteristics measured with electrical impedance spectroscopy on piezoelectric materials under conditions of externally applied electrical bias field in the range 0 to 2 kV/cm, temperature in the range 0 – 130°C, and uniaxial compressive pressure in the range 0 - 20 MPa.

Full elasto-electric matrices could be obtained over a range of temperature, uniaxial pressure and bias field with this system. However, additional fixtures need to be designed specifically for the length extensional bar. For the present stage of investigation, the samples tested were TE plates on the basis that this is the most general configuration and therefore most appropriate for early testing of variation of properties with varying experimental conditions.

Based on the application-oriented characterizations and analysis of the variations in key characteristics under the possible operating conditions, PZ54 behaves much more stable for the whole testing envelop, whilst PMN-PT has the potential for much higher performance; however it is only suitable for use within a limited operating envelope, which is recommended from the results reported in this work to be $20^{o}C \leq T \leq 80^{o}C$. DC bias field is also necessary if the piezocrystal is used for FUS or any other high power application to help maintain its high performance over a large range of operating conditions.

The last section of this chapter compares the performance of various ceramic and single crystal materials in FEA modeling. A unit cell model of the 1-3 composite was simulated using the material properties measured in previous sections, with a single pillar of piezoelectric material embedded in polymer epoxy. By concerning the unit cell of composite model between materials all operates at 1 MHz, with VF = 60 % and AR = 3.125:1, the desired thickness was reduced around 25% with piezocrystal materials if compared with conventional ceramic PZ26. The electrical impedance magnitudes at f_e of piezocrystals were 40% less. In contrast, the acoustic pressure output under same drive conditions were increased by up to 88%.

CHAPTER 6 ARRAY IMPLEMENTATION AND TEST

This chapter presents the implementation process for four faceted bowl array transducers and their test results. Transducer implementation starts with active element preparation, which involves composite fabrication and element dicing. Transducer assembly and electrical connection are also detailed in Section 6.1. The performance of these arrays is then evaluated in Sections 6.2 and 6.3 through basic electrical and functional measurements. The passive MRI compatibility of the arrays is also investigated with T1 weighted MRI images presented.

The outline of this chapter is listed below:

- Array implementation
- Basic transducer testing
- Functional transducer testing

6.1 Implementation of Faceted Array Transducer

Corresponding to Chapter 4The implementation of the array transducers requires a sequence of tasks to be completed which includes:

- The implementation of the active elements
- The implementation of electrical connections
- The assembly of the array transducers

The tasks above are presented in this section. Four transducers were developed following the same process, with one made using PZ26 ceramic plates as the initial proof of concept, and then three others using composite plates made from PZ26 ceramic, PZ54 ceramic, and PMN-29PT piezocrystal, respectively. All the practical work was carried out in the laboratory.

6.1.1 Implementation of Active Elements

For the PZ26 ceramic bowl array, the implementation of the active element required only to dice bulk ceramic plate into triangular plates with pre-designed dimensions. The available material had a thickness of 2 mm and a corresponding resonance frequency of 1 MHz therefore thinning by lapping was not required for this transducer.

The fabrication of piezocomposite arrays starts with the transformation of piezoelectric materials from the bulk phase to piezoelectric - polymer 1-3 composite. As indicated in Chapter 4, dicing and lapping processes are involved.

Composite Parameters

For comparison purposes between materials, the ideal situation is to have the composites of different materials with the same volume fraction (VF), aspect ratio (AR), and resonance frequency, as defined in the unit cell simulating models in Chapter Five. However, in practice it is not possible to keep all three factors exactly the same, and therefore only two out of three were chosen to be maintained in this work: the same resonance frequency, f_e, of 1 MHz and VF of 60%.

The aspect ratio is not a primary concern for two reasons. First, according to theoretical research by Hossack and Hayward (Hossack et al. 1991), the aspect ratio will not have significant effect on composite behaviours when the VF is sufficiently high, e.g. higher then 50%. In this work, the VFs of all three composites were designed to be 60% so aspect ratio is not crucial. Second, the composites will have different thicknesses for the same frequency due to their different piezoelectric material sound speeds, which means different dicing kerfs are required for materials to keep the same aspect ratio. However in practice, the available thicknesses of dicing blades are always limited to a few options, which eliminated the possibility to have the same aspect ratio for different composites.

Using resonance frequency and VF as inputs, the material properties of composites were predicted based on the calculations proposed by W.A Smith (Smith et al. 1991), in MATLAB. The program is attached as Appendix C-1. The predicted properties of composites, acoustic impedance, effective coupling coefficient, and composite thickness for instance, are presented in Appendix C-2.

The thickness of composite is one crucial parameter which will strongly affect the following processes of making the composites. Predicted thicknesses of composites in Appendix C-2 were used as guides to determine dicing parameters, such as dicing depths. The actual required thicknesses, however, were determined during the later lapping process, by monitoring the resonance frequency through impedance measurements on impedance analyser.

Composite Dicing

Resin bonded blades (R07 series, Disco Co., Japan) were used for all three materials. Same blades were used for the two ceramic materials and another kind with thinner thickness and bigger grit size for piezocrystal. The parameters used for dicing were also different, as listed in Table 6-1. The values were determined after several dicing trials to ensure a good trade-off between the best cutting finish and minimum dicing time. As noted previously, PMN-PT piezocrystal material requires a lower spindle speed and feed rate than ceramic. The cutting depth per peck for piezocrystal is also reduced to 0.3 mm; therefore 5 pecks are necessary to finish one single full cut.

Table 6-1 Dicing parameters for ceramic and piezocrystal materials

	Blade Grit Size	Spindle Speed (rpm)	Feed Rate (mm/s)	Cut Depth per Peck (mm)	Blade Thickness (um)
PZ26	320	10000	0.4	0.5	150
PZ54	320	10000	0.4	0.5	150
PMN-PT	600	8000	0.2	0.3	100

The actual kerfs for ceramic were found to be 10.7% wider than the blade thickness, and 13% wider for piezocrystal, as shown in Table 6-2. The soft but brittle piezocrystal material itself has a large effect on this result. A harder blade than the resin bonded one, such as a nickel bonded blade might be better option for cutting piezocrystal material but this was not available for the present work. After the dicing kerfs were observed from trials, the composite geometries were re-calculated and are also listed in Table 6-2. New pillar widths were obtained using Equation 4.7 on the basis of maintaining the same volume fraction for the three materials.

Table 6-2 Actual composite geometries for PZ26, PZ54 and PMN-PT materials

	Dicing Depth (mm)	Actual kerf width (um)	Dicing Pitch (mm)	Pillar Width (mm)	Volume Fraction (%)
PZ26	1.85	166	0.736	0.57	59.9
PZ54	1.85	166	0.736	0.57	59.9
PMN-PT	1.5	113	0.503	0.39	60.1

Composite Lapping

As indicated in Chapter 4, a lapping process is required to remove excess polymer epoxy from one side of the sample and uncut stock from the other. After lapping, piezoelectric pillars appear on both upper and lower surfaces and the composite plates will have a given thickness for the desired resonance frequency.

Figure 6.1 shows the final lapped thicknesses for PZ26, PZ54 and PMN-PT composites. The average and standard deviation were based on the thickness measurements of 15 square pieces for each material, with five points measured for each piece: four points at the corners and one centre point. The black dots are average thicknesses from these five points measurements for each composite piece.

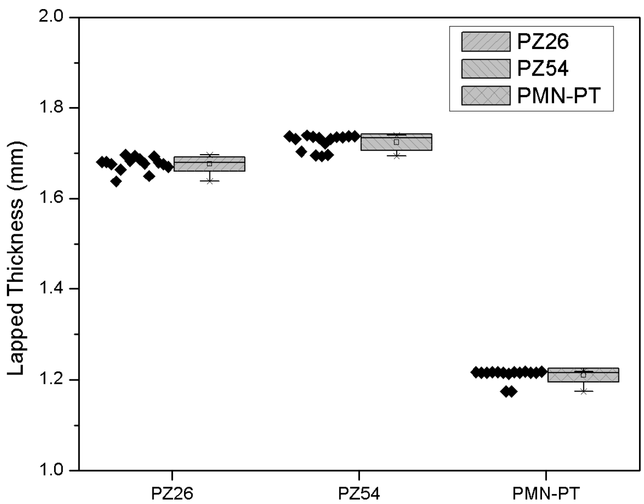

Figure 6.1 Lapped thickness of composite plates for PZ26, PZ54 and PMN-PT materials

Overall, the PZ54 composite plates have the largest standard deviation (SD), ±1.7%, following by PZ26, SD = ±1.59%. A possible reason is that the required thickness of PZ54 composite is more than that of PZ26 composite, leading to reduced material thickness removal, and therefore less control and possible adjustment for the final thickness. The piezocrystal composites have the best thickness uniformity, SD = ±1.48%. This might be attributed to removal of up to almost 600 μm of material which allows better control of the lapping thickness; the additional experience gained in lapping techniques is also believed to have contributed to this improvement, as the piezocrystal composites were made last.

To further analyse the data in Figure 6.1, Table 6-3 lists the final average thicknesses of 15 pieces of composite of each material and their variations. The aspect ratios are based on the average thickness and are slightly different between materials.

Before moving to the next step of diced into triangular elements, electrodes were established using conductive paint on both sides and the impedance spectra of the plates were measured. Both f_e and f_m were averaged for each material and are also presented in Table 6.3. Although having the smallest variation in thickness, the piezocrystal composite plates suffer the biggest variations in both resonance frequencies and impedance magnitudes. This is attributed to the fact that four out of 15 sample plates of PMN-PT material were ordered separately and came from a different material batch, with slightly different performance. The differences can be observed more clearly later with resonance frequencies measured for all the 96 array elements in the transducers plotted in Figures 6.8 (d) and 6.9 (d).

Table 6-3 Composite plates after lapping

	Average Thickness (mm)	**Thickness Variation (um)**	**Aspect Ratio**	**Average f_e (MHz)**	**Average f_m (MHz)**
PZ26	1.676	± 26.7	2.94	1.01 ± 0.012	1.18 ± 0.0128
PZ54	1.724	± 30.3	3.02	0.96 ± 0.012	1.1 ± 0.0135
PMN-PT	1.21	± 17.9	3.10	1.05 ± 0.026	1.39 ± 0.045

Element Dicing

As planned, 15 square composite plates were glued together in line and cut into triangular elements with three sets of pre-designed dimensions. Four plates with surface area of 15 x 15 mm^2 were glued for cutting out six HII triangles and the remaining 11 plates, with surface areas of 14 x 14 mm^2, for 12 DFG/DGF triangles and six HGG triangles, Table 4-6.

Four cutting passes were required to dice out the triangular elements, as shown in Figure 6.2: cut A1 is the first pass to determine a straight baseline for the triangles, with rotation angle 0^o. Cut B is the second pass with several cuts and a rotation angle of α1, following by Cut C with rotation angle of α2. The finishing pass is Cut A2 with 0^o rotation angle again and a pitch corresponding to the height of the triangle from the base (h) plus the width of the dicing kerf (k). Cuts B and C need special care in terms of the dicing pitches and their alignments, as the final dimensions of triangles are the combined results from both passes. With Cut B as an example, the dicing sketch is illustrated in Figure 6.2.

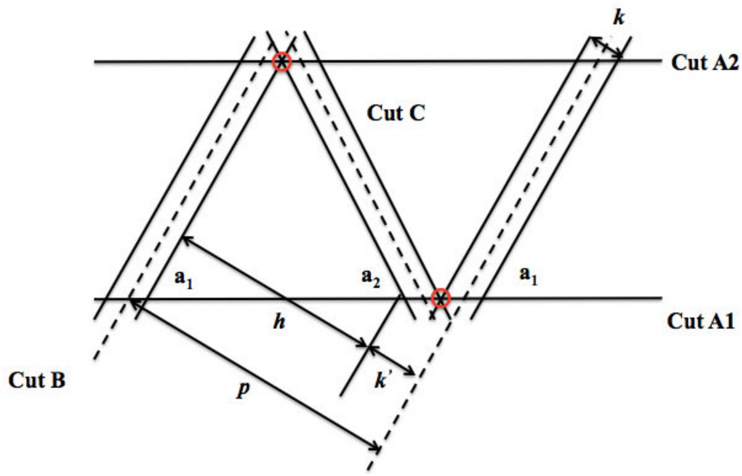

Figure 6.2 Dicing sketch for triangular elements. *Red circles*: reference spots for Cut C alignment

To obtain the correct dimensions, as designed, the actual dicing pitches for Cut B and Cut C can be determined through Equation 6.1:

$$p = h + k' + \frac{1}{2}k \qquad \text{Equation 6.1}$$

where $k' = k(\frac{1}{2} + \frac{\sin(a1)}{\sin(a2)})$ for Cut B, and $k' = k(\frac{1}{2} + \frac{\sin(a2)}{\sin(a1)})$ for Cut C; h is the height of the triangle from the corresponding side.

When the triangles are isosceles, like the HGG and HII elements, then Equation 6.1 can be simplified as:

$$p = h + 2k \qquad \text{Equation 6.2}$$

Before starting any dicing passes, the alignment is very important as well as the final dimension. Two crucial points were circled in Figure 6.2. The upper dicing edge of Cut C must meet the junction of Cut B and Cut A1; and the lower dicing edge of Cut A2 must meet the junction of Cut B and Cut C.

<u>96-element Sub dicing</u>

With 24 triangular plates diced out, the electrodes were applied to one side of the triangle with conductive ink and to the other with conductive paint. The second dicing procedure then followed to further define the 96 elements from the 24 triangles. Three dicing passes, Cuts A, B and C, along each side of the triangle were made to separate the triangle into four smaller triangles, with a dicing depth halfway through the composite thickness. Prior to dicing, the upper graticule line on the dicing saw screen was aligned to the side of triangular plate, Figure 6.3(b), and then shifted upwards a distance of $p = \frac{1}{2}h + 0.7k$. The constant 0.7 was determined after practical trials to equalize the surface areas of the four divided elements. Figure 6.3(a) presents one set of the sub-diced 24 triangular plates. The plates were stored in labeled boxes for easy identification.

(a) (b)

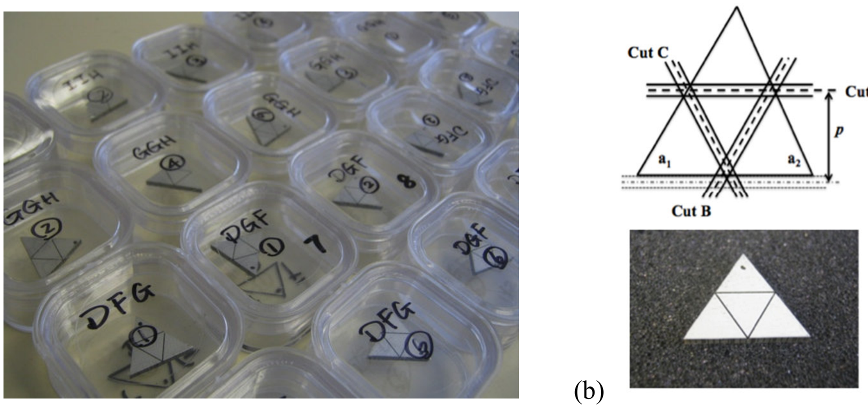

Figure 6.3 (a) Triangular elements prepared for one array transducer (b) Dicing sketch and the close-up of one of the triangular plates with four elements.

6.1.2 Electrical Connections

In order to drive the ultrasound transducers, electrical connections have to be established between individual piezoelectric elements and external electronics. This section describes the implementations of both interconnection and external-connection for the faceted array transducers.

Array Interconnection

Figure 6.4 shows the steps in making the interconnection stands for the array transducers. Figure 6.4(a) shows the flexible PCB using the design in Figure 4.12. The polyimide material at the bottom of the design has been removed by direct laser writing. Burn marks were found around/on the circuits; these were easily removed with acetone on a cotton bud. The continuity of each track was tested by digital multimeter and only the good circuits were used. As shown in Figure 6.4(b), the tested circuit was cut out along its overall contour and microcoaxial cables were then soldered to it. The circuit was then wrapped around the nut-stand and glued using general-purpose superglue (473-455, RS Components, Northants, UK). The edge of the circuit from where the connecting legs start had to be aligned carefully, level with the edge of the nut-stand. For those stands with only three connections, both the circuits and the nut-stands were cut in half, Figure 6.4(c). The soldered points were then covered by a layer of fast curing epoxy (Araldite® Rapid), Figure 6.4(d), not only for securing the connections but also for preventing any possible short circuit between signal and ground tracks. The connectors were then wrapped overall in insulating tape as shown in Figure 6.4(e). Figure 6.4(f) shows one set of interconnection stands for one faceted array. In total there are 19 stands in one set with 13 stands having six connections each and another six having three connections each.

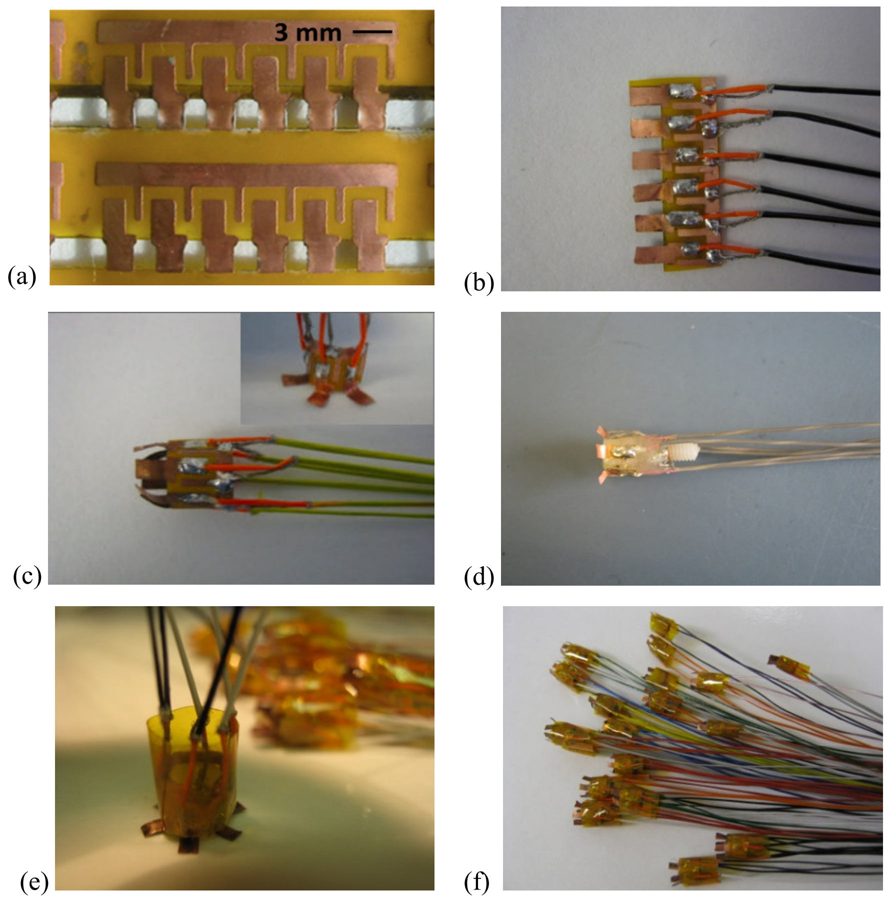

Figure 6.4 Implementation of array interconnections

Array External Connection

The double-sided PCBs for soldering the coaxial cables were fabricated in house. 12 designed artworks were patterned on a large photoresist board, with the alignment of artwork on opposite sides done manually with great care. After being developed, the PCB was sawn into 12 small pieces. A PCB connector was then soldered to each board. Cables were be soldered at the other end of the board, and the soldering joints were covered by fast curing epoxy. The boards were then varnished with insulating varnish (199-1480, RS Components, Northants, UK) and wrapped in insulating tape, Figure 6.5(b).

(a) 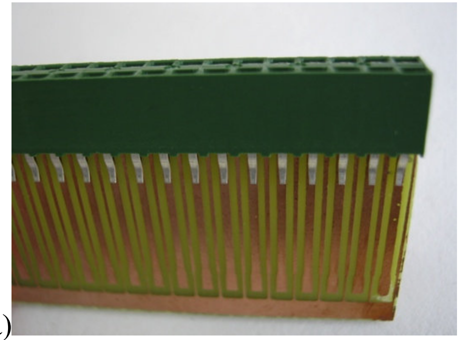

(b) 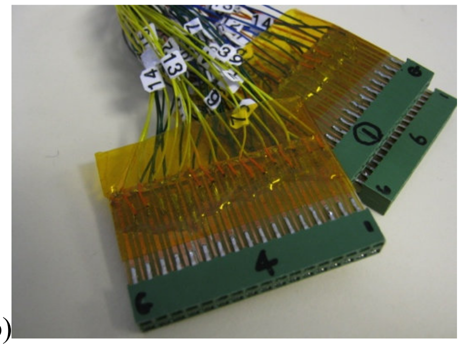

Figure 6.5 External Connector for array transducers (a) made-in-house PCB with connector (b) wired connector for array

Wiring the cables to external connectors was the last step in preparation for array assembly. The ground cables connecting the front face of the array were soldered to the ground traces on the board.

6.1.3 Assembling the Array Transducers

With the active elements and interconnectors prepared, the components of the array transducer were ready to be assembled. The implementation process has already been illustrated theoretically in Figure 4.18; this section will define more practical details.

Figure 6.6(a) shows the fabrication mould with the two spacers around it. The fabrication mould was tightly wrapped with cling film to assist with mould release afterwards. Liquid honey was then brushed on and the triangular piezoelectric elements were placed in position on the mould, section by section, as shown in Figure 6.6(b), till the geodesic dome structure was formed. With all elements in place, Figure 6.6(c), the elements were glued together and also to the transducer spacer. In practice, the gaps between the plates were quite small, around 200 μm in width, directly proportional to the sample thickness. Thus the application of filling epoxy was done under a microscope using a needle tip.

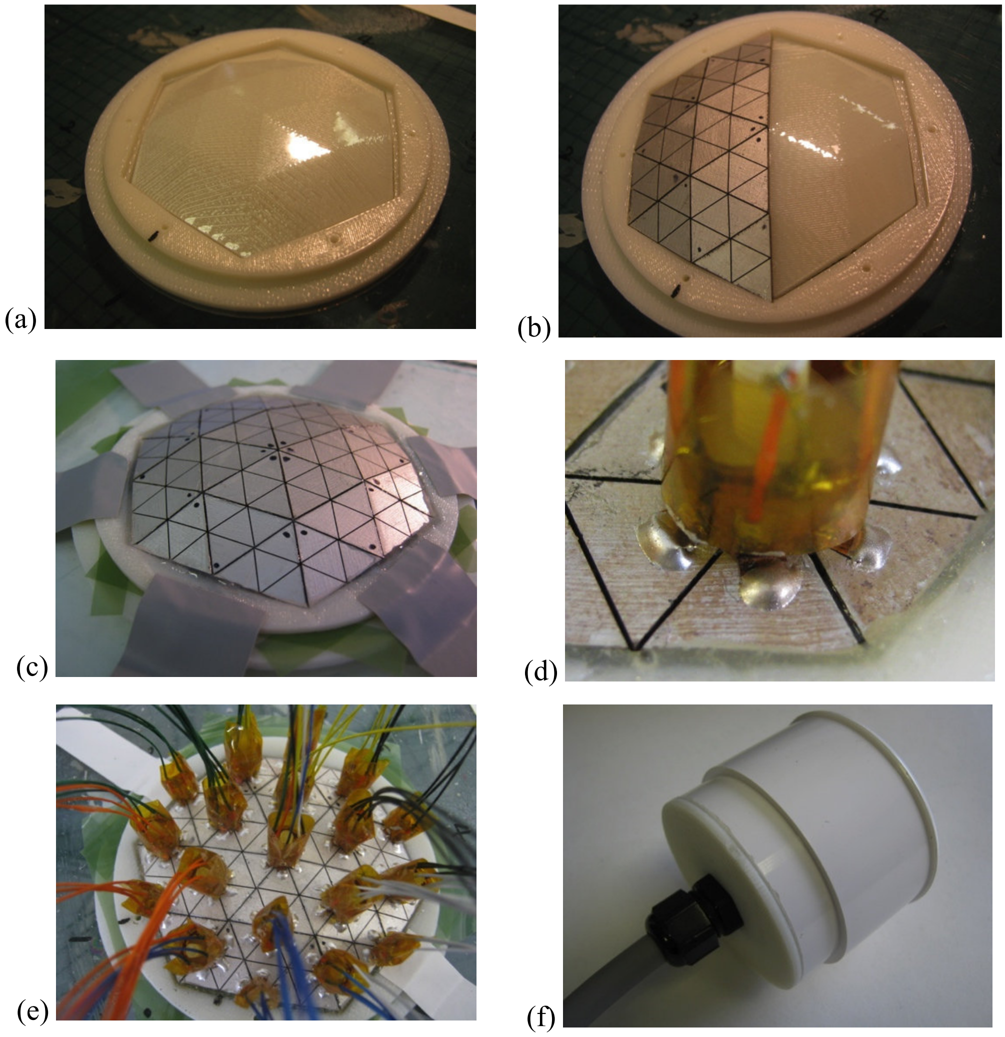

Figure 6.6 Assembling process of faceted bowl array transducer

Figure 6.6(d) is a close-up of one of the interconnection stands. Electrical connections between the copper legs and the piezoelectric elements were established with conductive epoxy. Considering the temperature limitation of piezocrystal array transducer, the baking time to cure the epoxy was 30 min at 55^{o}C. Figure 6.6 (e) presents the final status of the array with all the elements connected to coaxial cables with the aid of interconnection stands.

After bonding the assembly to its casing, the backing layer was applied. Extra attention was required for this step as the glass microballoon – epoxy mixture could be applied only through the space between the connection stands. Its stiff, powdery texture meant that the mixture had to be pressed firmly in place to ensure full and even contact between it and the piezoelectric elements. The assembly was then left under room temperature overnight for the epoxy to cure. The cured backing layer not only secured the connections but also provided mechanical support to the spherically sectioned structure.

Figure 6.6(f) shows the finished package of the array transducer. The array's rear cover was printed with a 3D prototyping machine, fitted to the casing with a hole in the centre for the cables. Each cable was labelled with a number corresponding to its connected element and the cables were fed through a cable sleeve and secured by a cable gland.

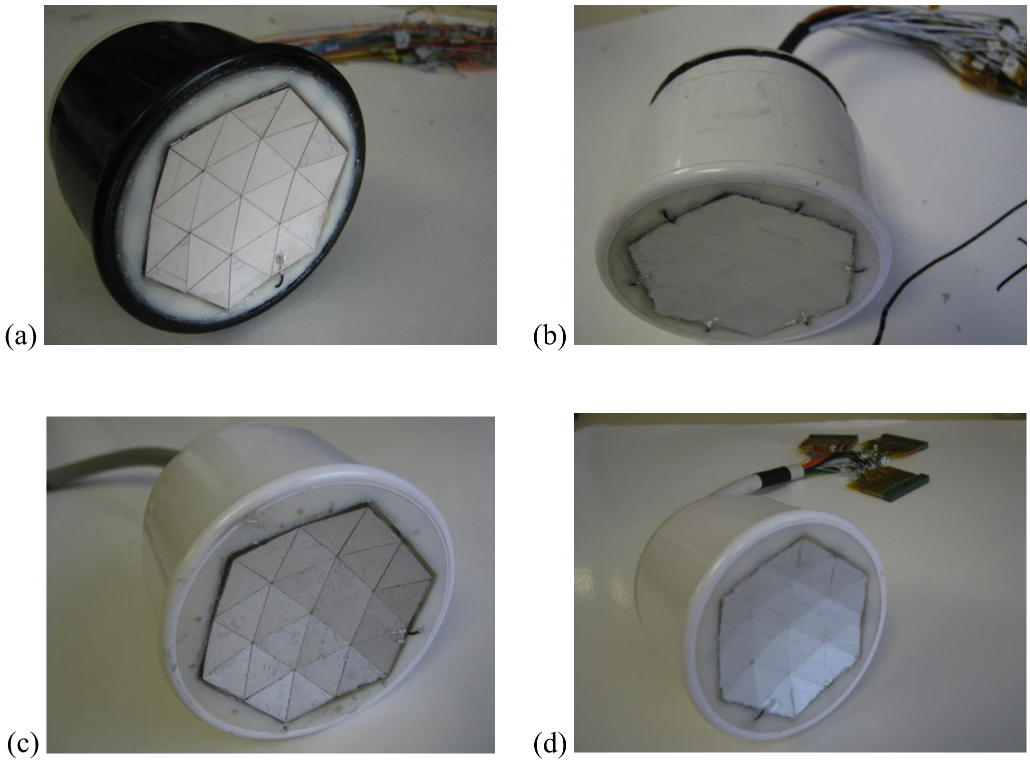

Figure 6.7 Faceted Array Transducer made of (a) PZ26 bulk ceramic; (b) PZ26 composite (c) PZ54 composite (d) piezocrystal PMN-29PT composite

Following the same procedure, four faceted arrays were built in this work, using PZ26 bulk ceramic, PZ26 composite, PZ54 composite, and piezocrystal PMN-PT composite, respectively. The finished arrays are shown in Figure 6.7.

6.2 Basic Array Testing

This section will present the results from basic tests carried out for the four faceted array transducers. Based on electrical impedance measurements, the working status of each element of the arrays can be checked; the uniformity of array elements, in terms of resonance frequency, for example, can be examined; and the effects of water loading can be determined, to represent coupling to tissue.

6.2.1 Complex Electrical Impedance Measurements

The primary characterization of the faceted array transducers is to connect their individual elements to the impedance analyser and record the impedance spectrum over a range of frequencies, centred at the resonance frequencies. Figure 6.8 shows the impedance magnitude and phase spectra of all elements from all four arrays. The frequency range for the PZ26 ceramic array is from 500 kHz to 1.4 MHz; while those for the other arrays are from 100 kHz to 2 MHz. This is because the triangle is not a standard shape for bulk ceramic, and the main thickness resonance and other resonances, particularly in the lateral direction, are all coupled and affect each other. The resonances cannot be separated clearly from each other on the impedance spectra, and more detailed scanning is therefore required, using a smaller frequency range.

Not all elements of the arrays worked properly, the problems occurring either during fabrication or operation. The impedance magnitude and phase of the non-working elements were all set to be zero for clear plotting, even though some failures manifested as short circuits and others as open circuit. There are 91 out of 96 elements working in the PZ26 ceramic array; 92 out of 96 working in the PZ26 composite array; 95 out of 96 working in the PZ54 composite array; and all 96 elements working in PMN-PT composite array. This order was also the order of fabrication. The broken elements of each array were marked on the array configuration diagram and can be found in Appendix G.

The sets of impedance spectra in Figure 6.8 were imported into MATLAB for further analysis. The frequencies at both minimum and maximum impedance magnitude were selected as f_e and f_m respectively and the results are plotted in Figure 6.9.

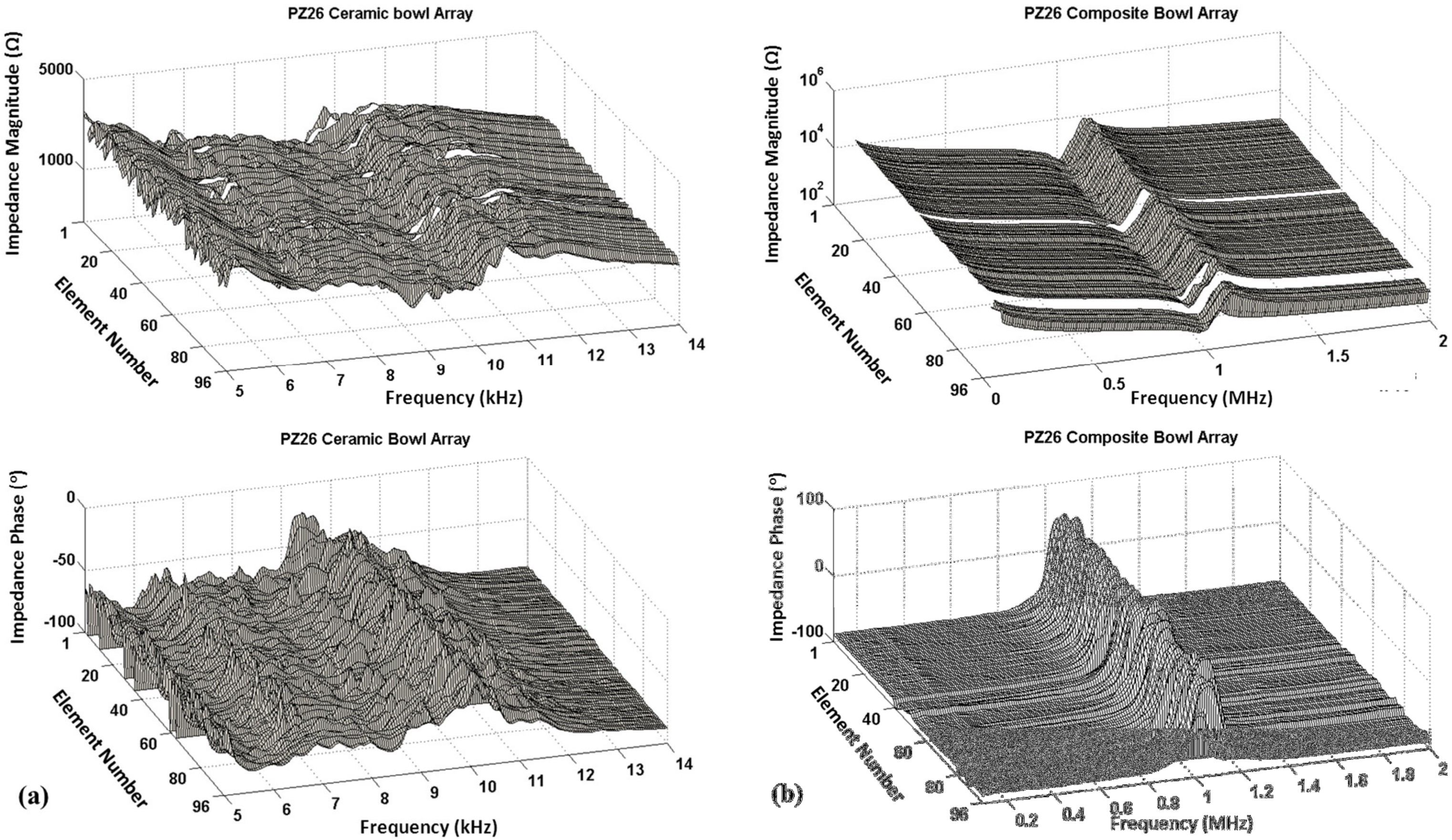

Figure 6.8 Complex electrical impedances of 96 individual elements: (a) PZ26 ceramic (b) PZ26 composite, (c) PZ54 composite, and (d) PMN-PT composite arrays

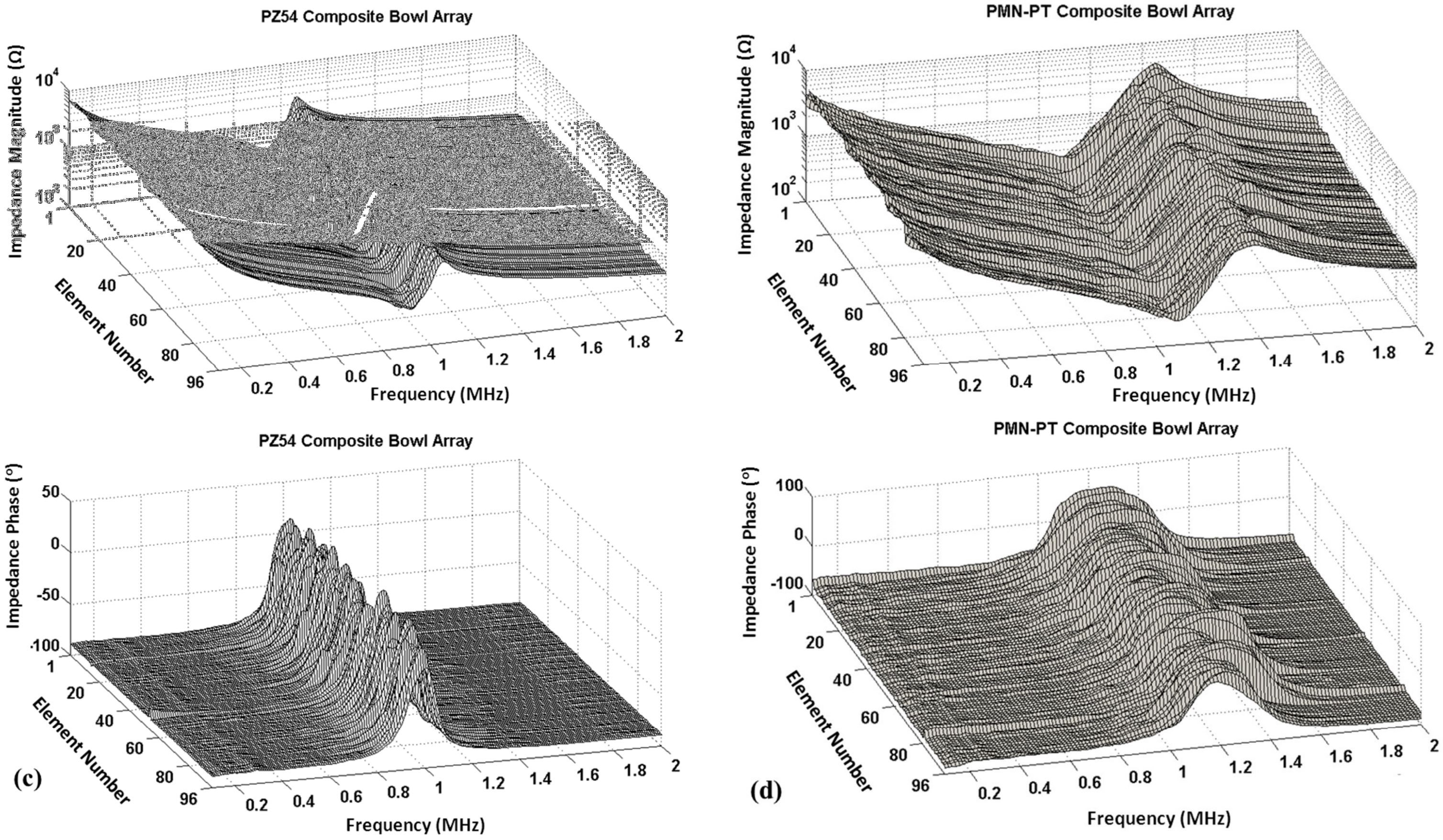

Figure 6.8 Complex electrical impedances of 96 individual elements: (a) PZ26 ceramic (b) PZ26 composite, (c) PZ54 composite, and (d) PMN-PT composite arrays

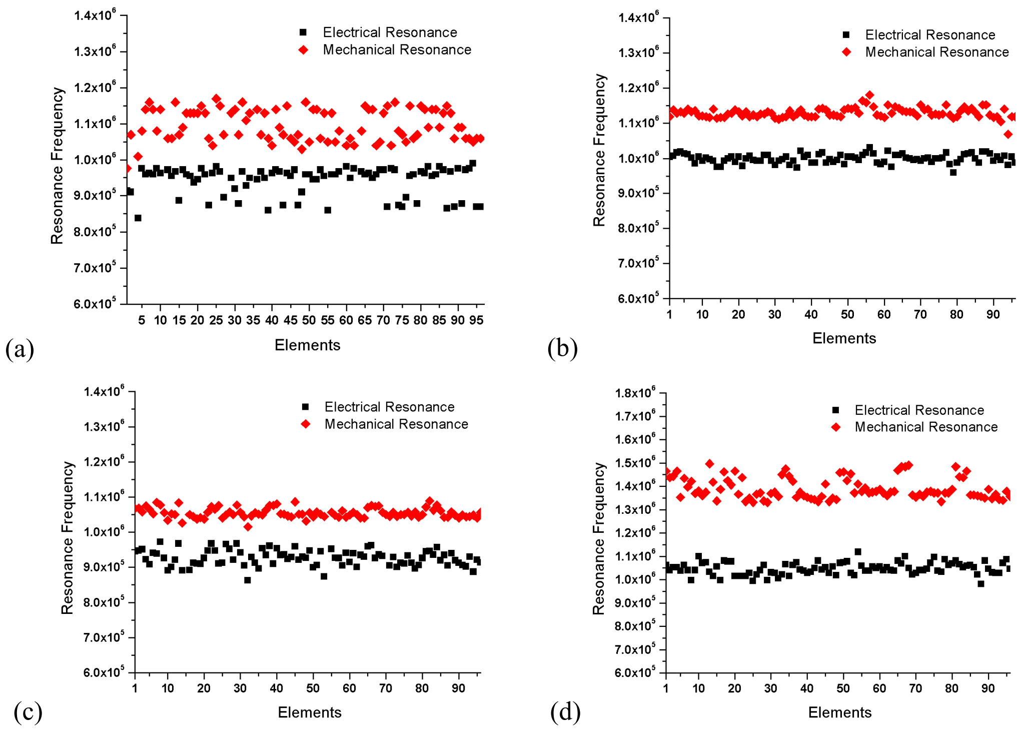

Figure 6.9 Resonance frequencies of individual element in faceted arrays made of (a) PZ26 ceramic; (b) PZ26 composite; (c) PZ54 composite; (d) PMN-PT composite.

Because of its difficult impedance spectra, there is much more variation in the extracted resonance frequencies for the bulk ceramic elements. It is believed that the variations are not caused by element non-uniformity but by the reduced accuracy of the result itself when compared with that from the other three composite arrays. The statistics of the extracted frequencies and their corresponding impedance magnitudes are listed in Table 6-4.

Table 6-4 Statistics of resonance frequencies and impedance magnitude

	f_e (MHz)	f_m (MHz)	$\lvert Z \rvert @ f_e$ (Ω)
PZ26 Ceramic Array	0.94 ± 0.047	1.09 ± 0.044	942 ± 168
PZ26 Composite Array	0.99 ± 0.013	1.13 ± 0.014	449 ± 109
PZ54 Composite Array	0.926 ± 0.022	1.055 ± 0.014	494 ± 73
PMN-PT Composite Array	1.048 ± 0.026	1.39 ± 0.045	241 ± 57

Despite the less accurate results of PZ26 ceramic array, the piezocrystal composite elements have the largest variations in both resonance frequencies between the three composite arrays. This corresponds with the measurements of the square composite plates in Section 6.1.1. The impedance magnitude at electrical resonance of piezocrystal composite is significantly decreased by up to 50% when compared to the other two ceramic composites, a highly desirable result for array implementation.

Effective coupling coefficients for the three composite elements were calculated using the extracted frequencies and Equation 4.6. The results are plotted in Figure 6.10. The averaged k_{eff} of the elements of the PZ26 composite array is 0.46 ± 0.02; 0.47 ± 0.06 for the PZ54 composite array, and 0.66 ± 0.03 for the PMN-PT piezocrystal array, a proportional increase of more than 40% compared to the PZ26 and PZ54 composites.

As seen in Figure 6.10, the element numbers were allocated on the x-axis from 1 to 96, and then divided into six sections by dotted lines, corresponding to their positions within the whole array configuration presented in Figure 4.13. An interesting trend was noticed for the piezocrystal elements, with the first few elements always showing higher values of k_{eff} than the rest of elements within each section, corresponding to the HII triangular plates. It is believed that the supply of piezocrystal bulk samples from two different batches was the main cause, since the HII plates were fabricated using the bulk samples ordered from the second batch whilst the rest of the plates were all made from material from the first order. This is a practical illustration of the problem of uniformity of piezocrystals across suppliers as discussed in Chapter 5.

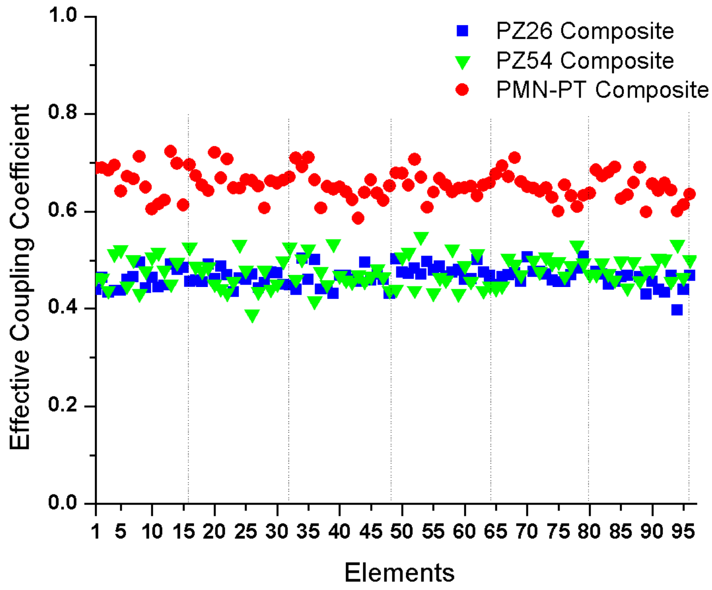

Figure 6.10 Effective coupling coefficients of individual element in composite faceted arrays

6.2.2 Water-loading Effects

Since water is usually used as the acoustic medium between a patient and FUS transducer and has an acoustic impedance close to tissue, it is useful to know how much a water load will affect performance. Based on electrical impedance measurements, the arrays were tested with their front faces placed in air and water, respectively, with the results reported in this section.

The results presented in Figure 6.11 are the preliminary characterization before the later functional tests in Section 6.3. Two drive configurations were investigated here, with the arrays driven with all elements connected in parallel and with just one element activated. In Figure 6.11, the impedance difference between the two driven configurations is apparent: connecting all elements of the arrays together has significantly decreased the impedance magnitude, as expected. This is due to the increased capacitance resulting from increased connection surface area. For future work, the area of the elements within the transducer could be designed specifically to optimize electrical impedances.

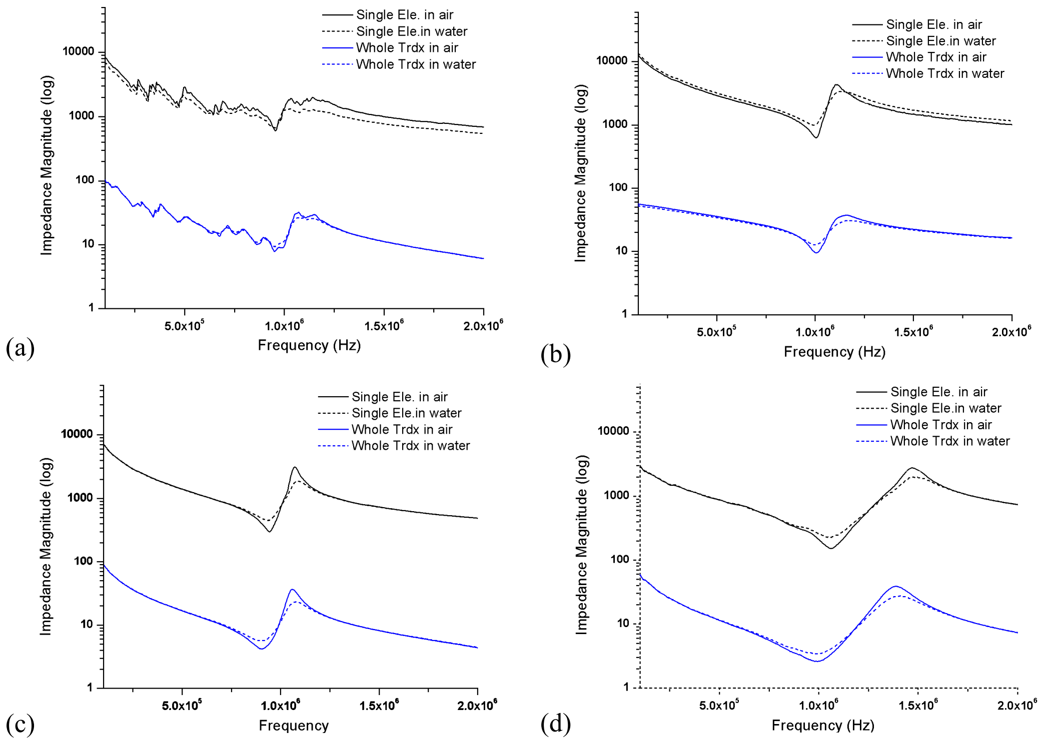

Figure 6.11 Impedance magnitude spectra of whole array and elements no.1 of (a) PZ26 ceramic; (b) PZ26 composite; (c) PZ54 composite; (d) PMN-PT composite, in air and water, respectively.

The practical rule to determine driving frequency is to pick a frequency near the device resonance and with its corresponding impedance as close as possible to 50 Ω. When the arrays were driven as a single channel, f_m was of particular interest and was chosen as the driving frequency in the experiments to determine the geometrical focusing capability of the arrays, as described in Section 6.3.1. In contrast, f_e was preferred as the driving frequency when only a single element was activated.

With the corresponding impedance magnitudes at the driving frequencies in air as references, the variations induced by the water loading have been extracted from Figure 6.11 and are listed in Table 6-5. The variations in driving frequencies are not shown as no significant changes were observed.

Table 6-5 Variations in impedance magnitude from water loading, referenced to air loading

	|Z| @ f_m (Whole array)	**|Z| @ f_e** (Element No. 1)
PZ26 ceramic Array	-18%	+11%
PZ26 composite Array	-17%	+58%
PZ54 composite Array	-36%	+57%
PMN-PT composite Array	-29%	+47%

PZ26 piezoceramic, as the hardest material used in this project, experienced less variation comparing with the three piezocomposite materials. Among the composite arrays, the water load damped the PZ54 array, made with softer ceramic, the most. It can be seen that the water damping effect is significant, therefore, for any further work with the transducers, for instance for impedance matching, it is their behaviour in water that should be considered.

6.3 Functional Array Testing

Following basic testing, the four arrays were subject to more advanced tests, referred to here as functional tests. As the key characteristics of a FUS device, the focusing and steering abilities of the faceted arrays were tested first, with results presented in Section 6.3.1. The acoustic outputs of the arrays were then tested with a radiation force balance. The measurements are reported in Section 6.3.2 and the results are compared between arrays or, in other words, between their four constituent piezoelectric materials. Lastly, the arrays were placed in a 3T MRI scanner to check passive MRI compatibility, with the results shown in Section 6.3.3.

6.3.1 Focusing and Steering Capability

The focusing and steering abilities of the faceted arrays were tested through acoustic field characterization using the equipment and methods described in Section 4.3.2. With the faceted array positioned facing downwards, three planes were mapped within the acoustic field of each array: the X-Y cross sectional plane at the focal distance (red), the X-Z axial plane (green) and the Y-Z axial plane (blue), as indicated in Figure 6.12.

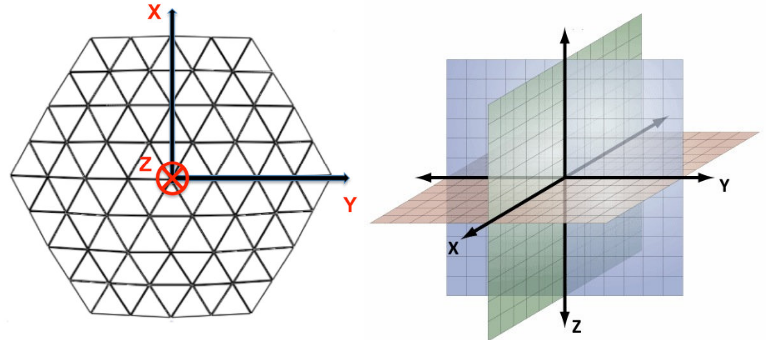

Figure 6.12 Mapping plane orientations for the faceted arrays

Focusing Capability

In order to test the focusing capability of the faceted structure, all the elements of the arrays were connected in parallel and the arrays were driven as a single channel by one signal generated by a single-channel signal generator. This allows the natural focus of the faceted geodesic dome structure to be examined. According to the impedance magnitude plots in Figure 6.11, the electrical impedances of the arrays are much closer to 50 Ω at f_m when the arrays are driven as a whole with a single signal. Therefore the arrays were driven at f_m for the natural focusing capability test. The output of the signal generator was set to be 5 $V_{p\text{-}p}$ for all four arrays.

The acoustic fields of the arrays were mapped firstly along the axial planes, X-Z and Y-Z; the focal distance was then determined by finding the maximum pressure point in the X-Z axial plane. The cross-sectional plane in which maximum pressure point was located was scanned afterwards and referred to as the X-Y focal plane. Figure 6.13 presents the normalized intensity fields generated by the transducers in each plane. The fields are presented here from left to right as the PZ26 ceramic array, the PZ26 composite array, the PZ54 composite array and the PMN-PT piezocrystal composite array, respectively.

The mapping range was 40 mm in the X and Y directions, from -20 to 20 mm with the array's geometrical center line as zero; and 80 mm in the Z direction, 20 mm - 100 mm away from the edge of the array, in other words, 26.275 - 106.275 mm from the physical centre of the array since the height of the geodesic structure is 6.275 mm.

It is apparent in Figure 6.13 that the ceramic array is able to achieve a good focus, which is a successful proof of concept of the faceted self-focused structure designed in this work. However, the composite arrays have poorer focusing qualities. It is believed that, in addition to the individual differences between arrays caused by assembly errors, the out-of-phase issue among the composite elements is the main reason.

Unlike the bulk elements in the PZ26 ceramic array, which undergo no extra processes beyond being diced into triangular shapes, the elements in composite arrays have been subject to the processes of dicing, epoxy curing, lapping and heating for bonding and de-bonding associated with lapping. Those processes can cause differences between the composite plates and therefore the elements of the arrays. Under these circumstances, the composite elements will not necessarily vibrate in phase, even if they are driven by the same signal and the acoustic beam pattern will therefore be affected within the field.

The focusing capabilities of the composite arrays actually correspond to the measurements made on the composite plates and the elements of the three different materials, with PMN-PT piezocrystal composite array having the largest element variation, as presented earlier, and the worst focusing. The acoustic field generated by the PMN-PT array has multiple foci and the absolute maximum pressure point does not occur along the geometrical central axis, unlike the other arrays. Thus the determination of the focal X-Y plane of the PMN-PT composite array was not based on the absolute maximum pressure value within the field, but on combined consideration of the symmetry of the beam pattern and the relative maximum pressure along the axis. As a result, the focal plane of PMN-PT composite array was located at a distance of 69.275 mm away from the physical centre point of the array, whilst the distances were 72.275 mm for the PZ26 ceramic array, 73.775 mm for the PZ26 composite array, and 76.275 mm for the PZ54 composite array, all close to the designed geometric focal distance of 75 mm.

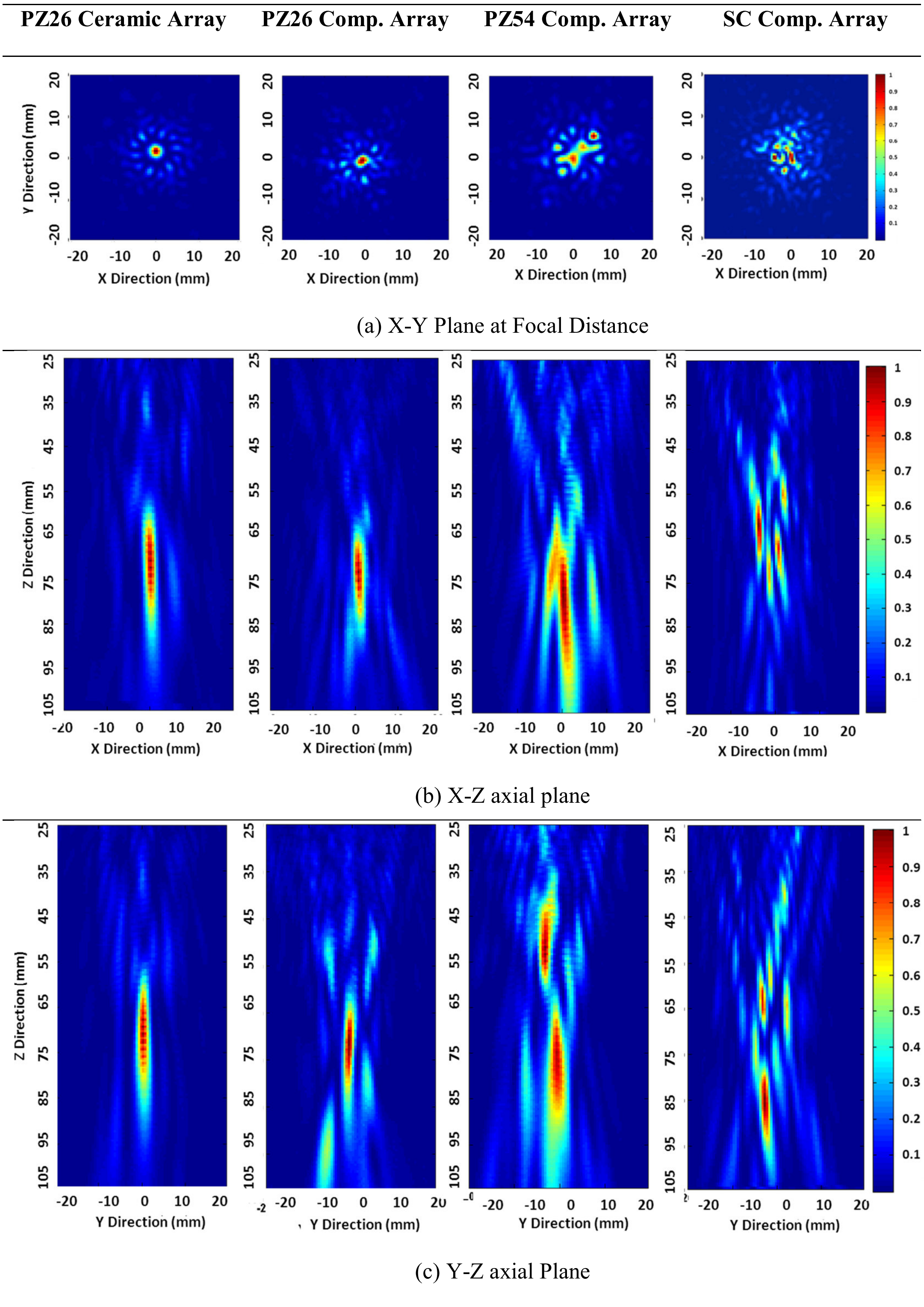

Figure 6.13 Normalized intensity fields generated by faceted array transducers: (a) XY plane; (b) XZ plane and (c) YZ plane, from left to right: PZ26 ceramic array, PZ26 composite array, PZ54 composite array and PMN-PT composite array

Optimized Focusing and Steering

From the acoustic fields mapped in the last section, the faceted sphere-sectioned array structure has shown acceptable geometric focus. However the need of phase correction for aberrations was obvious to optimize the focusing of the arrays, especially for the PZ54 and PMN-PT composite arrays. Using the multi-channel driving configuration detailed in Chapter Four, the arrays were connected to the 32-channel ultrasound transmit system, DSL32T (Diagnostic Sonar Ltd, Livingston, UK) and driven by 32 signals with individual phases. In the work reported here, the results of PMN-PT composite array, as the worst case, are presented.

The PMN-PT composite array was grouped into 32 channels and driven by a single frequency of 1 MHz. The DSL32T system provided a 5 $V_{p\text{-}p}$ voltage for all channels. Figure 6.14 shows the intensity field in the X-Y focal plane at 69.275 mm from the physical centre of the array. With the adjustment of phase to each channel, the hydrophone based correction of intrinsic phase aberration was applied to the array, in Figure 6.14(b). Compared to the mapped field without phase control, Figure 6.14(a), a single, high quality focus was obtained and the measured voltage amplitude at the focal point was increased by a factor of four from 40 $mV_{p\text{-}p}$ to 160 $mV_{p\text{-}p}$.

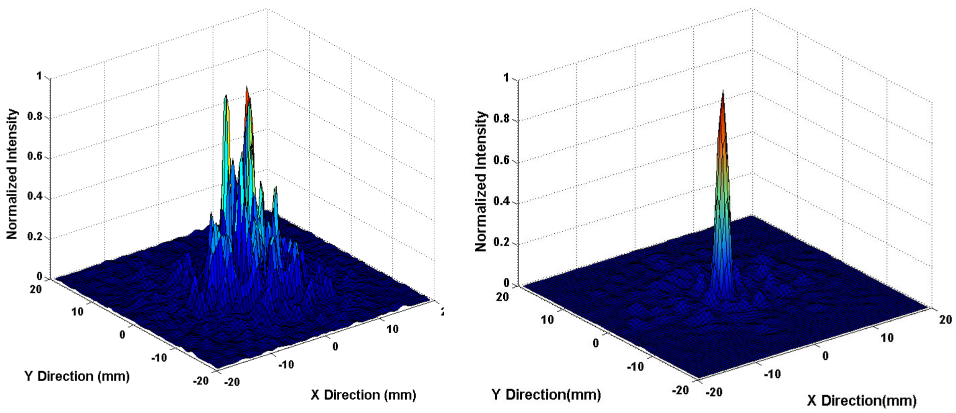

(a) (b)

Figure 6.14 Normalized Intensity field of PMN-PT composite array on X-Y plane, array focused at (0, 0, 69.275) mm (a) natural focus (b) optimized focus with phase control

The -3 dB (FWHM) beam width in Figure 6.14(b) was measured on its contour map, 1.5 mm in diameter. Based on Equation 3.9 and 3.10, the optimized focusing gain of the transducer is $G = 29.9$.

The phasing capability of the DSL32T system can not only correct focusing aberrations but also allows control of the focal position. The optimized focus of the PMN-PT composite array was shifted within a volume of 10 x 5 x 5 mm. As shown in Figure 6.15, a 40 x 60 mm^2 area in the X-Z plane was mapped with the focus shifted 5 mm ahead of the original focus and then 5 mm behind. The contour plots of the intensity fields are also presented in Figure 6.15.

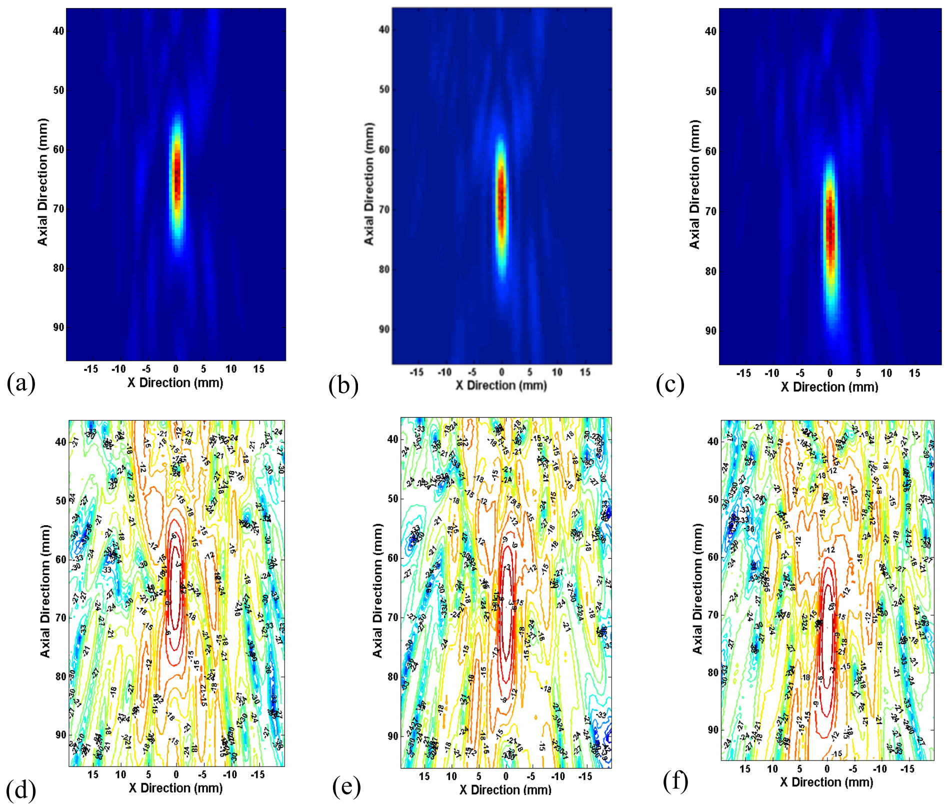

Figure 6.15 Optimized focus of PMN-PT composite bowl array at (a) (x, y, z) = (0, 0, 63.775) (b) (x, y, z) = (0, 0, 69.275) (c) (x, y, z) = (0, 0, 74.275) mm.

From the measurements, the actual maximum intensity points were found at 5.5 mm forward of the original focus, and 5 mm behind, respectively. The -3 dB focal region did not change much in diameter when moving the focus forwards but increased from 1.5 mm to 2 mm when moving backwards. The -3 dB length along the beam axis changed as well from 15 mm to 18 mm. The side lobes in the plots are all lower than -12 dB, comparing well with the acceptable level of -10 dB noted earlier.

With the focus shifted 5 mm behind its original position, it was then moved off the central axis a distance of 2.5 mm, thus focusing the acoustic beam at position (2.5, 0, 74) mm. Figure 6.16 shows the normalized intensity map and contour plots in the X-Y plane. As predicted, the array configuration allows less flexibility of shifting focus off axis, with one obvious side lobe, appeared with an intensity of -9 dB.

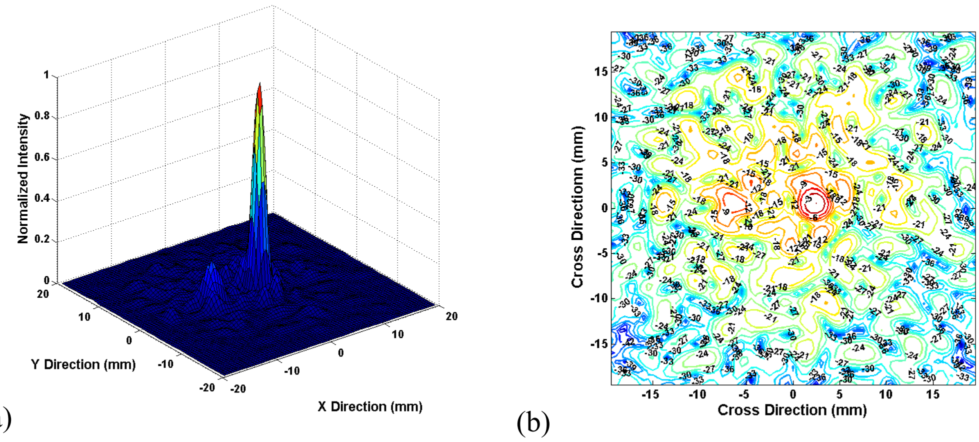

(a) (b)

Figure 6.16 Optimized focus at (2.5, 0, 74) mm (a) normalized intensity plot (b) normalized intensity contour plot

6.3.2 Acoustic Power Output

The experimental setup to carry out acoustic power output measurement was presented in Section 4.4.3. The results in Figure 6.17 and 6.18 were obtained from a single element, element number one, out of 96 elements in the arrays. As mentioned, two sets of experiments were carried out with frequency responses, linearity and acoustic power output compared between the four elements made with the different piezoelectric materials. Although efficiency could be calculated through measurements of electrical input power and acoustic output power, it was neglected here because of the mismatched electrical impedances.

Frequency Response

In Figure 6.17, element No. 1 in each array was activated in turn. The acoustic power outputs were recorded at driving frequencies in the range 500 kHz - 1.8 MHz. Since the electrical impedance is frequency dependent, the input voltages were adjusted slightly at each frequency to ensure the same electrical power was delivered to the element. For the work reported here, the forward electric power was chosen as 5 W.

The maximum acoustic outputs were found when the drive frequencies were close to f_e in Table 6-4 but not exactly the same, observed at 0.975 MHz for the PZ26 ceramic and composite elements and the PMN-PT composite element and 0.925 MHz for the PZ54 composite element. Without any extra impedance matching circuitry connected to the elements, the impedance magnitude of the PMN-PT composite element at the frequency of maximum output is respectively 66%, 72.4% and 38% less than the values for the PZ26 ceramic, PZ26 composite and PZ54 composite elements; correspondingly, the acoustic output is increased, respectively, by 207%, 71% and 25% compared with the measured values from PZ26 ceramic, PZ26 composite and PZ54 composite elements.

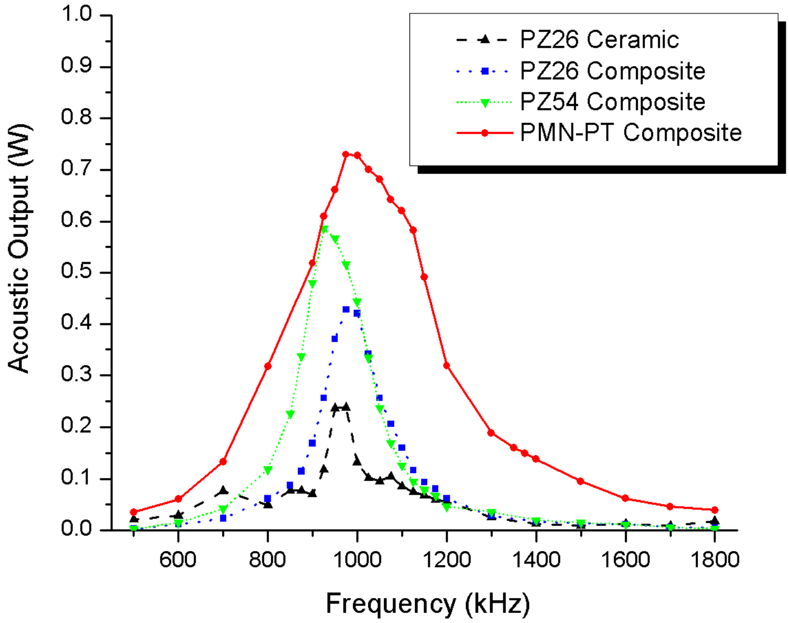

Figure 6.17 Frequency responses for different materials based on single-element acoustic output measurements

The PMN-PT composite element also has the broadest FWHM frequency bandwidth, at 370 kHz, from 830 kHz to 1200 kHz; the PZ54 ceramic composite, considered as the best ceramic for FUS, has a bandwidth of 175 kHz, from 870 kHz to 1045 kHz; for PZ26 ceramic, the composite form has significantly increased the operating bandwidth to 160 kHz (910 - 1070 kHz) from 100 kHz (920 - 1020 kHz) for the bulk PZ26 ceramic element.

Linearity

The elements were then driven at the maximum output frequency obtained from the first experiment, with the input electrical voltage increased stepwise. Because of the lack of electrical impedance matching, the input signal was still limited to a low level to prevent damaging the arrays and the power amplifier. the maximum voltage applied in this experiment was 2 $V_{p\text{-}p}$ from the signal generator, corresponding to 11 W electrical power from the power amplifier. Figure 6.18 presents the results from the four single elements. The acoustic outputs plotted are the averaged results from three repeated measurement cycles.

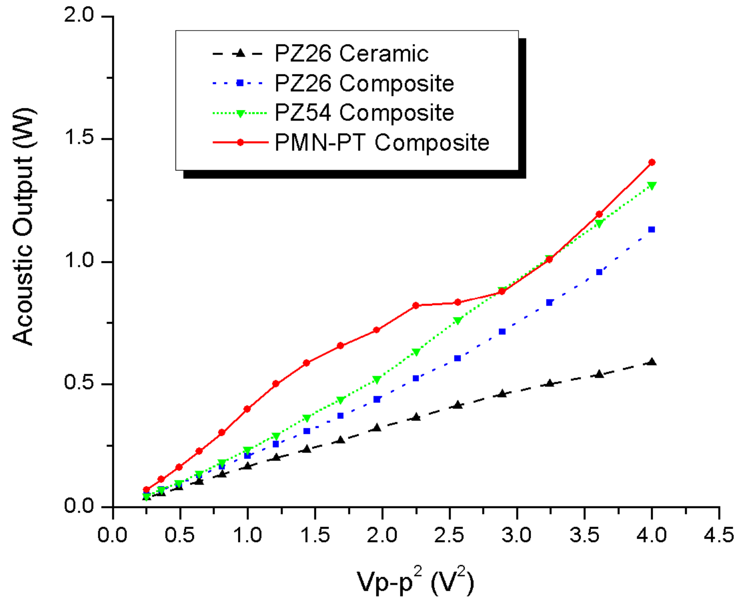

Figure 6.18 Linearity between input electrical power and output acoustic power

The acoustic outputs of the four materials generally follow the same trend as that presented in Figure 6.17, with the PZ26 ceramic element generating the least acoustic output and the PMN-PT composite element generating the most. However, the PMN-PT composite was less stable than the ceramic materials, either in bulk or composite form. The instability became serious with increasing input, and the PMN-PT composite started to lose its advantage in terms of the acoustic output. Although the last two measurements plotted in Figure 6.17 still show the largest outputs, the element itself had been heated up rapidly and the measured acoustic power was observed to vary over time.

The turning point occurred when the acoustic output reached a surface intensity of 3 W/cm^2 (element area: 28.4 mm^2). It is believed that, under this drive condition, the self-heating effect had raised the temperature within the composite element to beyond 60^{o}C, corresponding to the phase transition point presented in Figure 5.8.

The results shown in this section are further proof that piezocrystal material can offer better performance in terms of broader bandwidth, lower electrical impedance, higher efficiency and therefore more acoustic output. However, modifications to the piezocrystals are required for high power conditions, such as are offered by Generation II and III ternary piezocrystal. If PMN-PT piezocrystal is used for the FUS application, a DC bias field should be present as part of the driving system to extend the power limits and to reduce the possible risk of de-poling the piezoelectric elements. However, this carries a safety risk.

6.3.3 Passive MRI Compatibility

With the aim of MRI for guidance, the passive compatibilities of the four arrays are reported in this section, from measurements with a Siemens 3T MRI scanner using its body coil. Guided by the standard test method, ASTM F2119, the distortion and artefacts produced by the arrays in MRI were studied.

The experimental setup was presented in Figure 4.23. Prior to scanning, the coordinate system was defined as the default value, with Head first as entry direction and Supine for the patient position. Selected images in sagittal and transversal planes are presented in this thesis. The definitions of body plane, the patient coordinate system and encoding direction applied in this work are given in Appendix J-1 to 3.

As a reference, the phantom was scanned first without the array. Figure 6.19 shows the centred slices through the phantom. AP refers to the anterior – posterior direction, HF refers to head – to - foot direction, and RL refers to right – to - left. Generally speaking, there were no obvious differences between any two planes and two encoding directions, beyond the distortion caused by water movement.

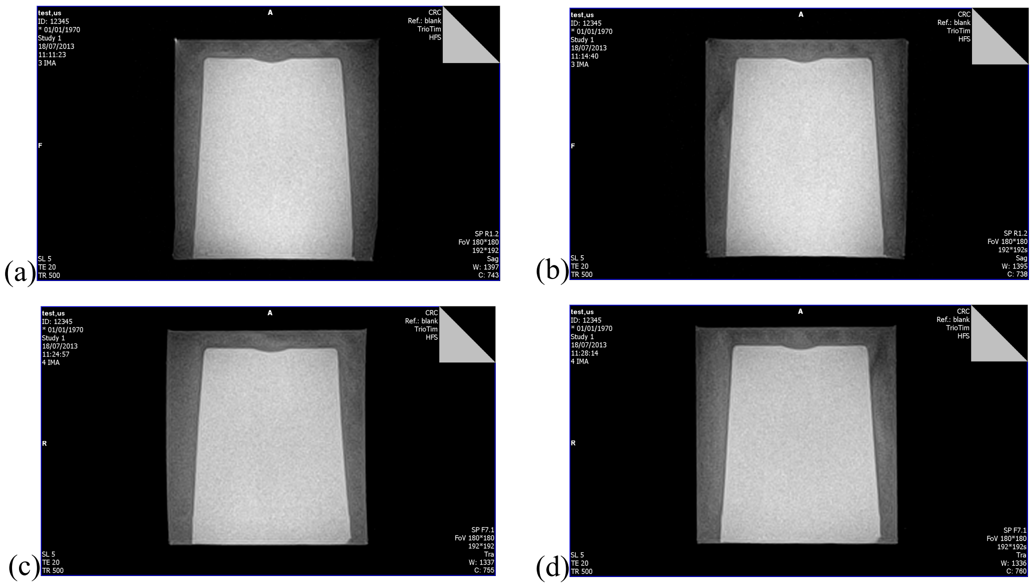

Figure 6.19 MR images with phantom only as reference (a) Sagittal AP (b) Sagittal HF (c) Transversal AP (d) Transversal RL

Using the same MRI sequences, the array transducer was placed on top of the phantom. The cable was positioned at the side of the water chamber, along the Sagittal plane. The four arrays were scanned in turn, with the results shown in Figure 6.20.

Sagittal AP **Sagittal HF** **Transversal AP** **Transversal RL**

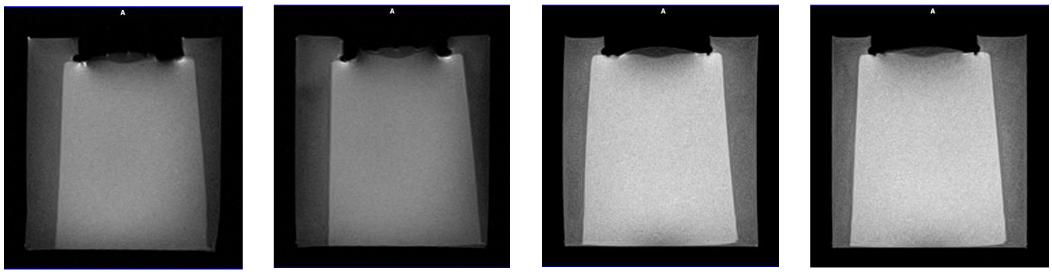

(a) PZ26 ceramic array

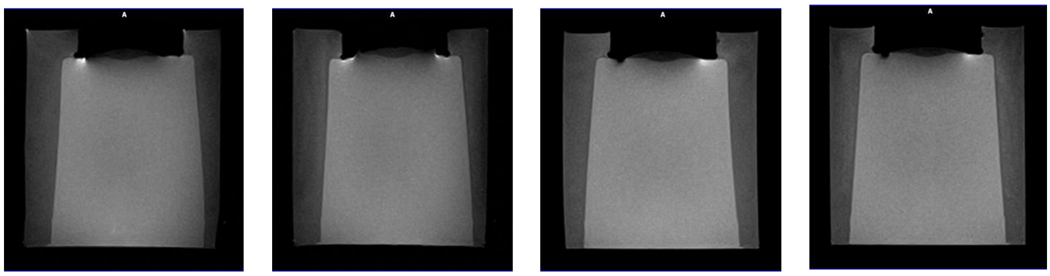

(b) PZ26 composite array

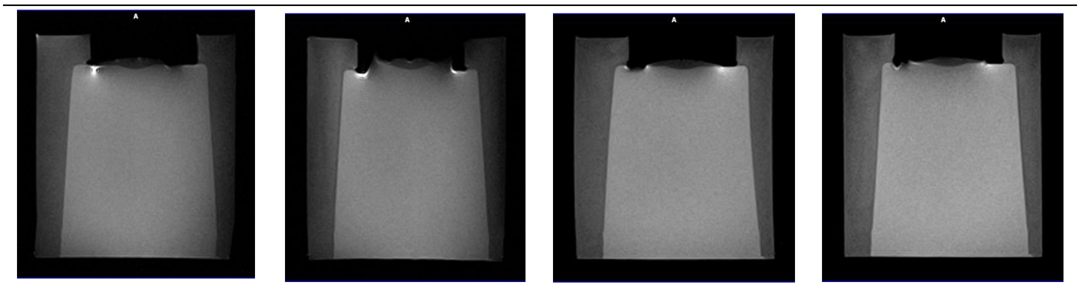

(c) PZ54 composite array

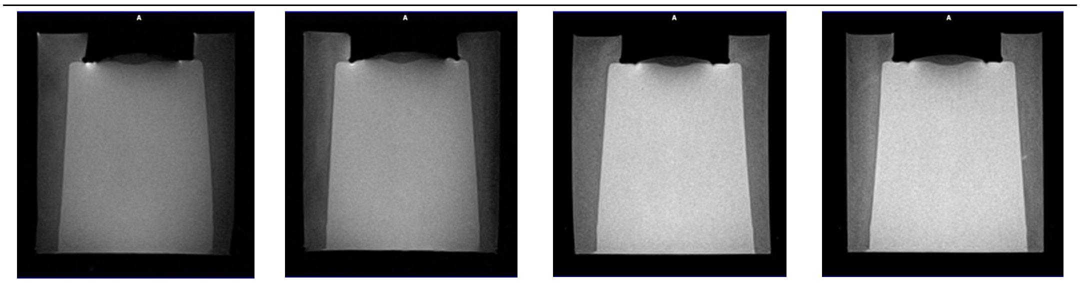

(d) PMN-PT composite array

Figure 6.20 MR images in Sagittal and Transversal plane, with four arrays positioned passively (a) PZ26 ceramic array (b) PZ26 composite array (c) PZ54 composite array (d) PMN-PT composite array

Artefacts were observed in all images for the passive arrays near the ground electrical connections. However no severe effects were observed in identifying the transducer location and shape, and no severe effects to the focal area within the phantom area of interest for FUS sonication, which is around 70 mm below phantom's top surface. In general, the scans in the sagittal plane show more artefacts than those in transversal plane; this might be effects of the cables and external connectors with solder and copper tracks. The variations across the four arrays were also observed, referring to the differences of fabrication between them. The biggest artefact was measured with the PZ54 composite array, with a distance of around 12 mm from the device boundary to the fringe of the artifact.

The artefacts may also be induced by the eddy current generation within the conductive silver electrodes coated on the surfaces of the piezoelectric elements. Figure 6.21 shows the MRI images of the PZ54 single element bowl transducer with phantom, following the same sequences as for the arrays. Having a relatively larger conducting area, the artifacts caused by the PZ54 single element bowl transducer were found more serious than those caused by the arrays.

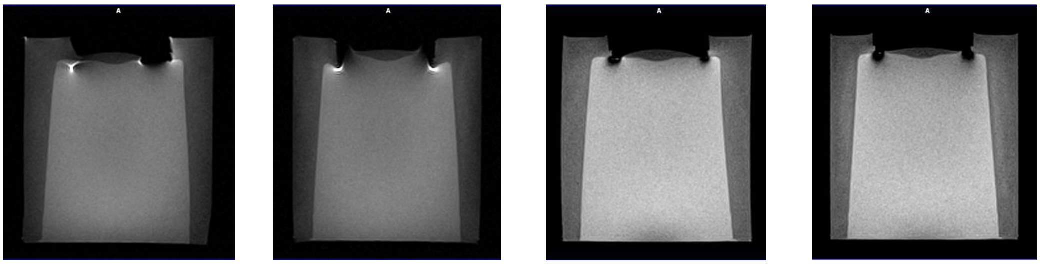

(a) (b) (c) (d)

Figure 6.21 MR images with phantom and PZ54 single element bowl transducer in plane and directions (a) Sagital AP (b) Sagital HF (c) Transversal AP (d) Transversal RL

6.4 Discussion and Conclusion

Chapter 6 has presented the implementation processes for four array transducers and their characterization results. Aiming to explore the practical issues associated with adoption of piezocrystal material for MRgFUS, a spherical-section, concave configuration of array was chosen, with faceted plates positioned geometrically in place to form the spherical structure.

Although this geometry of the array was not the best design for FUS application in clinics, such as the breast cancer treatment which was used as an exemplar in Chapter 2, it was chosen to be as similar as possible to that of the single element, spherical self-focusing bowl transducer made of PZ54 bowl shaped ceramic, so that the functional ability of the material could be evaluated by straightforward comparison.

Among the four array transducers, two were made with PZ54 ceramic and PMN-PT piezocrystal composites, these being of particular interest in this work for FUS application and following characterization in Chapter 5. The other two arrays were made with PZ26, a common high-power ceramic material, in bulk and composite forms, respectively. Discussions referring to the implementation and performance of the arrays are in Section 6.4.1, following by the overall conclusions of this chapter in Section 6.4.2.

6.4.1 Section Discussions

Composite fabrication

During the fabrication practices, the composite fabrication was the most time consuming and troublesome individual process. For ceramic composites fabricated in this work, especially for PZ54 ceramic composites, diced samples filled with epoxy were observed to bend during the curing process. This led to uneven, and unleveled surfaces on both sides of the composite samples, and thereby the consequent difficulties in lapping process for thickness control.

In practice, the PZ54 –Epofix epoxy composite with a VF = 60% was predicated to be around 1.8 mm thick, for a resonance frequency f_e = 1 MHz. Considering that the PZ54 piezoceramic samples available for the present work had a thickness of 1.95 mm, and the dicing depth should be bigger than the desired thickness, the dicing depth for PZ54 composites was chosen to be 1.85 mm. This left only 100 µm un-cut stock material. One possibility to explain the composite bending is such a thin substrate is too weak to hold the matrix of diced pillars when the height of the pillars is taken into account. The huge difference between pillar height and substrate thickness will cause an uneven distribution of internal stress, leading to bending of the whole sample during epoxy curing.

To this end, a modification was suggested to the process of making composites, represented in Appendix B-2. Compared to the normal process, two extra steps were added at the beginning. The bulk sample was placed in the PTFE mould first and embedded in Epofix epoxy polymer substrate, Step (a). After the epoxy was completely cured, the sample was released from the mould to undergo a lapping process to flatten its surface, Step (b). The flattened surface was used to bond samples for composite dicing, in which case the blade cut through the full sample thickness into the epoxy, with the pillars still attached to the epoxy substrate. The remaining processing steps were then the same as the normal process.

Although requiring more time and effort, the modified process reduced the bending issue quite significantly. This process was developed and tried after the composites used in the arrays had been prepared, however, the trials carried out showed it can benefit future fabrications under similar circumstances, and has practical implications related to the high price of piezocrystals because it minimizes the material lost during fabrication.

Triangular Elements

The 24 triangular elements for a single array transducer were obtained by gluing square plates in line and then dicing out triangular pieces. Considering the variations in lapped thicknesses and resonances of composite plates, it was predicted that, for those triangular plates consisting of two pieces from different square plates, the resonances might be out of phase. The ideal alternative is to order pre-cut triangular bulk piezoelectric plates, or even composite plates from the material supplier directly. However, the non-regular shape, neither square nor circular, would result in a significant amount of extra cost. Based on the quotes obtained in this work for PMN-29%PT piezocrystal, the cost of 15 square plates was around £1,600 whilst 24 triangular plates would have cost around £4,000. Taking the more economic option, square plates were ordered for this project, noting that the defocusing effects caused by imperfections in the arrays can be removed by applying phase correction to individual channels / elements.

Array performance

As described previously, the geometry of the geodesic faceted array was chosen in comparison of the single element, self-focusing PZ54 bowl transducer. Figure 6.22 is the normalized acoustic intensity field of the self-focusing PZ54 bowl transducer, in the axial direction; the -3dB focal area was 1.74 mm in diameter and 14.5 mm in length along the beam axis. Using Equations 3.9 and 3.10, the focusing gain of the perfect bowl shaped transducer was calculated to be G = 28.6. In comparison, residual phase aberrations were observed with the geodesic faceted arrays, especially with the ones made of pizeo-polymer composites. The defocusing was the combined result of the non-uniformity across samples, imperfect impedance matching, and residual mechanical errors in the device. By applying a hydrophone-based phase aberration correction, a high quality focus can be achieved, with the focusing gain also approaching 30. However, the intensity ratio of the main beam and secondary lobes of the geodesic faceted array was lower than that of the self-focusing bowl transducer. This might be improved with an increased number of electronic channels, by adding more 32T electronic modules to the current driving system.

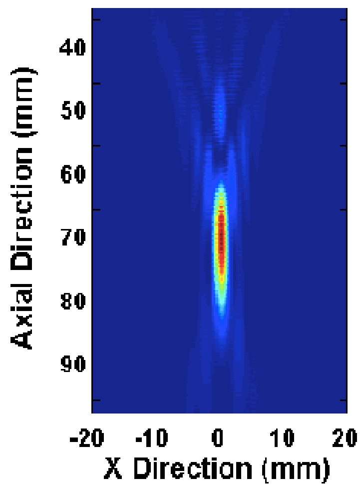

Figure 6.22 Normalized Intensity field of PZ54 single element bowl transducer in X-Y plane.

For the steering experiment presented with the PMN-PT array, the off-axis steering distance was limited to 2.5 mm. This corresponded to the result generated by the PZ26 composite array from the same experimental setup, not presented in this thesis because of its similarity. The small aperture, limited individual channels, and the 2D segmented annular element configuration are believed to have contributed to this result. In other words, for faceted arrays in which the apertures remain the same, the steering range can be increased by increasing the access to individual controllable channels, and / or using different channel configurations.

The arrays were generally characterized under low power conditions in the work presented here. Three issues hindered high power testing. First was the lack of bias field capability in the electronics drive system that the piezocrystal array would have required to maintain its high performance. This can be solved alternatively by simply using Generation II or III piezocrystals. The second issue was the unmatched electrical impedance for individual elements or the 32 driven channels, which not only increased the risk of damaging the device and instruments, but also affected the energy transmission efficiency. Although it could theoretically be done in the laboratory, the temporary 32-channel configuration and thereby the temporary impedances of each channel made the impedance matching work beyond the scope of this project. The final issue is that the FI toolbox system was designed originally for NDT applications where short pulse and high voltage are applied. The specific 32T module used in the present work was modified for FUS application to allow CW generation instead of short pulses but the maximum power and heat dissipation of MAX4940high voltage pulser still requires more investigation to optimise the power output of the driving electronics.

The passive MRI compatibility of the faceted arrays was encouraging. However it is important to emphasize that the experiments that have been reported here are only preliminary and that the current MRI settings can be improved a lot to increase the image quality.

6.4.2 Chapter Conclusions

In order to introduce piezocrystals into the application of focused ultrasound surgery, a spherical-sectioned, faceted array configuration was designed and fabricated in this work. Inspired by the geodesic dome structure, the array configuration has 24 triangular pieces arranged geometrically in space to form the spherical structure. By sub-dicing each triangular piece into four smaller elements, the number of the potential individual elements of the array had increased up to 96. In this work reported here, the piezocrystal array was driven by a modular 32-channel FI Toolbox instrumentation system (Diagnostic Sonar Ltd, Livingston, UK), based on a standard PXI chassis (National Instruments, Newbury, UK). As these had only 32 channels, the array elements were interconnected in groups of three. The array showed satisfactory field patterns, with some need for phase correction of residential aberrations. A 10 x 5 mm^2 volume beyond the array's natural focus was sonicated by shifting the focus and the acoustic intensity maps showed focused field patterns with sidelobes levels below -9 dB. Although further investigation is required, the results show that a valuable prototyping route for connecting FUS devices and modular electronics and that good focusing can be achieved with the geodesic array geometry. Additional work is also required to refine the electrode connection procedure, as a few connections deteriorated during testing of the arrays. Even though, the current results are encouraging.

For comparison purpose, besides the piezocrystal geodesic faceted array, three others were fabricated with different materials, PZ26 ceramic, PZ26 composite and PZ54 composite. From preliminary results, piezocrystal PMN-PT composite can offer excellent performance compared with conventional ceramic material currently used in FUS devices. Compared to PZ26 ceramic, PMN-PT composite material doubles the acoustic power output, triples the working bandwidth and reduces the electrical impedance magnitude to one-third of that PZ26 ceramic. With future full commercialization of the Generation II ternary and Generation III doped ternary piezocrystals, piezocrystal could be a potential material of choice for FUS application, offering higher transmission efficiency, broader frequency resonance bandwidth, and ease of impedance matching.

CHAPTER 7 CONCLUSIONS AND FUTURE WORK

7.1 Conclusions

The purpose of the work reported here was to explore the development of ultrasound transducers for MRI guided focused ultrasound surgery (MRgFUS), especially in terms of the potential to use new piezocrystal materials in their construction. A review of the literature showed that the new family of piezocrystals based on lead magnesium niobate doped with lead titanate, $(x)Pb(Mg_{1/3}Nb_{2/3})O_3-(1-x)PbTiO_3$ (PMN-PT) should provide enhanced performance with higher electromechanical coupling coefficients, broader bandwidth and greater sensitivity. The investigation that followed therefore aimed to address the feasibility and practical issues related to the adoption of these piezocrystal materials for FUS applications. Owing to the limited availability of Generation II and III ternary materials, this was addressed mainly with Generation I piezocrystal PMN-29%PT material.

It was noted that there was a relative lack of published material concerning the properties of piezocrystals and the variation in their behavior from sample to sample. Therefore the work started with piezocrystal characterization, along with comparison with a new ceramic material, PZ54 (Meggitt-Ferroperm, Kvistgaard, Denmark), specifically designed for FUS. Characterization was carried out under both ambient conditions and with elevated temperature and pressure. As results, full elasto-electric matrices were obtained under ambient conditions and the variation of piezoelectric properties with changing temperature and pressure were obtained using an appropriate experimental measurement system.

To extend the use of piezocrystal into the FUS application, a faceted spherical-section structure was then adapted from the geodesic dome in architecture to be used for ultrasound arrays. Four arrays of this design configuration were implemented with 96 triangular elements, using PZ26 bulk ceramic material; 1 – 3 ceramic-polymer composites made with PZ26 and PZ54; and 1 – 3 piezocrystal-polymer composite, made with PMN-29%PT. Tests with these four array transducers not only demonstrated the proof of the concept of the geodesic configuration, but also provided further comparison between piezoceramic and piezocrystal within FUS devices. The feasibility of connecting the arrays to commercial modular electronics was also investigated successfully.

More detailed conclusions relating to the various specific parts of the work are provided in Sections 7.1.1 and 7.1.2.

7.1.1 Piezoelectric Material Characterization

Piezoelectric material characterization was presented in Chapters 4 and 5, covering methods and results, respectively. Based on the IEEE standard on piezoelectricity and the aid of a commercial software package (PRAP, TASI Technical Software, Kingston, Canada), a test procedure was established to obtain full elasto-electric matrices of both *6mm*-symmetry piezoceramic and *4mm* piezocrystal. PZ54 ceramic and PMN-29%PT piezocrystal materials were fully tested in this work, under ambient temperature and pressure as basic characterization and then at elevated temperature and pressure as application-oriented characterization, with specific reference to FUS.

The full elasto-electric matrices obtained from basic characterization either completed or expanded the literature, therefore benefitting ultrasound researchers working on device design and performance modelling. The accuracy of the matrices was evaluated by comparison with published data, and by comparing modelled electrical impedance spectra with measurements. The properties of both the PZ54 ceramic and PMN-29%PT piezocrystal are generally in good agreement with properties reported by commercial suppliers.

The two materials were then explored under elevated temperature and pressure, with temperature in the range of $0 \le T \le 120\ ^{o}\mathrm{C}$ and pressure $0 \le P \le 5$ MPa for PZ54 ceramic, and temperature $0 \le T \le 130\ ^{o}\mathrm{C}$ and pressure $0 \le P \le 20$ MPa for PMN-29%PT piezocrystal. PMN-PT was also characterised with externally applied electrical bias fields in the range 0 – 2 kV/cm.

The experimental measurement system assembled to apply those conditions was configured with commercial equipment and only very limited custom-made jigs and fixtures, electrical circuitry, and calculation software. The results generated from this setup align with the literature, with PZ54 ceramic behaving more stably over varying conditions and PMN-PT piezocrystal suitable for use only within a limited operating envelope. The phase-transition temperature of PMN-PT pizeocrystal material was confirmed in this work to be around 80 - 90 ^{o}C. However, the limitation of temperature tolerance during fabrication is recommended to be within a maximum of 60^{o}C. The pressure limitation was found to be around 10 - 12 MPa before evidence emerged of a phase transition. The presence of DC bias field will also be required with Generation I piezocrystal materials for FUS transducers.

7.1.2 Geodesic Faceted Array Transducer

As far as piezocrystal material was investigated as a material of choice, a specific array configuration was designed to explore its adoption in a FUS device. In order to be able to move the focus over a range of interest relatively few elements and small time delays at this experimental stage, a concave geometry with a geometric focal point was chosen. However, the natural orientation of the crystal and its temperature limitation overruled the possibility either to curve the piezocrystal or thermoform concave composite. Instead, a faceted, spherical-section structure was devised, inspired by the geodesic design in architecture. This had 24 flat triangular plates positioned geometrically in place. Each of these plates was then further sub-divided into four smaller triangular elements to increase the total number of individual elements to 96 without increasing the fabrication difficulty that comes with placing elements in position. The final structure was approximately a hexagon in cross-section, with an aperture of approximately 62 mm. The geodesic faceted structure was designed to create a self-focusing structure for using piezocrystals, similar to the perfect spherical-sectioned bowl. The ideal array configuration for treating breast cancer is presently considered to have a cylinder ring shape and surround the breast, such as in the system developed by Philips, Figure 2.8(b). However, other researchers are using configurations first developed for applications in uterine fibroids, with devices resembling the arrays developed in this work. Although not the best clinical configuration for FUS targeting breast cancer, the multi-element phased arrays are thus considered as viable to carry out preliminary research in a laboratory environment and certainly to demonstrate parameters such as appropriate choice of materials.

Implementation of the faceted arrays was a challenge due to the curved 3-D structure. The fabrication process was explored with the aid of a specifically prototyped fabrication mould. Custom interconnection stands were designed and prepared to build the electrical connections in groups. With four prototypes implemented, the focal lengths were determined by acoustic field mapping and varied from 69.275 mm to 76.275 mm. As a proof of concept, the geometric focal gain this faceted structure was able to achieve G = 14.8, according to the acoustic field mapping of PZ26 ceramic array, With optimized phase control through external multi-channel electronics, focal gain was then improved to 29.9, based on the acoustic field result of PMN-PT composite array.

The connection of the arrays to FIToolbox driving electronics (Diagnostic Sonar Ltd., Livingston, UK) illustrated the feasibility to connect experimental ultrasound devices with this type of commercial driving system. Based on the existing FlexRIO's FPGA-based hardware (National Instruments, Berks, UK), the DSL32T transmission module was modified to provide high power, continuous driven conditions and offered a valuable prototyping route for FUS devices. Due to the availability of a maximum of 32 individual channels in the driving system, the array elements were re-configured into 32 channels with groups of three adjacent elements connected together. The focus of the array was then moved by applying phase delays to each channel. Results from the piezocrystal array showed its focus could be moved within a lateral ±2.5 mm and axial ±5 mm volume beyond the geometric focal point. Side lobes were limited to below the level of -9 dB in acoustic intensity.

To evaluate the potential to integrate these experimental devices with MRI guidance, the arrays were tested within a Siemens 3T MRI scanner. At the current stage, only passive compatibility of the four arrays was tested, guided by ASTM standard F2119. Three orientations were scanned, with each orientation having two sets of images, using both readout and phase-encode directions. Although image artefacts caused by the arrays were found, the boundaries of the array were clear enough so that the position of the array and the interface between array surface and phantom or tissue could be easily defined, providing a positive conclusion to the question of compatibility.

Most importantly, the performance of the piezoelectric materials was compared between the array elements. As expected, piezocrystal material PMN-PT performs better then piezoceramic in terms of efficiency and operating bandwidth, even when compared with PZ54 ceramic, specifically optimised for FUS. Shown in Figure 6.17, the acoustic outputs of these two materials were measured over a range of frequencies, under the same drive conditions.

At their resonance frequencies, the acoustic output of the piezocrystal is 25% more than that of PZ54 ceramic; similarly, the bandwidth is doubled. However, these advantages were not preserved with increased driving power. The inflection point was found when the acoustic surface intensity reached $3W/cm^2$, after which self-heating weakened and destabilize the performance of the piezocrystal. Therefore Generation II ternary and Generation III doped ternary piezocrystals, with higher temperature tolerance, are recommended by the author for future high power applications.

7.2 Future Work

The work presented in this thesis was a first-stage investigation into development of MRgFUS ultrasound devices based on the use of piezocrystal material. The various aspects of work involved for this purpose, such as the system setup development for characterizing piezoelectric materials, and the potential applications of the developed devices, open up the possibility of various future works.

7.2.1 Further Developments of the Characterization System

The measurement systems of the type outlined in this work were operated manually, which is time and labour consuming. Future development lies in system automation and optimization. The LabVIEW programming language is an attractive option to provide overall control of all components and operations such as acquiring data from impedance analyser and adjusting and monitoring external environmental conditions.

Due to the 1000 N maximum compressive load that the system could provide, the maximum pressure that could be applied to material samples was limited. This led to the need for extra machining of the test samples in the cases where higher pressure effects were required for investigation, such as for underwater sonar, and ultrasound-actuated surgical devices. Extra machining is highly undesirable as it can cause changes in the test samples. To avoid this, an updated system is being set up in Dundee, with increased loading capability up to 10 kN. The new system is part of the ESPRC funded project: Ultrasonic needles based on Mn-doped ternary piezocrystal (EP/K020013/1), between University of Glasgow, University of Dundee, Ethicon-Endo Surgery and Weidlinger Associates Inc, in which 60 MPa pressure conditions are desired to study the performance of materials and devices.

One practical issue that must be recognized is that the work reported here was carried out under externally-imposed environmental conditions instead of self-induced conditions. However, particularly in temperature, self-heating under high power is of more importance. With no direct method to isolate the impedance analyzer and the high power AC driving signal, an innovative setup is required to allow material characterization under high power operation. An investigation based on the current setup has started, using the voltage-and-current method to calculate electrical impedance of the sample under swept frequencies. The combination of measurements of electrical impedance and surface displacement was investigated as well, by integrating a laser vibrometer to this system. A thermal camera was also included in the new system to allow the uniformity of heating of the sample to be determined.

7.2.2 Future Work for Characterization of Piezoelectric Materials

The work reported here emphasized TE plates and corresponding available properties but further work is required particularly to obtain the full elasto-electric matrices and appropriate attenuation parameters under varying conditions. A full sample set of piezoelectric materials could be tested using the system built here, with a special fixture designed especially for LE bars. This will significantly benefit ultrasonic researchers evaluating the performance of devices under practical conditions by allowing them to import the relevant material properties under such conditions into models.

It was noticed during the work that the variation in the properties of nominally identical IEEE samples under ambient conditions was significant. Poor uniformity across material samples between manufactures and batches, especially for piezocrystal, hugely affect the accuracy and self-consistency of the full matrix obtained. The IEEE characterization methods require multiple samples to isolate resonance modes, which are, in the case of *4mm* piezocrystals, five geometries for six resonance modes, to complete the full matrix measurements. To minimise the variation and inaccuracy induced by multiple testing samples, the IEEE Working Group P1859 on Relaxor-based Single Crystals is now working on a new Standard for Relaxor Based Single Crystals for Transducer and Actuator Applications, in which investigation has been carried out to reduce the number of samples, leading to one or more new geometries allowing multiple resonances to be measured with one sample.

7.2.3 Future Material of Choice

Although Generation II and III ternary piezocrystal material were not available for this project to start full characterization and device development, small quantities were tested under atmospheric and/or elevated temperature and pressure for related work, in cooperation with Thales UK (Thales Underwater Systems Ltd, Somerset, UK). Further work should be carried out and follow the path blazed in this work, from basic to application-oriented characterization. The initial full matrix results of Generation II PIN-PMN-PT ternary material were presented in Section 5.1, Table 5.3, but these will rely on the availability of specific geometries from the material supplier to complete the work.

Preliminary tests were carried out with ternary samples with elevated temperature, and the phase transition temperature and de-poling temperatures have increased to 108^{o}C and

140°C, respectively. These measurements are in good agreement with data from commercial supplier and provide added evidence of the improvements that may be expected from Generation II and III piezocrystals. With the increased coercive field, E_C, and phase transition temperatures up to more than 100°C, the possibility to use thermoformed concave composite in FUS device can be brought into practice, and the risks of de-poling caused by self-heating can be reduced as well. In addition, the increased mechanical quality factor, Q_M, and E_C will allow Generation II and III materials, especially the doped ternary piezocrystal, to overcome the limitations of Generation I crystal, and to be more suitable material of choice for FUS and other high power applications.

7.2.4 Recommended Future Applications for Geodesic Array

The focusing and steering abilities of the geodesic arrays were tested in this work as preliminary characterization. Due to the time scale and instruments available, and the focus on the effects of the piezoelectric materials, various aspects of work could not be done within the scope of the present project and have to be listed below as future work.

High Power FUS Sonication

As FUS devices, the arrays will be driven under high power conditions in order to produce ultrasound sonication. However, there are two main issues restricting such sonication experiments: impedance mismatching between drive electronics and array elements; and limitation of maximum power dissipation of the driving electronics under continuous mode operation, as detailed in Chapter 6. This is going to lead to a six-month industrial secondment of the author at Diagnostic Sonar Ltd (Livingston, UK). During the secondment, the author will focus technically on high power operation with unusual electrical loads. One potential outcome is to deliver enough power into the arrays fabricated in this work, to ablate either TMM phantom or tissue samples thermally.

Positive MRI compatibility

Positive MRI compatibility of the arrays, in which case they are driven by external electronics within the MRI scanner, will be sensible to carry on only if the high power drive conditions can be accomplished. The requisite test procedure has already been put into practice with the single element, self-focusing PZ54 ceramic bowl transducer. Although the testing results were not presented in this thesis, the testing methods have been confirmed with both 1.5T GE HDx MRI integrated with the ExAblate 2100 conformal bone system (InSightec Ltd, Haifa, Israel); and the 3T Siemens Trio MRI systems following by post-proton resonance frequency (PRF) calculation. With the arrays positioned within the MRI scanner and driving electronics within the control room, the MRI artefacts when ultrasound is OFF and when ultrasound is ON, and the temperature increase within the area of interest should be measured to complete MRI compatibility testing of the FUS device.

Other Applications

With the array's focusing and steering abilities, one possible application of the geodesic array is a simple version of the sonic screwdriver (Demore et al. 2011). The array transducer can be positioned at the bottom of a sealed, custom-made chamber, filled with water, with the water level matching the focal plane of the array. By controlling and moving the focus in a circular path, radiation force generated by the ultrasound therefore can rotate the floating object on water surface. Ultrasound-mediated targeted drug delivery (UmTDD) is another possible application for the arrays where the energy requirement is relatively low.

All these experiments could be improved by adding the phase correction function into the controlling software, which will automatically overcome the phase aberration and improve the focusing ability.

REFERENCES

Ferroperm Full Data Matrix [online]. Avaliable: http://www.ferroperm-piezo.com, Ferroperm Piezoceramic A/F. Accessed on Aug, 2012.

PZFlex User Manual, WEIDLINGER ASSOCIATES® INC http://www.pzflex.com.

Al-Bataineh, O., Jenne, J., et al. (2012). "Clinical and future applications of high intensity focused ultrasound in cancer." Cancer Treat Rev **38**(5): 346-353.

Auboiroux, V., Dumont, E., et al. (2011). "An MR-compliant phased-array HIFU transducer with augmented steering range, dedicated to abdominal thermotherapy." Physics in Medicine and Biology **56**(12): 3563-3582.

Auld, B. A. (1981). "Wave propagation and resonance in piezoelectric materials." J. Acoust. Soc. Am. **70**(6): 1577-1585.

Bacon, D. R. (1984). "Finite amplitude distortion of the pulsed fields used in diagnostic ultrasound." Ultrasound in Medicine & Biology **10**(2): 189-195.

Baker, K. G., Robertson, V. J., et al. (2001). "A Review of Therapeutic Ultrasound: Biophysical Effects." Physical Therapy **81**(7): 1351-1358.

Bakker, J. F. and et al. (2009). "An ultrasound cylindrical phased array for deep heating in the breast: theoretical design using heterogeneous models." Physics in Medicine and Biology **54**(10): 3201.

Berg, W. A., Gutierrez, L., et al. (2004). "Diagnostic accuracy of mammography, clinical examination, US, and MR imaging in preoperative assessment of breast cancer." Radiology **233**(3): 830-849.

Bogdanov, S. V. (2000). "Acoustical method for the determination of the elastic and piezoelectric constants of crystals of classes 6mm and 4mm." Acoustical Physics **46**(5): 530-533.

Brosch, J., Morris, G. A., et al. (2001). Design and testing of an MRI compatible therapeutic transducer. Ultrasonics Symposium, 2001 IEEE.

Changgeng, L., Djuth, F. T., et al. (2013). "Micromachining techniques in developing high-frequency piezoelectric composite ultrasonic array transducers." Ultrasonics, Ferroelectrics and Frequency Control, IEEE Transactions on **60**(12): 2615-2625.

Chen, J. and Panda, R. (2005). Review: commercialization of piezoelectric single crystals for medical imaging applications. Ultrasonics Symposium, 2005 IEEE.

Chen, L., Rivens, I., et al. (1993). "Histological changes in rat liver tumours treated with high-intensity focused ultrasound." Ultrasound in Medicine & Biology **19**(1): 67-74.

Cheng Shiao, H. and et al. (2007). "Thermal therapy for breast tumors by using a cylindrical ultrasound phased array with multifocus pattern scanning: a preliminary numerical study." Physics in Medicine and Biology **52**(15): 4585.

Clifford, M. A., Banovac, F., et al. (2002). "Assessment of hepatic motion secondary to respiration for computer assisted interventions." Computer aided surgery : official journal of the International Society for Computer Aided Surgery **7**(5): 291-299.

Cobbold, R. S. C. (2007). Foundations of Biomedical Ultrasound. New York, Oxford University Press, Inc.

Damianou, C. and Hynynen, K. (1993). "Focal spacing and near-field heating during pulsed high temperature ultrasound therapy." Ultrasound Med Biol **19**(9): 777-787.

Daum, D. R. and Hynynen, K. (1999). "A 256-element ultrasonic phased array system for the treatment of large volumes of deep seated tissue." Ultrasonics, Ferroelectrics and Frequency Control, IEEE Transactions on **46**(5): 1254-1268.

Demore, C., Zhengyi, Y., et al. (2011). A sonic screwdriver: Acoustic angular momentum transfer for ultrasonic manipulation. Ultrasonics Symposium (IUS), 2011 IEEE International.

Do-Huu, J. P. and Hartemann, P. (1981). Annular Array Transducer for Deep Acoustic Hyperthermia. 1981 Ultrasonics Symposium.

Ebbini, E. S. and Cain, C. A. (1991). "A spherical-section ultrasound phased array applicator for deep localized hyperthermia." Biomedical Engineering, IEEE Transactions on **38**(7): 634-643.

Ellis, S., Rieke, V., et al. (2013). "Clinical applications for magnetic resonance guided high intensity focused ultrasound (MRgHIFU): present and future." J Med Imaging Radiat Oncol **57**(4): 391-399.

Fay, B., Rinker, M., et al. (1994). "Thermoacoustic sensor for ultrasound power measurements and ultrasonic equipment calibration." Ultrasound Med Biol **20**(4): 367-373.

Feng, Z., Zhao, X., et al. (2006). "Effect of poling field and temperature on dielectric and piezoelectric property of 〈001〉-oriented $0.70Pb(Mg_{1/3}Nb_{2/3})O_3$–$0.30PbTiO_3$ crystals." Materials Research Bulletin **41**(6): 1133-1137.

Ferenc A. Jolesz and Hynynen, K. H. (2007). MRI-Guided Focused Ultrasound Surgery. New York, USA, Informa Healthcare.

Fisher, B., Anderson, S., et al. (2002). "Twenty-Year Follow-up of a Randomized Trial Comparing Total Mastectomy, Lumpectomy, and Lumpectomy plus Irradiation for the Treatment of Invasive Breast Cancer." New England Journal of Medicine **347**(16): 1233-1241.

Fjield, T. and Hynynen, K. (1997). "The combined concentric-ring and sector-vortex phased array for MRI guided ultrasound surgery." Ultrasonics, Ferroelectrics and Frequency Control, IEEE Transactions on **44**(5): 1157-1167.

Fry, W. J., Fry, F. J., et al. (1955). "Ultrasonic Lesions in Mammalian Central Nervous System." Science **122**(3179): 1091.

Furusawa, H., Namba, K., et al. (2006). "Magnetic Resonance–Guided Focused Ultrasound Surgery of Breast Cancer: Reliability and Effectiveness." Journal of the American College of Surgeons **203**(1): 54-63.

Gao, J. (2011). Transcostal focused ultrasound surgery: treatment through the ribcage.

Gavrilov, L. R. and Hand, J. W. (2000). "A theoretical assessment of the relative performance of spherical phased arrays for ultrasound surgery." IEEE Trans Ultrason Ferroelectr Freq Control **47**(1): 125-139.

Gélat, P., Haar, G. t., et al. (2012). "The optimization of acoustic fields for ablative therapies of tumours in the upper abdomen." Physics in Medicine and Biology **57**(24): 8471.

Gianfelice, D., Khiat, A., et al. (2003). "MR Imaging–guided Focused US Ablation of Breast Cancer: Histopathologic Assessment of Effectiveness—Initial Experience1." Radiology **227**(3): 849-855.

Gin-Shin, C., Hsu, C., et al. (2008). Development of 1.5D cylindrical HIFU phased array. Ultrasonics Symposium, 2008. IUS 2008. IEEE.

Grewe, M. G., Gururaja, T. R., et al. (1990). "Acoustic properties of particle/polymer composites for ultrasonic transducer backing applications." IEEE Trans Ultrason Ferroelectr Freq Control **37**(6): 506-514.

Hand, J. W., Shaw, A., et al. (2009). "A random phased array device for delivery of high intensity focused ultrasound." Physics in Medicine and Biology **54**(19): 5675.

Hand, J. W., Shaw, A., et al. (2009). "A random phased array device for delivery of high intensity focused ultrasound." Phys Med Biol **54**(19): 5675-5693.

Hata, T., Takahashi, H., et al. (2004). "Magnetic resonance imaging for preoperative evaluation of breast cancer: a comparative study with mammography and ultrasonography." J Am Coll Surg **198**(2): 190-197.

Hayward, G. and Hyslop, J. (2006). "Determination of lamb wave dispersion data in lossy anisotropic plates using time domain finite element analysis. Part II: application to 2-2 and 1-3 piezoelectric composite transducer arrays." IEEE Trans Ultrason Ferroelectr Freq Control **53**(2): 449-455.

He, R. Z., Shou, W. D., et al. (2005). Dual-frequency High Intensity Focused Ultrasound (HIFU) Accelerating Therapy. 27th Annual International Conference of the Engineering in Medicine and Biology Society, 2005. IEEE-EMBS 2005.

Hill, C. R. (1970). "Calibration of ultrasonic beams for bio-medical applications." Phys Med Biol **15**(2): 241-248.

Hokland, S. L., Pedersen, M., et al. (2006). "MRI-guided focused ultrasound: methodology and applications." Medical Imaging, IEEE Transactions on **25**(6): 723-731.

Hossack, J. A. and Hayward, G. (1991). "Finite-element analysis of 1-3 composite transducers." Ultrasonics, Ferroelectrics and Frequency Control, IEEE Transactions on **38**(6): 618-629.

Huber, P. E., Jenne, J. W., et al. (2001). "A New Noninvasive Approach in Breast Cancer Therapy Using Magnetic Resonance Imaging-guided Focused Ultrasound Surgery." Cancer Research **61**(23): 8441-8447.

Hynynen, K., Chung, A., et al. (1996). "Feasibility of using ultrasound phased arrays for MRI monitored noninvasive surgery." Ultrasonics, Ferroelectrics and Frequency Control, IEEE Transactions on **43**(6): 1043-1053.

Hynynen, K., Pomeroy, O., et al. (2001). "MR Imaging-guided Focused Ultrasound Surgery of Fibroadenomas in the Breast: A Feasibility Study1." Radiology **219**(1): 176-185.

Hynynen, K. H. (2008). Fundamental principles of therapeutic ultrasound, MRI-Guided Focused Ultrasound Surgery. MRI-Guided Focused Ultrasound Surgery. F. A. Jolesz and K. H. Hynynen. New York, USA, Informa Healthcare USA, Inc.**:** 15-18.

Illing. RO, Kennedy. JE, et al. (2005). "The safety and feasibility of extracorporeal high-intensity focused ultrasound (HIFU) for the treatment of liver and kidney tumours in a Western population." Br J Cancer. **93**(8): 890－895.

Jaffe, B., Cook, W. R., et al. (1971). Piezoelectric ceramics. London and New York, Academic Press.

Jaffe, B., Roth, R. S., et al. (1954). "Piezoelectric Properties of Lead Zirconate-Lead Titanate Solid-Solution Ceramics." Journal of Applied Physics **25**(6): 809-810.

Jaffe, H. and Berlincourt, D. A. (1965). "Piezoelectric transducer materials." Proceedings of the IEEE **53**(10): 1372-1386.

Jemal, A., Bray, F., et al. (2011). "Global cancer statistics." CA: A Cancer Journal for Clinicians **61**(2): 69-90.

Jeong, J. S., Cannata, J. M., et al. (2010). "Dual-Focus Therapeutic Ultrasound Transducer for Production of Broad Tissue Lesions." Ultrasound in Medicine & Biology **36**(11): 1836-1848.

Jiang, W., Zhang, R., et al. (2003). "Characterization of piezoelectric materials with large piezoelectric and electromechanical coupling coefficients." Ultrasonics **41**(2): 55-63.

Jiang, X., Snook, K., et al. (2008). Micromachined PMN-PT single crystal composite transducers-15-75 MHz PC-MUT. Ultrasonics Symposium, 2008. IUS 2008. IEEE.

Junho, S. and Hynynen, K. (2009). Comparison of acoustic power calibration methods for therapeutic ultrasound transducers using PVDF membrane hydrophone, heterodyne laser vibrometery and radiation force measurements. Ultrasonics Symposium (IUS), 2009 IEEE International.

Junho, S. and Hynynen, K. (2010). "Feasibility of Using Lateral Mode Coupling Method for a Large Scale Ultrasound Phased Array for Noninvasive Transcranial Therapy." Biomedical Engineering, IEEE Transactions on **57**(1): 124-133.

Kennedy, J. E. (2005). "High-intensity focused ultrasound in the treatment of solid tumours." Nature Review Cancer **5**(4): 321-327.

Kennedy, J. E., ter Haar, G. R., et al. (2003). "High intensity focused ultrasound: surgery of the future?" British Journal of Radiology **76**(909): 590-599.

Kim, K., Zhang, S., et al. (2012). "Surface acoustic load sensing using a face-shear PIN-PMN-PT single-crystal resonator." IEEE Trans Ultrason Ferroelectr Freq Control **59**(11): 2548-2554.

Kin Wing, K., Chan, H. L.-W., et al. (1997). "Evaluation of the material parameters of piezoelectric materials by various methods." Ultrasonics, Ferroelectrics and Frequency Control, IEEE Transactions on **44**(4): 733-742.

Kino, G. S. (1987). Acoustic waves: Devices, imaging, and analog signal processing. Englewood Cliffs, New Jersey, Prentice-Hall

Kinsler, L. E., Frey, A. R., et al. (2000, p438-439). Fundamentals of Acoustics. New Jersey, USA, John Wiley and Sons Inc.

Krimholtz, R., Leedom, D. A., et al. (1970). "New equivalent circuits for elementary piezoelectric transducers." Electron. Lett. **6**(13): 398-399.

Li, X., Wu, W., et al. (2011). "80-MHz intravascular ultrasound transducer using PMN-PT free-standing film." IEEE Trans Ultrason Ferroelectr Freq Control **58**(11): 2281-2288.

Low, J. and Reed, A. (1994). Electrotherapy Explained: Principles and Practice. Oxford, England, Butterworth Heinemann**:** p159.

Lu, J. Y., Zou, H., et al. (1994). "Biomedical ultrasound beam forming." Ultrasound Med Biol **20**(5): 403-428.

Luo, J., Hackenberger, W., et al. (2008). Elastic, piezoelectric and dielectric properties of PIN-PMN-PT crystals grown by Bridgman method. Ultrasonics Symposium, 2008. IUS 2008. IEEE.

Luo, J., Hackenberger, W., et al. (2010). A high Qm relaxor ferroelectric single crystal: Growth and characterization. Ultrasonics Symposium (IUS), 2010 IEEE.

Lynn, J. G. and Putnam, T. J. (1944). "Histology of Cerebral Lesions Pro- duced by Focused Ultrasound." The American Journal of Pathology **20**: 637-649.

M von Siebenthal, G Székely, et al. (2007). "4D MR imaging of respiratory organ motion and its variability." Physics in Medicine and Biology **52**(6): 1547.

Madelin, G., Hosten, B., et al. (2005). "Comparison of laser interferometry and radiation force method of measuring ultrasonic power." Ultrasonics **43**(9): 769-774.

Marsac, L., Chauvet, D., et al. (2012). "MR-guided adaptive focusing of therapeutic ultrasound beams in the human head." Med Phys **39**(2): 1141-1149.

Mason, T. (1998). "A SOUND INVESTMENT." Chemistry and Industry **21**: 878-882.

McDannold, N. J., Vykhodtseva, N. I., et al. (2006). "Microbubble Contrast Agent with Focused Ultrasound to Create Brain Lesions at Low Power Levels: MR Imaging and Histologic Study in Rabbits1." Radiology **241**(1): 95-106.

McLaughlin, E. A., Liu, T., et al. (2005). "Relaxor ferroelectric PMN-32%PT crystals under stress, electric field and temperature loading: II-33-mode measurements." Acta Materialia **53**(14): 4001-4008

Melodelima, D., N'Djin, W. A., et al. (2007). Toric HIFU Transducer for Large Thermal Ablation. Engineering in Medicine and Biology Society, 2007. EMBS 2007. 29th Annual International Conference of the IEEE.

Melzer, A., Cochran, S., et al. (2012). "The importance of physics to progress in medical treatment." The Lancet **379**(9825): 1534-1543.

Merckel, L. G., Bartels, L. W., et al. (2013). "MR-guided high-intensity focused ultrasound ablation of breast cancer with a dedicated breast platform." Cardiovasc Intervent Radiol **36**(2): 292-301.

Mitragotri, S. (2005). "Healing sound: the use of ultrasound in drug delivery and other therapeutic applications." Nature Reviews Drug Discovery **4**(3): 255-260.

Mougenot, C., Köhler, M., et al. (2011). Large aperture transducer designed for MR-HIFU treatment of breast tumors. ISMRM: Interventional MRI: MR-Guided Focused Ultrasound, Montreal, Canada.

Mougenot, C., Salomir, R., et al. (2004). "Automatic spatial and temporal temperature control for MR-guided focused ultrasound using fast 3D MR thermometry and multispiral trajectory of the focal point." Magn Reson Med **52**(5): 1005-1015.

Nakahata, K. and Kono, N. (2012). 3-D Modelings of an Ultrasonic Phased Array Transducer and Its Radiation Properties in Solid. Ultrasound Waves. A. A. d. S. Júnior, InTech.

Newnham, R. E., Skinner, D. P., et al. (1978). "Connectivity and piezoelectric-pyroelectric composites." Materials Research Bulletin **13**(5): 525-536.

NYE, J. F. (1985). Physical Properties of Crystals: Their Representation by Tensors and Matrice. New York, Oxford University Press.

Oakley, C. G. and Zipparo, M. J. (2000). Single crystal piezoelectrics: a revolutionary development for transducers. Ultrasonics Symposium, 2000 IEEE.

Park, S.-E. and Shrout, T. R. (1997). "Ultrahigh strain and piezoelectric behavior in relaxor based ferroelectric single crystals." Journal of Applied Physics **82**(4): 1804-1811.

Patel, P. R., Luk, A., et al. (2008). "In vitro and in vivo evaluations of increased effective beam width for heat deposition using a split focus high intensity ultrasound (HIFU) transducer." International Journal of Hyperthermia **24**(7): 537-549.

Qiu, Z., Casey, G., et al. (2013). A Geodesic Array using Piezocrystal Composites For Focused Ultrasound Surgery Driven by Modular Multichannel Electronics. 2nd Focused Ultrasound Therapy Symposium, Rome.

Qiu, Z., Habeshaw, R., et al. (2012). New Piezocrystal Material in the Development of a 96-element Array Transducer for MR-guided Focused Ultrasound Surgery. 2012 International Society for Therapeutic Ultrasound Symposium.

Qiu, Z., Sadiq, M. R., et al. (2011a). Material characterization for medical applications under temperature and pressure conditions. Piezo 2011 Electroceramics for End-Users VI International conference, Sestriere, Italy.

Qiu, Z., Sadiq, M. R., et al. (2011b). "Characterization of piezocrystals for practical configurations with temperature- and pressure-dependent electrical impedance spectroscopy." Ultrasonics, Ferroelectrics and Frequency Control, IEEE Transactions on **58**(9): 1793-1803.

Raju, B. I., Hall, C. S., et al. (2011). "Ultrasound therapy transducers with space-filling non-periodic arrays." Ultrasonics, Ferroelectrics and Frequency Control, IEEE Transactions on **58**(5): 944-954.

Robertson, C. (2007). Hyperthermia with HIFU and Multimodal Examination of ex vivo Poultry Tissue. Bioengineering Unit. Glasgow, University of Strathclyde. **Master of Engineering**.

Roses, D. F. (1999). Breast Cancer. USA, Churchill Livingstone.

Sadiq, M. R., Qiu, Z., et al. (2011). Characterization of PMN-29%PT as a function of temperature and pressure. Ultrasonics Symposium (IUS), 2011 IEEE International.

Sapareto, S. A. and Dewey, W. C. (1984). "Thermal dose determination in cancer therapy." International Journal of Radiation Oncology*Biology*Physics **10**(6): 787-800.

Sapozhnikov, O. A., Pishchal'nikov, Y. A., et al. (2003). "Reconstruction of the normal velocity distribution on the surface of an ultrasonic transducer from the acoustic pressure measured on a reference surface." Acoustical Physics **49**(3): 354-360.

Savakus, H. P., Klicker, K. A., et al. (1981). "PZT-epoxy piezoelectric transducers: A simplified fabrication procedure." Materials Research Bulletin **16**(6): 677-680.

Schmitz, A. C., Gianfelice, D., et al. (2008). "Image-guided focused ultrasound ablation of breast cancer: current status, challenges, and future directions." Eur Radiol **18**(7): 1431-1441.

Seip, R., Chen, W., et al. (2005). "Annular and Cylindrical Phased Array Geometries for Transrectal High-Intensity Focused Ultrasound (HIFU) using PZT and Piezocomposite Materials." AIP Conference Proceedings **754**(1): 229-232.

Sherrit, S. and Mukherjee, B. K. (2007). "**Characterization of Piezoelectric Materials for Transducers**." Dielectric and Ferroelectric Reviews.(Cited as: arXiv:0711.2657).

Sherrit, S., Wiederick, H. D., et al. (1992). "Nun-iterative evaluation of the real and imaginary material constants of piezoelectric resonators." Ferroelectrics **134**(1): 111-119.

Shrout, T. R., Chang, Z. P., et al. (1990). "Dielectric behavior of single crystals near the (1−X) Pb(Mg1/3Nb2/3)O3-(x) PbTiO3 morphotropic phase boundary." Ferroelectrics Letters Section **12**(3): 63-69.

Singletary, S. E. (2002). "Surgical margins in patients with early-stage breast cancer treated with breast conservation therapy." Am J Surg **184**(5): 383-393.

Smith, W. A. and Auld, B. A. (1991). "Modeling 1-3 composite piezoelectrics: thickness-mode oscillations." Ultrasonics, Ferroelectrics and Frequency Control, IEEE Transactions on **38**(1): 40-47.

Smits, J. G. (1976). "Iterative Method for Accurate Determination of the Real and Imaginary Parts of the Materials Coefficients of Piezoelectric Ceramics." Sonics and Ultrasonics, IEEE Transactions on **23**(6): 393-401.

Sokka, S. D., King, R., et al. (2003). "MRI-guided gas bubble enhanced ultrasound heating in in vivo rabbit thigh." Physics in Medicine and Biology **48**(2): 223.

ter Haar, G. (2001). "Acoustic surgery." Physics Today **54**(12): 29-34.

ter Haar, G. (2007a). "Therapeutic applications of ultrasound." Progress in Biophysics and Molecular Biology **93**(1–3): 111-129.

ter Haar, G. (2007b). "Turning up the Power: High Intensity Focused Ultrasound (HIFU) for the Treatment of Cancer." Ultrasound **15**(2): 73-77.

ter Haar, G. and Robertson, D. (1993). "Tissue destruction with focused ultrasound in vivo." Eur Urol. **23**(suppl. 1): 8-11.

ter Harr, G., Clarke, R. L., et al. (1991). "Trackless surgery using focused ultrasound: Technique and case report." Minimally Invasive Therapy & Allied Technologies **1**(1): 13-19.

Veronesi, U., Cascinelli, N., et al. (2002). "Twenty-Year Follow-up of a Randomized Study Comparing Breast-Conserving Surgery with Radical Mastectomy for Early Breast Cancer." New England Journal of Medicine **347**(16): 1227-1232.

Vlastos, G. and Verkooijen, H. M. (2007). "Minimally Invasive Approaches for Diagnosis and Treatment of Early-Stage Breast Cancer." The Oncologist **12**(1): 1-10.

Wallace, M. F. (2007). Single Crystal Acoustic Transducers for High Performance Underwater Sonar Systems, University of West of Scotland. **Doctor of Philosophy**.

Wallace, M. F., Marin, P., et al. (2007). Effects of Increasing Environmental Temperature on the Practical Performance of PMN-PT and PZN-PT Single Crystals. Ultrasonics Symposium, 2007. IEEE.

Wang, Y., Tyrer, J., et al. (2007). "Measurement of focused ultrasonic fields using a scanning laser vibrometer." J Acoust Soc Am **121**(5 Pt1): 2621-2627.

Wang, Y. and Ye, F. (2007). "The Measurement of HIFU Field Using a Reflective Needle Hydrophone." AIP Conference Proceedings **911**(1): 3-7.

Welberry, T. R., Goossens, D. J., et al. (2010). "Monte Carlo Simulation Study of Diffuse Scattering in PZT, Pb(Zr,Ti)O3." Metallurgical and Materials Transactions A **41**(5): 1110-1118.

Wharton, I. P., Rivens, I. H., et al. (2007). "Design and development of a prototype endocavitary probe for high-intensity focused ultrasound delivery with integrated magnetic resonance imaging." J Magn Reson Imaging **25**(3): 548-556.

William L. Donegan and Spratt, J. S. (2002). Cancer of the Breast. USA, Saunders, Elsevier Science.

Wolny, W. W. (2005). "Application driven industrial development of piezoceramics." Journal of the European Ceramic Society **25**(12): 1971-1976.

Wu, F., Wang, Z., et al. (2003). "A randomised clinical trial of high-intensity focused ultrasound ablation for the treatment of patients with localised breast cancer." Br J Cancer. **89**(12): 2227–2233.

Wu, F., Wang, Z.-B., et al. (2004). "Extracorporeal high intensity focused ultrasound ablation in the treatment of 1038 patients with solid carcinomas in China: an overview." Ultrasonics Sonochemistry **11**(3–4): 149-154.

Wu, F., Wang, Z.-B., et al. (2005). "Extracorporeal high intensity focused ultrasound treatment for patients with breast cancer." Breast Cancer Research and Treatment **92**(1): 51-60.

Xuecang, G., Ritter, T. A., et al. (1998). Characterization of electromechanical properties of relaxor-PT piezoelectric single crystals. Ultrasonics Symposium, 1998. Proceedings., 1998 IEEE.

Ye, Z. G., Noheda, B., et al. (2001). "Monoclinic phase in the relaxor-based piezoelectric/ferroelectric Pb(Mg1/3Nb2/3)O3-PbTiO3 system." Physical Review B **64**(18): 184114.

Zhang, R., Jiang, B., et al. (2001). "Elastic, piezoelectric, and dielectric properties of multidomain 0.67Pb(Mg1/3Nb2/3)O3--0.33PbTiO3 single crystals." Journal of Applied Physics **90**(7): 3471-3475.

Zhang, R., Jiang, W., et al. (2002). "Elastic, Dielectric and Piezoelctric Coefficients of Domain Engineered 0.70Pb(Mg1/3Nb2/3)O3-0.30PbTiO3 Single Crystal." AIP Conference Proceedings **626**(1): 188-197.

Zhang, S., Lee, S.-M., et al. (2008a). "Elastic, Piezoelectric, and Dielectric Properties of 0.71Pb(Mg1/3Nb2/3)O3–0.29PbTiO3 Crystals Obtained by Solid-State Crystal Growth." Journal of the American Ceramic Society **91**(2): 683-686.

Zhang, S., Li, F., et al. (2011). Evaluation of PMN-PT based crystals for various applications. Applications of Ferroelectrics (ISAF/PFM), 2011 International Symposium on and 2011 International Symposium on Piezoresponse Force Microscopy and Nanoscale Phenomena in Polar Materials.

Zhang, S., Li, F., et al. (2013). "Relaxor-PbTiO3 single crystals for various applications." Ultrasonics, Ferroelectrics and Frequency Control, IEEE Transactions on **60**(8): 1572-1580.

Zhang, S., Luo, J., et al. (2008b). "Characterization of Pb(In1/2Nb1/2)O 3--Pb(Mg1/3Nb2/3)O3-PbTiO3 ferroelectric crystal with enhanced phase transition temperatures." Journal of Applied Physics **104**(6): 064106.

Zhang, S. and Shrout, T. R. (2010). "Relaxor-PT single crystals: observations and developments." Ultrasonics, Ferroelectrics and Frequency Control, IEEE Transactions on **57**(10): 2138-2146.

Zhang, S., Xia, R., et al. (2005). "Piezoelectric materials for high power, high temperature applications." Materials Letters **59**(27): 3471-3475.

Zhou, Y. (2011). "High intensity focused ultrasound in clinical tumor ablation." World J Clin Oncol. **2(1)**: 8-27.

Zhou, Y., Zhai, L., et al. (2006). "Measurement of high intensity focused ultrasound fields by a fiber optic probe hydrophone." J Acoust Soc Am **120**(2): 676-685.

APPENDICIES

Appendix A: Derivation of equations for calculating material coefficients

h = g * cD	
h33 =	g31 x cD13 + g32 x cD23 + g33 x cD33
	g31 x cD13 + g31 x cD13 + g33 x cD33
cD13 =	(h33 - g33 x cD33) / (2 x g31)
e = d * cE	
e33 =	d31 x cE13 + d32 x cE23 + d33 x cE33
	d31 x cE13 + d31 x cE13 + d33 x cE33
cE13 =	(e33 - d33 x cE33) / (2 x d31)
sE * cE = 1	
sE13 =	(1 - sE33 x cE33) / (2 x cE13)
sD * cD = 1	
sD13 =	(1 - sD33 x cD33) / (2 x cD13)
sE * cE = 1	
(4mm) sE12 (solution 1)=	(-1) x ({ [8pNs^2 x sE11 - (2-8/pi^2)]^2 - 64p^2 x Ns^4 x sE11^2 + 16p x Ns^2 x sE11 }^1/2 + 8pNs^2 x sE11 - 2 + 8/pi^2) / 8pNs^2
(4mm) sE12 (solution 2) =	({ [8pNs^2 x sE11 - (2-8/pi^2)]^2 - 64p^2 x Ns^4 x sE11^2 + 16p x Ns^2 x sE11 }^1/2 - 8pNs^2 x sE11 + 2 - 8/pi^2) / 8pNs^2
(6mm) sE12 =	(- sE11 x cE13 - sE13 x cE33) / cE13
d = e * sE	
d31 =	e31 x sE11 + e32 x sE21 + e33 x sE31
	e31 x sE11 + e31 x sE12 + e33 x sE13
e31 =	(d31 - e33 x sE13) / (sE11 + sE12)
d33 =	e31 x sE13 + e32 x sE23 + e33 x sE33
	e31 x sE13 + e31 x sE13 + e33 x sE33
e31 =	(d33 - e33 x sE33) / (2 x sE13)
sE * cE = 1	
	sE11 x cE11+ sE12 x cE12+ sE13 x cE13
cE12 =	(1 - sE11 x cE11- sE13 x cE13) / sE12
cE12 =	(- sE12 x cE11- sE13 x cE13) / sE11
cE11 =	(sE11 - (sE11 - sE12) x sE13 x cE13) / (sE11^2-sE12^2)
sD * cD = 1	
cD12 =	(1 - sD11 x cD11- sD13 x cD13) / sD12
cD12 =	(- sD12 x cD11- sD13 x cD13) / sD11
cD11 =	(sD11 - (sD11 - sD12) x sD13 x cD13) / (sD11^2-sD12^2)

Appendix B-1: Flowchart of composite preparation process

(a) Dice bulk sample into pillars in two directions

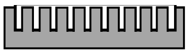

(b) Put diced sample into mould and fill epoxy on top; degas epoxy within vacuum chamber and left to cure

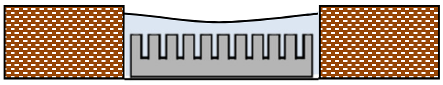

(c) After epoxy cured, lap composite on both sides till reaches to required thickness

(d) Cut off epoxy edges with dicing and glue composites together using fast curing epoxy

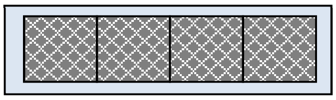

(e) Dice composites into triangular shape

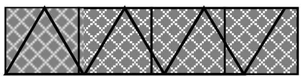

Appendix B-2: Modified flowchart of composite preparation process

(a) Place bulk material sample into mould and fill epoxy

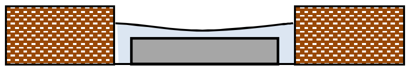

(b) Release sample from mould and lap surface flat

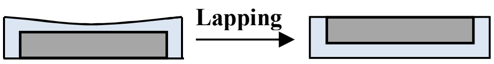

(c) Dice sample all through its thickness in two directions

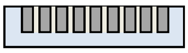

(d) Put diced sample back into mould and fill epoxy on top; degas epoxy within vacuum chamber and left to cure

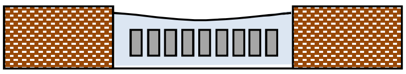

(e) Lap composite on both sides till reaches to required thickness

(f) Cut off epoxy edges with dicing and glue composites together using fast curing epoxy

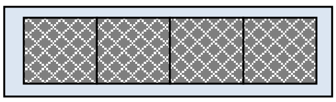

(g) Dice composites into triangular shape

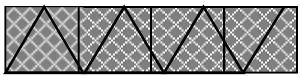

Appendix C-1: MATLAB program for computing the composite behaviour

```
%Calculates effective properties of composites, based on: W.A. Smith et al "Modeling 1-3
Composite Piezoelectrics...", IEEE Trans UFFC, vol. 38, no. 1, pp. 40-47, 1991.

% Author: Z Qiu, Univeristy of Dundee
% Created at 06 April 2011
% Amended at 19 Aug 2011, call subprogram PiezoProp

% properties calculated in "PiezoProp.m"

%% VF: use a single number or range of values

VF = 0.6;
fe = 1E6;   % electrical frequency

%% Material coefficients required for Piezo material:
 % densC, cE(3,3), cE(1,2), cE(1,3), e(3,3), e(3,1), epsS(3,3)

piezo = 'pmnpt29zq';
piezofile = 'PiezoProperties.mat';
PiezoProp(piezo, piezofile);
load(piezofile);

%% Material coefficients required for polymer:
%   densP, c11, c12, eps
polymer = 'epofixZ';
polymerfile = 'PolymerProperties.mat';
PolymerProp(polymer, polymerfile);
load(polymerfile);

eps0=8.854e-12;

%% Thickness mode oscillations
dens_ = VF*densC + (1-VF)*densP;
c33E_ = VF.*(cE(3,3) - (2*(1-VF)*(cE(1,3)-c12)^2 )./ (VF*(c11+c12)+(1-
VF)*(cE(1,1)+cE(1,2)))) + (1-VF)*c11 ;
e33_ = VF.* (e(3,3) - (2*(1-VF)*(cE(1,3)-c12)*e(3,1))./(VF*(c11+c12)+(1-
VF)*(cE(1,1)+cE(1,2))));
eps33S_ = VF.* (epsS(3,3) + (2*(1-VF)*e(3,1)^2)./(VF*(c11+c12)+(1-
VF)*(cE(1,1)+cE(1,2))))+ (1-VF)*eps;
eps33Sr_ = eps33S_/eps0;
c33D_ = c33E_ + (e33_.^2)./eps33S_;
kT_ = e33_./sqrt(c33D_.*eps33S_);      % coupling coefficient
Z_ = sqrt(c33D_ .* dens_);             % acoustic impedance
vl_ = sqrt(c33D_ ./ dens_);

freq = fe / sqrt(1-kT_^2)   % mechanical frequency
th_ = vl_./(2*freq);

%% display and plot
disp(' ')
disp('Net Composite Material Properties:');
disp(['Piezo material: ', piezo]);
disp(['Volume_ceramic (%) = ',num2str(VF*100,'%-7.0f')]);
disp(['eps33S_r_comp =      ',num2str(eps33Sr_,'%-7.1f')]);
disp(['c33E_comp (GPa) =    ',num2str(c33E_/1e9,'%-7.1f')]);
```

```
disp(['c33D_comp (GPa) =    ',num2str(c33D_/1e9,'%-7.1f')]);
disp(['e33_comp (C/m^2) =   ',num2str(e33_,'%-7.2f')]);
disp(['dens_comp (kg/m^3) = ',num2str(dens_,'%-7.0f')]);
disp(['vl_comp (m/s) =      ',num2str(vl_,'%-7.0f'),'']);
disp(['Z_comp (MRayl) =     ',num2str(Z_/1e6,'%-7.2f')]);
disp(['kT_comp =            ',num2str(kT_,'%-7.2f')]);
disp(['th_comp (mm) =       ',num2str(th_.*1e3,'%-7.3f')]);

if length(VF)>9
   figure(1);
   subplot(2,2,1), plot(VF, kT_);
   plottitle =('Effective Properties of composite piezoelectric');
   title('Piezoelectric Coulpling Coefficient')
   subplot(2,2,2), plot(VF, Z_/1e6);
   title('Acoustic Impedance')
   subplot(2,2,3), plot(VF, eps33Sr_);
   title('Relative Dielectric constant')
   subplot(2,2,4), plot(VF, vl_);
   title('Effective velocity of composite piezoelectric')
   figure(2);
   plot(VF, th_);
   title('Thickness of composite')
end
```

Appendix C-2: Calculated composite behaviour

Piezo material			PZ26	PZ54	PMN-29%PT
Volume_ceramic	(%)	=	60	60	60
fe_comp	(MHz)	=	1	1	1
fm_comp	(MHz)	=	1.205	1.166	1.488
eps33S_r_comp		=	425.2	934.6	575.9
c33E_comp	(GPa)	=	55	69.5	37.6
c33D_comp	(GPa)	=	79.9	94.4	83.3
e33_comp	(C/m^2)	=	9.68	14.37	15.26
dens_comp	(kg/m^3)	=	5108	5144	5330
vl_comp	(m/s)	=	3955	4285	3953
Zac_comp	(MRayl)	=	20.2	22.04	21.07
kT_comp		=	0.56	0.51	0.74
th_comp	(mm)	=	1.641	1.837	1.328

Appendix D: Fabrication process of printing PCB

Two simple designs were made in house for this project. The first design is for external connectors of the faceted bowl transducers, which has 34 straight tracks been cross-arranged for active and ground signals; the second design is a bit more complex which is used for grouping 96 elements into 32 channels, in order to connect the transducer to external driven system, DSL32CH in this work. The UV exposure unit, Etching tank and other related consumables for making the PCBs are all from MEGA Electronics Limited (Cambridge, UK).

(a)

(b)

Figure (a) UV exposure unit, LV 202E, (b) PA series Bubble Etching Tank, PA104, from MEGA Electronics Limited (Cambridge, UK)

The following steps are the actual steps used in this project to produce these two designs on double-sided photoresist broad (RS 397-0053**).**

1. **Preparing the artwork**

The designs were draw on computer first using free 2D CAD software (DraftSight, Dassault Systèmes S.A.). Printed a 1:1 artwork on a transparent film via a laser printer. Since a double-sided design is required in this work, the two sheets of artworks for each side need to be positioned in advance to ensure a good alignment. Once the sheets are aligned, three sides of four will be fixed using tape, like an envelope leaving one side for inserting the broad later.

2. **Exposing the photoresist broad**

Remove the protective black plastic from the photoresist broad, and position the broad into the previous made 'envelope'. A good contact should be ensures between the artwork sheets and broad. Place both in the UV exposure unit with one side down.

Closing the lid will start the exposure automatically. The timer was set to be 3 minute. After one side done, flip over the broad and repeat the process for the other side.

3. Developing the pattern

The artworks were designed using DesignSpark PCB software.

4. Spray washing

After the developing process, the board is washed immediately.

5. Etching

The developed and washed board is then placed into the etching tank and immersed into the etchant, with the lid on the air pump is turned on. The temperature is controlled at 45 ^{o}C and the etching should take approximately five minutes.

6. Resist Stripping

The PCB will now consist of an etched circuit still covered in the photoresist. This can be removed with the SN120 resist strip applicator. The photoresist should be striped off in approximately 2-3 minutes. Once the photoresist has been stripped from the circuit the board are then spray washed again.

7. Scrub Cleaning

The broad is then thoroughly dried and mechanically scrubbed and a PC180 Polifix Silica Block. This will ensure the copper circuit is perfectly clean by removing any oxidisation, passivation or chlorides left by the water as well. After scrubbing, the broad should be wiped with a clean dry tissue.

Appendix E-1 Measurement statistics of PRAP analyses for PZ54 ceramic

PZ54 Piezoceramic properties From Direct PRAP Result							
Property	real			Imaginary			Modes
k_t	0.4840	±	0.0036	-0.0017	±	0.0009	TE
k_{33}	0.5860	±	0.0130	-0.0280	±	0.0360	LE
k_{31}	0.3000	±	0.0017	0.0065	±	0.0040	LTE
k_{15}	0.5230	±	0.0240	-0.0069	±	0.0094	TS
e_{33}	22.2000	±	2.1000	-0.1310	±	0.0730	TE
e_{15}	11.8000	±	1.5000	-0.1900	±	0.3800	TS
h_{33}	1.65E+09	±	1.50E+08	-1.60E+05	±	1.55E+06	TE
h_{15}	9.20E+08	±	1.00E+08	-5.20E+06	±	1.91E+07	TS
d_{33}^{*}	3.22E-10	±	4.40E-11	-8.30E-12	±	3.59E-11	LE
d_{31}	-1.63E-10	±	1.20E-11	9.50E-13	±	1.36E-12	LTE RE
d_{15}	4.13E-10	±	4.70E-11	-1.30E-11	±	1.80E-11	TS
g_{33}	0.01470	±	0.00170	-0.00120	±	0.00200	LE
g_{31}	-0.00773	±	0.00060	0.00019	±	0.00019	LTE
g_{15}	0.02340	±	0.00180	-2.40E-04	±	4.90E-04	TS
c^E_{33}	1.19E+11	±	5.80E+09	3.90E+08	±	1.70E+08	TE
c^E_{55}	2.85E+10	±	1.70E+09	3.80E+08	±	3.40E+08	TS
c^D_{33}	1.56E+11	±	4.40E+08	1.69E+08	±	3.80E+07	TE
c^D_{55}	3.93E+10	±	3.60E+09	1.80E+08	±	2.10E+08	TS
s^E_{11}	1.37E-11	±	2.40E-13	-3.20E-14	±	2.80E-14	LTE RE
s^E_{12}	-4.95E-12	±	7.60E-15	-9.50E-15	±	2.40E-15	RE
s^E_{33}	1.38E-11	±	9.80E-14	-5.10E-13	±	4.20E-13	LE
s^E_{55}	3.51E-11	±	1.90E-12	-5.00E-13	±	4.70E-13	TS
s^D_{33}	9.13E-12	±	1.20E-13	1.20E-13	±	4.10E-13	LE
s^D_{55}	2.56E-11	±	1.90E-12	-9.80E-13	±	7.40E-14	TS
σ_p^E	0.3564	±	5.60E-04	7.90E-04	±	1.30E-04	RE
ε^T_{33}	2.10E-08	±	2.30E-09	6.20E-10	±	4.37E-09	LTE LE
ε^S_{33}	1.36E-08	±	1.60E-09	-7.90E-11	±	3.80E-11	TE LE
ε^T_{11}	1.78E-08	±	3.10E-09	-4.00E-10	±	8.60E-10	TS
ε^S_{11}	1.29E-08	±	2.10E-10	-1.50E-10	±	5.40E-10	TS

Appendix E-2 Measurement statistics of PRAP analyses for PMN-29%PT piezocrystal

PMN-29%PT Piezoceramic properties From Direct PRAP Result							
Property	real			Imaginary			Modes
k_t	0.5567	±	0.0062	0.0026	±	0.0023	TE
k_{33}	0.9000	±	0.0017	0.0010	±	0.0038	LE
k_{31}	0.4350	±	0.0350	0.0031	±	0.0052	LTE
k_{15}	0.3080	±	0.0170	-0.0039	±	0.0850	TS
k_{eff}	0.59	±	0.072	0.013	±	0.012	LTE Rotated
e_{33}	20.0000	±	1.1000	-0.0097	±	0.5123	TE
e_{15}	8.8500	±	0.9000	-0.5500	±	0.3400	TS
h_{33}	2.58E+09	±	9.20E+07	7.70E+07	±	4.90E+07	TE
h_{15}	8.15E+08	±	1.60E+07	3.60E+07	±	2.00E+07	TS
d_{33}	1.37E-09	±	1.80E-11	-4.00E-11	±	5.30E-11	LE
d_{31}	-6.50E-10	±	6.50E-11	3.60E-12	±	1.30E-11	LTE
d_{15}	1.29E-10	±	1.60E-11	9.50E-13	±	5.90E-12	TS
g_{33}	0.03060	±	0.00087	-0.00004	±	0.00072	LE
g_{31}	-0.01460	±	0.00200	0.00006	±	0.00069	LTE
g_{15}	0.01070	±	0.00028	4.00E-04	±	2.70E-04	TS
c^E_{33}	1.15E+11	±	1.30E+09	1.79E+09	±	2.10E+08	TE
c^E_{55}	6.89E+10	±	1.40E+09	7.00E+08	±	4.30E+08	TS
c^D_{33}	1.67E+11	±	3.10E+09	3.28E+09	±	5.50E+08	TE
c^D_{55}	7.61E+10	±	8.40E+08	5.60E+08	±	1.90E+08	TS
s^E_{11}	5.05E-11	±	3.80E-12	-9.10E-13	±	4.00E-13	LTE
$s^E_{45:Z11}$	2.05E-11	±	2.30E-12	-3.70E-13	±	2.40E-13	LTE Rotated
s^E_{33}	5.20E-11	±	1.50E-12	-1.40E-12	±	2.40E-12	LE
s^E_{55}	1.45E-11	±	3.00E-13	-1.52E-13	±	9.80E-14	TS
s^D_{33}	9.61E-12	±	3.50E-13	-1.70E-13	±	1.50E-13	LE
s^D_{55}	1.31E-11	±	1.40E-13	9.70E-14	±	3.20E-14	TS
ε^T_{33}	4.50E-08	±	6.40E-09	3.00E-10	±	2.24E-09	LTE LE
ε^S_{33}	8.20E-09	±	2.00E-10	-1.30E-10	±	2.90E-10	TE LE
ε^T_{11}	1.20E-08	±	1.40E-09	1.31E-09	±	3.90E-10	TS
ε^S_{11}	1.08E-08	±	1.10E-09	-1.14E-09	±	3.00E-10	TS

Appendix F-1 Full elasto-electric matrix for PZ26 ceramic

Elasto-electric matrix for PZ26 ceramic

Measured elastic compliance constants, S_{ij} (10^{-12} m^2/N), and elastic stiffness constants, C_{ij} (10^{10} N/m^2)

s^E_{11}	s^E_{12}	s^E_{13}	s^E_{33}	s^E_{55}	s^E_{66}
13.00	-4.35	7.05	19.60	33.20	34.70
s^D_{11}	s^D_{12}	s^D_{13}	s^D_{33}	s^D_{55}	s^D_{66}
11.60	-5.74	-3.47	10.50	23.10	34.70
c^E_{11}	c^E_{12}	c^E_{13}	c^E_{33}	c^E_{55}	c^E_{66}
16.80	11.00	9.99	12.30	3.01	2.88
c^D_{11}	c^D_{12}	c^D_{13}	c^D_{33}	c^D_{55}	c^D_{66}
16.90	11.20	9.33	15.80	4.34	2.88

Measured piezoelectric coefficients, d_{ij} (10^{-10} C/N), e_{ij} (C/m^2), g_{ij}(10^{-3} Vm/N), h_{ij}(10^8 V/m)

d_{33}	d_{31}	d_{15}	g_{33}	g_{31}	g_{15}
3.28	-1.28	3.27	28.00	-10.90	38.90
e_{33}	e_{31}	e_{15}	h_{33}	h_{31}	h_{15}
14.70	-2.80	9.86	23.70	-4.52	13.40

Measured piezoelectric coefficients, d_{ij} (10^{-10} C/N), e_{ij} (C/m^2), g_{ij}(10^{-3} Vm/N), h_{ij}(10^8 V/m)

k_t	k_{33}	k_{31}	k_{15}
0.47	0.68	0.33	0.55
ε^T_{r33}	ε^T_{r11}	ε^S_{r33}	ε^S_{r11}
1330	1190	700	828

Appendix F-2 Full elasto-electric matrix for Mn:PIN-PMN-PT piezocrystal

Elasto-electric matrix for Mn: PIN-PMN-PT piezocrystal

Measured elastic compliance constants, S_{ij} (10^{-12} m^2/N), and elastic stiffness constants, C_{ij} (10^{10} N/m^2)

s^E_{11}	s^E_{12}	s^E_{13}	s^E_{33}	s^E_{55}	s^E_{66}
45.40	-15.90	-28.10	62.40	15.40	27.80
s^D_{11}	s^D_{12}	s^D_{13}	s^D_{33}	s^D_{55}	s^D_{66}
34.40	-26.90	-3.90	9.20	13.90	27.80
c^E_{11}	c^E_{12}	c^E_{13}	c^E_{33}	c^E_{55}	c^E_{66}
12.80	11.10	10.80	11.30	6.50	3.60
c^D_{11}	c^D_{12}	c^D_{13}	c^D_{33}	c^D_{55}	c^D_{66}
13.30	11.70	9.00	17.00	7.20	3.60

Measured piezoelectric coefficients, d_{ij} (10^{-10} C/N), e_{ij} (C/m^2), g_{ij}(10^{-3} Vm/N), h_{ij}(10^8 V/m)

d_{33}	d_{31}	d_{15}	g_{33}	g_{31}	g_{15}
13.4	-6.1	1.3	39.7	-18.1	8.8
e_{33}	e_{31}	e_{15}	h_{33}	h_{31}	h_{15}
16.8	-5.2	8.6	34.2	-10.7	8.3

Measured piezoelectric coefficients, d_{ij} (10^{-10} C/N), e_{ij} (C/m^2), g_{ij}(10^{-3} Vm/N), h_{ij}(10^8 V/m)

k_t	k_{33}	k_{31}	k_{15}
0.58	0.92	0.39	0.31
ε^T_{r33}	ε^T_{r11}	ε^S_{r33}	ε^S_{r11}
3811	1326	553	1169

Appendix G: Array element working Statues

The elements marked in red are the individuals not working, originally either by shorting or opening. In order to remove the effects brought to the whole array, all non-working elements were disconnected from the external connection PCB adapters.

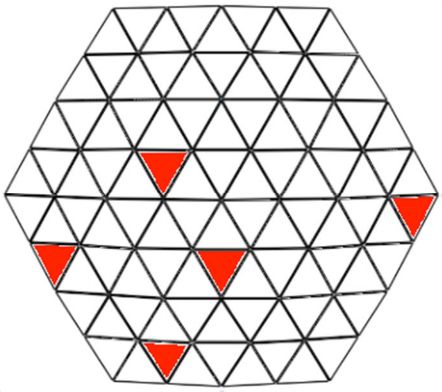 PZ26 ceramic array	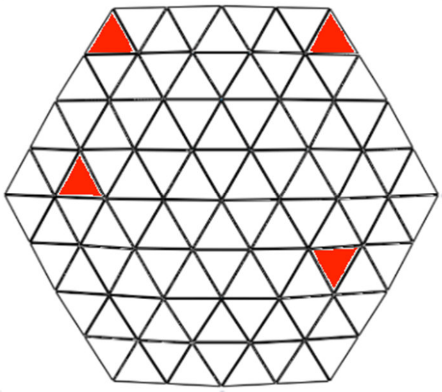 PZ26 composite array
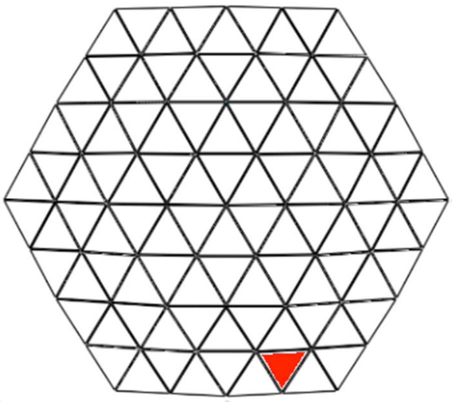 PZ54 composite array	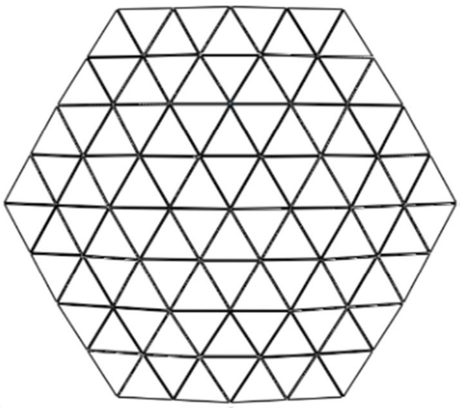 PMN-PT composite array

Appendix H: Array element configuration diagram with interconnection arrangement

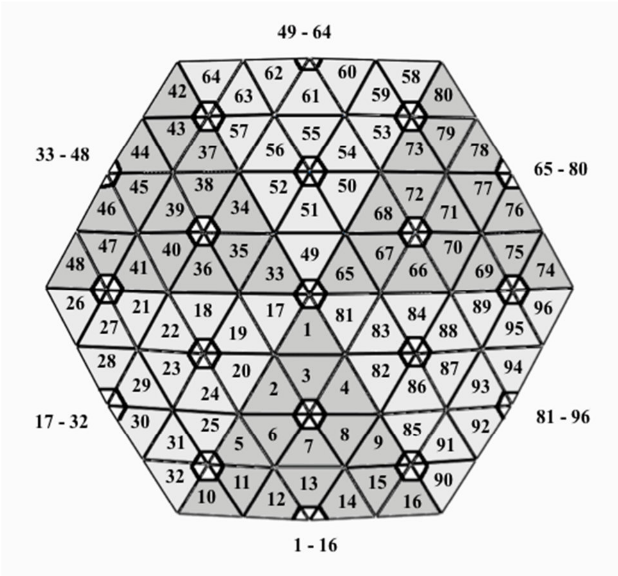

Appendix I: Array element arrangement for grouping into 32 channels

Channel No.	1	2	3	4	5	6	7	8
Element No.	46	43	63	60	80	77	74	94
	47	44	64	61	58	78	75	95
	48	45	42	62	59	79	76	96

Channel No.	9	10	11	12	13	14	15	16
Element No.	91	15	12	32	29	26	39	57
	92	16	13	10	30	27	40	37
	93	90	14	11	31	28	41	38

Channel No.	17	18	19	20	21	22	23	24
Element No.	54	72	69	87	9	6	24	21
	55	73	70	88	85	7	25	22
	56	53	71	89	86	8	5	23

Channel No.	25	26	27	28	29	30	31	32
Element No.	34	50	66	82	2	18	33	1
	35	51	67	83	3	19	49	81
	36	52	68	84	4	20	65	17

Appendix J-1: Definitions of The Human body Plane in MRI

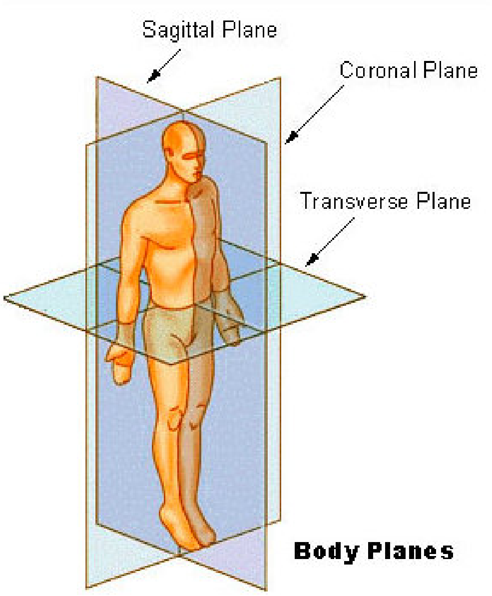

Appendix J-2: Definitions of Patient Coordinate System

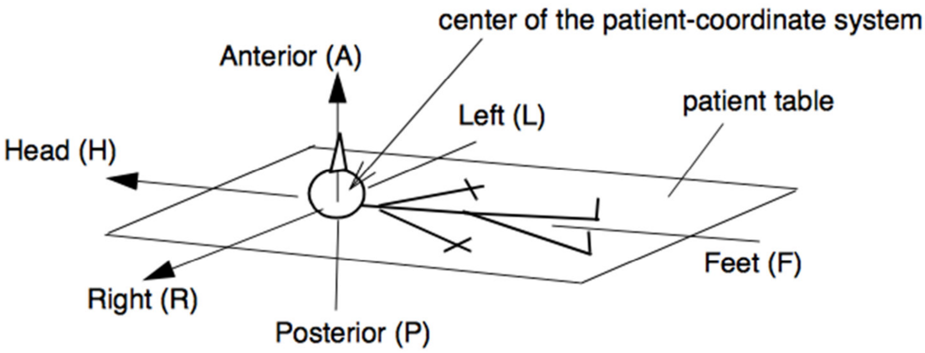

Appendix J-3: Views of three centred main slices of MRI